X-rays Tracing the Star Formation History of the Magellanic Clouds

Manami Sasaki
aus Tokio, Japan
München, den 21. Dezember 2001

Zusammenfassung

Röntgenstrahlung als Spuren der Sternentstehungsgeschichte in den Magellanschen Wolken

Manami Sasaki

Galaxien setzen sich aus Sternen und der den interstellaren Raum auffüllenden Materie zusammen. Am Ende der Sternentwicklung entstehen Weiße Zwerge, Neutronensterne, Schwarze Löcher sowie Supernova-Überreste, die aufgrund hoher Temperaturen Röntgenstrahlung emittieren. Deshalb liefern astronomische Beobachtungen im Röntgenbereich wichtige Erkenntnisse für das Verständnis des Aufbaus und der Entwicklungsgeschichte von Galaxien.

Die Große Magellansche Wolke (Large Magellanic Cloud, LMC) und die Kleine Magellansche Wolke (Small Magellanic Cloud, SMC), jeweils ca. 160.000 und 190.000 Lichtjahre von unserem Sonnensystem entfernt, befinden sich in unmittelbarer Umgebung unserer Milchstraße und sind somit die am besten geeigneten Objekte für die Untersuchung von Galaxien in ihrer Ganzheit. Während der Betriebsphase des Röntgensatelliten ROSAT in den Jahren von 1990 bis 1998 sind etwa 900 Beobachtungen von der LMC und der SMC durchgeführt worden, die das Bild der Magellanschen Wolken (MCs) im Röntgenlicht enthüllten.

Erstes Hauptziel dieser Doktorarbeit bestand darin, die erste umfassende Studie der Röntgenquellen in den MCs anhand von Archiv-Daten vom ROSAT "High Resolution Imager" (HRI) durchzuführen. Die Ergebnisse ermöglichen in Kombination mit den Quell-Katalogen von Haberl & Pietsch (1999a) und Haberl et al. (2000), die mit Hilfe der Daten von ROSAT "Position Sensitive Proportional Counter" (PSPC) erstellt wurden, eine ganzheitliche Untersuchung der MCs im Röntgenbereich. Da die Ortsauflösung des HRIs höher war als die des PSPCs, wurden insbesondere in den von Quellen dicht bevölkerten Regionen der MCs zusätzliche, neue Quellen entdeckt. Die ROSAT-Quellkataloge stellen nicht nur eine exzellente Grundlage für die Analyse der neu detektierten Quellen dar, sondern geben auch Aufschluss über die Quellpopulation in den MCs und ihrer bisherigen Entwicklung.

Für die Erstellung der Kataloge von Röntgenquellen, die mit dem ROSAT-HRI in den Feldern der LMC und der SMC detektiert wurden, standen im ROSAT-Archiv Daten von ca. 600 Beobachtungen zur Verfügung. In einem $10° \times 10°$ Ausschnitt des Himmels, der die LMC abdeckt, sind 397 Röntgenquellen detektiert worden; im $5° \times 5°$ Feld um die SMC sind es 121 Quellen. Diese ROSAT-HRI-Kataloge enthalten neben den Objekten in den Magellanschen Wolken auch Galaktische Sterne im Vordergrund oder Galaxien, Aktive Galaktische Kerne bzw. Galaxienhaufen im Hintergrund. Zur Bestimmung der Arten von Röntgenquellen sind die neuen Kataloge mit Ergebnissen von anderen Röntgensatelliten sowie mit verschiedenen Katalogen aus Beobachtungen in anderen Wellenlängenbereichen verglichen worden. Die Röntgeneigenschaften wie

Ausdehnung, Flussvariabilität und "Hardness Ratio" - das Verhältnis vom weichen Anteil der Röntgenstrahlung zum harten Anteil - in Kombination mit optischen und Nah-Infrarot-Eigenschaften führten zur Klassifikation der HRI-Quellen.

Röntgenquellen, die in der Entfernung von den MCs mit ROSAT detektiert werden konnten, sind Röntgendoppelsterne (X-ray binaries, XBs; Doppelsternsysteme mit einem Neutronenstern oder einem Schwarzen Loch), Supernova-Überreste (supernova remnants, SNRs) oder Superweiche Quellen (supersoft sources, SSSs; Doppelsternsysteme mit einem Weißen Zwerg). Sowohl SSSs als auch XBs und SNRs sind Vertreter der Endstadien der Sternentwicklung, sodass ihre räumliche Verteilung Aufschluss über die Entwicklungsgeschichte der Galaxien gibt.

Der HRI-Katalog für die LMC enthält 29 bereits bekannte SNRs und SNR-Kandidaten. Zusätzlich dazu sind in dieser Arbeit fünf neue HRI-Quellen in der LMC aufgrund ihrer Ausdehnung als weitere Kandidaten für SNRs vorgeschlagen worden. In der SMC sind vom HRI sieben SNRs beobachtet worden. Die HRI-Daten lieferten genaue Messungen der Struktur und Ausdehnung der SNRs.

Die Anzahl der detektierten SSSs in der LMC beträgt fünf, in der SMC sind es vier. Für die meisten dieser SSSs ist eine starke Flussvariabilität nachgewiesen worden.

In der LMC sind 10 bereits bekannte XBs und Kandidaten beobachtet worden, der SMC-Katalog enthält 17 solche Quellen. Die meisten dieser XBs sind massereiche XBs (high-mass X-ray binaries, HMXBs), die aus einem Überriesen-Stern oder einem Be-Stern als Begleitstern und einem Neutronenstern oder Schwarzen Loch bestehen. Besonders in der SMC ist bisher eine relativ große Anzahl von HMXBs mit Be-Sternen entdeckt worden (22 Doppelsternsysteme mit Be-Sternen und nur ein System mit einem Überriesen). Zwei weitere LMC-Quellen und 10 SMC-Quellen kommen als neue Kandidaten für XBs in Frage. Die Anzahl und Verteilung der XBs weisen darauf hin, dass vor etwa 10^7 Jahren eine aktive Sternentstehung in den MCs stattgefunden hat.

Der zweite Hauptteil der Arbeit beschäftigte sich mit der diffusen Emission des heißen Interstellaren Medium (ISM) der MCs. Durch die Analyse der Daten, die mit dem ROSAT-PSPC in den oben genannten Feldern der LMC und der SMC gewonnen wurden, ist zum ersten Mal die Temperaturverteilung des heißen ISM-Anteils in den MCs mit einer Auflösung von $15' \times 15'$ bestimmt worden. Das Ergebnis zeigt, dass sich das heiße, interstellare Plasma jeweils über die ganze LMC und die ganze SMC erstreckt mit Temperaturen von etwa 10^6 bis 10^7 K. Aus dem Leuchtkraft-Profil des heißen ISM wurde die integrale Leuchtkraft von $1.4 \times 10^{39} \, \mathrm{erg \, s^{-1}}$ für die LMC und $6.0 \times 10^{37} \, \mathrm{erg \, s^{-1}}$ für die SMC jeweils in den beobachteten Bereichen errechnet. Die Analyse der ROSAT-PSPC-Daten lieferte somit eine signifikante Messung am heißen ISM der MCs. Von besonderer Bedeutung sind die Ergebnisse zur SMC, deren diffuse Röntgenemission in der Vergangenheit nicht sehr detailliert untersucht worden war.

Es wird allgemein vermutet, dass der interstellare Raum durch Sternwinde und Supernova-Explosionen aufgeheizt wird. Expandierende Supernova-Überreste und interstellare Blasen, die von Sternwinden um massereiche Sterne ausgeformt werden, sammeln kälteres Gas ($T < 10^5$ K) auf. Dadurch entstehen in den Galaxien schalenförmige Strukturen, die im Radio-Bereich beobachten werden können. Die diffuse

Röntgenemission kann als Überlagerung der Strahlung vom heißen Gas im Inneren der Schalen aus kaltem Gas und der Strahlung aus dem Halo der Galaxien betrachtet werden. In beiden MCs stimmen die physikalischen Parameter wie Temperatur, Leuchtkraft und Stoßwellen-Geschwindigkeit gut mit den theoretischen Voraussagen über die Aufheizung des ISM durch Supernova-Überreste und Sternwinde überein. Dadurch werden nun durch Beobachtungen gestützte Anfangsbedingungen für die theoretische Beschreibung der weiteren Entwicklung des ISM geliefert. Hierbei führt es durch die Expansion des heißen Gases zur Fragmentation der Schalen und schließlich zur Bildung von sehr kalten, dichten Gaswolken, die sich größtenteils zu Sternentstehungsgebieten weiterentwickeln.

Weiterhin ermöglichte eine der ersten Beobachtungen des neuen Röntgensatelliten XMM-Newton die Durchführung der ersten Analyse der diffusen Emission der "supergiant shell" SGS LMC 2 am östlichen Rand des optisch sichtbaren Balkens der LMC anhand von Daten der "European Photo Imaging Camera" mit pn-Halbleiterstruktur (EPIC-PN). Diese besitzt im Vergleich zum ROSAT-PSPC eine verbesserte Energieauflösung, während die Ortsauflösung vergleichbar zum ROSAT-HRI ist. Auf der EPIC-PN-Aufnahme ist eine Region mit einem Durchmesser von etwa 100 pc zu erkennen, die sich durch eine stärkere diffuse Röntgenemission von ihrer Umgebung unterscheidet. Diese Region stimmt räumlich mit einer H II-Region in der LMC überein, sodass die diffuse Emission mit sehr hoher Wahrscheinlichkeit von der interstellaren Blase in der H II-Region stammt. Aus dem Spektrum konnte der physikalische Zustand des heißen, interstellaren Plasmas wie Elementhäufigkeit, Alter oder Ionisationsgrad genau ermittelt werden. Neben der Gas-Temperatur, die im Inneren der Blase höher als im umgebenden ISM ist, wurden aus den EPIC-PN-Daten weitere physikalische Parameter wie z. B. das Alter der interstellaren Blase hergeleitet.

Summary

X-rays Tracing the Star Formation History of the Magellanic Clouds

Manami Sasaki

Galaxies consist of stars and matter filling up the interstellar space. White dwarfs, neutron stars, black holes, and supernova remnants which all emit X-rays due to high temperature, are formed at the end of stellar evolution. Therefore, X-ray observations of galaxies are necessary to obtain crucial information for the better understanding of the galactic structure and evolution history.

The Large Magellanic Cloud (LMC) and the Small Magellanic Cloud (SMC) with a distance of 160.000 and 190.000 lightyears from the Solar system, respectively, are one of the closest galaxies to the Milky Way and offer an ideal site for studying the galaxies as a whole. From 1990 to 1998, ROSAT collected data of the LMC and the SMC in nearly 900 pointings, unveiling their entire picture in X-rays.

One of the main objectives of the thesis was to perform a profound analysis of the X-ray sources of the MCs based on the data of the ROSAT High Resolution Imager (HRI). In combination with the X-ray source catalogs of the ROSAT Position Sensitive Proportional Counter (PSPC) created by Haberl & Pietsch (1999a) and Haberl et al. (2000), the results of this thesis allow a extensive study of the MCs in the X-rays. Since the spatial resolution of the HRI was higher than that of the PSPC, additional new sources were detected, especially in crowded regions. These ROSAT source catalogs are not only an excellent basis for studying newly detected objects in the MCs, but also give information about the source population in the MCs and their evolution up to now.

Based on archival ROSAT HRI data of about 600 observations, complete source catalogs of the LMC and the SMC were created. For this purpose, data of the ROSAT HRI in a field of $10° \times 10°$ covering the LMC and in a $5° \times 5°$ region around the SMC was used. For the LMC region the catalog includes 397 sources and for the SMC region 121 sources. The catalogs contain not only X-ray sources within the MCs, but also Galactic stars in the foreground as well as galaxies, active galactic nuclei, or galaxy clusters in the background. In order to constrain the nature of the sources, the HRI catalog was cross-correlated with catalogs from other X-ray missions and data bases of other wavelength bands. The X-ray properties like hardness ratio (ratio between the soft component and the hard component of the X-ray emission), extent, flux variability combined with optical and near-infrared properties allowed to classify the X-ray sources.

Detectable sources at the distances of the MCs are X-ray binaries (XBs, binary systems with a neutron star or a black hole), supernova remnants (SNRs), or supersoft sources (SSSs, binary systems with a white dwarf). Since SSSs, XBs, and SNRs are objects at the final stages of the stellar evolution, their spatial distribution gives us clues about the evolution history of the galaxies.

The HRI catalog of the LMC contains 29 known SNRs and SNR candidates. Due to their extent, another five sources were suggested as candidates of SNRs in the LMC in this work. In the SMC, seven SNRs were observed by the HRI. Accurate measurements of the extent and the morphologies were obtained for the SNRs in the MCs.

As for the SSSs, five well known sources were detected in the LMC, and four in the SMC. Strong flux variability was verified for most of the SSSs.

Ten known XBs and candidates were observed in the LMC, 17 in the SMC. Most of these objects are high-mass X-ray binaries (HMXBs), i.e. binary systems consisting of a supergiant star or a Be star as companion star of either a neutron star or a black hole. Especially in the SMC, a relatively high number of HMXBs with Be stars were found so far (22 systems with Be stars and only one with a supergiant). Additional two LMC sources and ten SMC sources were classified as XB candidates. The number and distribution of the XBs indicate that an active star formation occured in the MCs about 10^7 years ago.

The second part of the thesis deals with the diffuse X-ray emission from the hot interstellar medium (ISM) in the MCs. Analyzing the ROSAT PSPC data of pointed observations within the same fields as for the ROSAT HRI data, the temperature distribution of the hot component of the ISM in the MCs was determined with a $15'$ $\times$ $15'$ resolution for the first time. The hot thin plasma of the ISM which extends over the whole LMC and the SMC has temperatures of 10^6 to 10^7 K. Furthermore, the X-ray luminosity profile of the hot ISM was also derived. The total luminosity within the observed area amounts to $1.4 \times 10^{39}\,\mathrm{erg\,s^{-1}}$ in the LMC and $6.0 \times 10^{37}\,\mathrm{erg\,s^{-1}}$ in the SMC. In this thesis, significant measurements of the hot ISM was achieved. The results on the SMC is of particular importance, since its diffuse X-ray emission had not been studied in detail so far.

High-temperature components of the ISM are thought to be caused in the surroundings of massive stars first by stellar winds which form interstellar bubbles, and later on by final supernova explosions. Around expanding bubbles and supernova remnants colder gas ($T < 10^5$ K) is swept up developing shells within galaxies. These shells were detected in radio observations. The diffuse X-ray emission is most likely a superposition of the emission from the hot gas in the interior of the cold gas shells and from the halo of these galaxies. In both MCs, the physical parameters, e.g. temperature, luminosity or shock velocity, agree well with the models of the heating of the ISM by supernova remnants and stellar winds. These values derived from observations can be used as initial conditions in models for further development of the ISM: Due to further expansion of the interior gas, the shells fragmentate and form clouds of very cold, dense gas, which are likely to evolve to star forming regions.

Finally, one of the first observations of the new X-ray satellite XMM-Newton allowed me to perform the first spectral analysis of the diffuse emission from the supergiant shell SGS LMC 2 at the eastern end of the optical bar of the LMC. Data of the pn-type European Photo Imaging Camera (EPIC-PN) was used, which has improved spectral

resolution in comparison to the ROSAT PSPC, whereas its spatial resolution is similar to that of the HRI. On the EPIC-PN image, a region with a diameter of about 100 pc distinguishes itself clearly from the surroundings by enhanced diffuse emission. This region coincides with a H II region within the LMC. The diffuse X-ray emission most likely arises from the interstellar bubble in the H II region. Physical parameters of the hot thin plasma like temperature, abundance, age, or ionization state was determined from the spectrum. The gas temperature of the bubble interior derived from the EPIC-PN data is higher than in the surrounding ISM. From the results of the spectral analysis physical parameters like the age of the bubble were computed.

Contents

List of Figures

List of Tables

Chapter 1

Introduction

From observations in the visible band, galaxies such as our Milky Way are known as large groups of stars, although observations in other wavelength bands reveal further components, e.g. neutral and ionized gas in the interstellar space as well as objects of the late stages of stellar evolution which mainly emit high energy radiation. The Large Magellanic Cloud (LMC) and the Small Magellanic Cloud (SMC) are companion galaxies of the Milky Way and allow us to resolve their stellar content in various wavelength bands. With the measured distances of about 50 kpc to the LMC and 59 kpc to the SMC (see review by van den Bergh, 1999) physical parameters like size, velocity, or luminosity of the objects in these galaxies can be determined accurately. Therefore, both the LMC and the SMC have been favorable targets of observers early on in the history of modern astronomy.

1.1 X-ray Observations of the MCs in the Past

The first observations of the Magellanic Clouds (MCs) in X-rays were realized in rocket missions using proportional and scintillation counters. The LMC was observed in 1968 as an X-ray source with an extent of about 12° (Mark et al., 1969). Two years later, i.e. in 1970, the SMC was measured (Price et al., 1971). In subsequent satellite missions (UHURU, SAS-3, Copernicus, Ariel-V, HEAO-1) discrete permanently bright sources LMC X-1, X-2, X-3, SMC X-1 (Leong et al., 1971), and LMC X-4 (Giacconi et al., 1972) as well as few transient X-ray sources were found in the MCs.

1.1.1 X-ray Survey

An extensive pointed survey of the MCs was performed by the Einstein Observatory between 1979 and 1981. The two imaging detectors on-board this satellite, the Imaging Proportional Counter (IPC) and the High Resolution Imager (HRI), were sensitive enough to detect X-ray binaries (XBs) and supernova remnants (SNRs) in the MCs. Long et al. (1981) published a list of 97 discrete X-ray sources in the direction of the LMC and the same data was re-analyzed by Wang et al. (1991), finally giving a list of 105 sources. A total of 54 discrete X-ray sources were identified with objects in

the LMC, most of the remaining sources were associated with foreground stars and background active galactic nuclei (AGN). Several sources were also found in the SMC (Seward & Mitchell, 1981; Bruhweiler et al., 1987; Wang & Wu, 1992). Further X-ray sources were found in EXOSAT observations (Pakull et al., 1985; Jones et al., 1985).

The next thorough survey of the MCs was carried out by ROSAT (Trümper, 1982) from 1990 to 1998 in the energy range of 0.1 – 2.4 keV. First results of the LMC observations of the ROSAT all-sky survey were presented by Pietsch et al. (1996). Haberl & Pietsch (1999a, hereafter HP99a) analyzed 212 pointed observations of the Position Sensitive Proportional Counter (PSPC) in the field of the LMC and created a catalog of 758 X-ray sources. For the SMC, Kahabka et al. (1999, hereafter KPFH99) presented the first ROSAT PSPC source catalog. After analyzing all the available PSPC pointings, Haberl et al. (2000, hereafter HFPK00) published a ROSAT PSPC catalog of discrete sources in the SMC containing 517 X-ray sources.

1.1.2   Resolving the Diffuse Component

With Einstein and ROSAT, high resolution X-ray imaging became possible and revealed diffuse X-ray emission both in the Galaxy and in the Magellanic Clouds. It indicated the existence of a very hot component in the interstellar medium (ISM) with temperatures of $10^6 - 10^7$ K besides the cold gas observed in radio and warm components seen in the optical or UV. First supergiant shells (SGS) of relatively cold, ionized matter in the MCs were identified on Hα+[N II] images as filamentary structures (Goudis & Meaburn, 1978; Meaburn, 1980). Shells, which are interpreted to be formed from matter swept up by expanding gas, can be also seen in H I emission maps as dense regions around voids in the neutral hydrogen distribution.

Based on Einstein IPC data, very hot gas in the LMC was mapped by Wang et al. (1991), and further detailed analysis of the diffuse X-ray emission was performed (e.g. Wang & Helfand, 1991a,b). SGS LMC 2 (Meaburn, 1980) is one of the supergiant shells discovered in the LMC and is located next to the star formation region 30 Doradus close to the optical bar of the galaxy. Wang & Helfand (1991b) analyzed the Einstein IPC data of the SGS LMC 2 comparing it to infrared and H I observations. They found a ring of X-ray emission surrounding a cold cavity in the ISM and measured a temperature of about 5×10^6 K.

Bomans et al. (1994) analyzed ROSAT PSPC pointings covering the northern part of SGS LMC 4 located in the north of the LMC. They derived a temperature of 2.4×10^6 K by fitting a thermal plasma spectrum. As for SGS LMC 2, ROSAT and ASCA observations allowed to measure a plasma temperature of $kT \approx 0.1 - 0.7$ keV (Points et al., 2000). Merged ROSAT PSPC images of the MCs were presented by Snowden & Petre (1994) and Snowden (1999). For the LMC 140 PSPC pointings were used and 20 for the SMC, and images were created in different spectral bands of the detector. In the LMC a hot plasma was found along the optical bar with temperatures between 4×10^6 and 8×10^6 K increasing from west to east. In the SMC no pronounced diffuse X-ray emission was detected.

1.2 Motivation

Massive stars finish their evolution in a supernova explosion and subsequently turn into hot thin plasma in the interstellar space, partly forming a neutron star or a black hole in addition. Less massive stars become white dwarfs. Binary systems consisting of a star and one of these compact objects at the final stage of stellar evolution radiate in X-rays, and are called e.g. X-ray binaries. The interstellar space around a massive star is heated up by the stellar wind and is filled by a very thin, high-temperature plasma. Since this hot interstellar plasma as well as the X-ray binaries and the supernova remnants are bright X-ray sources in a galaxy, observations of galaxies in X-rays are essential for understanding their structure and evolution.

However, our Galaxy is not the best suited target for analyzing the properties of a galaxy as a whole, since the Solar system is embedded in the Galactic disk. First of all, it is difficult to determine the distance to the objects with high accuracy. Extended sources like supernova remnants may not be covered in one observation if they are located close to the Sun due to their small distance. And last but not least, since X-rays are absorbed by interstellar matter, objects in the Galactic disk can only be observed if they are situated in our very neighborhood.

Among the closest galaxies to the Milky Way, the LMC and the SMC offer an ideal site for studying various kinds of objects in the galaxies. Both the LMC and the SMC were observed by ROSAT in nearly 900 pointings in a period of over eight years. The ROSAT observations covered the MCs almost completely and revealed their entire picture in X-rays for the first time. Therefore, a thorough study of the X-ray emission from the Magellanic Clouds has been started. The aim of this work is to establish a detailed picture of the high energy processes within a galaxy by producing a complete catalog of sources in the Magellanic Clouds in the soft X-ray band and by analyzing the hot component of the interstellar medium. X-ray observations combined with data in other energy ranges can be used to investigate the nature of individual X-ray sources as well as the statistical properties of different source classes in a galaxy as a whole. Since objects which can be detected in X-rays at the distances of the MCs are mainly X-ray binaries and supernova remnants as forms of final stellar evolution, their distribution in combination with the structure and physical state of the ISM will show regions within the galaxies developing most actively. This will help us to understand the evolution history of the MCs.

Chapter 2

X-ray Emission from the Magellanic Cloud Regions

Galaxies like our own Galaxy as well as the Magellanic Clouds contain various types of X-ray sources. Furthermore, there are additional foreground and background objects in the line of sight, which are either X-ray sources by themselves or attenuate penetrating X-rays by absorption. Therefore, X-ray images which we get from astronomical observations are superpositions of all the emission plus absorption in the field of the sky.

In this chapter, X-ray source classes crucial for this work are presented and processes which are responsible for their X-ray emission are outlined. The first section deals with the point and point-like sources observed in the MCs, foreground objects in our Galaxy in the direction of the MCs, and the objects behind. The second section will focus on the interstellar medium (ISM), which partly reaches sufficiently hight temperatures to radiate X-rays.

2.1 Point and point-like X-ray Sources in the Magellanic Cloud Fields

2.1.1 Supernovae and Supernova Remnants

Massive stars as well as some of the matter accreting stars in binary systems terminate their evolution in a strong explosion. This final light of a star can be seen as a very bright point source in the sky and led to the name of a 'supernova' (SN), a new object in the sky which is so powerful that the emission can be observed even if the object is located outside our Galaxy. In 1987 a supernova occurred in the LMC labeled SN 1987A, being close enough to identify a blue B3 supergiant as the progenitor in former optical observations. It is now one of the preferred objects to study the evolution of a supernova and the subsequent supernova remnant.

A star generates energy in thermonuclear burning throughout its lifetime. Hydrogen is first burned to helium in the stellar core, helium to carbon and oxygen, and

finally, if the star is massive enough, the nuclear burning continues up to iron. Gravity compresses the star and promotes further fusion of elements, whereas the high internal pressure prevents the star from collapse. Iron is the last stage of core burning, since its nuclear binding energy has a maximum, and subsequently, collapse sets in, if not counterbalanced by other forces.

Stars with masses less than the *Chandrasekhar mass* $M_{\mathrm{Chand}} = 1.44$ M$_\odot$ (M$_\odot$ = 1.989×10^{30} kg), are stabilized by degenerate electron pressure, i.e. the pressure of electrons populating all atomic levels up to the Fermi energy resists further squeezing, and the stellar collapse is stopped. At this time the core mainly consists of oxygen and carbon. Evolution of the star is terminated at this point, forming a compact star with a hot surface which is called a white dwarf.

More massive stars with initial masses larger than ~ 8 M$_\odot$ can evolve beyond this point and explode finally. Unequal initial mass causes different evolution of the stars, and thus various processes and appearance of the final supernova explosion. This can be observed as different types of lightcurves and optical spectra, as it is summarized below (for a review see Weiler & Sramek, 1988; Wheeler et al., 1990).

Supernova Type Ia

The lightcurves of SNe Type Ia are all very similar and indicate a common type of progenitor star. The brightness rises quickly to a maximum in about two weeks, followed by a rapid exponential decay for about 30 days and a succeeding slow decline until the supernova fades away in the optical light. SNe Type Ia have maximum absolute blue magnitude of $M_{B\,\mathrm{max}} = -(19.7 \pm 0.5)$ mag (corresponding to $L_{B\,\mathrm{max}} \approx 10^{10}L_\odot$ with L$_\odot$ = 3.846×10^{26} J s^{-1} = 3.846×10^{33} erg s^{-1}) with remarkably little scatter (e.g. Miller & Branch, 1990). For this reason, they can be used as distance indicators for cosmological studies (Branch & Tammann, 1992). The total energy of the optical radiation is $\sim 4 \times 10^{49}$ erg. The optical spectrum shows a variety of Doppler-broadened lines corresponding to velocities of $\sim 10\,000$ km s^{-1}. Remarkable is the absence of hydrogen lines. The ejected mass is probably in the range of 0.1 to 1.0 M$_\odot$.

Due to the similarity of optical properties, progenitors of SNe Type Ia are recognized to be white dwarfs in binary systems (Nomoto, 1982b,a). Mass is transferred from the companion to the white dwarf until the increasing gravity overwhelms the inner electron pressure. The burning of carbon and oxygen in the core is ignited causing a deflagration of the core and creation of radioactive ^{56}Ni. The nuclear fusion releases energy of $\sim 10^{52}$ erg which finally disrupts the star, and, in contrast to SNe Type II, a considerable fraction of the energy is converted into kinetic energy.

Supernova Type II

The lightcurves of SNe Type II rise more slowly to a maximum, which is less bright and broader than those of Type I. The shapes differ for each supernova suggesting variations in the explosion mechanism. Depending on the shape of their lightcurves, they are classified either as SNe Type II-L (linear) or as SNe Type II-P (plateau).

SNe Type II are only found in spiral galaxies and are associated with star formation regions. Since the spectra show broad emission lines of hydrogen (Minkowski, 1941), SNe Type II are thought to be explosions of young stars with hydrogen-rich envelopes. The mean velocity is 5000 km s^{-1}, considerably lower than in SNe Type Ia, and the total ejected mass is ~ 5 M$_\odot$, about 10 times higher than in a SN Type Ia.

Stars with initial masses higher than ~ 10 M$_\odot$ evolve very rapidly during a lifetime of only $\leq 10^7$ yr. In these stars not only hydrogen in the stellar core is fused to helium, but the burning continues to the outer layers, creating a shell of helium, while heavier elements are formed in the inner core. The central core consists of iron, surrounded mainly by silicon, oxygen, neon, carbon, helium, and hydrogen in the outermost layers. Though the central iron stops fusing, the adjacent silicon is converted to iron, thereby increasing the core mass. The core starts shrinking and gravity overcomes the electron pressure. Finally protons and electrons are compressed to transform into neutrons and the core collapses until nuclear density is reached. Energy is released explosively by infalling stellar matter. A shock wave arises, which ejects the outer layers outwards. This shock is additionally driven by neutrinos created in the transformation from protons and electrons to neutrons (Burrows et al., 1995; Janka & Müller, 1996). In the center the neutron star remains. The total energy of the whole collapse reaches 10^{53} erg and is mainly carried off by neutrinos. The visually radiated energy is $\sim 10^{49}$ erg, the kinetic energy of the supernova remnant is $\sim 10^{51}$ erg.

Supernova Type Ib

There are supernovae with lightcurves similar to those of SNe Type Ia in shape, although being fainter. Their spectra show absorption lines of helium but none of silicon in the maximum light, and oxygen emission lines arise in the later phase (O I λ 5577, [O I] $\lambda\lambda$ 6300, 6364). These SN Type Ib are believed to result from massive stars which have lost all their hydrogen envelope (Woosley et al., 1993). Moreover, matter was lost in stellar winds and the star is located in a medium containing stellar material, which can be observed as growing emission lines in the late time spectra. Wolf-Rayet stars, massive stars with high mass loss, are likely progenitors. Therefore the explosion process is similar to that of SN Type II.

Supernova Type Ic

Supernovae showing similar properties as SN Type Ib, but little evidence of helium in the spectrum of the first two months, especially He I λ 5786, are classified as SN Type Ic. They are thought to be closely related to the SN Type Ib, but distinguish by e.g. different abundance of helium and oxygen in the envelope (Wheeler & Harkness, 1990).

Subsequent Expansion

Supernovae are stellar events releasing the highest amount of energy in normal galaxies, which is transferred to the debris of the star and its surroundings. In the explosion

stellar matter is thrown out with an initial velocity of $5\,000 - 15\,000\,\mathrm{km\,s^{-1}}$, heating up both the ejecta and the surrounding material to temperatures, at which X-rays are radiated. A cavity of low density gas is formed by the supernova remnant (SNR) which persists for $\sim 10^6\,\mathrm{yr}$ before merging with the ISM. The X-ray luminosity ($\sim$ $0.1 - 10.0$ keV) is $L_\mathrm{X} = 10^{35-37}$ erg s^{-1}. The remnant is also visible in radio, since electrons are accelerated in the magnetic fields of the remnant and radiate synchrotron emission. In the optical or radio the SNR is visible for $\sim 3 \times 10^4\,\mathrm{yr}$. Further description of the evolution of a SNR is presented in Section 3.2.2.

2.1.2 X-ray Binaries

Soon after X-ray observations with rocket flights became possible, newly discovered, powerful X-ray sources like Sco X-1 or Cyg X-2 could be optically identified in the late 1960s. The stars associated with the bright X-ray sources are surprisingly faint in the optical (13th to 15th magnitude) and show a blue continuum without absorption features, but emission lines of hydrogen and ionized helium. The presence of ionized helium in the so-called 'X-ray stars' indicates high temperatures for the origin of emission lines. The Uhuru X-ray satellite discovered two 'X-ray stars', Her X-1 and Cen X-3, showing permanent X-ray pulsations with periods of a few seconds and additional eclipses. They were recognized to be interacting close binary systems, in which mass is transferred from one component to the other more compact object. Since the periods are so short, the compact object is most likely a spinning neutron star, which releases the gravitational energy of the in-falling mass by X-rays and is called 'X-ray pulsar'. The X-ray spectrum of these sources is hard with most of the emission seen between 1 and 10 keV, with a luminosity of $L_\mathrm{X} = 10^{36-39}$ erg s^{-1} in their bright phases.

Satellite observations led to discoveries of further X-ray binaries (XBs) and established the following classes of interacting binary systems emitting X-rays: High Mass X-ray Binaries (HMXBs) and Low Mass X-ray Binaries (LMXBs) mainly differing in the mass and the type of the companion star (e.g. Verbunt, 1993; Bildsten et al., 1997).

High Mass X-ray Binaries

In HMXBs, the compact object which is either a neutron star or a black hole, orbits a massive early-type (OB I–III) supergiant star which provides matter for mass transfer in strong stellar winds or Roche-lobe overflow (Corbet, 1986; Nagase, 1989). In optical observations only the bright supergiant is visible. UV observations show that the stellar winds have mass loss rates of 10^{-6} to 10^{-5} M$_\odot$ yr^{-1} driven by the strong radiation field of these stars imparting momentum to material in the outer layers. The compact object, which has a powerful magnetic field, accretes matter as it moves through the matter escaping from the star. X-rays are emitted close to the magnetic poles of the compact object when gravitational energy is released. Therefore, the spinning compact object behaves like a lighthouse from which emission maxima are detected when the X-ray beam points to our direction. Orbital periods are typically in the order of days to months, and spin periods range from 10 to $10\,000$ s.

There is a second type of HMXBs with Be stars as companions. Be stars are B giants (luminosity class III–IV) which show emission lines in their optical spectra and are variable in intensity. It is thought that Be stars lose mass around the equator forming a ring because of their fast rotation. If the neutron star, which orbits a Be star, passes through the ring, the X-ray output is increased. The orbital periods of Be/X-ray binary systems are longer than those of supergiant systems, i.e. in the order of months to years, whereas the spin period is $\sim 0.1 - 1000$ s.

Low Mass X-ray Binaries

Observations of the distribution of X-ray binaries in our Galaxy tell us that the HMXBs are mainly found in the spiral arms. This is not surprising, since this is the place where young stars and associations are born. In contrast, LMXBs are found in the bulge and are associated with older, less massive ($M \lesssim 1$ M$_\odot$) stars (Verbunt, 1993; van der Klis, 2000).

Matter flows from the low mass donor star to a neutron star or to a black hole and creates an accretion disk around the compact object. Typical orbital periods of LMXBs range from minutes to days. In X-rays three types of variability are known: millisecond variability, which is characteristic for the accretion by the compact object releasing gravitational energy, kilohertz quasi-periodic oscillations which are thought to be caused by orbital motions in the inner accretion flow, and finally the bursts for few seconds with a slow decay and change in temperature which can be interpreted as resulting from thermonuclear burning on the surface of the neutron star.

2.1.3 Supersoft Sources

X-ray observations by ROSAT unveiled a new class of luminous X-ray binaries with very soft X-ray spectra, the supersoft sources (SSSs, Trümper et al., 1991). First objects of this class were CAL 83 and CAL 87 in the LMC, which were discovered by Einstein the first time. Most of the X-ray emission arises below 0.5 keV, in a significantly softer range than the X-ray binaries discussed before. Their peak X-ray luminosity can exceed $L_{\rm X} = 10^{38}$ erg s^{-1} (review by Hasinger, 1994; Kahabka & van den Heuvel, 1997).

The ROSAT observations led to the commonly accepted model by van den Heuvel et al. (1992), which assumes a white dwarf forming a close binary system with an evolved main-sequence or post main-sequence star. The origin of the supersoft X-ray radiation is thought to be the steady state nuclear burning on the surface of the white dwarf with masses of 0.7 to 1.2 M$_\odot$, which occurs if the white dwarf accretes matter from the companion at a mass transfer rate of $\sim 10^{-7}$ M$_\odot$ yr^{-1}. The mass of the companion star is in the range of 1.5 to 2 M$_\odot$. Eclipses were found indicating orbital periods of hours to days.

2.1.4 Foreground and Background Sources

In this work, we are interested in X-ray emitting sources which belong to the Magellanic Clouds in order to study the characteristics of the LMC and the SMC. XBs, SSSs, and SNRs in the MCs were detected by the ROSAT, since they are luminous X-ray sources within a galaxy.

There are other stellar X-ray sources as well, but for most of them the luminosity is more than 10^3 times lower than that of XBs, SNRs, or SSS. If we consider that the distance of the MCs is ten to hundred times larger than the mean distance to the Galactic objects, the measured flux becomes more than 100 times lower for MC sources ignoring attenuation by matter in the line of sight. This is the reason, why less X-ray luminous objects discussed in the following can not be detected yet in the fields of the MCs unless they belong to our Galaxy. Furthermore, bright X-ray sources located behind the MCs are detected as well. Therefore, the foreground and background objects have to be distinguished in order to separate them from the MC sample.

Galactic Foreground Stars

Late-type stars like the Sun radiate X-rays from their coronae with temperatures of $\sim 10^6$ K enveloping the outermost layer of the stars. As observations of the Sun and other stars have shown, the X-ray luminosity is a function of the age of the star and its rotation velocity. Through the photosphere with temperatures of $\sim 3000-10\,000$ K the chromosphere and the corona are heated up by processes arising from the hydrogen convection zone: Due to the differential rotation of the star, its magnetic field is distorted and bundles of field lines extend outward into the corona creating loops with high electric current. Magnetohydrodynamic waves from convective perturbations and oscillations of the field lines as well as the sudden reconnection of the magnetic field lines in loops are thought to be responsible for the heating of the corona. The mean X-ray luminosity of the Sun is $L_{X\odot} \approx 10^{28}$ erg s^{-1}; typically $L_X \approx 10^{27}$ erg s^{-1} for cool stars. High variability and X-ray emission can also be observed from binary systems of stars or from young stars like T Tauri stars (Gahm, 1980; Feigelson & Decampli, 1981), which still have not reached the main sequence in the Hertzsprung-Russell-Diagram ($L_X \approx 10^{31}$ erg s^{-1}).

Background Objects

Extragalactic sources which radiate X-rays and shine through the Magellanic Clouds are active galactic nuclei (AGN), cluster of galaxies, and nearby galaxies. While nearby galaxies are observed as extended X-ray sources, AGN are bright point sources ($L_X = 10^{40-47}$ erg s^{-1}). They are powerful center regions of galaxies with a non-thermal spectrum extending from the radio to the γ-range (Antonucci, 1993).

Combining the results in the entire observable electromagnetic spectrum, models have been developed describing the AGN as an axially symmetric system with a supermassive black hole ($M = 10^{6-10}$ M$_\odot$) in the center in an accretion disk. Gas

accelerated in the direction of the black hole is partly collimated and forms a jet perpendicular to the accretion disk. The accretion disk itself is embedded in a gaseous disk consisting of a molecular torus and a dusty disk with a radius of ~ 100 pc.

2.2   Hot Interstellar Medium

From observations in the radio and the optical it was known, that the interstellar medium of the Milky Way consists of cool clouds ($T \lesssim 10^2$ K) of neutral hydrogen atoms with densities of $n \approx 10$ cm^{-3} embedded in warm ($T \simeq 10^4$ K, $n \approx 0.1$ cm^{-3}) intercloud medium of partially ionized H I and H II. Since the 1970s, observations in the UV and X-rays showed the presence of hot gas at coronal temperatures ($T \approx 10^6$ K) in the ISM. In the hot ISM the pressure can be assumed to be uniform, amounting to $p \approx 3 \times 10^{-18}$ bar $= 3 \times 10^{-12}$ dyn cm^{-2} in the Galactic plane (Spitzer, 1990), since disturbances in the hot media travel with sound velocities higher than 100 km s^{-1}, which means more than 10 kpc in less than 10^8 years. In addition, the electron densities and ion densities are assumed to be of the same order, because the hydrogen atoms being the main component of the ISM, are fully ionized at coronal temperatures.

2.2.1   Theoretical Concepts and First Observations

Coronal temperatures in the ISM were already suggested by Spitzer (1956) in a work based on observational evidences of the presence of clouds at large distances from the Galactic plane. Observed as absorption features in optical spectra of bright stars at high Galactic latitudes, these clouds can only persist in an environment with pressure comparable to that in the Galactic plane, and indicate the existence of hot tenuous gas. Cox & Smith (1974) suggested that supernova remnants may produce an interconnecting tunnel system of coronal gas in the ISM. Moreover, McKee & Ostriker (1977) found that the volume fraction of hot interstellar gas is so high, that the ISM consists of disconnected regions of H I and H II embedded in a substrate of low density coronal gas. So if the coronal gas is connected, the energy of shock waves is not lost due to radiation, but remains almost completely in the interconnected coronal region.

Hot gas can be found in the galactic disk, since shocks of high velocity ($v > 10$ km s^{-1}) were thought to occur in the ISM due to supernova explosions and stellar winds of early-type stars. Cooling of the coronal gas is very inefficient (see Sec. 2.2.2), and thus once heated, the hot gas of the ISM may persist for millions of years or longer, and forms a structure like a foam within the galaxy.

Indications of the existence of the hot component were obtained from UV and X-ray observations. First UV observations of coronal gas were reported by Rogerson et al. (1973), Jenkins & Meloy (1974), and York (1974). They found O VI resonance doublet absorption lines in the spectra of stars at 1032 and 1037 Å with velocities not correlating with stellar velocities (York, 1977; Jenkins, 1978a,b). The existence of O VI absorption lines in the spectra of stars with weak or nonexistent stellar winds favor its interstellar origin. From the degree of ionization and the line width, temperatures of $\sim 5 \times 10^5$ K were derived.

Coronal gas at even higher temperatures was found in the soft X-ray background (Williamson et al., 1974; Tanaka & Bleeker, 1977). Inoue et al. (1979) who observed the emission line of O VII at 0.57 keV, confirmed the thermal nature of the soft X-ray emission and determined a temperature of $\sim 5 \times 10^6$ K. A large fraction of the ISM is hot gas in which clouds of colder gas are embedded. Warmer regions, for instance responsible for Si III absorption in stellar spectra (e.g. Shull & York, 1977; Cohn & York, 1977) are often associated with clouds.

With the ROSAT all-sky survey a complete data set of the soft X-ray background at high angular resulution (arcminutes) was obtained, and Galactic halo emission was identified as one component of the soft X-ray background, based on shadowing effects of H I clouds (Burrows & Mendenhall, 1991; Snowden et al., 1991). The Solar System is located in a superbubble with hot gas, the so called Local Bubble. Next to it there is the Loop I superbubble of a similar size. The diffuse emission from these bubbles were studied in detail using ROSAT data (e.g. Egger & Aschenbach, 1995; see also Breitschwerdt et al., 1998 for an overview).

2.2.2 X-ray Luminosity of Hot Gas

In order to describe the spectrum of a low density hot gas, extensive calculations of atomic physics are necessary, including a large set of cross-sections and emission lines. The main processes maintaining ionization equilibrium of a hot optically thin plasma are collisional ionization and radiative plus dielectronic recombination. For low densities, the ionization rate is a function of temperature. The X-ray luminosity is given by

$$L = \int n_e n \Lambda \mathrm{d}V, \tag{2.1}$$

n_e being the electron number density, n the gas atom number density, and Λ the cooling function for the gas. In coronal gas of cosmic abundances, the electron number density is assumed to be almost equal to the gas number density with $n_e \approx 1.23n$, thus

$$n_e = 1.23n = \frac{p}{2.23kT} \tag{2.2}$$

with the Boltzmann's constant $k = 1.381 \times 10^{-23}$ J K^{-1}. At temperatures $T > 3 \times 10^7$ K, all elements except iron are almost fully ionized.

The dominant cooling mechanism above 3×10^7 K is bremsstrahlung for which the rate coefficient is

$$\Lambda_{\mathrm{ff}} \approx 2.3 \times 10^{-24} \ T_6^{1/2} \ \ [\mathrm{erg \ cm^3 \ s^{-1}}] \tag{2.3}$$

(Raymond et al., 1976; McCray & Snow, 1979) with $T_6 = T/(10^6$ K). For lower temperatures ($0.1 \leq T_6 \leq 30$) the radiative cooling is dominated by collisional excitation of lines with the line cooling rate:

$$\Lambda_{\mathrm{L}} \approx 1.6 \times 10^{-22} \ T_6^{-0.6} \ \ [\mathrm{erg \ cm^3 \ s^{-1}}] \tag{2.4}$$

for Solar abundances. For environments other than Solar, Λ_{L} needs to be corrected by a factor for metalicity ζ ($\zeta_\odot = 1.0$). The cooling time t_c is defined as the time required

to convert all the internal energy of the gas into radiative energy, if the cooling rate remains constant:

$$\frac{\frac{3}{2}(n + n_{\mathrm{e}})kT}{t_{\mathrm{c}}} = n_{\mathrm{e}}n\Lambda. \tag{2.5}$$

For the hot ISM with $T = 10^6$ K and $n = 5 \times 10^{-4}$ cm^{-3} we get $t_{\mathrm{c}} = 3 \times 10^9$ yrs. So the energy dissipation by cooling is negligible, although it is responsible for the X-ray emission. The gas remains hot and observable in X-rays for long times. The temperature of the hot interstellar gas can be determined from observations by fitting X-ray spectra. In doing so detailed theoretical emission spectra are needed in addition to the bremsstrahlung spectrum, because emission lines dominate for $T \leq 3 \times 10^7$ K.

2.2.3   Energy Sources

Massive, early-type stars lose matter as stellar winds (e.g. Hutchings, 1970; Lucy & Solomon, 1970) and inject mass and energy into the ISM. They act as energy sources for the interstellar medium through their stellar winds, radiations fields, and finally by supernova explosions. Accurate values for mass loss rates and wind velocities can be derived from radio and UV observations. All stars with an initial main sequence mass greater than ~ 15 M$_\odot$ lose a substantial fraction of their mass in a powerful stellar wind throughout their lifetime, with mass loss rates of

$$\frac{\mathrm{d}M}{\mathrm{d}t} \approx 1.3 \times 10^{-16} \left(\frac{L_*}{\mathrm{L}_\odot}\right)^{1.7} \quad [\mathrm{M}_\odot \ \mathrm{yr}^{-1}], \tag{2.6}$$

L_* being the stellar bolometric luminosity (Abbott, 1982). Thus a massive star loses mass with a typical mass loss rate of $\mathrm{d}M/\mathrm{d}t \approx 10^{-6}$ M$_\odot$ yr^{-1}. For comparison, the mass loss rate of the Sun is $(\mathrm{d}M/\mathrm{d}t)_\odot = 10^{-14}$ M$_\odot$ yr^{-1}. The energy of the stellar wind is slowly and continuously fed into the ISM, creating an interstellar bubble (Castor et al., 1975; Weaver et al., 1977, see also Sec. 3.2.1), whereas in a supernova the total energy of $E_0 \simeq 10^{51}$ erg is released at once in a strong explosion (see Sec. 3.2.2).

Abbott (1982) studied the interaction of winds from B and A supergiants, O stars, and Wolf-Rayet stars in the Solar neighborhood with the ISM and compared the different processes of stellar energy input within the Galaxy. Summing up the radiative luminosity of a sample of over 100 stars, the mean stellar radiation of 3×10^{40} erg s^{-1} kpc^{-2} was computed, arising mainly from O stars. The estimated energy input by stellar winds is 2×10^{38} erg s^{-1} kpc^{-2}, as compared to supernovae in the Solar neighborhood with 1×10^{39} erg s^{-1} kpc^{-2}. Although the energy output by radiation dominates those of stellar winds and supernovae, the importance of the three processes for the interaction of the ISM are comparable, since the energy conversion into thermal energy of the ISM for stellar radiation is less efficient (10%) than for stellar winds (50%) or supernovae (70%). Furthermore, almost the entire converted energy of the radiation field goes into heating of H I and H II regions, whereas stellar winds and supernova explosions are responsible not only for heating of H II regions, but also for kinetic energy of bulk motion and mechanical heating of coronal gas.

Chapter 3

Heating of the ISM by Shock Waves

3.1 Theoretical Description of Shock Waves

In supernova explosions and stellar winds, stellar material expands into the interstellar space at high velocities. Since velocities of the order of $1000 - 10\,000\,\mathrm{km\ s^{-1}}$ are achieved in these systems, shock waves arise both in the ejecta and the surroundings and heat up the interstellar medium.

Sound and shock waves arise in compressible media in which the mean free path of the particles is small in comparison to the size of the volume element. The volume element again has to be considerably smaller than the whole system, and in such cases physical values like temperature or pressure can be derived for the considered volume. In a thin high-temperature gas as we have in the hot ISM, the mean free path l_f of the particles is of the order of 100 pc, because the gas density is low ($l_\mathrm{f} \propto T^3$, Spitzer, 1956). However, due to the magnetic fields in the ISM, shock waves are created despite the large mean free path, since energy of charged paticles is dissipated during their motions in the magnetic fields. Therefore this type of shock waves is called collisionless.

In this chapter the concepts of shock formation are outlined and physical parameters introduced which are crucial for the understanding of the shocked gas (see also Dyson & Williams, 1980; Landau & Lifschitz, 1991). For this purpose, sound waves are explained first, which are the main process occurring in a compressible medium. In addition astrophysical processes responsible for the heating of the ISM are discussed, building up on the theories of shock waves.

3.1.1 Continuous Flow of Compressible Gas

Sound waves can be understood as disturbances with small amplitudes propagating adiabatically in a compressible gas since the entropy does not change to first order. Looking at an unit volume of gas $\mathrm{d}V$, the velocity changes v of the gas inside is very small ($v \ll c_\mathrm{loc}$, c_loc being the local sound velocity), and so are the deviation of pressure p' and density ρ' compared to its pressure $p_0 = const$ and density $\rho_0 = const$ in equilibrium.

For describing the physical conditions we need the basic equations of hydrodynam-

ics. Since in fluid mechanics it is generally assumed that mass within a gas element can neither be created nor annihilated, change in mass in the volume element must be equal to the mass flow through the area surrounding the volume element. Independence of the choice of volume element results in the *continuity equation*:

$$\frac{\partial \rho}{\partial t} + \text{div}(\rho \vec{v}) = 0. \tag{3.1}$$

The force acting on a gas element is caused by the gas pressure p. Using partial derivatives with respect to fixed coordinates, the equation of motion can be written in a form that is known as the *Euler equation*:

$$\frac{\partial \vec{v}}{\partial t} + (\vec{v}\nabla)\vec{v} = -\frac{1}{\rho}\text{grad}p. \tag{3.2}$$

In the approximation for small amplitudes the Equations (3.1) and (3.2) for an adiabatic flow can be combined to one equation by introducing a velocity potential ϕ by

$$\text{grad}\phi = \vec{v} \tag{3.3}$$

to the following equation for ϕ:

$$\frac{\partial^2 \phi}{\partial t^2} - c^2 \Delta \phi = 0 \tag{3.4}$$

with

$$c = \sqrt{\left(\frac{\partial p}{\partial \rho}\right)_s}. \tag{3.5}$$

Equation (3.4) describes a plane wave moving with the sound velocity c, and is valid for all three velocity components v_x, v_y, and v_z. Differentiation with respect to time gives wave equations for p and ρ as well.

The local sound velocity is a characteristic parameter of compressible media and a measure for the propagation of disturbances. The definition of the sound velocity c in Equation (3.5) is valid for compressive media in general, not only for small amplitude sound waves. Using the adiabatic compressibility

$$\kappa_s = -\frac{1}{V}\left(\frac{\partial V}{\partial p}\right)_s \tag{3.6}$$

and the isothermal compressibility

$$\kappa_T = -\frac{1}{V}\left(\frac{\partial V}{\partial p}\right)_T \tag{3.7}$$

which are related in the following way:

$$\kappa_T = \frac{c_p}{c_v}\kappa_s, \tag{3.8}$$

16

c_v and c_p being the specific heat capacities, we get

$$\left(\frac{\partial p}{\partial \rho}\right)_s = \frac{c_p}{c_v}\left(\frac{\partial p}{\partial \rho}\right)_T. \tag{3.9}$$

Assuming c_v and c_p to be constant, the equation of state for an ideal gas

$$\frac{p}{\rho} = \frac{pV}{M} = \frac{RT}{\mu} \tag{3.10}$$

(M is the mass of the gas in the volume V, $R = 8.31451$ J mol^{-1} K^{-1} the gas constant and μ [kg mol^{-1}] the mass of one mol gas), yields:

$$c = \sqrt{\frac{\gamma RT}{\mu}} \tag{3.11}$$

with the adiabatic constant

$$\gamma = \frac{c_p}{c_v}. \tag{3.12}$$

For monoatomic gas we have $\gamma = 5/3$, for biatomic gas $\gamma = 7/3$. The internal energy of the ideal gas is

$$\epsilon = c_v MT = \frac{pV}{\gamma - 1} = \frac{Mc^2}{\gamma(\gamma - 1)} \tag{3.13}$$

and the enthalpy

$$w = c_p MT = \frac{\gamma pV}{\gamma - 1} = \frac{Mc^2}{\gamma - 1}, \tag{3.14}$$

which are related as $\epsilon = w - pV$.

3.1.2 Shock Waves

In the last section it was shown, that a sound wave can be described as a plane wave propagating with local sound velocity c_{loc}. The distribution of physical parameters like velocity v of gas flow, pressure p, and density ρ is continuous, and the profile of the wave is conserved.

At strong expansions caused by stellar winds or supernovae, however, disturbances of the medium have high amplitudes. For this reason, we consider a continuous adiabatic flow with arbitrary amplitude. *Continuity equation* (Eq. (3.1)) and *Euler equation* (Eq. (3.2)) yield a propagating wave with velocity $u = v \pm c_{\mathrm{loc}}$, i.e. every point of the wave profile moves with u. Thus the propagation of the disturbance with c_{loc} is superposed on the gas motion with velocity v. Both $c_{\mathrm{loc}} = c_{\mathrm{loc}}(\rho)$ and $v = v(\rho)$ are functions of ρ, and each point of the wave moves with a different velocity $u = u(\rho)$. Although for sound waves with small amplitudes these dependences are negligible and the velocities are assumed to be constant, for bigger amplitudes the different velocities result in modification of the wave profile. Since the expansion velocity in a gas element of higher density is higher than in low density elements, the gas particles in the compressed region with $u = v + c_{\mathrm{loc}}$ overtake the particles in rarefied gas and steepen the wave profile into a discontinuity.

17

Discontinuous Flow

Discontinuities in physical values velocity v, pressure p, and density ρ in non-stationary flow are called shock waves and in general propagate through the gas. For describing the physics of shock waves, we choose the rest frame of the shock front. The shock front is located in the y-z-plane, the gas moves perpendicular to it from one side (region 1) to the other side (region 2) in an one-dimensional flow along the x-axis. In reality the shock front propagates into region 1. The following conservation laws must be fulfilled:

- Mass flow:

$$\rho v_x = const, \tag{3.15}$$

- Energy flow:

$$\rho v_x \left(\frac{\vec{v}^2}{2} + w \right) = const, \tag{3.16}$$

- Momentum flow:

$$x: \quad p + \rho v_x^2 \quad = \quad const, \tag{3.17}$$
$$y: \quad \rho v_x v_y \quad = \quad const, \tag{3.18}$$
$$z: \quad \rho v_x v_z \quad = \quad const. \tag{3.19}$$

Since there is mass flow through the discontinuity, it is $\rho v_x \neq 0$, and from Equations (3.18) and (3.19) it follows that v_y and v_z are continuous, whereas there is a jump in the distribution of v_x, p, and ρ. So $v_{y1} = v_{y2}$ and $v_{z1} = v_{z2}$, and using v instead of v_x, the conservation laws can be written as:

$$\rho_1 v_1 \quad = \quad \rho_2 v_2 = j, \tag{3.20}$$
$$\frac{v_1^2}{2} + w_1 \quad = \quad \frac{v_2^2}{2} + w_2, \tag{3.21}$$
$$p_1 + \rho_1 v_1^2 \quad = \quad p_2 + \rho_2 v_2^2, \tag{3.22}$$

j is called the flow density. We further introduce the specific volumes

$$V_1 = \frac{1}{\rho_1}, \quad V_2 = \frac{1}{\rho_2} \tag{3.23}$$

and from Equations (3.20) and (3.22) we obtain

$$v_1 = jV_1, \quad v_2 = jV_2 \tag{3.24}$$

and

$$p_1 + j^2 V_1 \quad = \quad p_2 + j^2 V_2 \tag{3.25}$$
$$\Rightarrow \quad j^2 \quad = \quad \frac{p_2 - p_1}{V_1 - V_2}. \tag{3.26}$$

Thus the gas velocity change at the shock front is

$$v_1 - v_2 = \sqrt{(p_2 - p_1)(V_1 - V_2)}. \tag{3.27}$$

For the change of enthalpie we obtain with Equations (3.21), (3.24), and (3.26)

$$w_1 - w_2 - \frac{1}{2}(V_1 + V_2)(p_1 - p_2) = 0, \tag{3.28}$$

and for the internal energy

$$\epsilon_1 - \epsilon_2 + \frac{1}{2}(V_1 - V_2)(p_1 + p_2) = 0. \tag{3.29}$$

The Equation (3.29) is called the *Hugoniot relation.*

Increase of Entropy

For shock waves the conditions of Equations (3.20) – (3.22) must hold. In addition, the entropy of the gas rises by the passage of the shock wave (*Rankine-Hugoniot jump conditions*), and the increase of entropy implicates dissipation of energy and changes in physical properties of the gas. This is accomplished by processes within the very thin layer of the gas corresponding physically to the shock front, where a fraction of the kinetic energy is converted into thermal energy. The thickness of this transition layer is defined by the conservation laws of mass flow, energy flow, and momentum flow for the regions in front of and behind the shock front, so that the necessary increase of entropy is realized. The shock front moves with a velocity higher than the local sound velocity ($v_1 > c_{\text{loc}}$), but in the shocked gas behind the discontinuity the flow is subsonic ($v_2 < c_{\text{loc}}$).

Change in Temperature and Velocity

In order to obtain the relations between observable parameters of the gas in front of and behind the shock, we first replace the enthalpy in Equation (3.28) by Equation (3.14) and get:

$$\frac{V_2}{V_1} = \frac{(\gamma + 1)p_1 + (\gamma - 1)p_2}{(\gamma - 1)p_1 + (\gamma + 1)p_2}. \tag{3.30}$$

The equation of state for ideal gas further yields:

$$\frac{T_2}{T_1} = \frac{p_2 V_2}{p_1 V_1} = \frac{p_2}{p_1}\left[\frac{(\gamma + 1)p_1 + (\gamma - 1)p_2}{(\gamma - 1)p_1 + (\gamma + 1)p_2}\right]. \tag{3.31}$$

Using Equation (3.26) we get

$$j^2 = \frac{(\gamma - 1)p_1 + (\gamma + 1)p_2}{2V_1}, \tag{3.32}$$

which can be used to obtain

$$v_1^2 = j^2 V_1^2 = \frac{V_1}{2}[(\gamma-1)p_1 + (\gamma+1)p_2], \tag{3.33}$$

$$v_2^2 = j^2 V_2^2 = \frac{V_1}{2}\frac{[(\gamma+1)p_1 + (\gamma-1)p_2]^2}{[(\gamma-1)p_1 + (\gamma+1)p_2]}. \tag{3.34}$$

In the limit of shock waves with very high intensity it is $(\gamma-1)p_2 \gg (\gamma+1)p_1$ and we get with Equations (3.20), (3.30), and (3.31):

$$\frac{v_2}{v_1} = \frac{V_2}{V_1} = \frac{\rho_1}{\rho_2} = \frac{\gamma-1}{\gamma+1} \tag{3.35}$$

$$\frac{T_2}{T_1} = \frac{(\gamma-1)p_2}{(\gamma+1)p_1} \tag{3.36}$$

The relation between the temperature T_2 behind the shock front and the velocity of the gas v_1 in front of the shock relative to the shock front can be obtained from Equations (3.10) and (3.33):

$$v_1 = \sqrt{\frac{\gamma+1}{2}p_2 V_1} = \sqrt{\frac{\gamma+1}{2}\frac{RT_2}{\mu}\frac{V_1}{V_2}} = \sqrt{\frac{\gamma+1}{2}\frac{\gamma+1}{\gamma-1}\frac{R}{\mu}T_2} \tag{3.37}$$

For monoatomic gas $(\gamma = \frac{5}{3})$ Equation (3.35) yields $v_2/v_1 = \rho_1/\rho_2 = \frac{1}{4}$, and the temperature in the shocked gas is

$$T_2 = \frac{3}{16}\frac{\mu}{R}v_1^2. \tag{3.38}$$

3.1.3 Similarity Solutions

Hydrodynamic problems which are independent of position, but depend on velocity scales, are called self-similar. The requirement for self-similarity is met, when the characteristic dimensional scales of the gas flow are predetermined by the initial conditions with only two parameters of independent dimensions. For instance, gas flow in a medium with constant heat capacities and initial conditions $p = p_0, \rho = \rho_0$, the parameters of the flow are pressure p and density ρ.

For solving the hydrodynamic equations, similarity relations are introduced which connect position and time coordinates. We define a new function $R = R(t)$ of time t with the dimension of length r, only using t and the given initial parameters p_0 and ρ_0, as well as a dimensionless variable $\xi = r/R(t)$, the similarity variable. Thus the parameters become functions of ξ and the system is self-similar for different times t, and for given t it differs in the new measure ξ along r, which increases with time.

Both interstellar bubbles and supernova explosions can be described with similarity solutions. The first value fixed by the initial conditions is the gas density ρ_0 of the ambient ISM. For interstellar bubbles driven by stellar winds the second initial parameter is the mechanical power L_w of the winds, for supernova explosion it is the total energy E_0 which is released at once.

3.2 Shock Waves in the ISM

Shock waves form when the gas flow reaches a velocity higher than the local sound velocity. From Equation (3.11) the sound velocity for monoatomic gas is

$$c_{\text{loc}} = \sqrt{\frac{\gamma RT}{\mu}} = \sqrt{\frac{5RT}{3\bar{m}N_A}}. \tag{3.39}$$

$\bar{m}$ is the mean mass of the particles and $N_A = 6.022 \times 10^{23}$ mol^{-1} Avogadro's constant. For a fully ionized gas with cosmic abundances we can set for the mean mass of particles $\bar{m} = 0.61$ m$_{\text{p}}$, m$_{\text{p}} = 1.673 \times 10^{-27}$ kg being the proton mass. The sound velocity becomes

$$c_{\text{loc}} = 150 \times \sqrt{T} \quad [\text{m s}^{-1}] \tag{3.40}$$

with T in [K]. In the colder part of the ISM with temperatures $T < 10^4$ K, the local sound velocity is $c_{\text{loc}} < 15$ km s^{-1}. Since stellar winds reach velocities of $v_{\text{w}} = 1000$ – 2500 km s^{-1} and SN explosions even $v_{\text{SN}} \approx 10^4$ km s^{-1}, shock waves are formed immediately. If the star is located in a preheated environment like in an association with many OB stars or in a superbubble, we get $c_{\text{loc}} = 150$ km s^{-1} for $T = 10^6$ K, thus the velocities of stellar winds or supernova explosions are still higher. If the expansion velocity of the supernova remnant drops below the limit of c_{loc}, the system expands continuously until it hits the boundary between the hot region and the cold ISM and forms a shock front instantaneously.

3.2.1 Interstellar Bubbles

The evolution of interstellar bubbles was studied in detail by Castor et al. (1975) and Weaver et al. (1977). Massive early-type stars emit matter into the ISM in a steady, spherically symmetric stellar wind with a constant terminal wind velocity v_{w} and mass loss rate $\mathrm{d}M/\mathrm{d}t$ (see Eq. (2.6)). Stellar winds are driven by momentum transfer from the radiation field to the outer atmospheric layers with a mechanical power of

$$L_{\text{w}} = \frac{1}{2} \frac{\mathrm{d}M}{\mathrm{d}t} v_{\text{w}}^2. \tag{3.41}$$

A typical value of the mass loss rate $\mathrm{d}M/\mathrm{d}t = 10^{-6}$ M$_\odot$ yr^{-1} and the wind velocity $v_{\text{w}} = 2000$ km s^{-1} give $L_{\text{w}} = 1.26 \times 10^{36}$ erg s^{-1}. The wind interacts with the ambient interstellar gas which can be assumed to have uniform particle density n_0 and cosmic abundances, and forms a bubble around the star. There are four stages during the evolution of a wind-driven stellar bubble:

I.   Free expansion at wind velocity for the first few 100 years.

II.   Adiabatic expansion for few 1000 years. The bubble expands so fast, that radiative losses in the gas do not have any effect.

III. 'Snowplow'-phase: swept-up interstellar gas collapses into a thin, cold shell as a result of radiative cooling.

    a.   The shocked stellar wind still conserves energy.
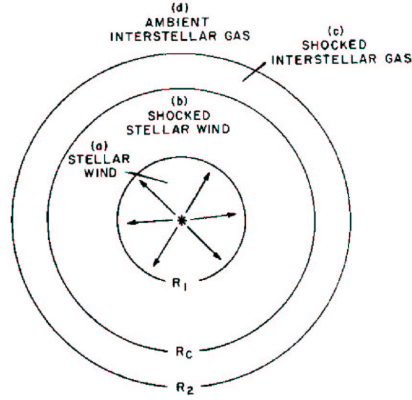
Figure 3.1: Schematic view of regions and boundaries of an interstellar bubble presented by Weaver et al. (1977). Same notation is used in the text.

    b. Radiative losses also affect the dynamics of the shocked stellar wind.

IV. If the star lasts long enough the thin shell dissipates into the surrounding medium as the flow tends to a steady state.

The basic differential equations for the stellar wind driven bubble are the *continuity equation* (see Eq. (3.1))

$$\frac{\partial \rho}{\partial t} + v\frac{\partial \rho}{\partial r} + \rho\frac{\partial v}{\partial r} + 2\frac{\rho v}{r} = 0, \tag{3.42}$$

the *Euler equation* (see Eq. (3.2))

$$\frac{\partial v}{\partial t} + v\frac{\partial v}{\partial r} + \frac{1}{\rho}\frac{\partial p}{\partial r} = 0, \tag{3.43}$$

and energy conservation for the adiabatic flow

$$\left(\frac{\partial}{\partial t} + v\frac{\partial}{\partial r}\right)(p\rho^{-\gamma}) = 0 \tag{3.44}$$

with $\gamma = 5/3$.

Early Stage

The expansion of the bubble can be described by an adiabatic flow without thermal conduction. The whole system can be divided into four spherical zones (see also Fig. 3.1):

(a) $0 \leq r \leq R_1$:   freely expanding hypersonic stellar wind,
(b) $R_1 < r \leq R_c$:   hot, shocked stellar wind,
(c) $R_c < r \leq R_2$:   swept-up interstellar gas, and
(d) $R_2 < r$:   ambient interstellar gas with density ρ_0.

R_2 is the outer boundary of the bubble. At R_c between regions (b) and (c) there is a contact discontinuity between the shocked stellar wind and the swept-up interstellar gas. The energy is fed into the system at a constant rate L_w. Neglecting gravity and assuming a spherically symmetric adiabatic flow, the shock front at R_2 can be regarded as independent of the flow in the very interior and region (c) can be described by a similarity solution. For R_2 we form an expression with the dimension of r using the initial parameters L_w [kg m^2 s^{-3}] and ρ_0 [kg m^{-3}]:

$$R_2 = \alpha \left(\frac{L_w t^3}{\rho_0} \right)^{\frac{1}{5}} \tag{3.45}$$

with α being a constant which is to be determined. If we define a new dimensionless variable

$$\xi = \frac{r}{R_2(t)} \tag{3.46}$$

the velocity v, pressure p, and density ρ become functions of ξ. The self-similar solutions of the Equations (3.42), (3.43), and (3.44) are found, using the initial conditions

$$v(R_2) = \frac{3}{4}\dot{R}_2, \quad \rho(R_2) = 4\rho_0, \quad \text{and} \quad p(R_2) = \frac{3}{4}\rho_0 \dot{R}_2^{\,2} \tag{3.47}$$

for the velocity, density, and pressure right behind the shock front (see Eqs. (3.35) and (3.37)). The velocity v in Equation (3.47) is the gas velocity relative to the rest frame of the star, whereas the velocity v_2 in Equation (3.35) is relative to the shock front. Thus $v(R_2) = \dot{R}_2 - v_2$.

Region (b) is filled with shocked stellar wind. At R_1 there is a shock front separating region (b) from the freely streaming stellar wind in region (a). The flow in region (b) is not self-similar, since R_1/R_c varies with time, but it is almost isobaric due to high temperature. Equations (3.42), (3.43), and (3.44) can be integrated by taking the initial and boundary conditions into account, and Weaver et al. (1977) obtain $\alpha = 0.88$. For the velocity of the outer shock we get

$$\dot{R}_2 = \frac{\mathrm{d}R_2}{\mathrm{d}t} = \frac{3}{5}\alpha \left(\frac{L_w}{\rho_0} \right)^{\frac{1}{5}} t^{-\frac{2}{5}} = 0.528 \left(\frac{L_w}{\rho_0} \right)^{\frac{1}{5}} t^{-\frac{2}{5}}, \tag{3.48}$$

while the velocity of the inner shock is v_w. With an ambient density of $n_0 = 1$ cm^{-3}, i.e. $\rho_0 = n_0 \, \bar{m} = 1.02 \times 10^{-24}$ g cm^{-3}, $t = 10^4$ yr yields $\dot{R}_2 = 140$ km s^{-1} and $t = 10^6$ yr $\dot{R}_2 = 22$ km s^{-1}. The temperature right behind the shock front can be computed applying the relation Equation (3.38)

$$T_{(c)} = \frac{3}{16} \frac{\mu}{R} \dot{R}_2^{\,2}. \tag{3.49}$$

Thus for $t \approx 10^4$ yr the ambient gas is heated up to temperatures of $T = 10^{5-6}$ K by the expanding bubble. Only a small fraction of the interior of an interstellar bubble is filled by the stellar wind, surrounded by a region of hot ($T_{(c)} \approx 10^6$ K) and low density ($n_{(c)} \approx 10^{-3}$ cm^{-3}) gas, a mixture of the shocked stellar wind and the interstellar gas.

Creation of the Shell

When the time scale for radiative cooling of the swept-up interstellar gas becomes comparable to the age of the bubble, region (c) collapses into a thin, almost isobaric shell. The inner part of the shell is a H II-region with a temperature of $T_{(c)} \approx 10^4$ K, whereas the temperature in region (b) is $T_{(b)} > 10^6$ K. During this 'snowplow' phase lasting almost the whole bubble lifetime, the bubble is modified by thermal conduction from region (b) to region (c). Colder mass evaporates from region (c) to region (b) and becomes the predominant source of mass for region (b), although for region (c) the depletion of mass is still negligible. The conductive energy flux is balanced by the mechanical energy flux in reverse direction caused by mass evaporation and by the radiative losses at the interface.

Since the shocked material between R_1 and R_2 is very hot, this region is assumed to have uniform pressure. In addition, the internal energy of this region dominates the kinetic energy of the shell, and because of $R_1 \ll R_2$ we can write for the total energy:

$$E = \frac{3}{2}\frac{4\pi}{3}R_2^3 p. \tag{3.50}$$

The momentum and energy balance equations become:

$$\frac{\mathrm{d}}{\mathrm{d}t}\left(\frac{4\pi}{3}R_2^3\,\rho_0\frac{\mathrm{d}R_2}{\mathrm{d}t}\right) = 4\pi R_2^2 p, \tag{3.51}$$

$$\frac{\mathrm{d}E}{\mathrm{d}t} = L_\mathrm{w} - 4\pi R_2^2 p \frac{\mathrm{d}R_2}{\mathrm{d}t} \tag{3.52}$$

Solving Equations (3.50), (3.51), and (3.52) yields

$$E = \frac{5}{11}L_\mathrm{w}t \tag{3.53}$$

$$R_2 = \left(\frac{250}{308\pi}\frac{L_\mathrm{w}t^3}{\rho_0}\right)^{\frac{1}{5}} \tag{3.54}$$

Thus for the 'snowplow' phase we get $\alpha = 0.76$ which is lower than in the early stage, i.e. R_2 increases more slowly due to collapse of region (c).

So the stellar wind creates a large cavity of low density in the ISM before the massive star dies. At the age of $t = 10^6$ yrs, 30% of the wind energy becomes thermal energy of the coronal gas, 10% kinetic energy of expansion, and the rest is emitted as radiation (Weaver et al., 1977; Abbott, 1982). Assuming $\mathrm{d}M/\mathrm{d}t = 10^{-6}$ M$_\odot$ yr^{-1} and $v_\mathrm{w} = 2000$ km s^{-1}, the boundary between the hypersonic stellar wind (region (a)) and the shocked region (b) is found at $r \approx 5$ pc, whereas the hot region (b) of low density gas extends up to $r \approx 30$ pc. This gas is a soft X-ray source with X-ray luminosity of $L_\mathrm{X} = 10^{33-35}$ erg s^{-1}. The total energy input to the ISM from a massive star by stellar wind is comparable to the characteristic energy of a supernova explosion.

3.2.2 Supernova Explosions

In contrast to interstellar bubbles, at the end of the lifetime of a massive star, almost the entire stellar mass is expelled in supernovae in a strong explosion depositing the energy of $E_0 \simeq 10^{51}$ erg in the stellar debris and the ISM. Since the expansion velocity is much higher than the sound velocity, a spherically expanding blast wave shock is produced with a very low density, high-temperature interior. Due to the shock wave the ambient ISM is compressed. After the blast wave has swept-up as much mass as the ejecta mass, the supernova remnant continues expanding adiabatically with a constant kinetic energy. The pressure difference between the shocked ISM and the hot ejecta drives a second shock wave back into the interior (Ardavan, 1973; McKee, 1974; Mansfield & Salpeter, 1974), the reverse shock. This inward moving shock is a direct result of the interaction between the ejecta and the ISM and causes a deceleration of the ejecta. Due to the shock waves the ISM and the ejecta are heated up to X-ray emitting temperatures.

While in the shock front itself there is a temperature jump (see Sec. 3.1.2), the temperature decreases continuously to some terminal temperature behind the shock front. This relaxation layer has a thickness of the order of 1 pc, while the supernova remnant has reached a size of several parsecs. If the thickness of the outer most layers becomes of the order of the thickness of the relaxation layer, radiative losses become important and a thin cold shell forms which expands as a 'pressure-driven snowplow' (Cox, 1972; McKee & Ostriker, 1977; Chevalier, 1977). Once the temperature of the remnant has decreased by adiabatic expansion, so that radiative cooling cannot be neglected any longer in the whole interior, the evolution of a SNR is terminated in a subsequent 'momentum-driven snowplow' phase (Cioffi et al., 1988).

Adiabatic Expansion of the Supernova Remnant

In the first few hundred years, emission from the ejecta in the softer X-ray bands ($\sim$1 keV) dominates the harder ($\sim$10 keV) blast wave emission, whereas in the following adiabatic expansion phase the predominant X-ray emission is caused by the blast wave for a long time of up to 10^4 years. The remnant expands adiabatically into the ISM where surrounding gas is swept up, and can be described by the *Sedov-Taylor-solution* (Sedov, 1946a,b; Taylor, 1950a,b). The pressure jump at the shock front is very high

$$\frac{p_2}{p_1} \gg \frac{\gamma + 1}{\gamma - 1} \tag{3.55}$$

and the density changes according to Equation (3.35) as a result of the *Rankine-Hugoniot jump conditions*. The remnant can be described as an adiabatic flow of spherically expanding ideal monoatomic gas ($\gamma = 5/3$). The flow is defined by the density ρ_0 [kg m^{-3}] of the surrounding ISM gas and the explosion energy E_0 [kg m^2 s^{-2}]. Therefore the distance to the center of the system can be written as

$$R = \beta \left(\frac{E_0 t^2}{\rho_0} \right)^{\frac{1}{5}} \tag{3.56}$$

with β being a constant which still must be determined. The expansion velocity of the blast wave into the undisturbed gas is

$$v_b = \frac{\mathrm{d}R}{\mathrm{d}t} = \frac{2}{5}\beta\left(\frac{E_0}{\rho_0}\right)^{\frac{1}{5}}t^{-\frac{3}{5}} = 0.461\left(\frac{E_0}{\rho_0}\right)^{\frac{1}{5}}t^{-\frac{3}{5}} \tag{3.57}$$

with $\beta = 1.15$ (Truelove & McKee, 1999). If we assume $\rho_0 = 1.02 \times 10^{-24}$ g cm^{-3} ($n_0 = 1$ cm^{-3}) and $E_0 = 10^{51}$ erg, we get $v_b = 2300$ km s^{-1} at $t = 10^3$ yr, yielding a temperature of $T = 7 \times 10^7$ K (~ 6 keV). The typical X-ray luminosity of a SNR is $L_{\mathrm{X}} = 10^{35-37}$erg s^{-1}.

3.2.3 Formation of Supershells

OB stars are mainly found in clusters and associations, comprising about 20 to 40 early-type stars (McCray & Kafatos, 1987). About 10% are O stars with masses larger than 30 M$_\odot$. The interaction of all the massive stars in the OB associations with the ambient ISM result in large cavities and surrounding supershells. In the earlier phases of the evolution, the ionizing radiation of the most massive O stars and their stellar winds dominate the energy input to the ISM. After $\sim 5 \times 10^6$ yr the O stars leave the main-sequence and terminate finally as supernovae. Supernovae continue with an almost constant rate until the least massive star of ~ 7 M$_\odot$ explodes. Therefore, supernova explosions occur not only in cold environments, but more likely in hotter regions with low density which was heated up either by former supernovae or stellar winds. In those systems each supernova explosion causes a blast wave propagating through the hot ISM and depositing 72% of the total energy released by the SN as thermal energy (McCray & Snow, 1979). The remaining 28% of kinetic energy of the blast wave is lost to radiation when it hits the denser supershell of cold material. In total the stellar winds and the repeated supernovae produce a huge expanding supershell of the size of $r \geq 100$ pc with concentrated H I and H II gas, visible as large structures within the galaxies.

Due to expansion, the size of the supershell can become comparable to the density scale height of H I gas of the galactic disk. The supershell breaks through the galactic H I layer, shifting matter of the interstellar space into the galactic halo, whereas in the galactic plane, the supershell continues to evolve according to the 'Snowplow'-model. Hot interstellar gas leaving the gravitational potential of the galactic disk forms a galactic wind (Johnson & Axford, 1971; Mathews & Baker, 1971) and can also fall back to the disk due to thermal instability (galactic fountain, Shapiro & Field, 1976; Bregman, 1980). The existence of galactic corona which spreads out into the galactic halo, can be observed as soft X-ray emission from the galaxy extending far beyond the optical disk.

Chapter 4

Data Analysis

4.1 X-ray Observatories

4.1.1 ROSAT

The German X-ray observatory ROSAT (Trümper, 1982) developed by the Max-Planck-Institut für extraterrestrische Physik (MPE) was launched in June 1990 carrying an X-ray telescope (XRT) and a wide-field camera (WFC) for observations in the extreme ultraviolet (XUV). The XRT covered the energy range of 0.1 to 2.4 keV and consisted of a fourfold nested Wolter type I mirror assembly with paraboloid and hyperboloid mirrors (Aschenbach, 1988). The telescope with a focal length of 2.4 m was equipped with three detectors, two of which were Position Sensitive Proportional Counters (PSPCs, Pfeffermann et al., 1987) with a moderate energy resolution. The third detector was a High Resolution Imager (HRI, David et al., 1996) with a few arcseconds spatial and no energy resolution.

Beside the pointed observations for studying astronomical objects in detail, the main aim of the ROSAT mission was the first all-sky survey with the imaging X-ray and XUV telescopes. It was carried out from August 1990 to January 1991 using the WFC and the PSPC and was followed by pointed observations with the PSPC and the HRI. In the following the detectors PSPC and HRI used for the pointed observations are discussed.

Position Sensitive Proportional Counter (PSPC)

The PSPCs were multi-wire proportional counters fabricated at MPE. PSPC-1 was chosen as the primary detector of the mission and was used for the Performance-Verification and Calibration phase in the beginning. Also the all-sky survey was performed with PSPC-1 until it was destructed by accidental pointig towards the Sun because of an Attitude Measurement and Control System error on January 25 1991. All the following observations were carried out with PSPC-2.

The PSPCs consisted of a gas-filled chamber with gold plated tungsten wires as anodes and platinum iridium wires as cathodes. The active detecting part of the PSPC included two cathodes K1 and K2 and the anode A1 located between the two

cathodes. There was an additional anode A2 which was read out as anti-coincidence counter for particle background rejection. The gas was a mixture of about 65% argon, 20% xenon, and 15% methane. In front of the detector a filter wheel was mounted with four options: open and closed positions, a boron filter, and a position carrying calibration sources which produced an Al Kα line at 1.49 keV. The field of view of the PSPC had a diameter of 2°, the energy resolution was $E/\Delta E \approx 1 - 4$. The detector had an entrance window made of polypropylene which was coated with carbon and lexan in order to block UV emission. The window with a diameter of 8 cm was carried by a support structure ('rib') consisting of a circle (28 mm diameter) and eight radial struts with two additional mesh systems below. Since shadowing of X-rays could occur behind the rib and the mesh grid wires, the satellite performed a slow regular motion diagonally to the entrance window wire grids ('wobble') during the observations.

High Resolution Imager (HRI)

The HRI on-board ROSAT was a two-dimensional position sensitive detector using two micro-channel plates (MCPs). It was provided by the Smithsonian Astrophysical Observatory in the USA, as an improved version of the successful HRI on-board Einstein with higher quantum efficiency. MCPs consisted of several million of channel electron multiplier, i.e. semi-conducting glass channels. In operation a potential of about 1 kV was applied along the channel. In-falling photons or charged particles released electrons from the wall of the channel which were accelerated along the channel and released secondary electrons by hitting the wall. These were collected at the anode at the other side of the channels. The HRI MCPs had a diameter of 36 mm while the readout system had a working area of 27 mm × 27 mm. Based on observations of known point sources in the Andromeda galaxy, the plate scale was determined to be $0''.499$ per pixel. The spatial resolution of the HRI was $1''.7$ (FWHM) and the diameter of the field of view was $38'$.

4.1.2 XMM-Newton

The X-ray observatory of the X-ray Multi-Mirror Mission (XMM) was designed by ESA for studying X-ray sources with a high collecting area in the 0.1 – 10.0 keV band. Launched on December 10, 1999, the spacecraft XMM-Newton is equipped with a set of three imaging highly nested Wolter type telescopes of 7.5 m focal length (58 mirrors per telescope, Aschenbach et al., 2000) and an additional optical and UV telescope, the Optical Monitor. The focal instruments of XMM-Newton consist of three European Photon Imaging Cameras (EPICs) each completing a telescope, and two Reflecting Grating Spectrometers (RGSs). Two of the EPICs are X-ray charge-coupled devices (CCDs) based on the conventional MOS technology (EPIC-MOS), the third detector uses pn-CCDs (EPIC-PN). The RGSs are used for high-resolution spectroscopy and are mounted on the telescopes with EPIC-MOS in prime focus right behind the mirror module. In each of the two telescopes the collected and focused X-ray radiation is partly diverted towards a CCD strip in the secondary focus by a dispersing grating stack. The undispersed radiation is focused on the EPIC-MOS for imaging

observations. The EPIC-PN camera (Strüder et al., 2001) which was developed at the MPE, is located behind the third telescope without RGS. Each EPIC can be operated with one of the three filters: thin, medium, or thick.

EPIC-PN

The EPIC-PN is a silicon drift detector composed of 12 monolithic pn-CCDs with a total area of 6 cm × 6 cm. The pixel size is 150 μm × 150 μm, corresponding to 4$''$1 × 4$''$1. The sensitive thickness of silicon is 280 μm making the CCDs sensitive in a range up to 15 keV. In the energy range of 0.1 – 10.0 keV, the quantum efficiency is higher than 90%, decreasing to $\sim$ 50% at 15 keV. The lower limit for the energy response ($\sim$ 0.15 keV) is defined by the radiation entrance window. The energy resolution of the EPIC-PN is $E/\Delta E \approx 20 - 50$. In order to achieve a good time resolution, events are read out in each column, and there are different modi of data acquisition. Data used in this work was taken in the 'full window' mode in which all pixels of all CCDs are read out.

4.2   ROSAT HRI Data

To obtain data for scientific evaluation, original data coming from the XRT instruments were processed by the Standard Analysis Software System (SASS) and event files were produced which contain all events and information like original detector coordinates, corresponding sky positions, pulse height, and arrival time. Though additional files like images or preliminary lists of detected sources were outputs of the SASS as well, for the scientific work presented here only event files and housekeeping files of the observations with information about master veto rate (see Sec. 4.3.1) or attitude were used.

Data of all ROSAT observations are collected in the ROSAT archive and can be used for various studies of the X-ray emission in the energy range of 0.1 – 2.4 keV. The Magellanic Clouds were extensively covered by pointed observations of ROSAT. Based on the PSPC pointings, source catalogs were created by Haberl & Pietsch (1999a, HP99a) and Haberl et al. (2000, HFPK00) for both the LMC and the SMC. In order to have a complete catalog of X-ray sources in the ROSAT band, all available HRI data of the Magellanic Cloud regions were analyzed within this thesis work, resulting in HRI source catalogs of the MCs which were published in Sasaki et al. (2000a,b). In Tables A.1 and A.2 the HRI data taken from the ROSAT archive in order to create the source catalogs are listed with observation date, pointing direction, and exposure time. Detailed description of how the catalogs were produced follows in the subsections below.
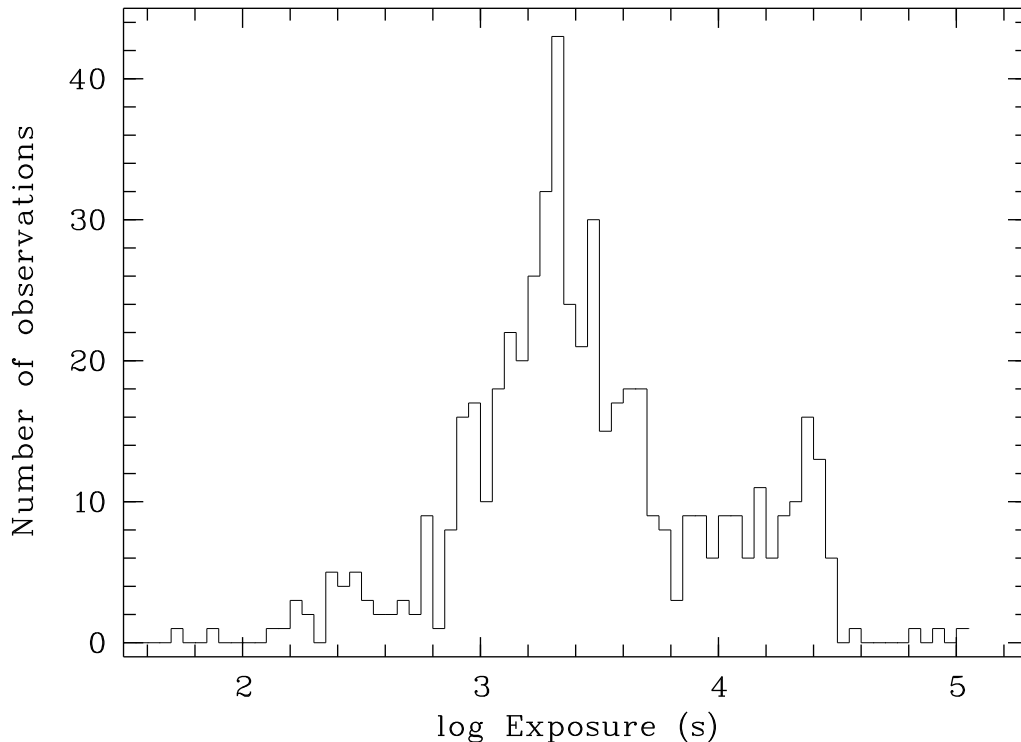
Figure 4.1: Histogram of exposure times of HRI observations pointed to the LMC.

4.2.1 Source Detection

LMC

The LMC was observed by the ROSAT HRI in more than 500 pointings during the operational phase of ROSAT between 1990 and 1998. 543 observations with exposure times of 50 to 110 000 s (Fig. 4.1) in a field of $10° \times 10°$ around RA = 05^h 25^m 00^s, Dec = $-67°$ $43'$ $20''$ (J2000.0) were used. The observed regions and the exposure times are shown in Figure 4.3.

The analysis was carried out using three detection methods available in EXSAS (Zimmermann et al., 1994). For each pointing X-ray sources were searched using the sliding window methods with local background and with a spline fitted background map. The resulting detection lists were merged and a maximum likelihood algorithm was performed on the new list. Sources were accepted if their telescope off-axis angle was smaller than $15'$ during the observation and the likelihood of existence larger than 10, i.e. the existence probability was higher than $P = 1 - \exp(-\mathrm{ML}_{\mathrm{exi}}) = 1 - 4.5 \times 10^{-5}$.

For point and point-like sources the extent was determined in the maximum likelihood routine by fitting the source intensity distribution with a Gaussian profile. The count rates resulting from this calculation are correct only for sources with small extent and a brightness profile peaking in the center. Therefore, for extended sources like SNRs with ring-like structure, the net count rates were additionally determined
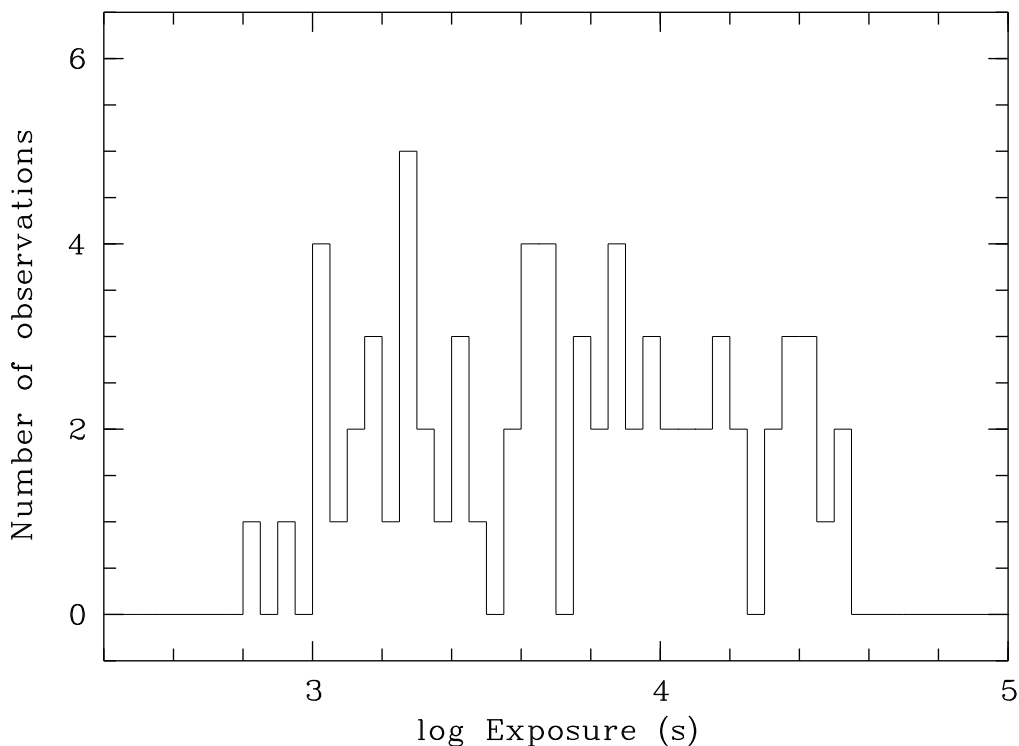
Figure 4.2: Histogram of exposure times of HRI observations pointed to the SMC.

interactively by integrating the counts within a circle around the source. For estimating the background the counts were averaged in a ring around the source, distant enough not to be influenced by the source emission.

In order to minimize the background noise, HRI observations with pointing directions within a radius of 1′ were merged after correcting the coordinates of the pointings (see Sec. 4.2.3) or adjusting the position with the help of bright point sources in the field of view. This was possible for 56 different regions in the LMC. Source detection was also performed on these data and additional faint sources were found which were not detectable in single pointings.

The final source lists obtained for each pointing and co-added observations were merged to one list and multiple detections of a source were reduced to one detection for each source. For this purpose the detection with the highest positional accuracy was chosen. After screening manually in order to delete spurious detections like knots in extended emission, the HRI catalog of the LMC finally contains 397 distinct sources.

SMC

The SMC was covered in a $5° × 5°$ field around RA $= 01^h \, 00^m \, 00^s$, Dec $= -73° \, 00′ \, 00″$ (J2000.0) by 71 pointings of the ROSAT HRI. The total exposure time is shown in Figure 4.4 as contours plotted over a grey scale PSPC image (HFPK00). The number of the analyzed HRI pointings with integration times higher than 100 seconds

31

is demonstrated in Figure 4.2.

For data analysis same procedures as developed for the LMC were applied to the SMC data using the EXSAS software package. Again pointings with directions within a radius of $1'$ were merged in order to increase the significance of source signals. For 18 regions in the SMC new deeper data could be created. In the end we obtained a HRI source catalog with 121 sources in the SMC region.

4.2.2   Cross-correlation with PSPC Catalogs

The HRI source catalogs both for the LMC and the SMC were cross-correlated with catalogs of the PSPC pointings (HP99a; HFPK00). in order to find coincidences between the sources detected by the different ROSAT detectors. In PSPC observations the MCs were covered more homogeneously, but due to the moderate spatial resolution of the PSPC, in crowded regions many sources could be resolved by the HRI only.

In PSPC data the events can be separated into different energy bands, as the PSPC has a moderate energy resolution. The energy bands commonly used are: $0.1 - 0.4\,\mathrm{keV}$ (soft, S), $0.5 - 2.0\,\mathrm{keV}$ (hard, H), $0.5 - 0.9\,\mathrm{keV}$ (hard1, H1), $0.9 - 2.0\,\mathrm{keV}$ (hard2, H2), and broad ($0.1 - 2.4\,\mathrm{keV}$). As indicators for the shape of the X-ray spectrum, hardness ratios can be determined from the count rates in the different bands. The hardness ratios are defined as:

$$\mathrm{HR1} = \frac{\mathrm{H} - \mathrm{S}}{\mathrm{H} + \mathrm{S}}, \quad \mathrm{HR2} = \frac{\mathrm{H2} - \mathrm{H1}}{\mathrm{H2} + \mathrm{H1}}. \tag{4.1}$$

Hard sources have $\mathrm{HR1} \approx 1.0$ and $\mathrm{HR2} \approx 1.0$, whereas softer sources have $\mathrm{HR2} \approx -1.0$.

For 138 HRI sources in the LMC also PSPC catalog entries were found. Thus for most of these sources PSPC hardness ratios are known. Since the HRI had no spectral resolution, no information on the X-ray spectrum was obtained for the new HRI detections. In the SMC region, 75 out of 121 HRI sources were also detected by the PSPC.

4.2.3   Correction of the ROSAT HRI Positions

Boresighting

ROSAT observations suffer from intrinsic positional uncertainty of the XRT pointing (see ROSAT USER'S HANDBOOK, *http://wave.xray.mpe.mpg.de/rosat/doc/ruh*) which was found out during the calibration phase of ROSAT, when boresighting was performed for the PSPC and the HRI separately. A detailed study of positions derived from ROSAT observations was carried out at MPE comparing the X-ray coordinates of known bright X-ray targets to those given in catalogs like the SIMBAD data base of the Centre de Données astronomiques de Strasbourg. The X-ray positions of both PSPC and HRI observations showed a systematic offset of $\sim 7'' - 10''$. Therefore an additional correction of the mean offset was implemented to the SASS. However, deviation between the X-ray and optical coordinates with a scattering of few arcseconds was still measured. This is now thought to be caused by variations in quantum efficiency between the pixels of the star tracker which was used for positioning of the XRT
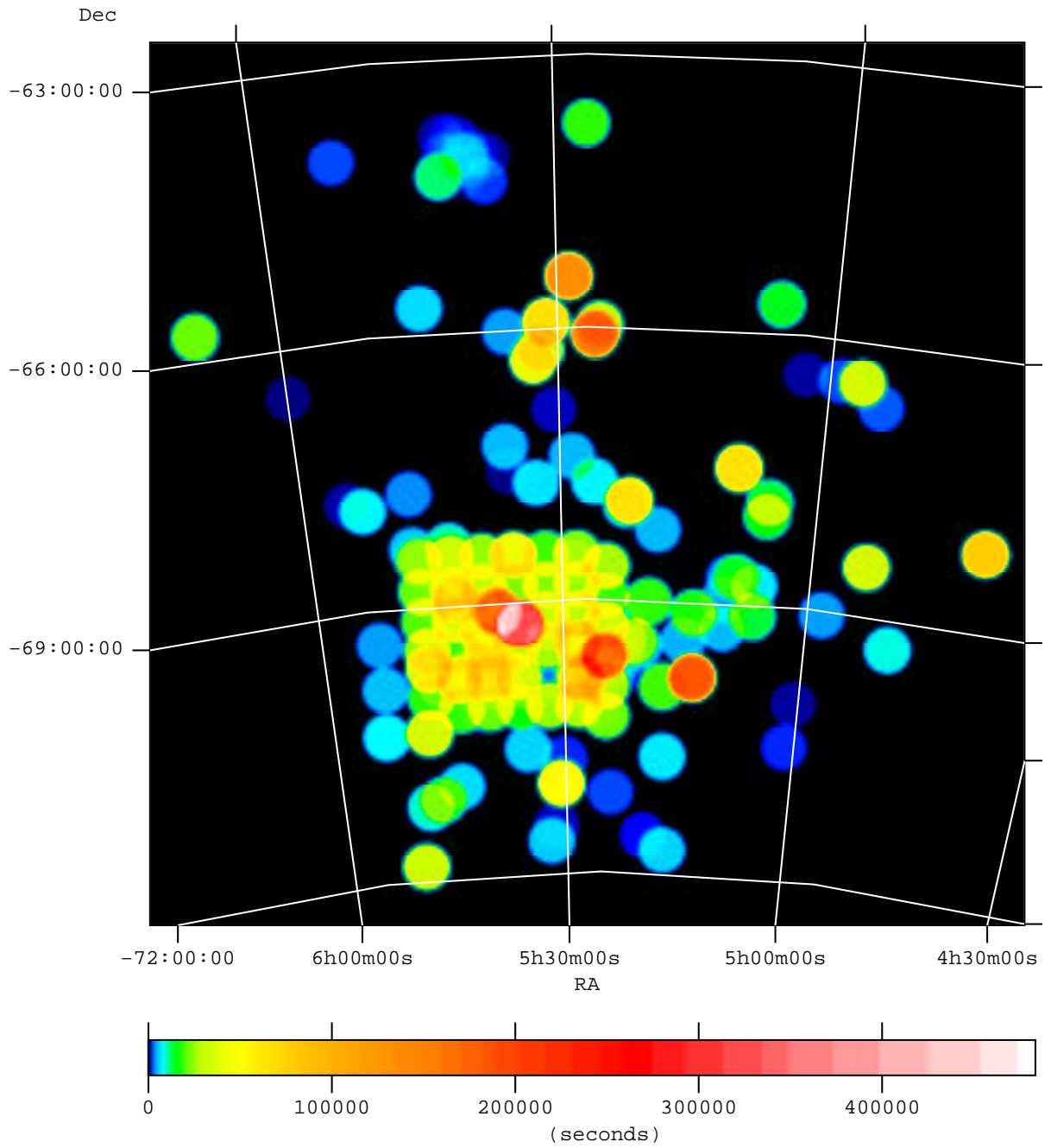
Figure 4.3: Exposure map of the HRI pointings in the LMC field.

33
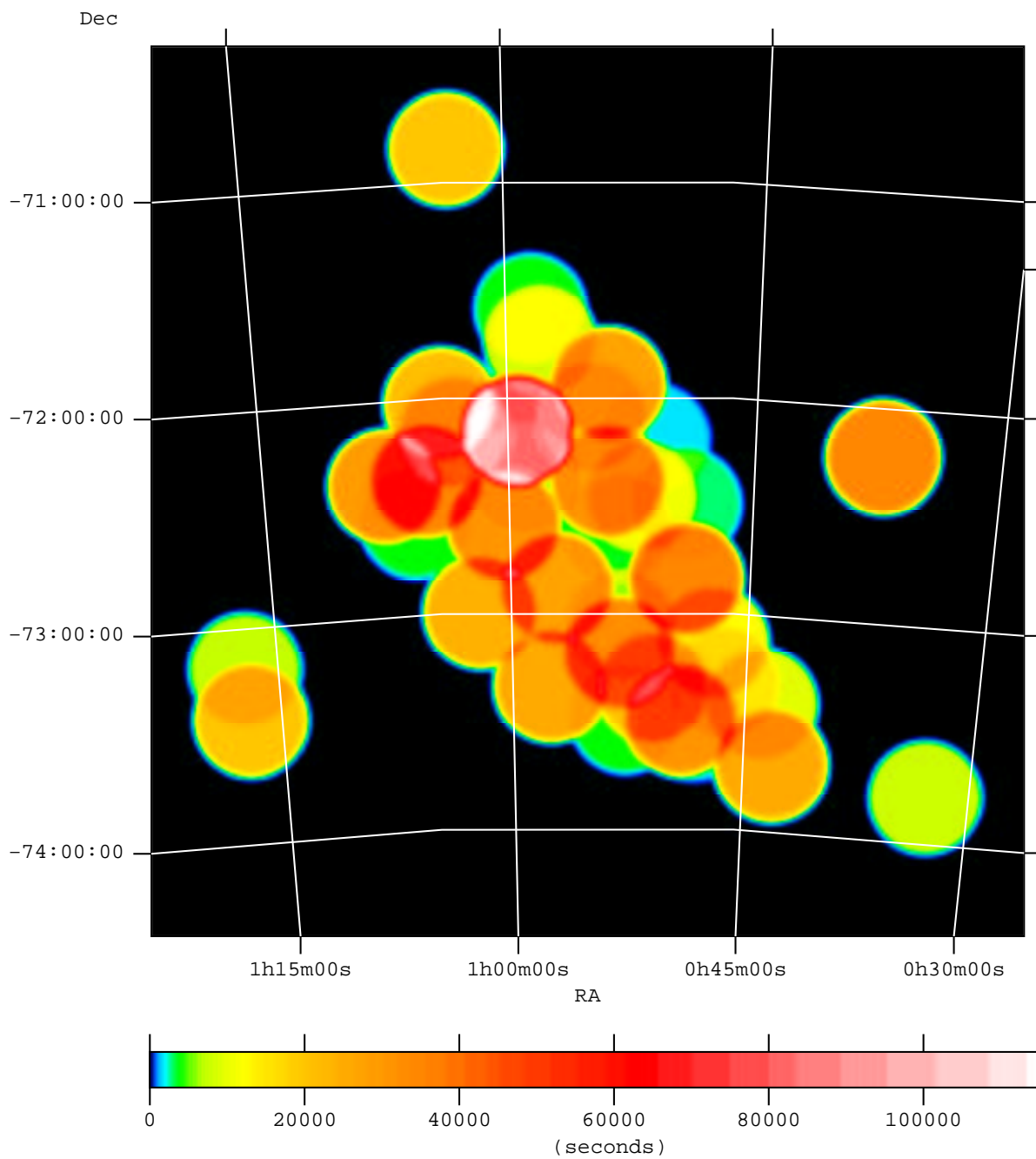
Figure 4.4: Exposure map of the HRI pointings in the SMC field.

with the help of guide stars. As latest studies have shown, though all the discrepancies have been corrected, there is still a random boresight offset of $5'' - 7''$.

The coordinates of sources detected in ROSAT observations are determined in the standard EXSAS (Zimmermann et al., 1994) source detection routine which also gives the statistical error of the positions. To obtain the total positional error of the X-ray sources, the systematic boresight error must be taken into account additionally, except for pointings where objects with known optical counterparts were observed and the pointing direction can be corrected with the help of the accurate optical coordinates. Especially for the HRI observations, this was a crucial part of the data analysis since for point sources detected by the HRI the X-ray positions were determined with an accuracy of the order of arcseconds thanks to the high spatial resolution of the HRI, and thus likely optical counterparts could be found.

Correction of the HRI Coordinates

In order to determine more accurate coordinates for the HRI sources, the HRI catalogs were cross-correlated with the SIMBAD data base of the Centre de Données astronomiques de Strasbourg and the TYCHO catalog from the observations of the ESA Hipparcos Space Astrometry Satellite (Hoeg et al., 1997). For X-ray sources which were identified with known objects, coordinates calculated in the source detection routine were compared to high-accuracy positions available in the TYCHO catalog or in the literature.

First, the X-ray position was corrected to TYCHO coordinates. For X-ray sources without any TYCHO counterpart, but identified on the ESO Digitized Sky Survey (DSS) frame with other stars on this frame which were listed in the TYCHO catalog, more accurate coordinates were calculated for HRI sources by determining the offset between the TYCHO and DSS positions and between the HRI and DSS position. Other sources could be identified with objects in the SIMBAD data base or in the literature and their positions were corrected after checking their positions on DSS frames. Correction of coordinates for one source implied improved coordinates for all detections of this source in different pointings and for other sources in same pointings. Those secondary corrections again allowed correction of further pointings if the sources were detected several times.

Positional Error

If an X-ray source in a pointed observation is identified with an object with accurately known coordinates, the systematic error can be reduced for all detected X-ray sources from the same observation. The remaining systematic error for all sources in these pointings is

$$\sigma_{\mathrm{sys,p}} = \sqrt{\sigma_{\mathrm{opt}}^2 + \sigma_{\mathrm{stat,s}}^2} \ , \tag{4.2}$$

σ_{opt} being the error of the optical position and $\sigma_{\mathrm{stat,s}}$ the statistical 90% confidence error of the identified X-ray source used for correction. For all other sources of which the X-ray position could not be corrected, a systematic error of $7''$ was used, which

was a good estimate for the boresight error determined by comparison with catalog objects (see above). The total positional error is finally given by:

$$\sigma_{\mathrm{tot,X}} = \sqrt{\sigma_{\mathrm{sys,p}}^2 + \sigma_{\mathrm{stat,X}}^2} \; . \tag{4.3}$$

For the LMC 254 out of 397 source positions were corrected. Thus the mean positional error is reduced from $8\overset{''}{.}3$ to $6\overset{''}{.}4$ for the whole catalog. For position corrected sources only, the mean positional error is $5\overset{''}{.}1$. In the SMC catalog 99 out of 121 positions could be improved. The mean positional error was originally $8\overset{''}{.}1$, but after the correction $5\overset{''}{.}6$, and $4\overset{''}{.}9$ for corrected sources only.

4.3 ROSAT PSPC Data

Since the Magellanic Clouds were surveyed by ROSAT almost completely during its operational phase, the archival data of the PSPC are best suited for spectral analysis of the galaxies as a whole. All available PSPC pointings in the ROSAT archive covering the Magellanic Clouds were analyzed in order to have an almost full coverage of the MCs and high photon statistics (see Tables A.3 and A.4). For the LMC 223 and for the SMC 31 pointings with exposure times of up to 65 ksec were used. For investigating diffuse X-ray emission of the Magellanic Clouds, spectral analysis was performed in smaller regions resulting in a temperature distribution in the galaxies with high spatial resolution.

4.3.1 Background Reduction

Complete ROSAT catalogs of distinct X-ray sources were created for both galaxies from all PSPC and HRI observations (HP99a; HFPK00; Sasaki et al. 2000a,b; see also Sec. 4.2). Therefore the contamination by all point and point-like X-ray sources emitting in the ROSAT band could be eliminated from all data. The extraction radii were computed according to the point spread function of the observations on the one hand, and the brightness and the extent of the sources on the other hand.

In PSPC observations there is a contamination in lower pulse height channels due to afterpulse events (APE, Plucinsky et al., 1993; Snowden et al., 1994). They occur within 0.37 ms after and not further away than few arcmin from a preceding event in channels lower than 18 and are thought to be caused by negative ion formation close to the anodes. The APE were eliminated using the EXSAS routine `process/ape` which searches for APEs in the event file and creates a cleaned event file.

Next, the data was analyzed according to the housekeeping information of each observation obtained from the EXSAS routine `process/hk`. In doing so time intervals with higher background can be selected out of the data. One part of the background is caused by X-rays of Solar origin scattered by the Earth atmosphere (Snowden & Freyberg, 1993). The mainly contributing scattering mechanisms are Thomson scattering by oxygen, helium, and molecular nitrogen and fluorescent scattering by molecular

nitrogen (Kα) and atomic oxygen (Kα). As an indicator for the Solar X-ray background the oxygen column density N_{O} in the housekeeping data was used which gives the oxygen column density along the line of sight through the Earth's residual atmosphere. To eliminate the scattered Solar X-ray background, at first, time intervals with Solar zenith angle (angle between the Sun, the Earth, and the telescope) greater than 120° were selected in the housekeeping data. This means that the satellite was in the shadow of the Earth and the effect of the Solar X-rays scattering was low. For this night-side observation the mean $\langle N_{\mathrm{O}} \rangle$ and the standard deviation σ of N_{O} was computed. With the help of these numbers events in time intervals with N_{O} not exceeding the upper limit of $\langle N_{\mathrm{O}} \rangle + 1\sigma$ were finally selected from the event files.

Being a high energy particle detector, proportional counters are sensitive to cosmic rays as well. The particles falling through the detector also ionize the counter gas and cause signals. Therefore the detector is equipped with an additional anode which is linked with the active detector anode in anti-coincidence, and the vetoing during the observation is measured (master veto). For preliminary particle background elimination intervals were chosen with master veto rate lower than 170 cts/sec. As last step, time intervals with enhanced count rates of unknown origin (short time and long time enhancements) were excluded which can be seen as an increase of the measured photons in the housekeeping data.

4.3.2 Creating Spectra

The cleaned event files of the single pointings were merged for the SMC and the LMC resulting in data which correspond to a cheesed image for each of the MCs. For a spatially resolved spectral analysis of the diffuse emission from the MCs, the data were divided into boxes of the size $0\overset{\circ}{.}25 \times 0\overset{\circ}{.}25$. Only boxes containing more than 1000 events were used for the following spectral analysis to have enough photon statistics. In Figure 4.5 the merged data and the selected regions are shown.

In the reductional steps, the particle background was eliminated only by excluding time intervals of high master veto rate. To completely dispose of the contribution of the high energy particles, their spectrum was modeled and subtracted from all the analyzed spectra. According to Snowden et al. (1992) and Plucinsky et al. (1993, 1996) the particle spectrum consists of three components. The first component is the internally produced spectrum of particles measured when the filter wheel of the PSPC is closed by a ~ 2 mm thick aluminum mask so that no X-rays are penetrating (S_{FWC}). There are two additional components which are measured when the filter wheel is open, but the detector out of focus: Al Kα line at ~ 1.5 keV which is excited when the filter wheel is open and particles fall through the optical path of the telescope (S_{Al}), and the externally produced flat increase of the whole spectrum (S_{Ext}). Since they are caused by in-falling particles, they are all well correlated with the master veto rate. Each component of the particle background spectrum can be parameterized as follows (CH: pulse height channel):

$$S_{\mathrm{FWC}}(CH) \quad = \quad \left[\, 39.66\, CH^{-2.91} - 3.96 \times 10^{-6}\, CH + 0.0045 \,\right]\, CH^{-1} \qquad (4.4)$$
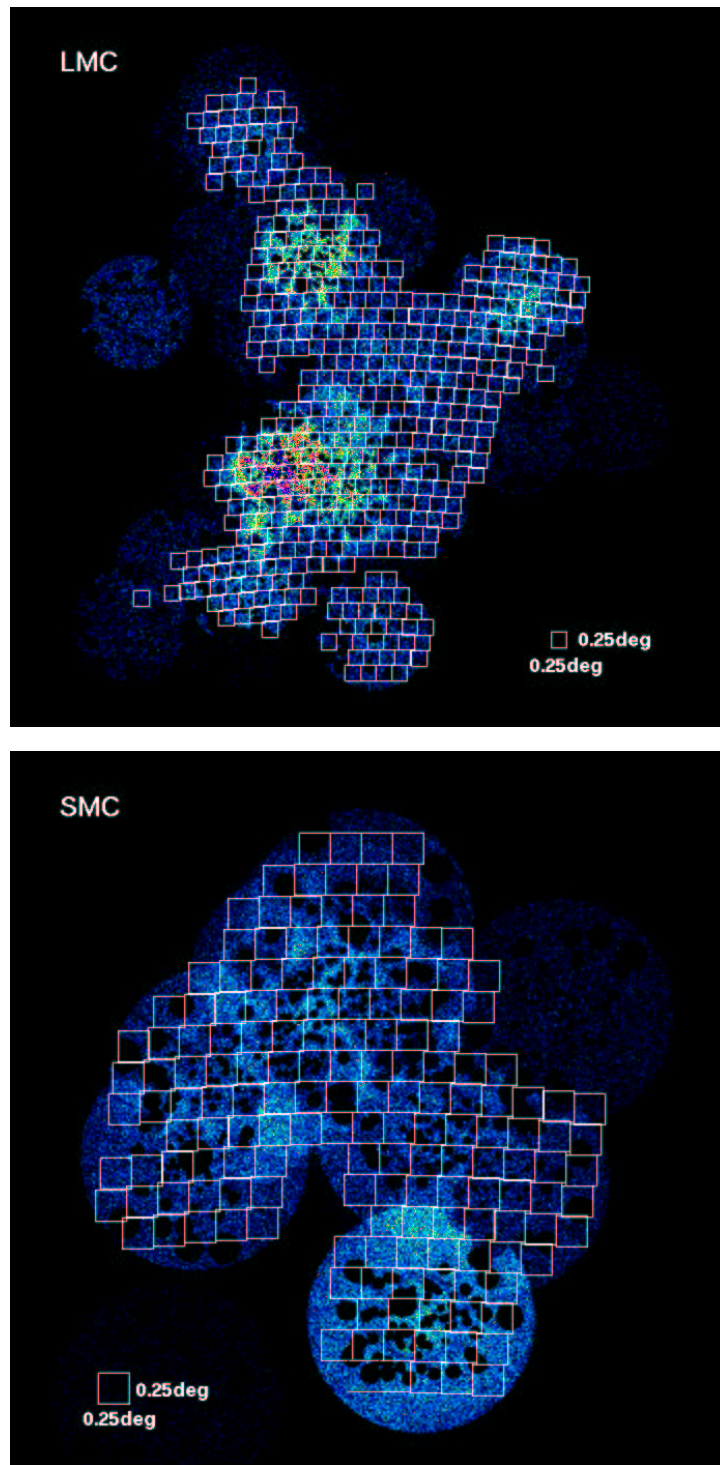
Figure 4.5: Areas for which spectra were extracted from the merged PSPC data of the MCs. They are overlaid on images created out of the merged data after cutting out the point and point-like sources. Since the data hasn't yet been exposure-corrected, there are bright regions correlating with the pointings.

$$S_{\text{Al}}(CH) = [\,0.835\,CH^{-0.75} \times \exp\{-0.716(12.247 - \sqrt{CH})^2\}\,]\,CH^{-1} \quad (4.5)$$
$$S_{\text{Ext}}(CH) = [\,-4.47 \times 10^{-6}\,CH + 0.00493\,]\,CH^{-1} \quad\quad\quad\quad (4.6)$$

Particle background dominates in higher energy ranges, because the cosmic X-ray background is relatively low and the X-ray mirror reflectivity of the telescope decreases significantly in these higher energy ranges. So counts in pulse height channels higher than 230 can be more or less ascribed to high energy particles and are used for normalizing the particle background spectrum. Finally we obtain for the total particle background:

$$
\begin{aligned}
S(MV, CH) = &\, [\,(0.018 + 7.37 \times 10^{-4}\,MV) \times S_{\text{FWC}} \\
&+ (-0.004 + 2.29 \times 10^{-4}\,MV) \times S_{\text{Al}} \\
&+ (0.007 + 2.21 \times 10^{-4}\,MV) \times S_{\text{Ext}}\,] \times N_{230} \quad (4.7)
\end{aligned}
$$

MV: mean master veto rate
N_{230}: normalization of the spectrum with counts in channels higher than 230

Events of the PSPC data were binned into spectra in each selected $0°\!.25 \times 0°\!.25$ box. The particle background spectrum was modeled for each spectrum taking the components $S_{\text{FWC,Al,Ext}}$ into account as defined in the Equations (4.4) to (4.6), and determining the master veto rate for the selected events. After normalizing with number of events in the channels above No 230, the modeled background spectrum (Eq. (4.7)) was subtracted from the total spectrum.

4.4   XMM EPIC-PN Data

During the calibrational phase, the XMM-Newton observatory pointed on the SNR B 0540–69 lying close to the giant H II region 30 Doradus in the LMC. Since this pointing covers a part of the supergiant shell (SGS) LMC 2 (Meaburn, 1980) with enhanced X-ray emission, it was ideal to verify the feasibility of the new X-ray telescope for the purpose of studying the diffuse emission spectrum.

For this analysis EPIC-PN data of the observation No 125120101 of satellite revolution 85 processed through the XMM-Newton Science Analysis System (XMM-SAS) was used. The observation was performed with medium filter in full frame mode and a total exposure time of 38.1 ks. The integrated lightcurves of the data for all CCDs show an almost constant background except for a time interval of ~ 1.3 ks with high background emission. Events within this time interval were excluded from the data before subsequent processing. For the data analysis the XMM-SAS version of October 2000 was used. Two extended regions were selected for spectral analysis (see Sec. 6.2) taking single pattern events only, i.e. the electron clouds caused by the hitting photons were extended on only one or two pixels.

Vignetting

In the course of making spectra, events extracted from the data still had to be corrected for the vignetting of the telescope, the out-of-time events, and the background. For

vignetting correction, auxiliary response files (ARFs) from the calibration of the mirror modules were used to rescale the spectra depending on the energy and the off-axis angle of the events. The ARFs contain the vignetting scaling factors for a certain energy value and the off-axis angle with respect to the pointing center. For each event the energy value is given in the events file, and the off-axis angle can be derived from the position of detection. The appropriate correction factor was interpolated from the off-axis angles and energy values given in the ARFs. The events were all scaled with these factors before binning the events file into a spectrum.

Out-of-time events

Out-of-time (OOT) events are caused by X-rays hitting the CCDs during the readout of the detector, as the CCDs are sensitive all the time. The information about position get lost for these detections, and the OOT events are displaced along the readout column. This effect becomes visible in the image in particular for bright sources as straight line along the columns through the source (see Fig. 6.10). OOT events are included in the event files and have to be excluded for eliminating the contamination of other sources located in the same column. Therefore, an OOT event file was produced using the XMM-SAS by integrating all events in a column and distributing them equally in the column. For the regions to be analyzed, the OOT events were selected in the same way as the total events of the frame. Since the readout time is 6.3% of the collecting time, the spectra of the OOT events were scaled with a factor 0.063 and subtracted from the total spectra.

Background

In the spectra of the diffuse emission, there are background components caused by the detector itself and by the X-ray background (i.e. cosmic background and Galactic foreground). For estimating the background, an XMM EPIC-PN observation of May 24, 2000 (Rev. 84, No 125110101) was chosen, because the data, obtained in full frame mode and with medium filter, contained no diffuse emission and only a small number of point sources which were cut out. There was a background enhancement in the second half of the observation. Thus only time intervals in the beginning with low background were used with an exposure time of ~ 5 ks. The events were selected from the same CCDs as for the regions of diffuse emission. They were corrected for vignetting and OOT events as well. The background spectrum was rescaled considering the differences in selected area of the field of view and in the exposure times, and in the end subtracted from the spectra of the diffuse emission.

Chapter 5

Point and Point-like X-ray sources

The Magellanic Clouds were observed by ROSAT repeatedly and almost full coverage was yielded. Analyzing the source content of the Magellanic Clouds in X-rays, we are able to study their structure, stellar population, and the evolution history, as well as the properties of the single objects within. Complementary to the PSPC source catalogs of HP99a and HFPK00, source catalogs were created with data from HRI observations, since the HRI provides data with higher spatial resolution. The Figures 5.1 and 5.2 show the Magellanic Clouds seen by the HRI. Data used for the analysis (see Sec. 4.2) were exposure corrected and merged.

Tables B.1 and B.2 in Appendix B contain the entire catalogs of the sources detected by the HRI in the fields of the MCs. They give the corrected coordinates (see Sec. 4.2.3), final positional errors, existence likelihood of the maximum likelihood algorithm, HRI count rates, extent, extent likelihood, PSPC count rates and the corresponding PSPC catalog number with hardness ratios. Sources were sorted by the coordinates Right Ascension (RA) and Declination (Dec) and were numbered serially. The source numbers of the Tables B.1 and B.2 (LMC n or SMC n, respectively, n being the number in the tables) are also used in the text.

5.1 Classification of HRI Sources

For knowing the nature of the objects seen in X-rays, it is crucial to find counterparts in other wavelength bands. Thanks to the higher spatial resolution of the HRI, for similar photon statistics observations with the HRI yielded smaller positional error circles and consequently more accurate source positions compared to the PSPC results. Therefore likely counterparts in the optical or near-infrared could be determined for several sources, which was not possible only with PSPC data.

5.1.1 Cross-correlation with Source Catalogs

In the course of data analysis the HRI source catalogs have already been cross-correlated with the PSPC catalogs (HP99a, HFPK00) as well as with the SIMBAD data base and the TYCHO catalog (see Sec. 4.2.3). In order to get further information

ROSAT HRI

LMC

Declination (J2000)

-64°

-66°

-68°

-70°

6^h0^m 5^h30^m 5^h0^m 4^h30^m
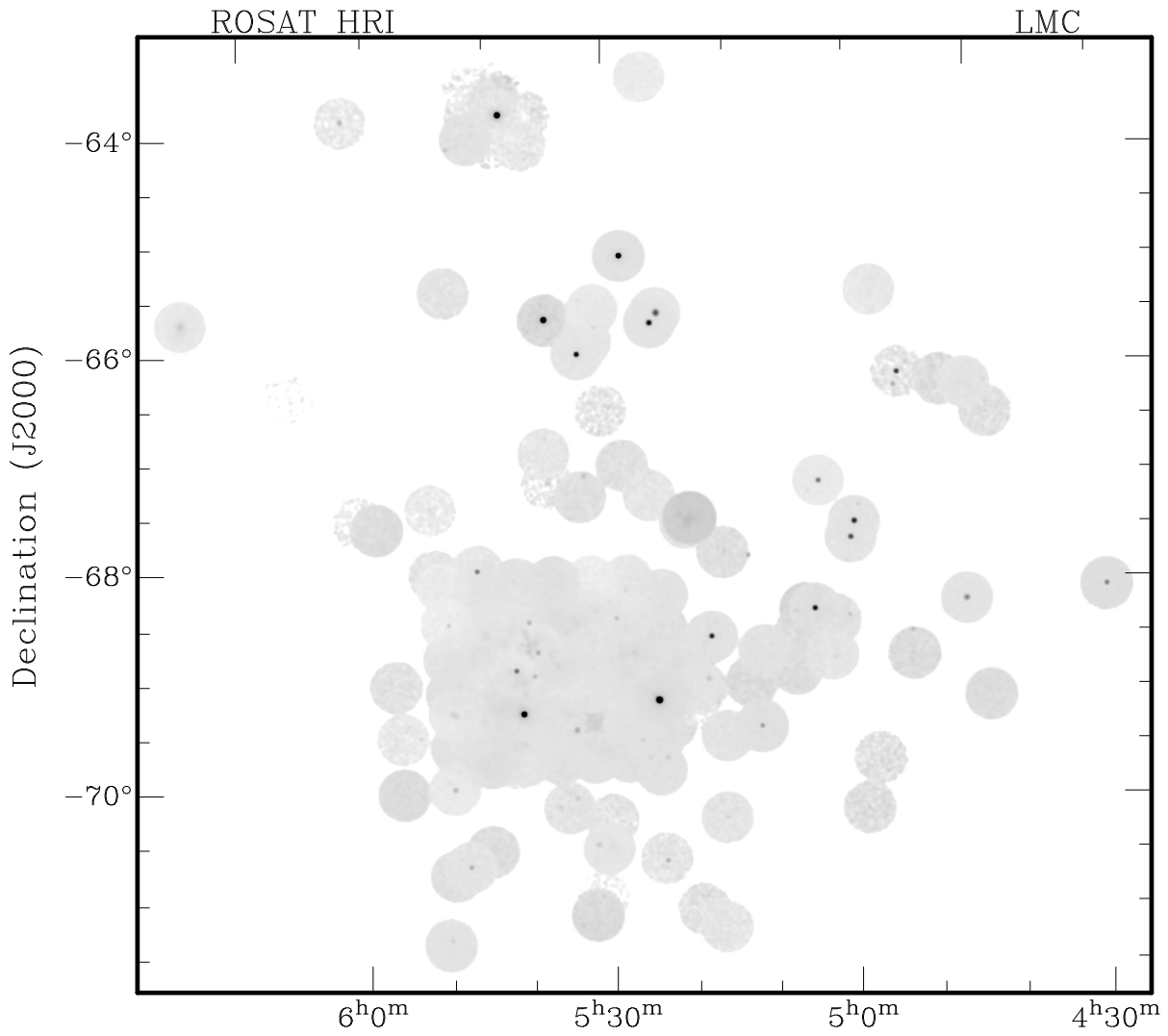
Figure 5.1: Exposure corrected merged image of the ROSAT HRI pointings in the $10° \times 10°$ field around RA = 05^h 25^m 00^s, Dec = $-67°$ $43'$ $20''$ (J2000.0) covering the LMC.

42
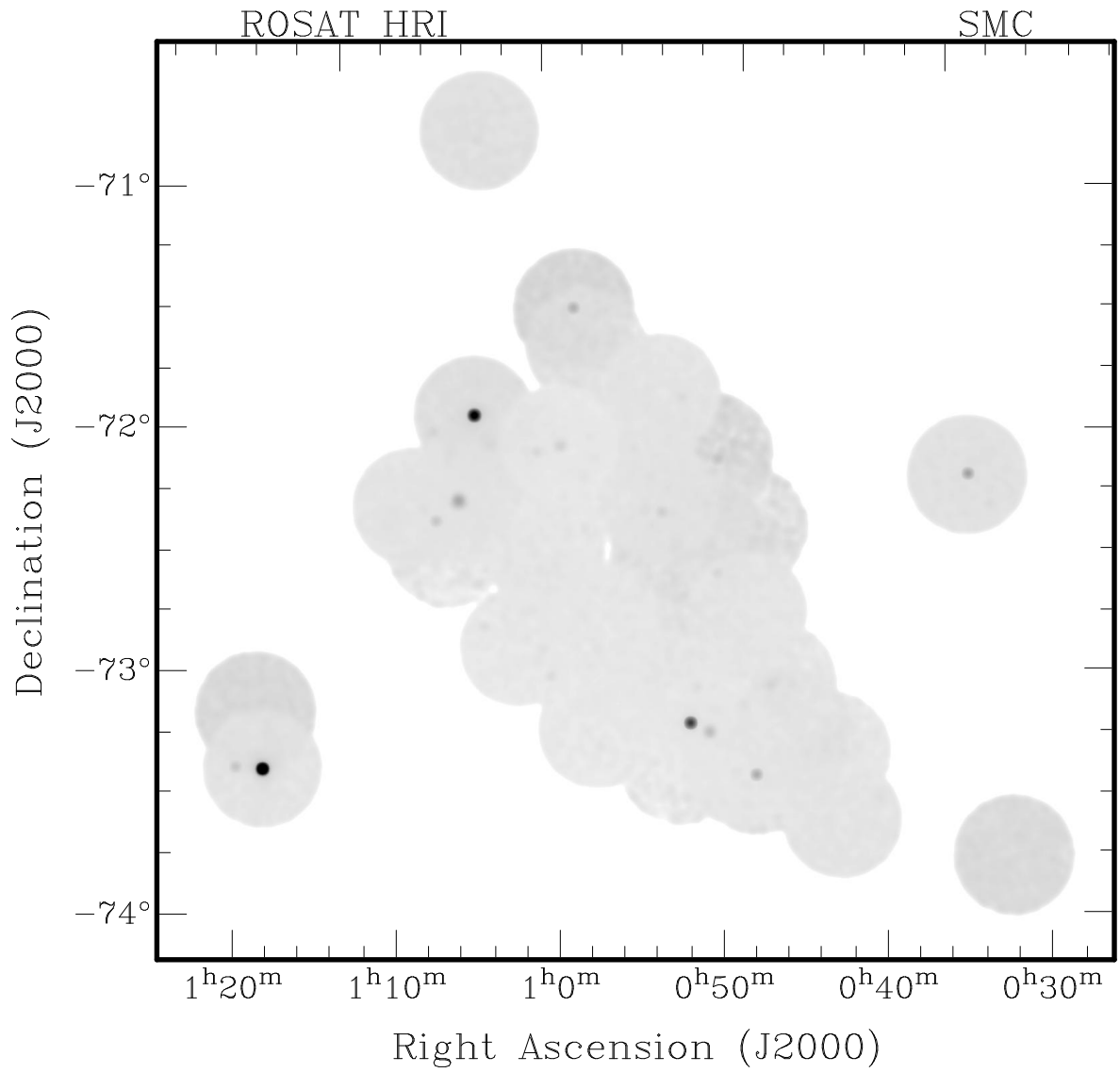
Figure 5.2: *Exposure corrected merged image of the ROSAT HRI pointings in the $5° \times 5°$ field around RA = $01^h\ 00^m\ 00^s$, Dec = $-73°\ 00'\ 00''$ (J2000.0) covering the SMC.*

about the HRI sources and find objects which were seen in other wavelengths and might be associated to the X-ray sources, the HRI catalogs were also cross-correlated with the USNO-2.0 catalog produced by the United States Naval Observatory (Monet, 1996, 1998), the Deep Near Infrared Survey of the Southern Sky (DENIS) Point Source Catalog (Cioni et al., 2000, hereafter CLH00), and other lists found in literature.

Furthermore, Hα and [O III] surveys have been carried out in the SMC by Meyssonnier & Azzopardi (1993) and Murphy & Bessell (2000). These catalogs were additionally compared to SMC HRI source lists and helped us to find new X-ray binary candidates (see Sec. 5.4.2).

5.1.2 Classification Criteria

The HRI source catalogs contain samples of known supersoft sources (SSSs), X-ray binaries (XBs), supernova remnants (SNRs), Galactic foreground stars and background active galactic nuclei (AGN) or galaxy clusters. This was found out by comparing the HRI positions with those listed in catalogs or publicatios about single objects. In total 100 LMC sources and 46 SMC sources were identified with known objects in the MCs, Galactic foreground stars, or background objects. Criteria for classifying objects can be derived from their X-ray characteristics and the brightness of likely counterparts in different wavelength bands.

Source Extent

HP99a have shown that extent and extent likelihood as well as the hardness ratios measured by the PSPC have characteristic values for different source classes and can be used as classification criteria. In Figure 5.3 extent and extent likelihood of the HRI sources are shown. The extent is calculated in the maximum likelihood algorithm and gives the value resulting from fitting Gaussians. Therefore, in some cases it might be the extent of knots which were found within the extended source rather than that of the whole source.

Identified SNRs, marked with open squares, are distributed in the region with large extent and high extent likelihood. Crossed squares indicate known SNR candidates and filled squares sources newly classified as SNR candidates in this work. Point sources have lower extent likelihood unless they were extremely bright like AB Dor (LMC 180), LMC X-1 (LMC 311), or RX J0439.8-6809 (LMC 4) where the deviation of the point spread function from the assumed Gaussian profile becomes significant.

X-ray to Optical Flux Ratio

The accurate HRI positions make it possible to identify likely optical counterparts. For optical sources within the error circle of the X-ray position, the B and R magnitudes were determined from the USNO-A2.0 catalog. The flux ratio was computed from the B magnitude and the X-ray count rates applying the equation

$$log(f_X/f_{opt}) = log(3 \times \text{HRI counts/s} \times 10^{-11}) + 0.4B + 5.37 \qquad (5.1)$$
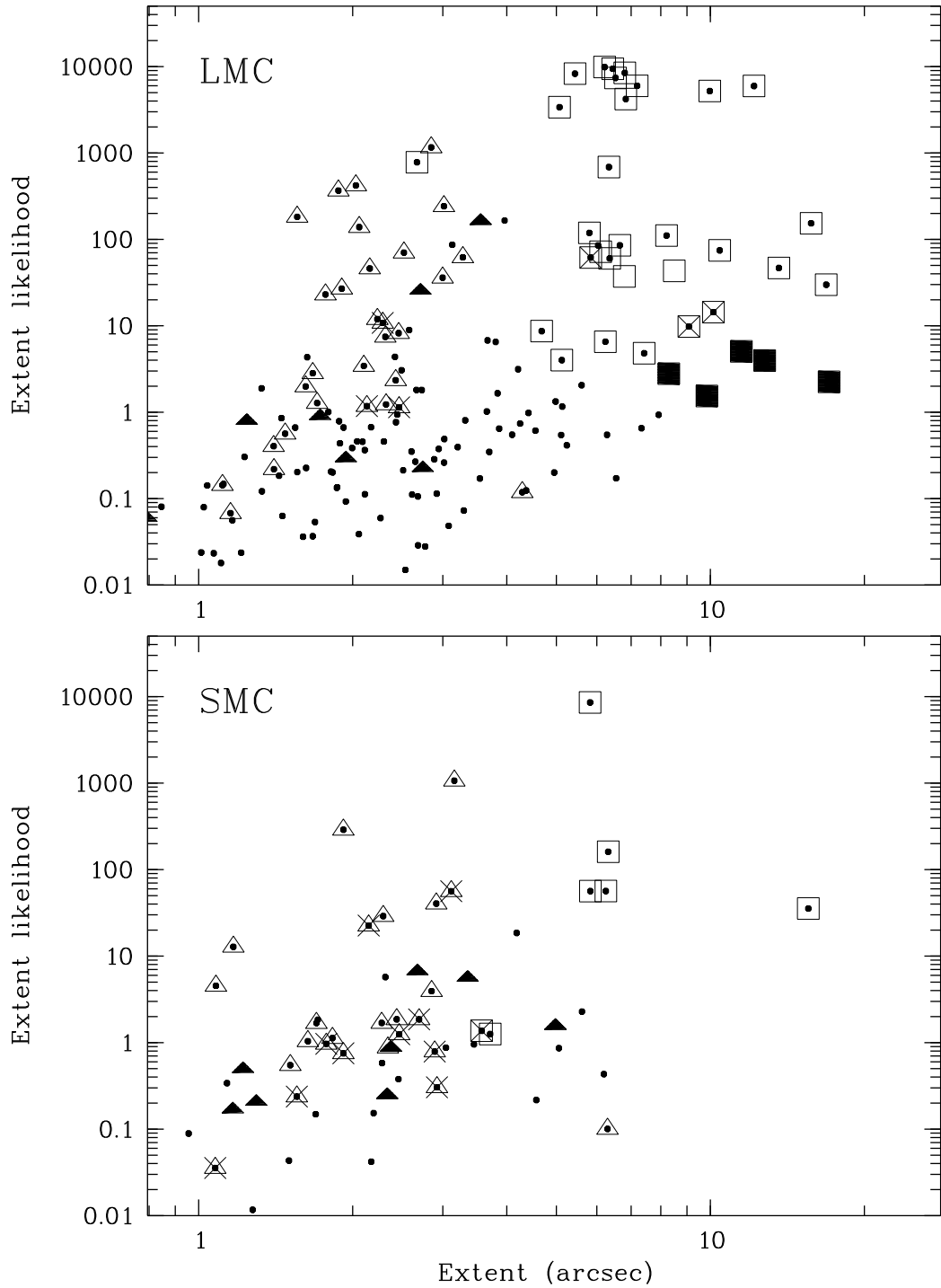
Figure 5.3: Source extent is plotted over extent likelihood as small dots for all LMC and SMC sources, for which the HRI measured an extent. SNRs are additionally marked with squares and known point sources with triangles. Open symbols are used for identified sources, crossed symbols for candidates known from literature, and filled symbols for new classifications.
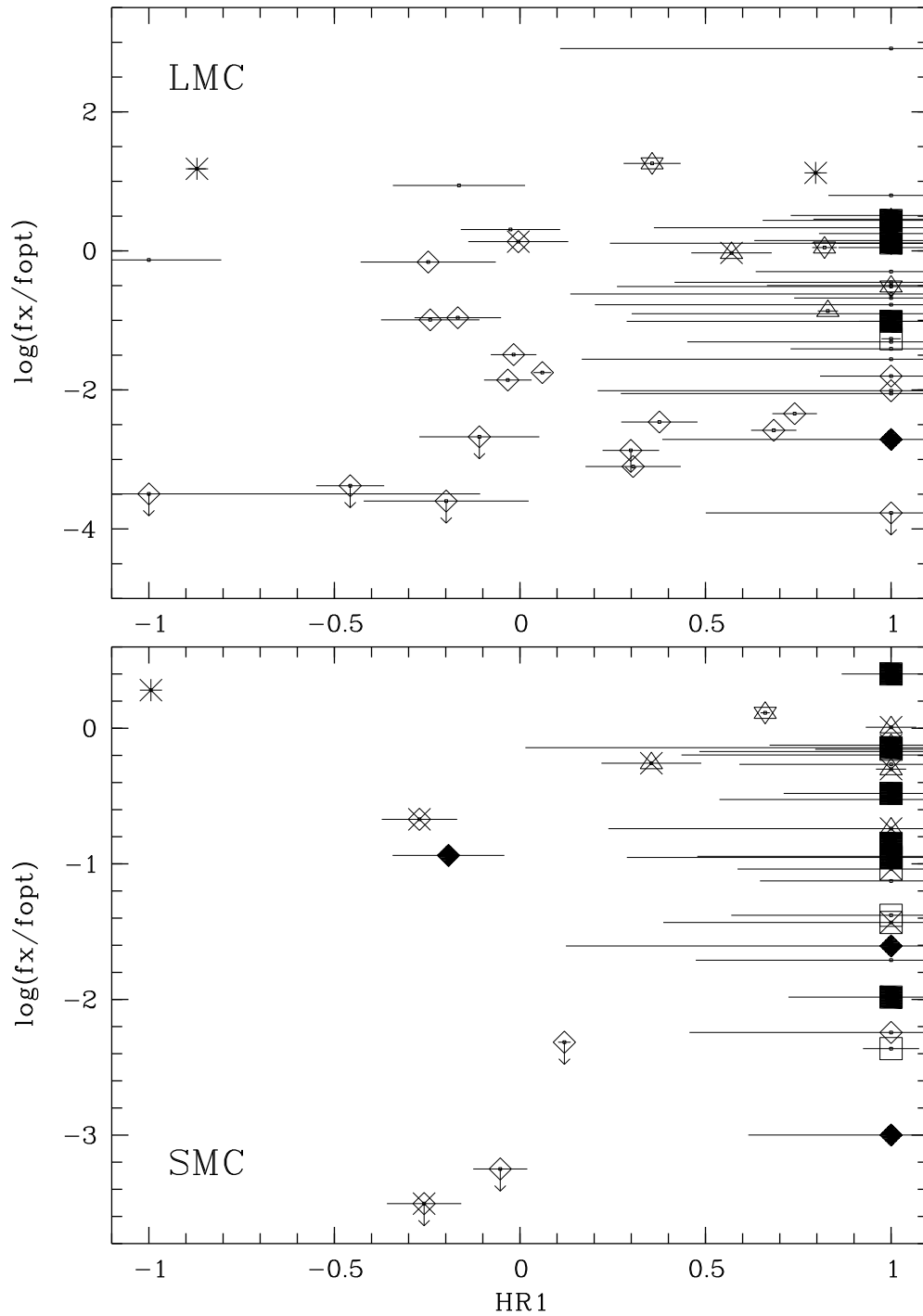
Figure 5.4: Flux ratio log(f_X/f_{opt}) over hardness ratio HR1 for all HRI sources with accepted or likely optical counterparts and PSPC detections. SSSs are indicated by asterisks, SNRs by stars, XBs by squares, Galactic stars by lozenges, and AGN by triangles. Open symbols are used for objects which are known from literature. Already known candidates are marked with crossed symbols and new classifications with filled symbols.

(Maccacaro et al., 1988; HP99a). The relation used for PSPC observations in HP99a was applied here for HRI sources converting the HRI count rates to PSPC count rates by multiplying by the factor of 3.0 which is typical for hard sources (see Sec. 5.2.1). Originally this value was calculated for V magnitude. But since the V magnitude could be determined only for a small sample, we decided to use the B magnitude. It gives a clue for identifying foreground stars, because for stars $\log(f_X/f_{opt})$ is negative usually. For very bright stars, the B magnitude is not given in the USNO-A2.0 catalog. In those cases B was set to 11.0 for calculating $\log(f_X/f_{opt})$, yielding an upper limit. In Figure 5.4 the $\log(f_X/f_{opt})$ values are plotted over the PSPC hardness ratio HR1 for HRI sources which were detected by the PSPC as well, and have likely optical counterparts.

Stars in general have negative $\log(f_X/f_{opt})$, for AGN it is around zero, and for SSSs and XBs it is mostly positive, in particular when they were observed in their X-ray active phase. Combination of $\log(f_X/f_{opt})$ and the hardness ratios provides a tool to identify foreground stars. For the SNRs $\log(f_X/f_{opt})$ gives no quantitative information, but it is an indicator that this source class is bright in X-ray, i.e. $\log(f_X/f_{opt}) > -1$.

5.2   Variability

Timing analysis of the X-ray flux tells us whether the X-ray emission is variable or not, and is another tool for determining the object types. SNRs change their morphologies and emission over thousands of years, but on time scales of years or less, their total luminosity stays almost constant, whereas stars show variation of their X-ray flux. X-ray sources in binary systems show permanent flux variations and bursts, and a large number of AGN are known to be variable over the whole range of the electromagnetic spectrum. 80 to 90 % of the HRI sources in the LMC and the SMC were detected in more than one ROSAT pointing and thus allowed variability studies on time scales of days to years.

5.2.1   Lightcurves

HRI Count Rates

For point and point-like sources longterm lightcurves of HRI observations were produced with observation-averaged count rates or upper limits determined by the maximum likelihood algorithm, whereas for extended sources count rates integrated within a circle around the source were used (see Sec. 4.2.1).

For some very bright sources the count rates were integrated interactively as well, because an apparent extent resulted from the maximum likelihood algorithm. An apparent extent is computed if the high photon statistics of the bright sources causes a significant deviation from the assumed model for the point spread function. But it could be shown that in these cases there is no substantial difference between the interactively determined count rates and the values from the maximum likelihood algorithm (see Fig. 5.5)
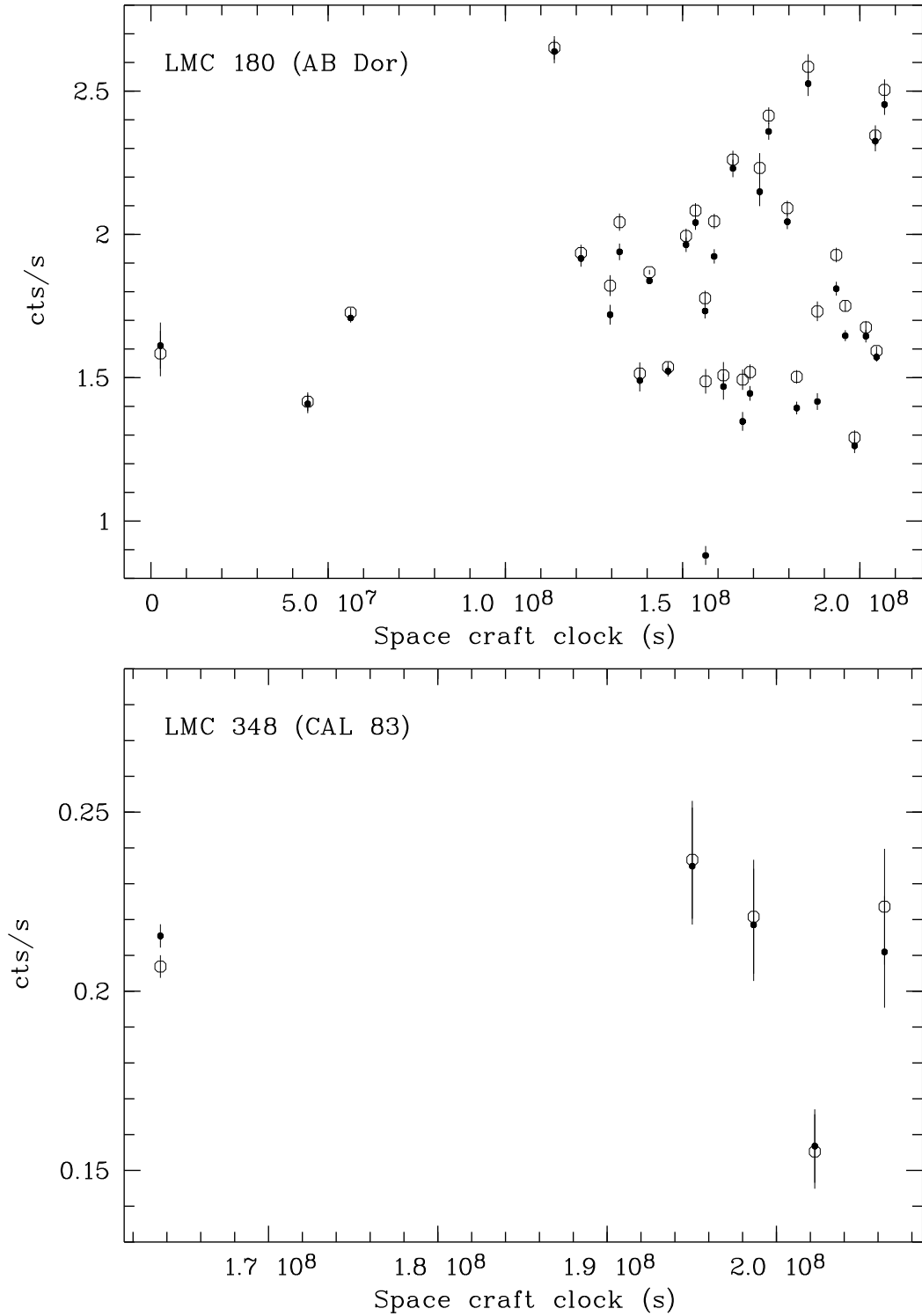
Figure 5.5: Lightcurves of AB Dor and CAL 83 with HRI count rates. Dots are used for values from the maximum likelihood algorithm, open circles for values determined by integrating the counts manually. Zero point of the space craft clock is 1990, June 21 21:06:50 UT.

48

Converted PSPC Count Rates

In order to obtain a complete lightcurve of the ROSAT observations, also PSPC count rates and upper limits (0.1 – 2.4 keV) were calculated for sources detected by the HRI. PSPC count rates were determined in all pointing data in the ROSAT archive covering the sources. The mean value was calculated from these count rates and compared to the HRI mean count rates (see Fig. 5.7). The resulting conversion factor is close to 3.0, only variable sources marked with large dots show significant deviation. Sources close to another bright object or sources in regions with high diffuse emission, e.g. 30 Dor or N 44 in the LMC, could not be resolved in some PSPC observations and yielded misleadingly large converting factor.

In Figures 5.6 a – c the conversion factor from PSPC to HRI count rates is plotted over the absorbing hydrogen column density $N_{\mathrm{H}} = 10^{20} - 10^{23}$ cm^{-2}. PSPC and HRI count rates were calculated in simulations using the response matrices for three different spectral models in the energy range of 0.1 to 2.4 keV. SSSs with a soft black body spectrum can be modeled with $kT = 10.0 - 50.0$ eV and foreground absorption by the Galaxy and the MCs ($N_{\mathrm{H}} = 10^{20} - 10^{21}$ cm^{-2}). AGN and XBs in general show a power law spectrum with N_{H} up to 10^{22} cm^{-2} because of intrinsic absorption in addition to foreground absorption. A Raymond & Smith model (Raymond & Smith, 1977) is used to describe the thermal spectrum of hot thin plasma, radiated by e.g. SNRs. For most of the point and point-like X-ray sources, PSPC count rates can be converted into HRI count rates by dividing by a typical value of 3.0, though for very soft sources this scale factor can be larger.

For the majority of the point and point-like X-ray sources observed both by the PSPC and the HRI, corresponding HRI count rates were calculated from the PSPC count rates for the time intervals during the PSPC observations, and finally lightcurves were made including all count rates from ROSAT pointings.

5.2.2   X-ray Variability

A χ^2-test for a constant count rate was performed and the factor between the maximum and minimum flux was computed for each lightcurve, so that significant flux variations could be discovered. Together with the reduced χ^2 this flux factor was used to characterize variability on long time scales of days to years. For SNRs we expect constant integrated flux, however the flux factor was in the range of 1.0 to 1.8. This may be caused by differences in the off-axis angles and/or the extraction of the extended source. In general, variations below a factor of 2.0 should therefore be handled with care as they might indicate no real variability but false integration of the source flux because of the extent or the existence of a nearby bright source.

Finally 26 HRI sources in the LMC field show significant variability with reduced $\chi^2 > 5$ corresponding to a probability > 0.9999 (see Table 5.1). Four of them are newly classified HRI sources (LMC 49, LMC 300, LMC 313, and LMC 364, see Sec. 5.4.1). The list of variable sources in the SMC field contains 16 HRI sources. Two sources (SMC 74 and SMC 95) are new candidates for high mass X-ray binary systems with Be star (Sec. 5.4.2) and source SMC 35 is suggested as a Galactic foreground star.
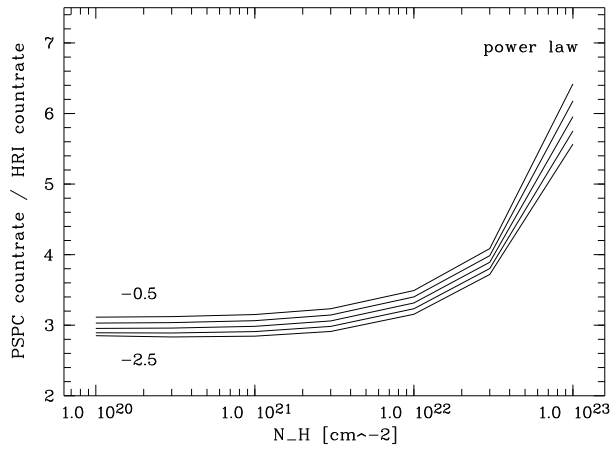
a. power law spectra with photon index
$\Gamma = -2.5, -2.0, -1.5, -1.0, -0.5.$
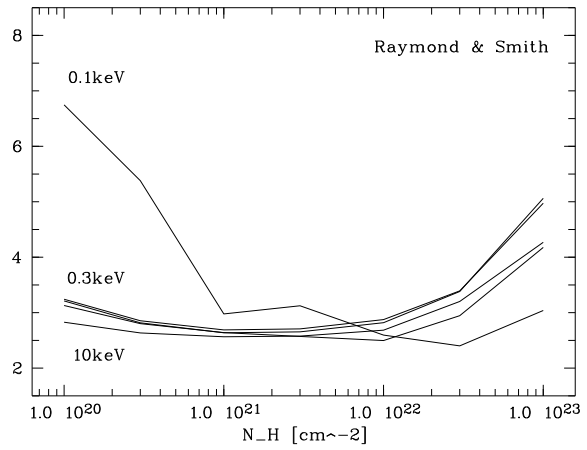
b. Raymond & Smith spectra with
$kT = 0.1, 0.3, 1.0, 3.0, 10.0$ keV.
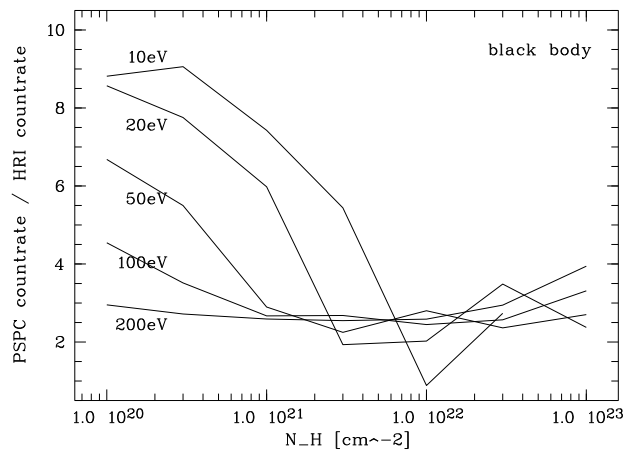
c. black body spectra with $kT = 10 - 200$ eV.

Figure 5.6: PSPC/HRI conversion factor as function of N_H for power law, Raymond & Smith, and black body spectra.
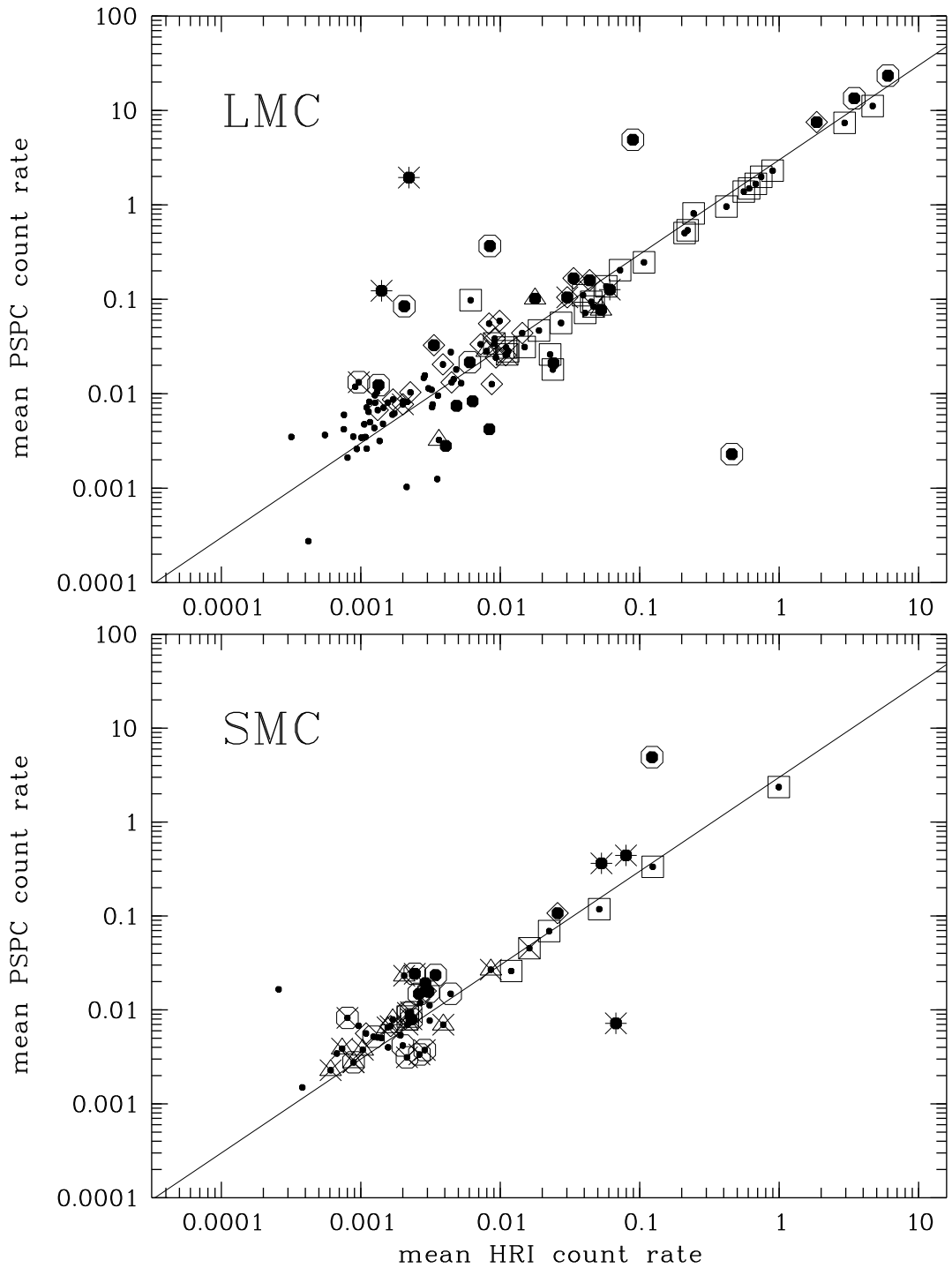
Figure 5.7: The mean of observation-averaged count rates obtained from pointed PSPC observations versus those from HRI observations: All sources observed by both detectors are plotted with small dots. In addition SNRs are marked with squares, XBs with hexagons, SSSs with asterisks, AGN with triangles, and stars with lozenges. Crossed symbols indicate already known candidates and variable sources are additionally marked with larg dots. In each diagram a line is drawn for a PSPC/HRI conversion factor of 3.

51
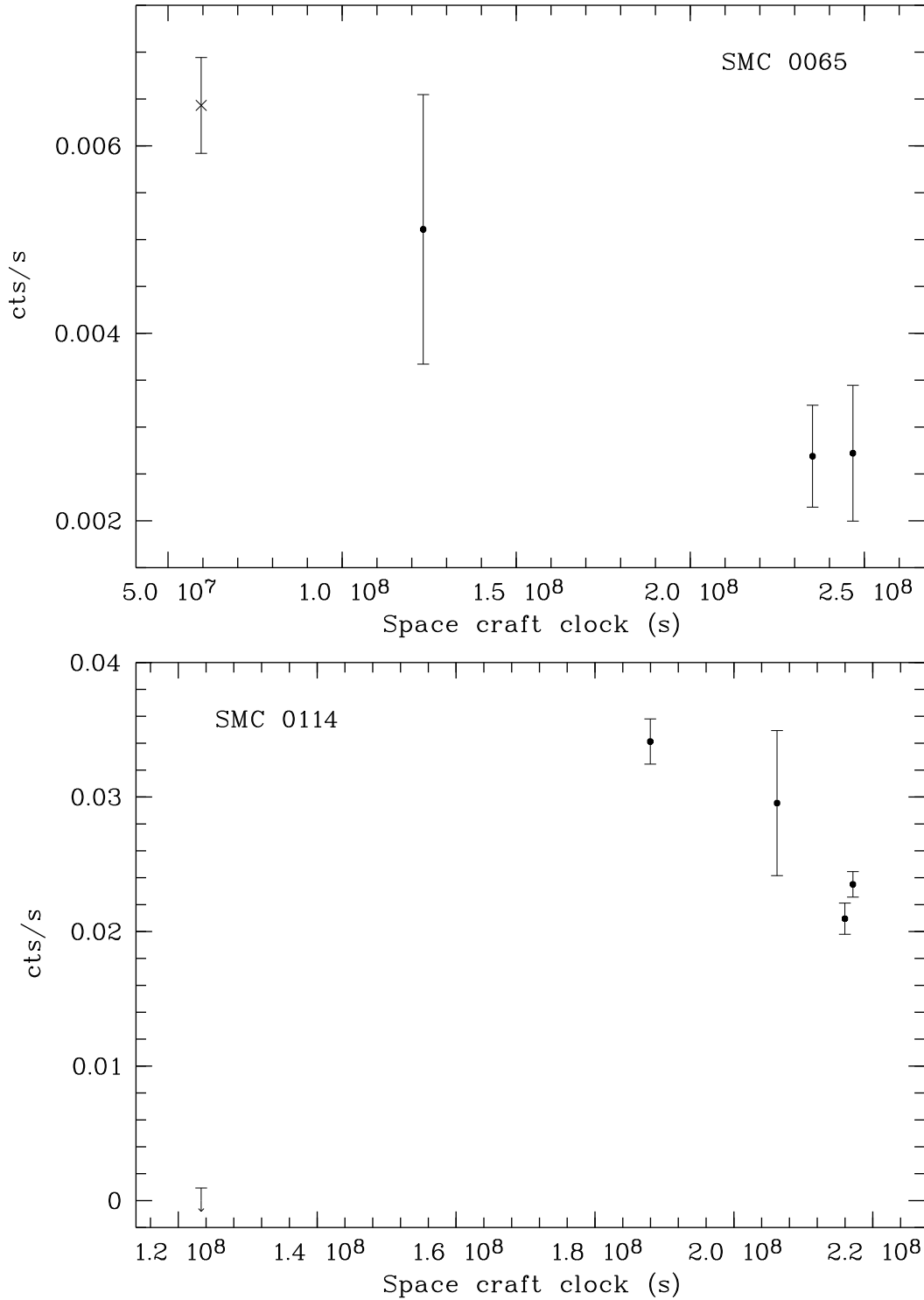
Figure 5.8: Lightcurves of sources SMC 65 and SMC 114. Dots for HRI count rates, cross for converted PSPC count rate. For SMC 114 an upper limit was determined in one HRI observation. Zero point of the space craft clock is 1990, June 21 21:06:50 UT.

Furthermore, sources SMC 65 and SMC 114 indicate X-ray flux variability, but were not classified due to lack of further information. Their lightcurves are shown in Figure 5.8.

5.3   Identification of HRI Sources with known Objects

5.3.1   LMC

For 97 HRI sources out of 138 which were also detected by the PSPC, the HRI observation yielded smaller positional error circles and consequently more accurate source positions compared to the PSPC results. Therefore, likely optical counterparts could be determined for several sources, which was not possible with PSPC data only. 100 HRI sources were identified with known objects in the LMC, foreground stars, or background objects mainly based on their position and X-ray properties.

Galactic Foreground Stars

By cross-correlating the HRI source catalog with SIMBAD and TYCHO catalogs and using the finding charts presented by Schmidtke et al. (1994, hereafter SCF94), Cowley at al. (1997, hereafter CSM97), and Schmidtke et al. (1999, hereafter SCC99) 39 sources were identified with Galactic foreground stars. Most of them could be also identified with the help of UBV photometry results presented by Gochermann et al. (1993) and Grothues et al. (1997). Point sources were found on DSS2 images at the positions of the HRI sources within the error circles, making their identification as optical counterparts very likely.

Based on hardness ratios of the PSPC observations, two point sources were suggested as foreground star candidates by HP99a (LMC 189 and LMC 349). Their hardness ratios are within the range characteristic for stars (HP99a). They were detected by the HRI as well and the DSS2 image shows a single optical point source within the improved HRI error circle in both cases.

Supernova Remnants

Most SNRs in the LMC are extended X-ray sources which could be resolved by the HRI. They typically show extents of about $5'' - 20''$ and high extent likelihood ($>$ 10.0). A total of 24 known SNRs were observed by the HRI, four HRI sources are identified with known SNR candidates (LMC 50, LMC 231, LMC 310, and LMC 315). For both LMC 231 and LMC 310 the measured hardness ratios are typical for SNRs. LMC 50 has a harder X-ray spectrum with HR1 = 1.00±0.10 and HR2 = 0.34±0.07.

Supersoft Sources

SSSs have very soft X-ray spectra and so far seven SSSs have been discovered in the LMC (HP99a). Two of them were sources of the Einstein LMC survey (Long et al., 1981): CAL 83 (LMC 348) and CAL 87 (LMC 363). Five additional SSSs were found

Table 5.1: HRI sources in the MC fields with significant flux variability.

1	2	3	4	5	6	7
No	Rate HRI [cts s^{-1}]	Rate PSPC [cts s^{-1}]	$\frac{F_{max}}{F_{min}}$	Red. χ^2	DOF	Remarks
LMC 19	*4.6e-1	*2.3e-3	6.0e+02	376.1	1	HMXB RXJ0502.9-6626 (CAL E)
LMC 20	5.3e-2	7.7e-2	4.5	163.5	2	AGN RXJ0503.1-6634
LMC 23	2.4e-2	2.1e-2	3.4	61.9	1	
LMC 49	*4.9e-3	*7.5e-3	4.3	9.4	4	<XB> or <AGN>
LMC 65	2.2e-3	1.9	2.6e+04	663.9	45	SSS RXJ0513.9-6951
LMC 103	4.1e-3	2.8e-3	1.1e+01	10.2	6	foreground star HD 35862
LMC 124	1.8e-2	1.0e-1	4.9	19.6	20	AGN RXJ0524.0-7011
LMC 155	*8.3e-3	*4.2e-3	1.3e+02	18.7	30	Nova LMC 1995
LMC 167	1.4e-3	1.2e-1	2.6e+02	51.6	26	SSS RXJ0527.8-6954
LMC 180	*1.9	*7.5	1.1e+02	691.6	74	foreground star AB Dor
LMC 193	3.4e-2	1.7e-1	2.6	7.0	8	foreground star HD 269620
LMC 202	2.0e-3	8.5e-2	1.0e+03	11.9	20	HMXB RXJ0529.8-6556
LMC 218	8.4e-3	3.7e-1	3.4e+02	99.9	10	HMXB EXO053109-6609
LMC 233	6.0e-3	2.2e-2	6.6e+01	7.9	13	HMXB RXJ0532.5-6551
LMC 239	*8.9e-2	*4.9	3.7e+02	10247.6	25	HMXB LMC X-4
LMC 293	4.4e-2	1.6e-1	2.1	9.4	18	foreground star CAL 69
LMC 300	5.4e-3		1.9e+02	414.6	2	<foreground star>, source not resolved by the PSPC
LMC 306	*6.0	*23.4	2.5	1838.8	22	HMXB LMC X-3
LMC 311	3.5	13.5	1.6	576.1	29	HMXB LMC X-1
LMC 313	*6.3e-3	*8.3e-3	3.7	9.3	3	<foreground star>
LMC 348	4.3e-2		2.8e+02	775.9	6	SSS CAL 83, one PSPC point., source near rim
LMC 349	3.0e-2	1.0e-1	2.0e+01	7.2	5	foreground star? [HP99b]
LMC 352	1.3e-3	1.2e-2	3.1	10.0	2	HMXB RXJ0544.1-7100 [HP99a]
LMC 363	6.1e-2	1.3e-1	1.5	36.8	3	SSS CAL 87
LMC 364	1.2e-2		3.1e+01	158.4	1	<XB> or <AGN>, one PSPC pointing, source near rib
LMC 375	3.3e-3	3.3e-2	4.5	6.1	4	foreground star HD 39756
SMC 7	1.0e-01	4.4e-01	2.5	112.1	8	SSS 1E0035.4-7230
SMC 10	4.4e-03	1.6e-02	2.0	8.1	2	foreground star HD 3880
SMC 23	1.7e-02	7.2e-03	2.9e+01	475.1	3	SSS RXJ0048.4-7332
SMC 35	1.0e-02		3.7e+02	14.1	3	<foreground star> SkKM 62
SMC 44	4.9e-03	2.4e-02	5.5e+03	2973.0	6	HMXB RXJ0052.1-7319
SMC 46	3.0e-03	1.5e-02	4.5e+02	9.4	9	HMXB RXJ0052.9-7158
SMC 51	2.7e-03		3.1e+02	95.0	4	HMXB? XTEJ0053-724 [CML98]
SMC 65	4.3e-03	1.9e-02	2.4	10.4	3	
SMC 74	2.2e-03	7.9e-03	2.5e+04	8.7	9	<Be/X>
SMC 79	9.4e-02	3.6e-01	2.6	115.5	5	SSS 1E0056.8-7146
SMC 93	2.9e-04	<9.1e-03	3.5e+02	9.9	7	HMXB Be/X RXJ0101.0-7206
SMC 95	2.9e-03	2.4e-02	1.2e+01	8.1	9	<Be/X>
SMC 101	4.3e-03	1.6e-02	2.2	8.3	3	HMXB SAXJ0103.2-7209
SMC 114	1.6e-02		6.7e+01	119.6	4	
SMC 118	3.7e-01	4.9e+00	2.1e+02	24762.9	8	HMXB SMC X-1
SMC 120	3.4e-02	1.1e-01	2.6	12.1	8	foreground star HD 8191

Notes to columns No 2 and 3: For point and point-like sources count rates are the mean of output values from maximum likelihood algorithm for single pointings (0.1 – 2.4 keV). For extended sources and bright sources with apparent extent the average of integrated count rates in single pointings was taken (* in front of the number). < in front of the count rate indicates that the value is an upper limit.

Notes to column No 6: Degrees of freedom.

Notes to column No 7: Sources classified in this work are put in < >. Abbreviations for references in square brackets are given in Appendix B.

with the help of the ROSAT PSPC. In the HRI pointings a total of five LMC SSSs were observed and all of them were detected with high existence likelihood.

X-ray Binaries

Characteristic for most X-ray binaries is the hard X-ray spectrum and flux variability. In HRI observations nine bright sources could be identified with well known high mass X-ray binaries (HMXB). The point source RX J0532.7-6926, here LMC 238, has been suggested to be a low mass X-ray binary (LMXB) candidate by Haberl & Pietsch (1999b, hereafter HP99b) and was also detected by the HRI. In HP99b a lightcurve with PSPC and HRI measurements is presented and variability is discussed in detail. Between 1990 and 1993 the source showed an exponential intensity decay.

AGN

Nine known background AGN with redshifts between 0.06 and 0.44 (SCF94; CSM97; Crampton et al., 1997) were re-identified in the HRI pointings. Because of its positional coincidence with the radio source PKS 0552-640 and its hardness ratios measured by the PSPC, the source corresponding to LMC 389 of the HRI observations had been classified as AGN candidate (No 37 in HP99a). On the DSS2 frame an optical source with $B = 16.1$ within the HRI error circle is identified as the most likely optical counterpart.

ROSAT Sources with Hard X-ray Spectrum

Nine sources detected by the HRI were identified with sources in the PSPC catalog (HP99a) showing a hard X-ray spectrum. But from the HRI observations no additional information could be obtained. Thus the HRI sources are simply classified as hard X-ray sources because of the hardness ratios of their PSPC detections.

5.3.2   SMC

Performing a similar analysis as for the LMC, 46 HRI sources were identified with known SMC objects, foreground stars, or AGN based on their accurate positions from HRI observations and the X-ray properties like extent or PSPC hardness ratios (HFPK00).

Foreground Stars

Besides four foreground stars, two known candidates (SMC 18 and SMC 86) were observed by the HRI. SMC 18 and SMC 86 were detected by the PSPC and classified as foreground stars by KPFH99 and Filipović et al. (2000, hereafter FHP00). The HRI observations give positions more accurate than the PSPC (total positional error of $5''.6$ and $7''.2$, respectively). At the HRI positions an optical source was found for each case, with $R = 11.3$, $\log(f_X/f_{opt}) = -3.51$ for SMC 18 and $R = 13.1$, $\log(f_X/f_{opt}) = -0.67$ for SMC 86 confirming the proposed classification.

Supernova Remnants

Six known SNRs were detected by the HRI. For these SNRs extents larger than $5\rlap{.}''8$ were measured by the HRI with a likelihood higher than 35 (see Fig. 5.3), except for SNR 0056-72.5 which has no significant extent.

Source SMC 22 is identified with a PSPC source which was suggested as a SNR candidate by KPFH99. The extent of the HRI source calculated in the maximum likelihood algorithm is only $3\rlap{.}''6$. However, the HRI image shows that the source is only the brightest knot in an extended emission, confirming the classification as a SNR candidate.

Supersoft Sources

Four SSSs were found in the HRI observations which were also detected in PSPC observations. For three out of these four sources (SMC 7, SMC 23, and SMC 79) flux variability could be verified by the HRI observations (see Sec. 5.2.2).

X-ray Binaries

Ten known HMXBs in the SMC were detected both by the PSPC and by the HRI. Two additional HMXBs, AX J0051-722 and SMC X-3, were observed by the HRI only. Sources SMC 51 and SMC 73 are HMXB candidates which were observed by other X-ray satellites and are well known from literature. Sources SMC 39, SMC 81, and SMC 88 were suggested as X-ray binaries by KPFH99. KPFH99 additionally classified the sources SMC 12 and SMC 83 either as AGN or as XB candidates. For both sources there is a likely optical counterpart within the HRI error circle with $B = 16.8$ and 17.3, respectively. The hardness ratios are: HR1 = 1.00±0.61, HR2 = 0.43±0.16 for SMC 12 and HR1 = 1.00±1.30, HR2 = 1.00±1.93 for SMC 83.

AGN

Source SMC 8 is a known AGN with redshift z = 0.922 (Tinney et al., 1997). The hardness ratios are HR1 = 1.00±1.09, HR2 = –0.06±0.12. The optical counterpart seen on DSS2 at the HRI position, which is the same as reported by Tinney et al. (1997), has $B = 18.6$ ($\log(f_X/f_{opt}) = -0.49$). Source SMC 59, showing both radio (SMC B0053-7227, Filipović et al., 1998, hereafter FHW98) and X-ray emission, was classified as an AGN candidate by KPFH99. A faint optical source ($B = 18.6$) can be found at the HRI position resulting in $\log(f_X/f_{opt}) = -0.30$. For the source SMC 112, also an AGN candidate (FHP00), no optical counterpart was found. The PSPC pointing shows a hard source (HR1 = 1.00±0.37, HR2 = 0.46±0.09). Seven HRI sources were classified as AGN candidates by KPFH99. For them likely optical counterparts exist with brightness $17 < B < 19$. The computed $\log(f_X/f_{opt})$ are around –0.50.

Sources with Hard X-ray Spectrum

Sources SMC 60, SMC 116, and SMC 117 coincide with PSPC sources showing hard X-ray spectra (HFPK00). No likely optical counterparts were found in the error circles of the sources. The X-ray sources showed no flux variation. Thus these sources were classified as hard X-ray sources based on PSPC observations.

5.4   New Cassifications

The extensive detection list produced from the HRI pointings towards the MCs allows us to search for new candidates for different source types. In the course of studying the newly discovered HRI sources, the following parameters were of prime importance: count rates, source extent, extent likelihood, flux variability, and counterparts in other wavelengths. By comparing positions of X-ray sources with those of stars measured in the optical and near-infrared, one can conclude if the X-ray source is in coincidence with a Galactic foreground star. Therefore the HRI source catalog was cross-correlated not only with the TYCHO and USNO-A2.0 catalogs, but also with the DENIS catalog. Hardness ratios determined by PSPC are additional parameters for classifying hard X-ray sources not belonging to the Galaxy as candidates for XBs or AGN. Tables 5.3 and 5.4 summarize the new classifications of this work and give crucial parameters like the extent, optical and near-infrared brightness, as well as the hardness ratios. In Appendix C DSS2 images around these sources except for SNR candidates are presented with X-ray position and positional error.

5.4.1   LMC

SNR Candidates

Investigating the extent, five HRI sources (LMC 197, LMC 284, LMC 288, LMC 307, and LMC 338) are suggested as SNR candidates as their extent is larger than $8''$ (see Fig. 5.3). Since they were not detected by the PSPC because of short exposure times, there is no spectral information about these sources which might be crucial for further improvement of the classification.

Foreground Stars

In comparison to Magellanic Cloud members or background objects, foreground stars are brighter in R as shown in the color-magnitude diagram (Fig. 5.9). For the near-infrared CLH00 estimated the number of foreground stars and Magellanic Cloud members in the DENIS catalog by studying color-color and color-magnitude diagrams of the DENIS data. As they showed, sources with $J - K_s$ lower than $\sim$1.0 are most likely foreground stars with increasing probability for smaller $J - K_s$ and smaller $I - J$ that such a classification is correct.

For eight HRI sources (LMC 28, LMC 90, LMC 217, LMC 229, LMC 287, LMC 300, LMC 313, LMC 347) probable optical counterparts were found within the error
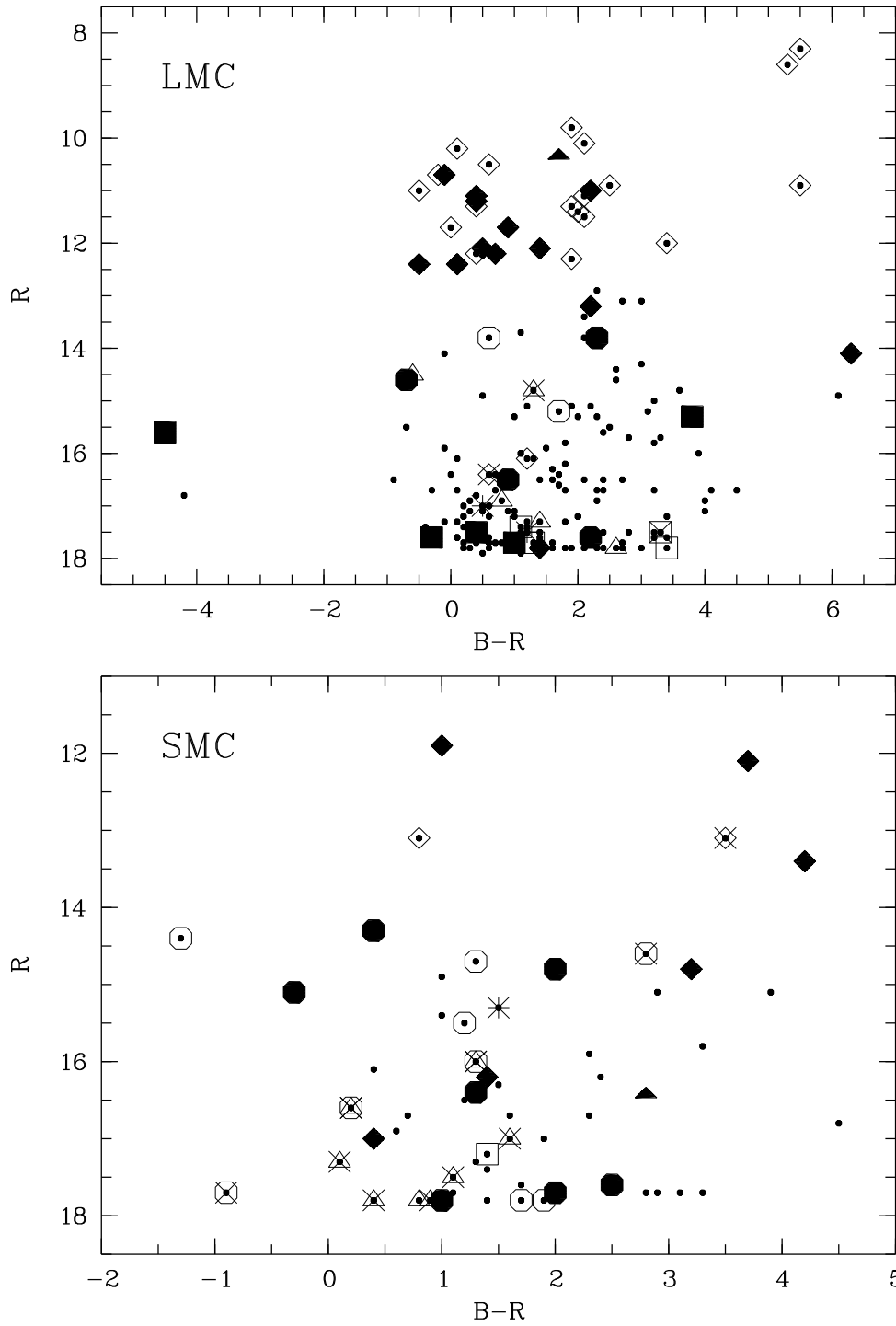
Figure 5.9: Color-magnitude diagram for HRI sources in the MCs correlating with entries in the USNO-A2.0 catalog. Small dots are used for all sources. Extra asterisks indicate SSS, open squares SNRs, open hexagons XBs, open triangles AGN, and open lozenges foreground stars. Already known candidates are marked with crossed symbols, so an overlay of open triangle, open hexagon, and cross marks hard sources as candidates either for AGN or XB. Filled symbols are new classifications.
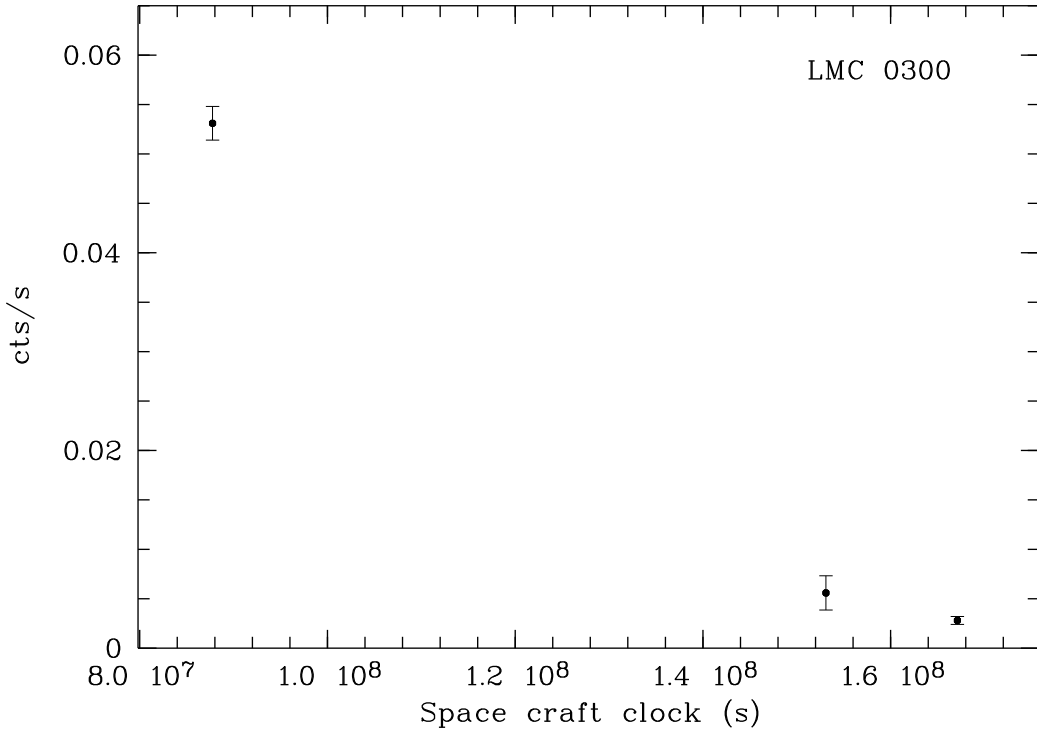
Figure 5.10: Lightcurve of source LMC 300. The count rates were obtained from HRI observations only, as there is a nearby source (LMC 296) and the sources could not be resolved by the PSPC. Zero point of the space craft clock is 1990, June 21 21:06:50 UT.

circle which are all bright ($B < 13.0, R < 12.5$), and their $\log(f_X/f_{opt})$ is negative ($<$ –2.0). For this reason these sources are classified as foreground stars. The lightcurve of LMC 300 (Fig. 5.10) shows a strong decrease of the X-ray emission with a factor of 10 in two years indicating that the HRI observations were performed after an emission maximum. The point source in the optical DSS2 image (App. C.1) at the HRI position is very likely the optical counterpart with a B magnitude of $B = 12.6$, $R = 12.1$ according to the USNO-A2.0 Catalog and $\log(f_X/f_{opt}) = -2.67$.

In addition, the near-infrared brightness and color of seven sources (LMC 7, LMC 11, LMC 29, LMC 37, LMC 54, LMC 135, LMC 290) is in a range typical for foreground stars, which can be seen in Figure 5.11. These sources with $J < 12.5$ and $J - K_s < 0.7$ were classifed as Galactic stars as well. Six sources (LMC 29, LMC 37, LMC 90, LMC 135, LMC 217, and LMC 313) were observed by the PSPC and the hardness ratios are available.

LMC Stars as Candidates for High Mass X-ray Binaries

Two X-ray point sources detected by the HRI were identified with known LMC O and B stars because of the positional coincidence (LMC 328 and LMC 332, $B = 12.0$ and 13.9, respectively; Sanduleak, 1970; Brunet et al., 1975). With HRI data no variability investigations could be carried out for these X-ray sources in spite of the existence of
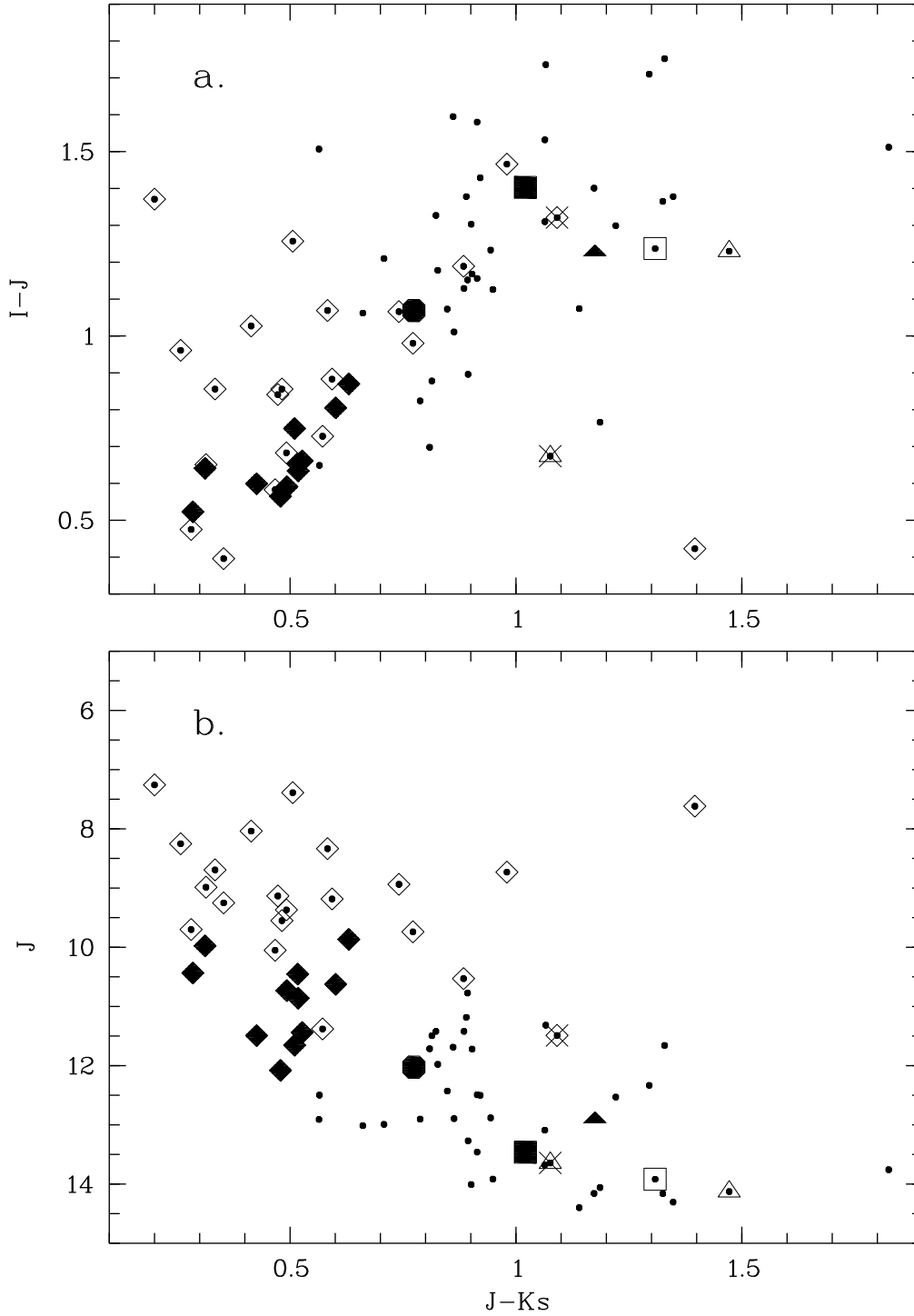
Figure 5.11: Color-color (a) and color-magnitude (b) diagram for HRI sources in the LMC field correlating with objects in the DENIS catalog. Open lozenges are used for objects coinciding with foreground stars, triangles with AGN, squares with SNRs, and hexagons with XBs. Known candidates are marked with crosses, new classified sources are indicated with filled symbols.
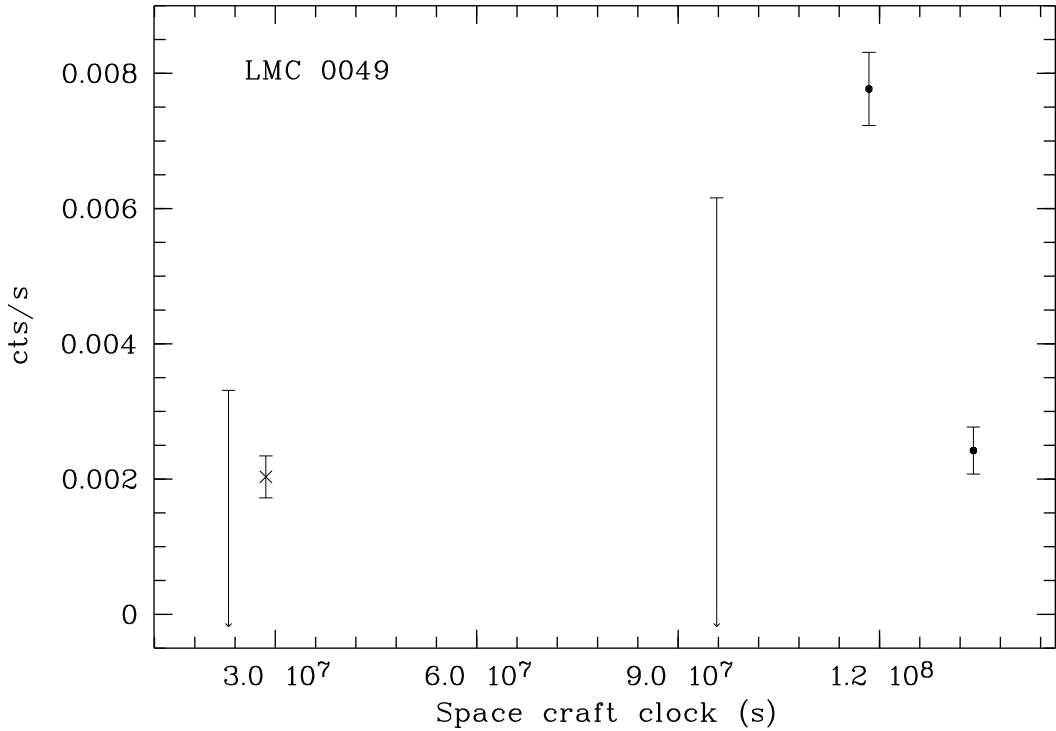
Figure 5.12: Lightcurve of LMC 49. Dots for HRI count rates, cross for converted PSPC count rate. Upper limits are plottet as well. Zero point of the space craft clock is 1990, June 21 21:06:50 UT.

many pointings in their direction, because they were both detected only once and in other pointings the upper limits were too high for this purpose. But their identification with optically selected LMC stars allows us to classify them as candidates for high mass X-ray binaries.

Sources with Hard X-ray Spectrum: Candidates for AGN or X-ray Binary

Based on hardness ratios and other characteristics measured by the HRI like flux variability or f_X/f_{opt} three HRI sources which were also detected by the PSPC could be classified as candidates either for an X-ray binary or for an AGN.

The point source LMC 49 shows significant flux variations (Fig. 5.12) and has a hard and/or highly absorbed X-ray spectrum (HR1 = 1.00±0.71, HR2 = 0.26±0.16). On the DSS2 image a likely optical counterpart with a B magnitude of $B = 16.1$ (according to the USNO-A2.0 Catalog) is found (App. C.1). Therefore this source has been classified as a candidate either for an X-ray binary or AGN.

Sources LMC 230 and LMC 364 are further candidates for X-ray binary or AGN due to their hard X-ray spectrum (HR1 = 1.00±0.35, HR2 = 1.00±0.98 and HR1 = 1.00±0.21, HR2 = 1.00±0.60 respectively). Since source LMC 230 has a small positional error, a probable optical counterpart can be found by a cross-correlation with the USNO-A2.0 catalog. This counterpart is faint ($B = 19.8$), and we obtain

61

a high $\log(f_X/f_{opt})$ of 0.44. For source LMC 364, there is a relatively faint optical source ($B = 17.4$) within the error circle visible on the DSS2 image which might be the counterpart ($\log(f_X/f_{opt}) = 0.11$).

5.4.2 SMC

Also for the SMC new X-ray sources were classified with the help of their properties obtained from HRI observations. First, extended sources were searched, which could suggest new SNR candidates, but without any result. No new source with significant extent was detected.

Sources Classified as Galactic Foreground Stars

In the SMC HRI catalog, there are in total 14 sources correlating with entries in the DENIS catalog. Apart from one source, $J - K_s < 1.1$ was measured for them. Since sources observable both in near-infrared and in X-rays are mainly Galactic stars or AGN in the background, seven out of these 13 sources with $J - K_s < 1.1$ (SMC 16, SMC 26, SMC 35, SMC 68, SMC 80, SMC 89, and SMC 121) were classified as foreground stars. In Figure 5.13a they show a good correlation between $J - K_s$ and $I - J$ which is also shown by CLH00. For most of them the USNO-A2.0 catalog give $R < 14.0$ and likely optical counterparts can be seen in the DSS2 images within the error circles (App. C.2). In addition the source SMC 25 was classified as a foreground star since an optical counterpart with $R = 10.8$ was found.

Candidate for AGN

In the near-infrared color-color diagram (Fig. 5.13a) there is an outlying source (SMC 64). Looking at the color-magnitude diagram (Fig. 5.13b) it is the source with the highest $J - K_s$ and highest J. For comparison magnitudes and colors for a sample of AGN determined by Maiolino et al. (2000) are plotted as well. The near-infrared and optical brightnesses of the HRI source SMC 68 correspond well with those typical for AGN ($B = 19.2$, $R = 16.4$). Therefore it was classified as an AGN.

Candidates for AGN or X-ray Binaries

For the source SMC 71 no optical counterpart can be found on the DSS2 frame. In the USNO-A2.0 catalog there is a faint object ($B = 20.1$, $R = 17.6$) within the error circle, and with $\log(f_X/f_{opt}) = 0.40$ the HRI source is bright in X-rays. The PSPC spectrum of this source is hard (HR1 = 1.00±0.13, HR2 = 0.38±0.09) favoring its classification as XB or AGN. Another five HRI sources (SMC 5, SMC 53, SMC 72, SMC 78, and SMC 85) are associated with hard PSPC sources with HR1 = 1.00 and HR2 $\geq$ 0.25. For all of them large errors were determined for HR1, but not for HR2 (HR2 – error$_{HR2}$ > 0.00), resulting from the fact that the source is so hard that the photon statistics were low in the softer bands. In the USNO-A2.0 catalog, only a faint or no optical source is found within the error circle of the HRI position. This can be
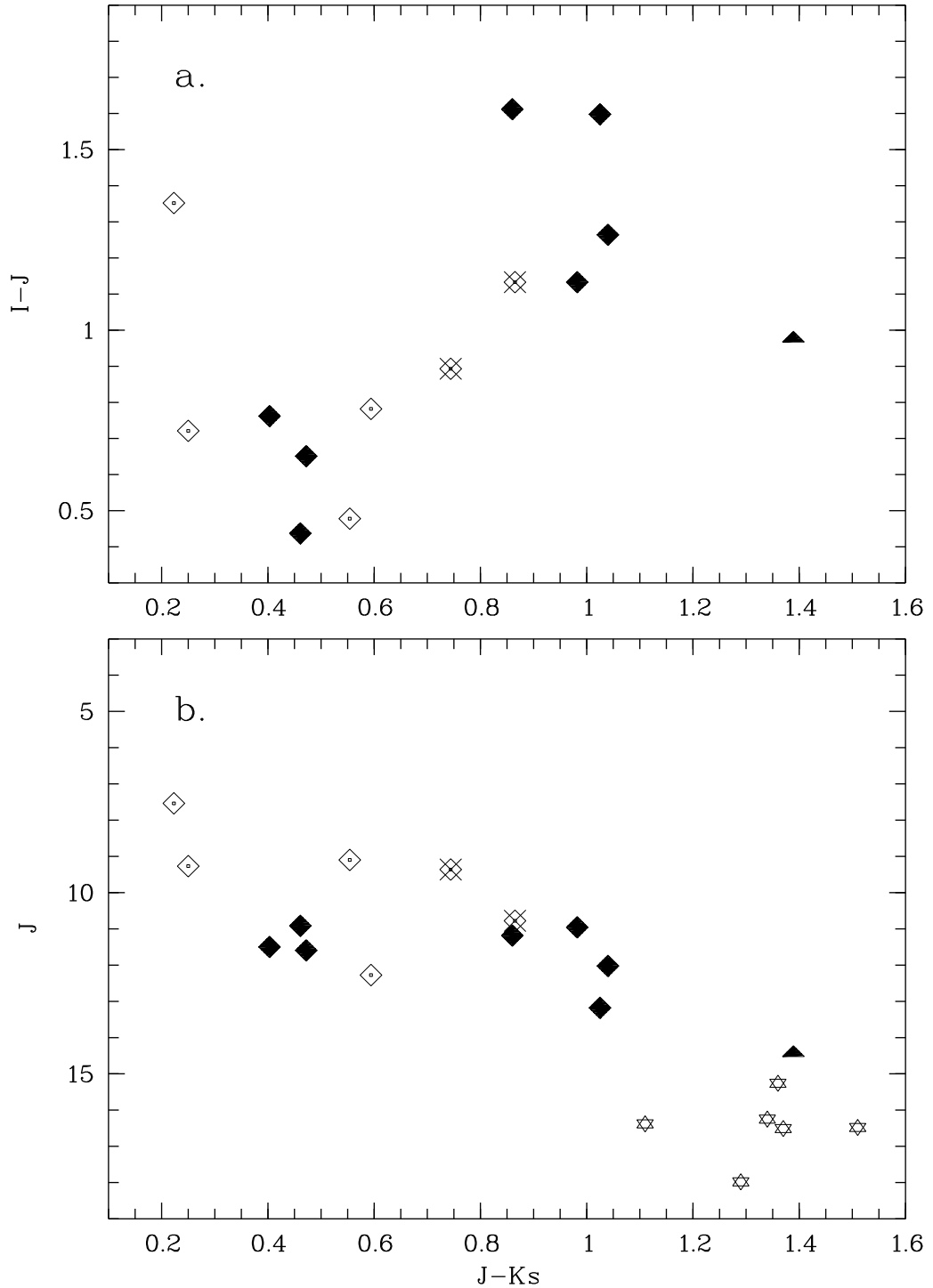
Figure 5.13: Color-color (a) and color-magnitude (b) diagram for HRI sources in the SMC field correlating with objects in the DENIS catalog. Open lozenges for foreground stars, crossed for candidates, and filled for new classifications. The filled triangle mark the source classified as AGN. Stars signify AGN observed by Maiolino et al. (2000).

also verified on the DSS2 images (App. C.2). These HRI sources were classified as XB or AGN.

Sources suggested as Be/X-ray Binary Systems

High mass X-ray binaries can be devided into two subclasses (Sec. 2.1.2) depending on the companion star: In a supergiant system the massive star is an OB supergiant. If the compation is a B giant with pronounced Balmer emission lines, the system is called a Be/X-ray binary system. Cross-correlation of the HRI catalog as well as the PSPC catalog (HFPK00) with the catalogs of Hα emission-line stars created by Meyssonnier & Azzopardi (1993) and Murphy & Bessell (2000) showed that over 50 ROSAT sources in the SMC coincide with emission-line stars. 13 sources are already known Be/X-ray systems, for further five X-ray pulsars which had been optically unidentified, correlating emission-line stars were found. The more accurate HRI coordinates were used for sources detected by the HRI, otherwise PSPC coordinates were compared to the optical coordinates. Based on the hardness ratios measured by the PSPC and the existence of an emission-line star within the position error circle, a total of 24 sources with hard X-ray spectrum were suggested as Be/X-ray binaries. Nine out of these 24 were also detected by the HRI (see Tab. 5.4). One additional HRI source (SMC 108) is a Be/X-ray binary candidate as well, because only one bright optical object is located within the small error circle of the HRI position, which is an emission-line star. On the DSS2 images in Appendix C.2 the emission-line stars are additionally marked with a cross.

Two out of the ten sources (SMC 74 and SMC 95) show significant X-ray flux variability in the ROSAT observations. Although in several pointings only upper limits were determined, in other observations flux increase of almost one magnitude was measured (Fig. 5.14). Such variability in lightcurves are characteristic for Be/X-ray binaries.

5.5   Source Distribution

Thanks to the high spatial resolution of the HRI, many sources could be detected both in the outer regions and in the optical bar region of the LMC. In Figure 5.15 HRI sources identified with known objects and known candidates are plotted on a grey scale PSPC image (0.1 – 2.4 keV) of the LMC (from HP99a). Not only background AGN or foreground stars, but also LMC members are located in different regions of the LMC and show no spatial preferences. There are still more than 250 non-identified point sources which are homogeneously distributed in all LMC regions which were covered by ROSAT HRI pointings as it is shown in Figure 5.16. In contrast, in PSPC observations not many additional sources could be detected in the regions with strong diffuse emission, because the lower spatial resolution hindered in distinguishing between extended and point-like emission (HP99a). The HRI allows to study the extent of the sources to scales of arcseconds. Therefore SNR candidates could be found not only in regions without surrounding diffuse emission. Four out of five newly
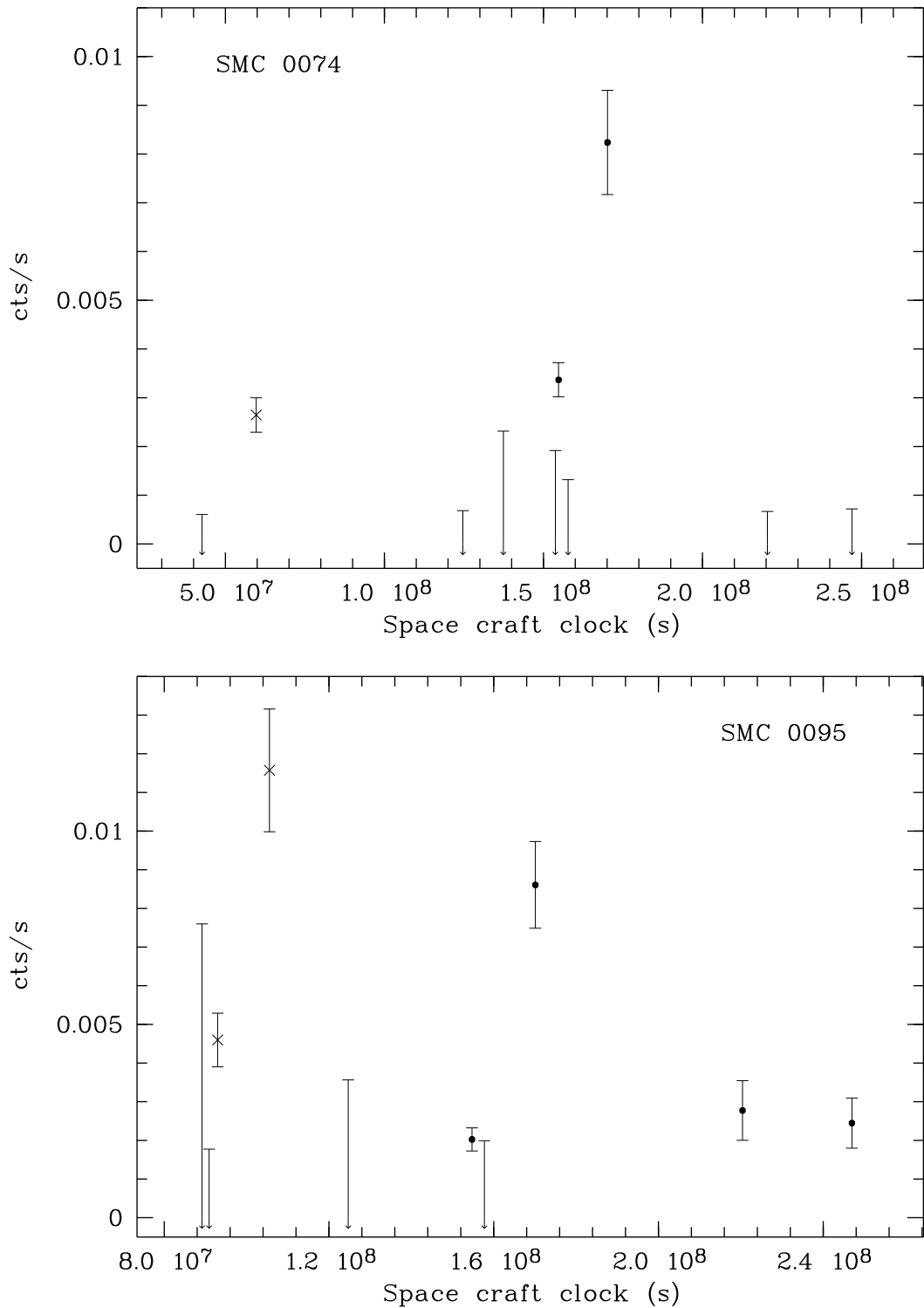
Figure 5.14: Lightcurves of sources SMC 74 and SMC 95. Crosses for converted PSPC count rates, dots for HRI count rates. Upper limits are plottet as well. Zero point of the space craft clock is 1990, June 21 21:06:50 UT.

65

Table 5.2: Number of classified X-ray sources in the MC regions observed by the HRI.

1	2	3	4	5	6	7
Source	LMC			SMC		
class	identified	candidates	new	identified	candidates	new
SNR	24	4	5	6	1	
SSS	5			4		
XB	9	1	2	12	7	10
AGN	9	1		1	9	1
hard: XB or AGN		9	3		3	6
foreground star	39	2	15	4	2	8

Notes to columns No 2 and 5: Sources identified with known objects in catalogs and literature.
Notes to columns No 3 and 6: Candidates reported in literature.
Notes to columns No 4 and 7: New classifications of this work.

suggested SNR candidates are located in regions with diffuse emission between 30 Dor and LMC X-1 (see Fig. 5.16). Within and around the optical bar region several new stellar sources and candidates for X-ray binary or AGN were found.

The HRI observations in the SMC field mostly covered the main body of the SMC (see Fig. 4.4), which is the reason that most of the identified and new sources are located in this region (Figs. 5.17 and 5.18). In this work 25 sources are newly classified as foreground star, XB, or AGN. There are still 50 unclassified HRI detections broadly distributed over the field observed by the HRI. The source distribution shows that there is a deficiency of X-ray sources in the central part of the SMC around RA = 00^h 55^m, Dec = $-72°$ $40'$ (J2000.0).

In Table 5.2 the numbers of detected sources are compared between the LMC and the SMC. In the LMC the number of SNRs is larger than in the SMC by a factor of four roughly in accordance with the ratio of the areas covered by the observations. The number of known SSSs detected in ROSAT observations is comparable in the two clouds. Nevertheless, the number of X-ray binaries in the SMC, and in particular the number of the candidates is higher than in the LMC maybe partly due to the fact that a thorough search for Be/X-ray binary candidates has been carried out for the SMC by comparing the X-ray catalogs with the catalogs of emission line objects (Sec. 5.4.2). Most of the XBs in the SMC found so far are binary systems with Be-star companions, only one supergiant system (SMC X-1) known so far. Be/X-ray binaries evolve from binary star systems with a stellar mass of ~ 20 M$_\odot$ in about 1.5×10^7 yrs, whereas X-ray binaries with supergiants have shorter evolution time due to the higher mass of the companion star. The large number of Be/X-ray binary systems in the SMC makes a burst of star formation about 1.5×10^7 yrs ago most likely.
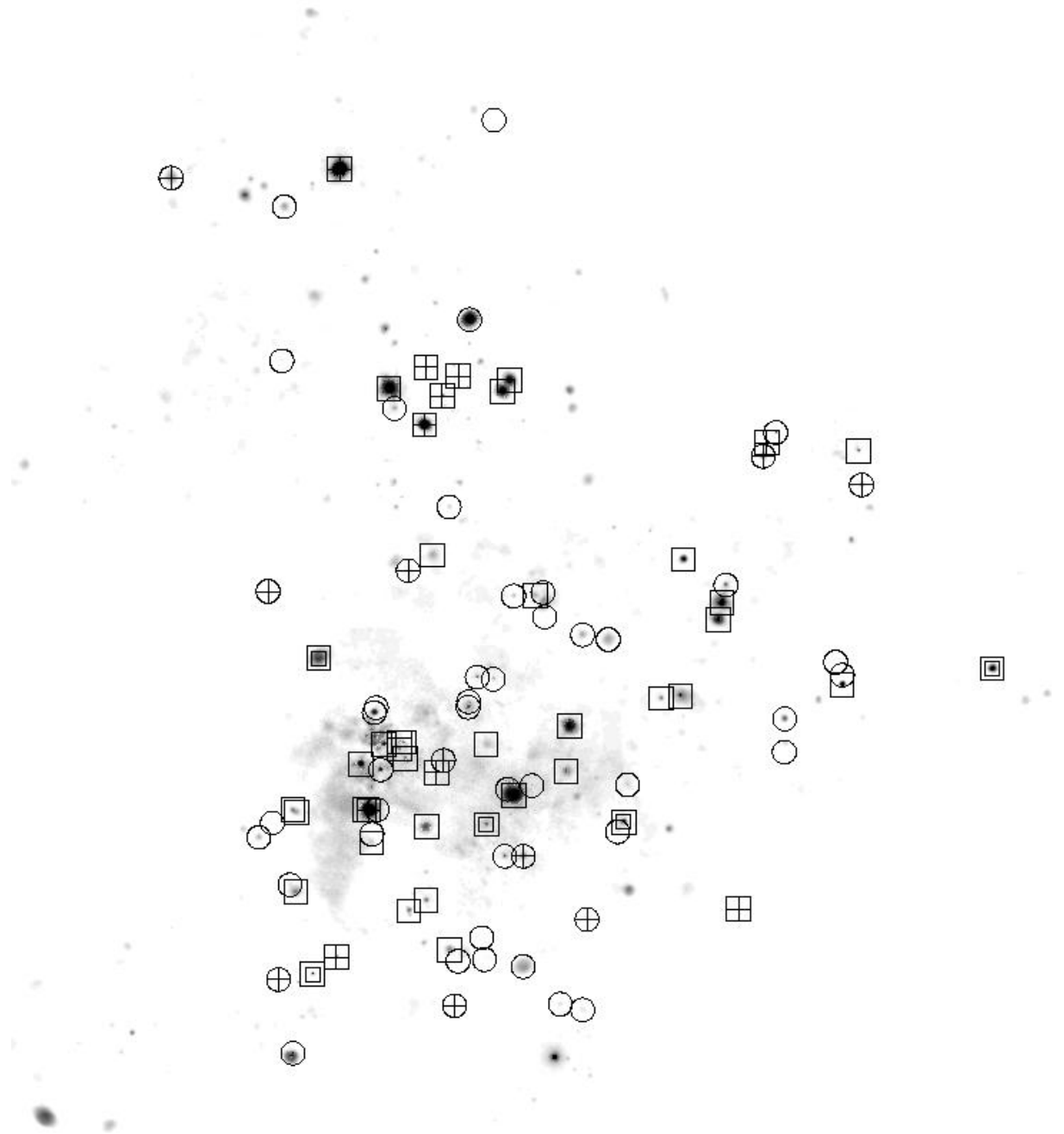
Figure 5.15: Identified HRI sources are plotted on a grey scale PSPC image (0.1 – 2.4 keV) of the LMC. Squares are SNRs, circles foreground stars, double squares SSSs, crossed squares XBs, and crossed circles AGN. Candidates from literature are included for each source class.
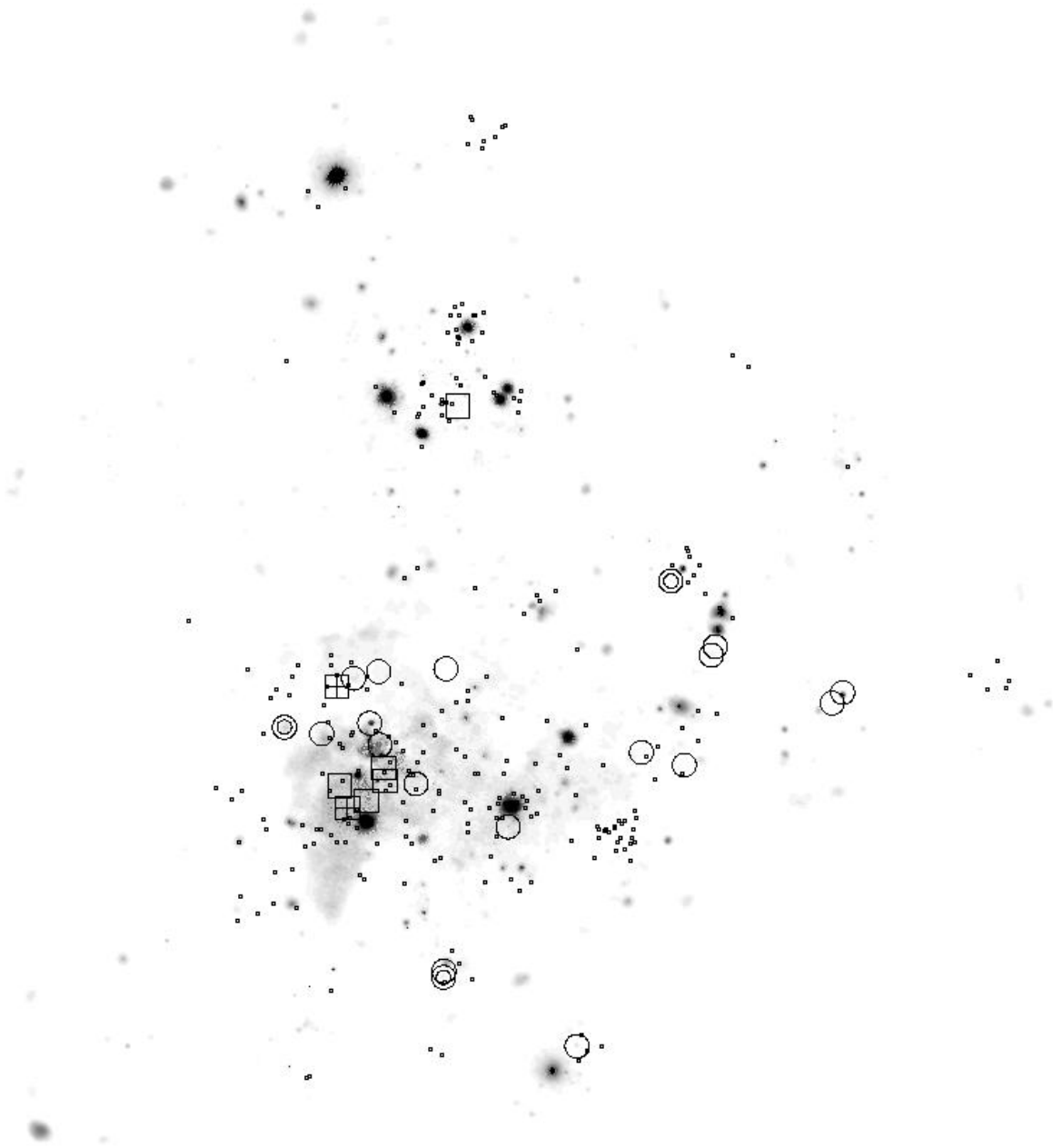
Figure 5.16: The distribution of unidentified and newly classified HRI sources in the LMC region is shown. Unidentified HRI sources are plotted as dots, squares are sources classified as SNR candidates, circles as stellar sources, crossed squares as XB candidates, and double circles as candidates for XB or AGN.
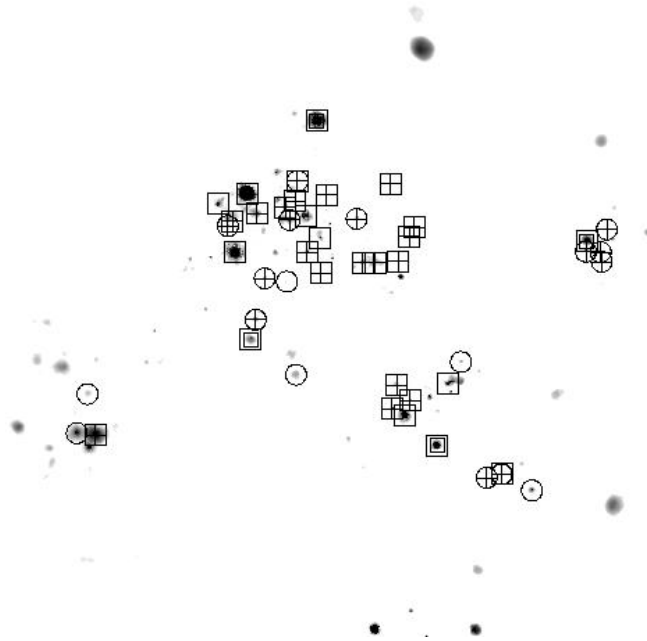
Figure 5.17: Distribution of identified HRI sources in the SMC region plotted on a grey scale image (0.1 – 2.4 keV) obtained from the PSPC data. Squares are used for SNRs, double squares for SSSs, crossed squares for XBs, crossed circles for AGN, and circles for foreground stars. Candidates from literature are included for each source class.
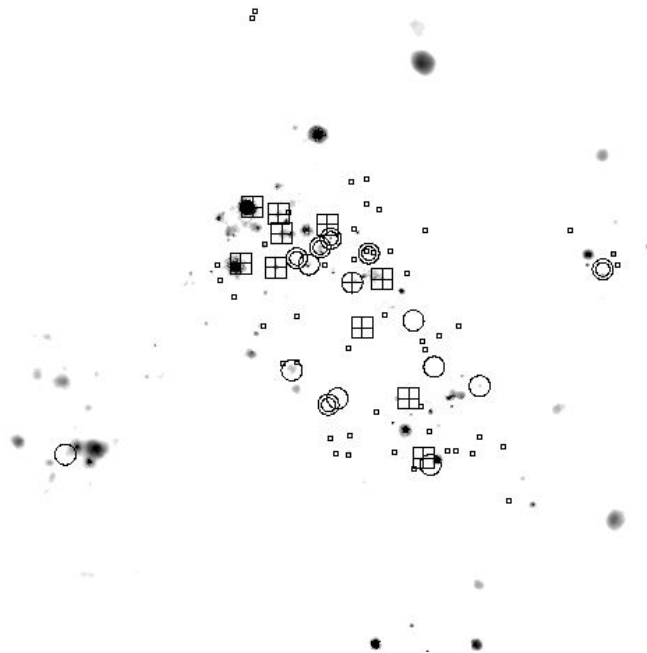
Figure 5.18: Unidentified and newly classified HRI sources in the SMC field are shown. Unidentified HRI sources are plotted as small squares, circles are sources classified as foreground star, crossed squares as XB candidates, crossed circle as AGN, and double circles as AGN or XB candidates.

Table 5.3: *Classified HRI sources in the LMC region with brightness of the likely optical counterparts.*

1	2		3	4	5	6	7	8	9	10	11	12	13	14
No	RA (J2000.0)	Dec	r_{90} ['']	r_{ext} ['']	B	R	I	J	K_s	$\log(f_X/f_{opt})$	No PSPC	HR1	HR2	Class
197	05 29 39.2	-66 08 06	20.1	17.1±10.8										
284	05 37 28.6	-69 23 18	13.4	9.8± 7.6										
288	05 37 36.2	-69 16 42	9.7	11.5± 5.5										<SNR>
307	05 39 27.9	-69 33 12	12.0	12.8± 6.5										
338	05 42 01.2	-69 24 44	11.9	8.3± 5.6										
7	04 53 36.5	-68 27 45	3.6	1.7± 1.5	13.5	12.1	11.4	10.6	10.0	-2.67				
11	04 54 27.8	-68 33 53	4.5	0.0± 0.0	15.4	13.2	12.6	12.1	11.6	-2.24				
28	05 05 58.4	-68 10 30	8.4	2.7± 3.4	12.5	12.4	11.5	10.9	10.3	-2.89				
29	05 06 16.7	-68 15 09	9.7	0.0± 0.0	19.2	17.8	12.1	11.4	10.9	0.11	635	1.00±0.76	-0.05±0.19	
37	05 08 06.2	-69 13 43	8.3	0.8± 2.7	13.2	11.0	10.6	10.0	9.7	-2.70	844	1.00±1.22		
54	05 12 21.3	-69 08 29	7.5	0.0± 0.0			12.4	11.7	11.1					
90	05 17 47.8	-71 44 05	11.4	1.9± 2.3	11.5	11.1	11.0	10.4	10.2	-3.26	1305	1.00±1.34	0.45±0.15	
135	05 25 22.5	-69 49 16	4.9	0.0± 0.0	20.4	14.1	11.3	10.7	10.2	0.33	1025	1.00±0.64	1.00±2.40	<fg star>
217	05 31 13.1	-68 25 48	7.7	0.0± 0.0	12.6	11.7				-3.07	661		1.00±1.10	
229	05 32 15.6	-71 04 26	4.8	0.0± 0.0	11.9	12.4				-3.48				
287	05 37 35.9	-68 25 57	7.4	0.0± 0.0	10.6	10.7				-3.42				
290	05 37 50.3	-69 04 23	2.4	0.0± 0.0			10.7	9.9	9.2					
300	05 38 42.4	-68 52 41	1.5	0.8± 1.3	12.6	12.1				-2.67				
313	05 39 59.9	-68 28 42	7.1	2.7± 1.2	11.6	11.2	11.1	10.5	9.9	-2.71	668	1.00±0.62	1.00±1.88	
347	05 43 22.2	-68 56 39	6.4	1.2± 1.1	12.9	12.2	12.1	11.5	11.1	-2.59				
328	05 41 22.2	-69 36 29	6.6	0.0± 0.0	[1]12.0									<HMXB>
332	05 41 37.1	-68 32 32	4.5	0.0± 0.0	13.9	14.6				-2.22				
49	05 10 28.7	-67 37 41	7.1	0.0± 0.0	16.1	13.8	13.1	12.0	11.3	-1.01	559	1.00±0.71	0.26±0.16	<XB> or <AGN>
230	05 32 18.5	-71 07 43	2.9	0.0± 0.0	19.8	17.6				0.44	1238	1.00±0.35	1.00±0.98	
364	05 46 55.7	-68 51 35	7.0	3.6± 1.0	17.4	16.5				0.11	747	1.00±0.21	1.00±0.60	

Notes to columns No 5 and 6: B and R magnitudes from USNO-A2.0 catalog.

[1] from TYCHO catalog.

Notes to columns No 7 to 9: I, J, and K_s magnitudes from DENIS catalog.

Notes to columns No 11 to 13: Source number and hardness ratios from HP99a.

Notes to column No 14: fg: foreground.

Table 5.4: Classified HRI sources in the SMC region with brightness of the likely optical counterparts.

1	2		3	4	5	6	7	8	9	10	11	12	13	14
No	RA (J2000.0)	Dec	r_{90} ['']	r_{ext} ['']	B	R	I	J	K_s	$\log(f_X/f_{opt})$	No PSPC	HR1	HR2	Class
16	00 45 10.9	-73 04 17	7.5	0.0± 0.0	15.8	12.1	12.2	11.6	11.1	-1.61	397	1.00±0.88	-0.18±0.12	
25	00 48 55.6	-73 33 37	3.3	0.0± 0.0	11.0	10.8				-3.68				
26	00 48 59.0	-72 58 13	5.3	0.0± 0.0			12.3	11.5	11.1					
35	00 50 49.3	-72 41 53	4.3	0.0± 0.0	17.6	13.4	12.1	11.0	10.0	0.01				<fg star>
68	00 56 50.3	-73 10 38	9.9	0.0± 0.0	12.9	11.9	11.4	10.9	10.5	-3.00	426	1.00±0.38	0.34±0.15	
80	00 59 13.6	-72 22 25	8.9	0.0± 0.0	18.0	14.8	13.3	12.0	11.0	-0.80				
89	01 00 36.5	-73 00 35	7.1	1.2± 1.2	17.4	17.0	12.8	11.2	10.3	-0.63				
121	01 19 39.2	-73 27 32	7.0	0.0± 0.0	17.6	16.2	14.8	13.2	12.2	-0.94	488	-0.19±0.15	-1.00±1.95	
64	00 55 49.3	-72 28 37	6.5	0.0± 0.0	19.2	16.4	15.4	14.4	13.0	-0.46				<AGN>
5	00 36 04.7	-72 18 44	3.8	0.0± 0.0	18.8	17.8				-0.85	198	1.00±3.45	1.00±0.49	
53	00 54 32.1	-72 18 13	3.7	2.4± 2.2							196	1.00±1.37	1.00±0.59	
71	00 57 31.7	-72 13 01	3.9	0.0± 0.0	20.1	17.6				0.40	170	1.00±0.13	0.38±0.09	<XB> or
72	00 57 35.5	-73 12 56	9.2	5.0± 3.8							435	1.00±0.84	0.25±0.16	<AGN>
78	00 58 20.7	-72 16 18	6.3	2.3± 3.0							185	1.00±0.81	0.58±0.09	
85	01 00 12.0	-72 20 17	5.3	0.0± 0.0	19.7	17.7				-0.14	204	1.00±0.99	1.00±0.58	
28	00 49 30.8	-73 31 09	3.0	2.7± 1.7							511	1.00±0.45	0.32±0.17	
36	00 50 57.2	-73 10 06	3.3	0.8± 2.8							421	1.00±0.33	0.52±0.12	
48	00 53 24.1	-72 27 20	3.1	1.3± 1.6							246	1.00±0.59	1.00±1.29	
57	00 54 56.0	-72 45 06	9.7	0.0± 5.2	16.8	14.8				-0.95	324	1.00±0.71	0.58±0.14	
74	00 57 49.3	-72 07 55	3.5	1.2± 1.5							136	1.00±0.22	0.58±0.11	<Be/X>
95	01 01 19.5	-72 11 18	3.6	3.4± 1.9							159	1.00±0.98	1.00±0.47	
96	01 01 36.4	-72 04 18	4.3	0.0± 0.0	17.7	16.4				-0.48	121	1.00±0.29	0.18±0.09	
97	01 01 53.3	-72 23 35	10.3	0.0± 0.0	14.7	14.3				-1.98	220	1.00±0.28	0.68±0.08	
105	01 03 37.2	-72 01 35	3.6	0.6± 1.3							106	1.00±7.13	0.41±0.07	
108	01 04 35.9	-72 21 48	4.0	0.0± 0.0	14.8	15.1				-2.25				

Notes to columns No 5 and 6: B and R magnitudes from USNO-A2.0 catalog.

Notes to columns No 7 to 9: I, J, and K_s magnitudes from DENIS catalog.

Notes to columns No 11 to 13: Source number and hardness ratios from HFPK00.

Notes to column No 14:
fg: foreground.
Be/X: X-ray binary system with Be star as companion.

Chapter 6

Hot Interstellar Medium of the Magellanic Clouds

The small distances to the Magellanic Clouds allow us to separate the emission from distinct sources within the galaxies from that arising from surrounding gas. Not only the discrete point sources and extended SNRs, but also diffuse emission coming from the interstellar medium (ISM) can be observed and studied in detail. In the ISM stars are born out of the densest regions, whereas massive stars transfer matter back to the ISM in stellar winds and supernova explosions. Therefore, the diffuse component of the X-ray emission from galaxies will give us clues for a better understanding of the interaction between stars and the ISM as well as the matter cycle within the galaxies.

6.1 Diffuse X-ray Emission seen by the ROSAT PSPC

Archival data of ROSAT PSPC pointings were used for analyzing the spectral properties of the diffuse emission in the Magellanic Clouds. Data reduction and extraction of spectra were described in Section 4.3. The succeeding steps of modeling and spectral parameterizing are demonstrated in the following.

6.1.1 Absorption of X-rays by the ISM

X-rays traveling through the ISM are absorbed due to photoionization of atomic and molecular gas as well as interstellar dust grains. In the course of spectral analysis, the X-ray spectra obtained from observations must be corrected for this modification. Latest studies of absorption of X-rays in the ISM are presented by Wilms et al. (2000). They discuss updated photoionization cross sections and abundances in the ISM and describe the effect of interstellar grains in detail.

The total photoionization cross section is a sum of the cross sections of the contributing particles:

$$\sigma_{\mathrm{ISM}} = \sigma_{\mathrm{gas}} + \sigma_{\mathrm{molecules}} + \sigma_{\mathrm{grains}}. \tag{6.1}$$
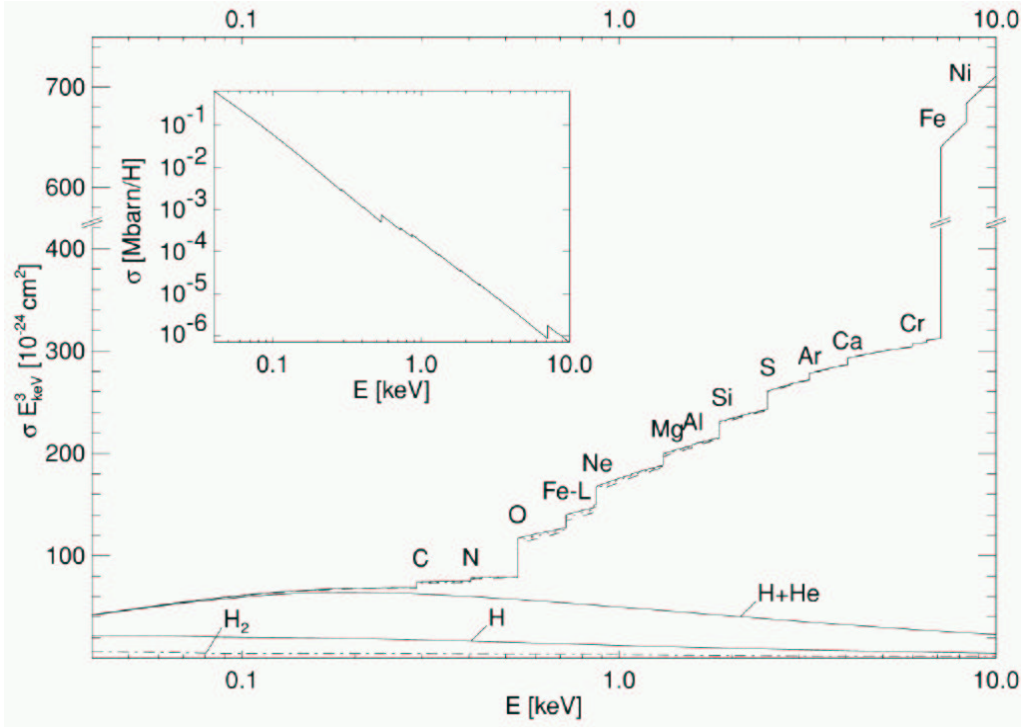
Figure 6.1: *Absorptivity per hydrogen atom of the ISM presented by Wilms et al. (2000) as* σE^3. *The cross section is normalized to the total hydrogen number density* N_{H}. *The dotted and dashed lines show the absorptivity including the effects of grains, and the contribution of* H_2 *is displayed as dot-dashed line. The inset shows the cross section without the factor* E^3.

The observed X-ray spectrum is given by

$$I_{\mathrm{obs}}(E) = e^{-\sigma_{\mathrm{ISM}}(E)N_{\mathrm{H}}} I_{\mathrm{orig}}(E). \tag{6.2}$$

In order to obtain the cross section σ_{gas} of the gaseous, non-molecular phase of the ISM, the photoionization cross sections of the atoms and ions weighted by the abundances must be summed up. For the contribution of the molecules, only molecular hydrogen needs to be taken into consideration. In the case of the grains, the X-ray absorption mainly occurs on the grain surface. This means that the material within the grains does not contribute to σ_{ISM} and therefore the absorptivity of the ISM with grains is lower than the absorptivity of a gaseous medium without grains.

Figure 6.1 shows the X-ray absorptivity of the local ISM. For energies higher than $\sim 0.5\,\mathrm{keV}$ the absorption is dominated by the metals. The X-ray opacity inferred from observations of H I is a lower limit, since substantial additional X-ray absorption is contributed by He, C, N, O, etc. in the ISM. Therefore the contributions of heavier elements must be considered. But the effects by the H_2 clouds and grains along the line of sight are small and can be neglected unless spectral analysis of high accuracy $(1 - 2\%)$ is carried out.

6.1.2 Background and Foreground Components in the Spectra

Before modeling the spectral contribution of the MCs, components in the spectra coming either from the cosmic background or from the Galaxy in the foreground had to be determined. For this purpose, spectra of regions within the selected $10° \times 10°$ and $5° \times 5°$ fields including the LMC and the SMC, respectively, but distant enough from the MCs were analyzed first. For the LMC, pointings to the south ecliptical pole lying northeast of the LMC, and for the SMC, pointings to the southeast of the SMC were suitable.

For the spectra, the cosmic background in the hard band and thermal emission from the Galactic foreground in the soft bands were taken into account. The cosmic background is well described by a highly absorbed powerlaw with photon index $\Gamma = 1.4$ as e.g. ASCA observations have shown (Gendreau et al., 1995; Chen et al., 1997; Miyaji et al., 1998). It is absorbed by heavier elements both in the MCs (see below) and in the Galaxy ($N_{\mathrm{H\,Gal}} = 3 - 8 \times 10^{20}\mathrm{cm}^{-2}$, Dickey & Lockman, 1990). The foreground is described by two thermal components as a composition of the Local Bubble and the Galactic halo emission for which two Raymond & Smith models (Raymond & Smith, 1977) were used. The halo emission is absorbed by the Galactic $N_{\mathrm{H\,fg1}} = N_{\mathrm{H\,Gal}}$, whereas the absorption of the Local Bubble emission $N_{\mathrm{H\,fg2}}$ is about one order lower. From observations by ROSAT, the softest component was verified to be thermal with a plasma temperature corresponding to $kT_{\mathrm{fg2}} = 0.09$ keV (Miyaji et al., 1998). In order to obtain the other parameters of the background+foreground spectrum, the spectra of regions as mentioned above were modeled using following components: 1. powerlaw for the cosmic background (fixed absorbing column density $N_{\mathrm{H\,Gal}}$ and fixed Γ), 2. Raymond & Smith spectrum for the Galactic halo (fixed absorption with $N_{\mathrm{H\,fg1}} = N_{\mathrm{H\,Gal}}$, kT_{fg1} to be determined), and 3. Raymond & Smith spectrum for the Local Bubble (fixed kT_{fg2} and varying $N_{\mathrm{H\,fg2}} \leq N_{\mathrm{H\,Gal}}$ for the absorption). The fit of the spectra from regions close to the MCs resulted in $kT_{\mathrm{fg1}} = 0.18$ keV for the halo emission which is in good agreement with former ASCA and ROSAT results. Furthermore, values for $N_{\mathrm{H\,fg2}}$ and the emission measures of the spectral components were obtained, which were applied for the later spectral fitting of the MC data.

6.1.3 Modelling the Diffuse Emission from the Magellanic Clouds

All the spectra of the MCs were first fitted with a spectral model only containing contributions of the background and the foreground in order to verify whether there is additional emission or not. In the next step, the diffuse emission from the MCs was fitted with an additional absorbed Raymond & Smith component yielding the characteristic temperature T_{MC} and the absorption $N_{\mathrm{H\,MC}}$. For the abundances in the MCs, correction factors ζ reported by Russell & Dopita (1992) were used: 0.5 for the LMC, and 0.2 for the SMC. Again the Galactic foreground was considered as an additional component using the temperatures $T_{\mathrm{fg1}}, T_{\mathrm{fg2}}$, emission measures, and absorption column densities $N_{\mathrm{H\,fg1}}, N_{\mathrm{H\,fg2}}$ as mentioned above. The cosmic background was modeled with the values for the photon index Γ and the emission measure as determined previously, but the absorption by both the MCs and the Galaxy ($N_{\mathrm{H\,MCtot}}$ and $N_{\mathrm{H\,fg}}$

$= N_{\mathrm{H\,Gal}}$) was taken into account. For the total absorbing column density $N_{\mathrm{H\,MCtot}}$ of the MCs, values from the H I column density maps were used which were derived from the Australia Telescope Compact Array (ATCA) aperture synthesis mosaic survey and the 64 m Parkes single dish telescope observations (for the LMC: Kim et al. 2001 and for the SMC: Stanimirovic et al. 1999). All of these parameters for the background and foreground components were fixed in the models.

The existence of additional diffuse X-ray emission from the MCs was verified for each $0\overset{\circ}{.}25 \times 0\overset{\circ}{.}25$ box, and the model yielding the lower reduced χ^2 was chosen as the correct one. Another important criterium for the acceptance of a model including MC emission was the temperature of the thermal plasma emission. For $T_{\mathrm{MC}} < 0.1$ keV, the foreground absorption of the X-rays becomes high, modifying the intrinsic luminosity by factors of about 10. Consequently, additional emission component with small values of T_{MC} might be modeled, although in reality there is only very low additional emission which should be better ascribed to variations of the Galactic foreground emission. In such cases, the absorption and the intrinsic flux become very high, pretending a very strong emission. Therefore, only spectra which are modeled with $T_{\mathrm{MC}} \geq 0.1$ keV were accepted as due to MC emission. This temperature criterium had no significant influence on the selection for the SMC. In the LMC however, LMC emission with low T_{MC} which seemed to be unreal were selected out particularly in the marginal regions.

For all spectra with evidences for a MC component, the temperature T_{MC} of the emitting interstellar plasma, the local absorbing column density in the MCs $N_{\mathrm{H\,MC}}$, and the emission measure $EM_{\square}$ (see Eq. (6.3) for definition) for the analyzed boxes were obtained for both the LMC and SMC. The determined temperatures range from 0.1 keV up to 1.5 keV which means that in both MCs hot gas with temperatures from 10^6 K to higher than 10^7 K is found. The fit results are listed in Appendix D in a table with box positions, absorption $N_{\mathrm{H\,MC}}$, temperature T_{MC}, emission measure, and additionally derived physical parameters of the emitting gas (Tables D.1 and D.2).

Since each spectrum with the determined temperature T_{MC} can be assigned to a certain region in the MC fields, images of the fit results were created by filling the square regions with derived temperature values. They are shown in Figures 6.2 and 6.4 for the LMC and the SMC, respectively. Figures 6.3 and 6.5 show the temperature images once more, but with superimposed contours of the reduced χ^2 of the spectral fit. In regions with low photon statistics it was difficult to achieve a good fit, resulting in high reduced χ^2. The reduced χ^2 of the eastern part of the SGS LMC 2 is high as well (red. $\chi^2 \approx 2 - 3$). In this case, the photon statistics were very high and the spectral analysis showed, that for the diffuse emission more than one thermal Raymond & Smith component was needed to reproduce the spectrum in a satisfying way.

In all these images the pixel values were set to zero in regions without data. Therefore, the margin of the regions with $T_{\mathrm{MC}} > 0$ is mainly caused by the fact that there was no or not enough data for the analysis in the adjacent regions (see Fig. 4.5). Also in Figures 6.6 to 6.9 in Section 6.1.5, the regions with pixel values > 0 are not characteristic for the extent of the total diffuse emission, but for the regions for which data was available.

6.1.4 Errors of the Spectral Parameters

For all spectral parameters of the diffuse X-ray emission from the MCs, uncertainties of the background and the foreground emission as well as the attenuation of X-rays by matter in the foreground cause a systematic error in addition to the statistical errors from the spectral fit. The statistical errors σ_{stat} of the parameters T_{MC}, $EM_{\square}$, and $N_{\mathrm{H\,MC}}$ were determined by fitting the spectra with all the other parameters fixed (background and foreground components, absorption of these components, and abundances). For T_{MC} the statistical error is $\sim -9\%, +15\%$, for $EM_{\square} \sim -14\%, +150\%$, and for $N_{\mathrm{H\,MC}} \sim -50\%, +140\%$.

Systematic Error

The estimation of the background and foreground components in the spectrum was based on the work on cosmic X-ray background by Gendreau et al. (1995), Chen et al. (1997), and Miyaji et al. (1998). Since ASCA data was mainly used for the analysis presented by these authors, the spectral range which was studied extended up to 10 keV. Therefore, reliable information was given especially for the hard X-ray background: $\Gamma = 1.4 \pm 0.1$. Furthermore, Miyaji et al. (1998) analyzed ROSAT and ASCA data simultaneously and obtained $kT_{\mathrm{fg2}} = 0.09 \pm 0.01$ keV for the softest component which can be assigned to the foreground emission. These values given, the background and foreground emission spectra of regions as described in Section 6.1.2 were analyzed by varying the values for Γ and T_{fg2} in ranges specified by their errors. In doing so, the error of the harder foreground component was determined: $kT_{\mathrm{fg1}} = 0.18^{+0.05}_{-0.01}$ keV.

Background and foreground emission components are not the only sources of systematic error of spectral modelling, but the uncertainty of the strength of X-ray absorption by matter in the line of sight must be considered as well. As it was shown in Section 6.1.1, the contribution by molecules and grains is negligible. However, if clouds are located in the line of sight, the absorption will be higher than estimated from the H I column density maps both for the Galaxy and for the MCs. Since the H I column density maps have moderate spatial resolution, single clouds cannot be resolved, and the values used for the Galactic foreground absorption ($N_{\mathrm{H\,fg}}$) and the absorption of the cosmic background by the MCs ($N_{\mathrm{H\,MCtot}}$) are average values with an inaccuracy of a factor of ~ 2.

In order to estimate the systematic error σ_{sys} of the spectral analysis of the ISM of the MCs, all the uncertainties mentioned so far were taken into consideration and arbitrarily selected regions were fitted with all possible combinations of the lower and upper limits of Γ, T_{fg1}, T_{fg2}, $N_{\mathrm{H\,fg}}$, and $N_{\mathrm{H\,MCtot}}$. Finally, the systematic errors for the parameters of the spectral component assigned to the MC emission were obtained: for the temperature T_{MC} the systematic error is $\sim -5\%, +8\%$, for $EM_{\square} \sim -10\%, +150\%$, and for $N_{\mathrm{H\,MC}} \sim -5\%, +20\%$.
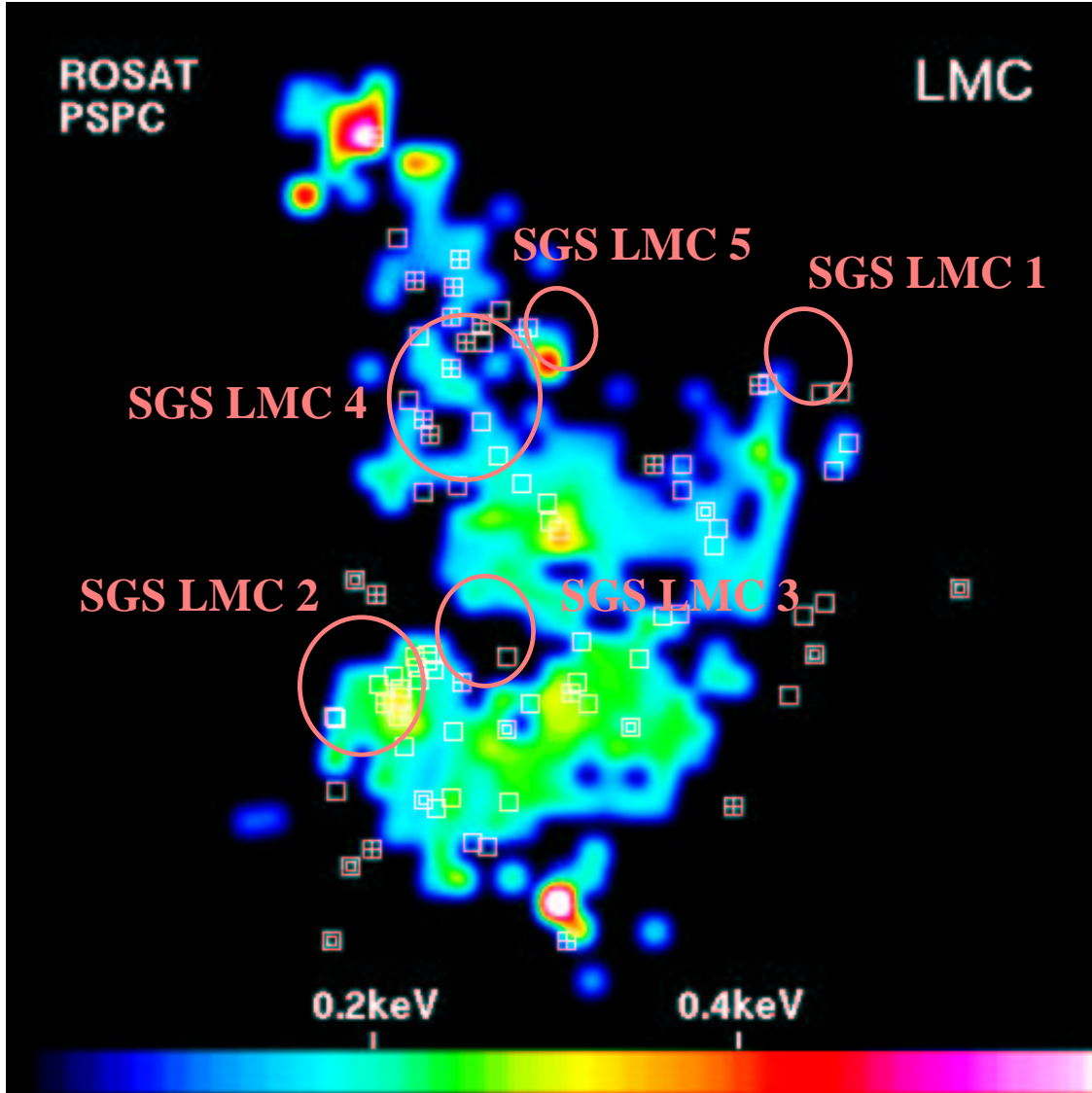
Figure 6.2: Temperature distribution image of the LMC. Square regions of the size $0°\!\!.25 \times 0°\!\!.25$ selected for spectrum extraction were filled with temperature values determined by spectral fitting. The image was then smoothed with a Gauss-filter. Positions of SNRs observed by ROSAT are shown by squares, those of XBs by crossed squares, and for SSSs by double squares. In addition the positions of five supergiant shells (Meaburn, 1980) are indicated by ellipses.
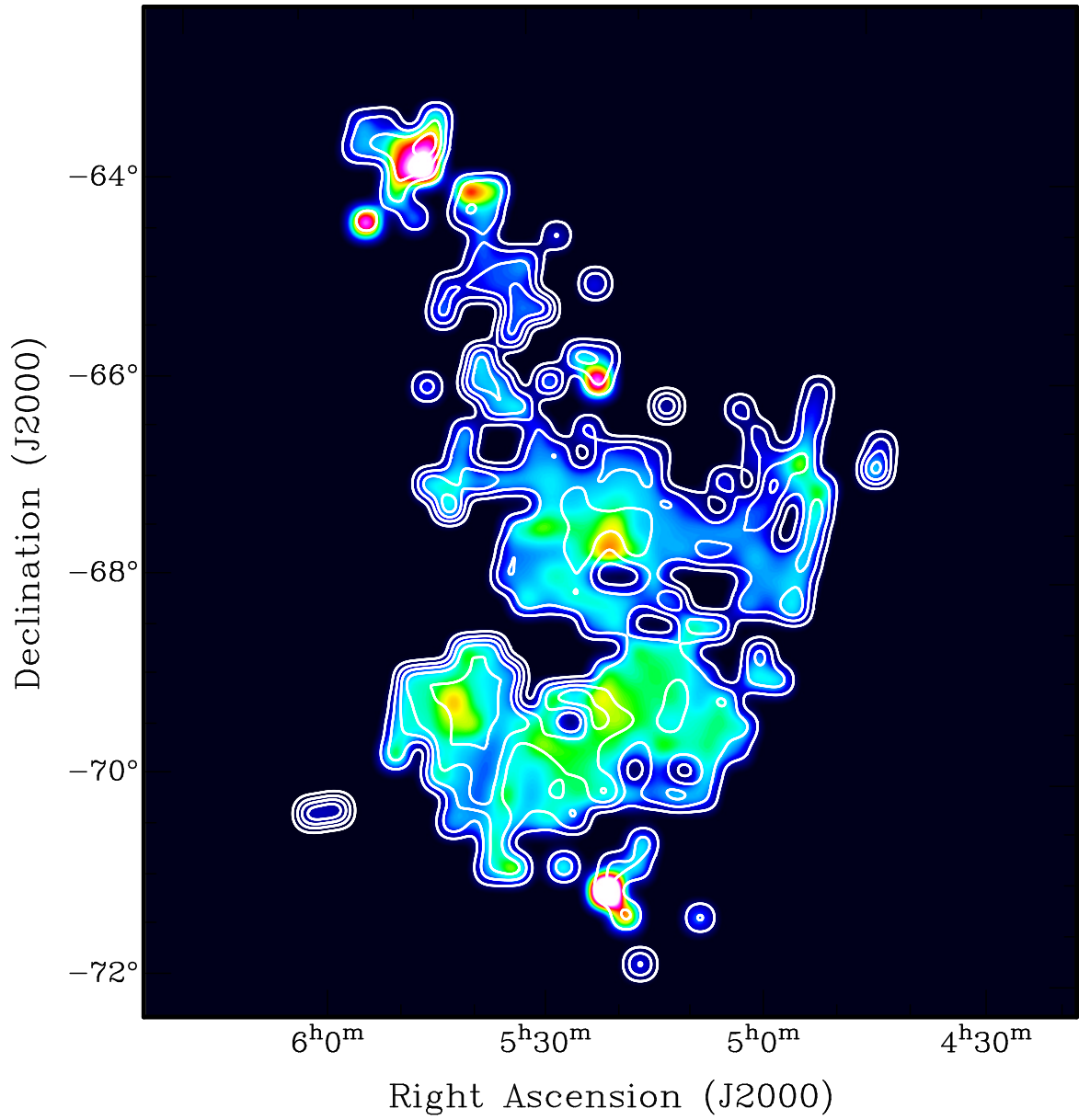
Figure 6.3: Contours of the reduced χ^2 of the fit (0.5 to 2.5 in steps of 0.5) are overlaid on the temperature image.
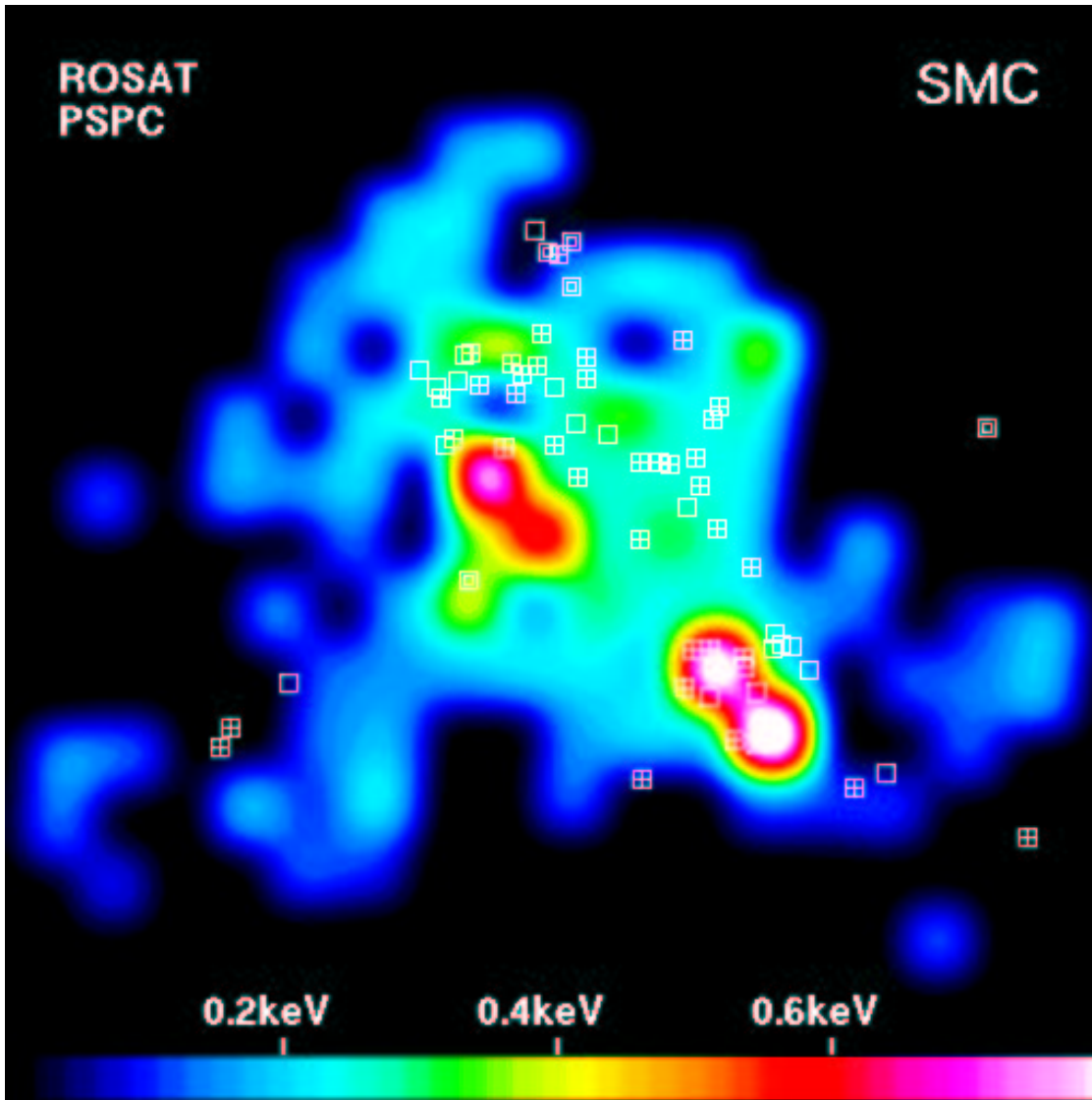
Figure 6.4: Temperature distribution image of the SMC. Same symbols as in the LMC figure are used to show SNR, XB, and SSS positions.
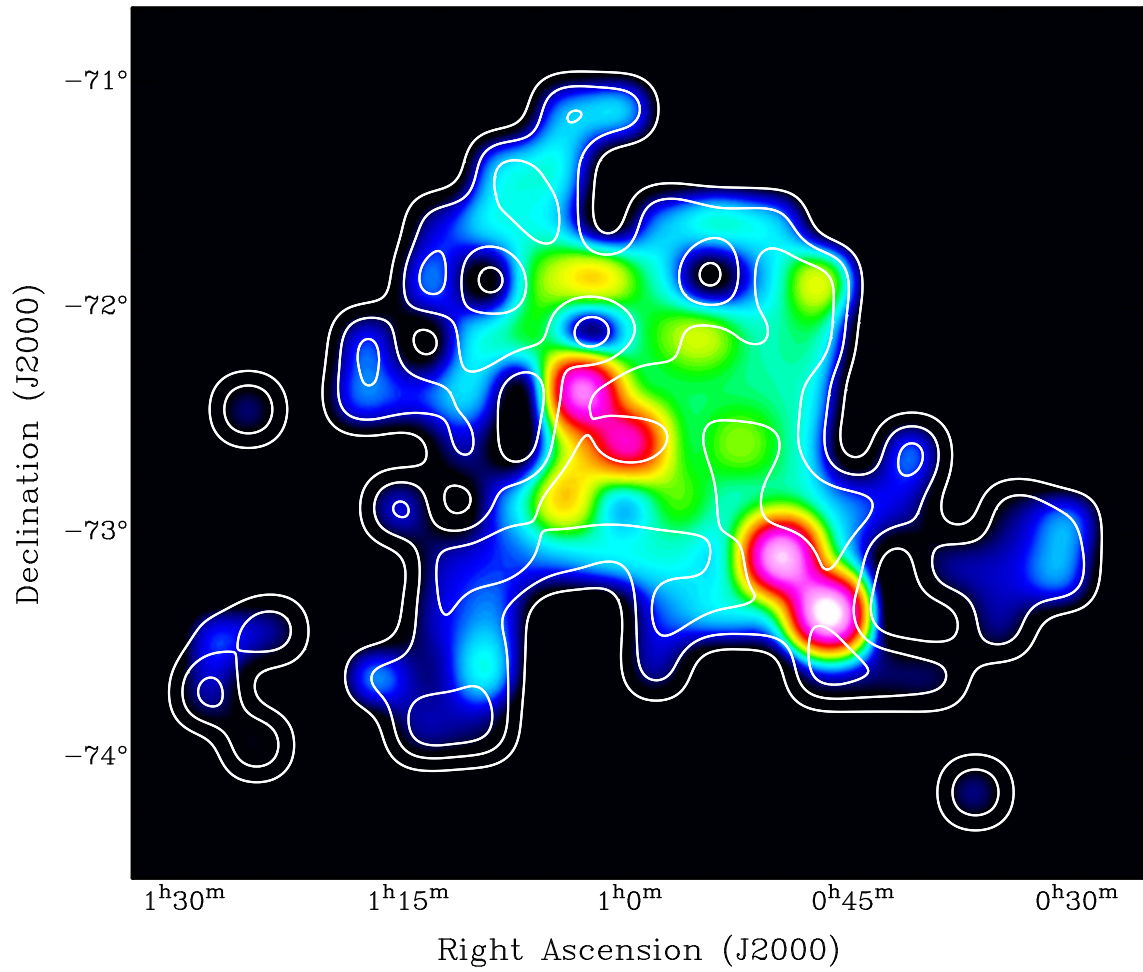
Figure 6.5: Reduced χ^2 of the fits in the SMC as contours (0.5, 1.0, 1.5) overlaid on the temperature image.

6.1.5 Physical Properties of the Hot ISM

X-ray Luminosity

The surface brightness of the hot ISM in a selected volume can be derived from the X-ray spectrum, since the emission measure for the $0°25 \times 0°25$ box was obtained from the spectral fit in the following way:

$$EM_\square = \frac{1}{10^{14} \times 4\pi D^2} \int n_e n \mathrm{d}V \quad [\mathrm{cm}^{-5}], \tag{6.3}$$

with both the electron density n_e and gas density n in $[\mathrm{cm}^{-3}]$ and D being the distance to the source in [cm]. We use $D_{\mathrm{LMC}} = 50$ kpc $= 1.54 \times 10^{23}$ cm and $D_{\mathrm{SMC}} = 59$ kpc $= 1.82 \times 10^{23}$ cm (van den Bergh, 1999). For the spectral band which is observed by ROSAT ($0.1 - 2.4$ keV), Equation (2.4) for the cooling function is:

$$\Lambda = 1.6 \times 10^{-22} T_6^{-0.6} \zeta \quad [\mathrm{erg}\,\mathrm{cm}^3\,\mathrm{s}^{-1}] \tag{6.4}$$

where ζ is the correction factor for metalicity with $\zeta_{\mathrm{LMC}} = 0.5$ and $\zeta_{\mathrm{SMC}} = 0.2$. The temperature is given as $T_6 = T/(10^6$ K). Using Equation (2.1), the unabsorbed luminosity of the gas in the $0°25 \times 0°25$ box is

$$L_\square = \int n_e n \Lambda \mathrm{d}V = EM_\square \times 10^{14} \times 4\pi D^2 \times \Lambda \quad [\mathrm{erg}\,\mathrm{s}^{-1}]. \tag{6.5}$$

$L_\square$ was derived from D, ζ, and the values $EM_\square$ and T_6 resulting from the spectral fit. In the same way as the temperature images in Figures 6.2 and 6.4 were created, images for the luminosity distribution were created by filling the square regions with $L_\square$ and smoothing them. The luminosity of the hot gas in a $0°25 \times 0°25$ region ranges from 4.5×10^{34} to 1.9×10^{37} erg s^{-1} in the LMC and from 2.1×10^{33} to 1.1×10^{37} erg s^{-1} in the SMC. The total luminosity of the diffuse emission from the MCs was calculated by summing up the luminosities $L_\square$ of the $0°25 \times 0°25$ regions. For the LMC, the obtained total luminosity is 1.4×10^{39} erg s^{-1}, for the SMC it is 6.0×10^{37} erg s^{-1}, both results with an uncertainty of $\sim -50\%, +200\%$.

In Figures 6.6 and 6.7 the significance of the luminosity of the diffuse emission is presented. The computed values of $L_\square$ are listed in Appendix D.

Geometry of the Hot Gas

After the interstellar gas was heated up by a shock front, the high temperature is maintained because of the negligible cooling, as it was shown in Section 2.2.2. Matter is mostly gathered to form a shell, so in its interior the gas can be treated as an ideal gas, and the density of the hot ISM can be estimated using the ideal gas equation. For coronal gas of cosmic abundances, the gas consists of atoms and electrons, densities of which are related as $n_e = 1.23n$. Since the metalicity is lower than in the Solar neighborhood both for the LMC and SMC, it is $n_e = (1 + 0.23\zeta)n$. Therefore the number density for ideal gas is

$$n = \frac{p}{(2 + 0.23\zeta)\,kT}. \tag{6.6}$$
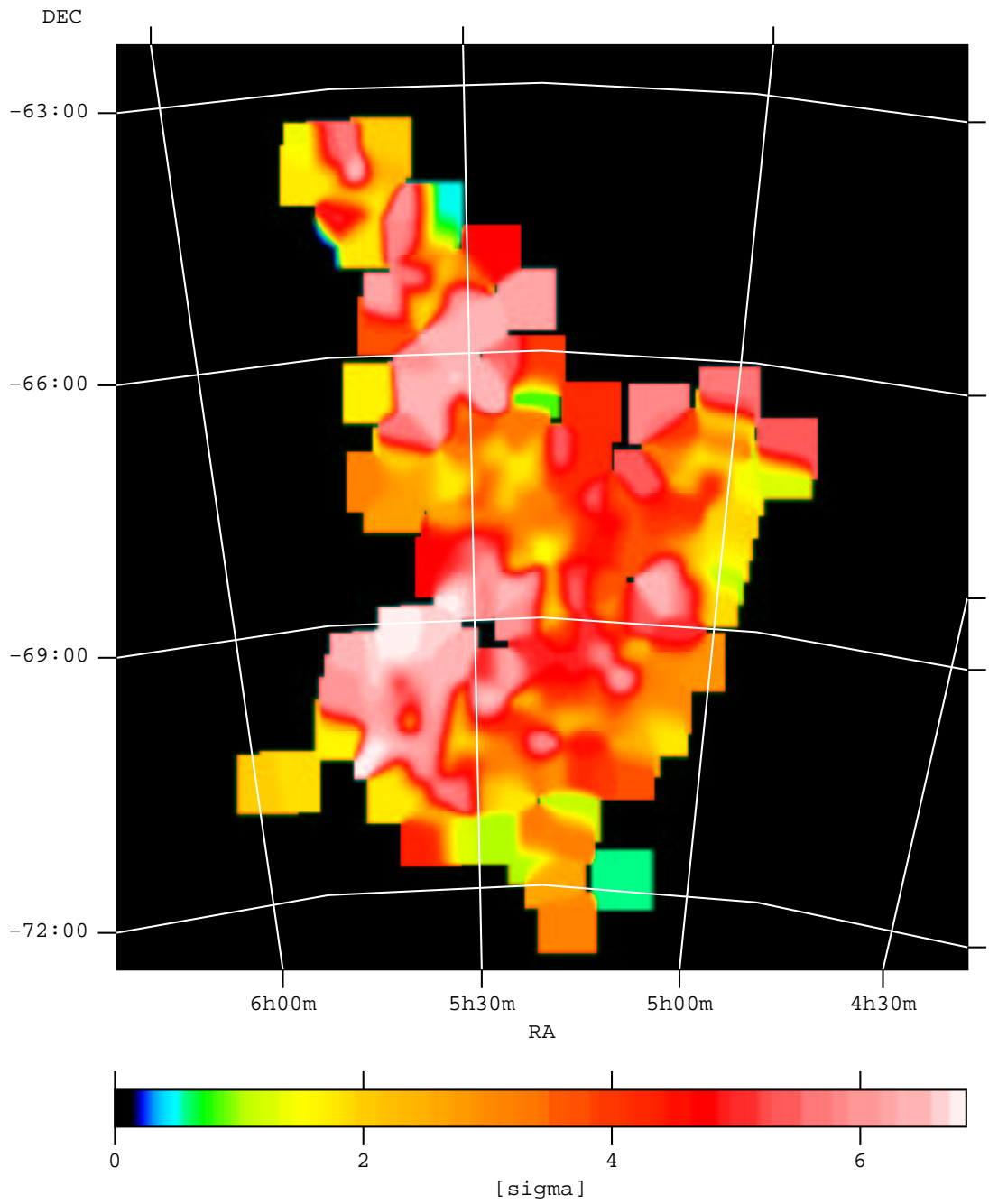
Figure 6.6: Image showing the significance of the luminosity of the diffuse X-ray emission in the LMC. The luminosity was derived from the results of the spectral fit and divided by the 1σ error.
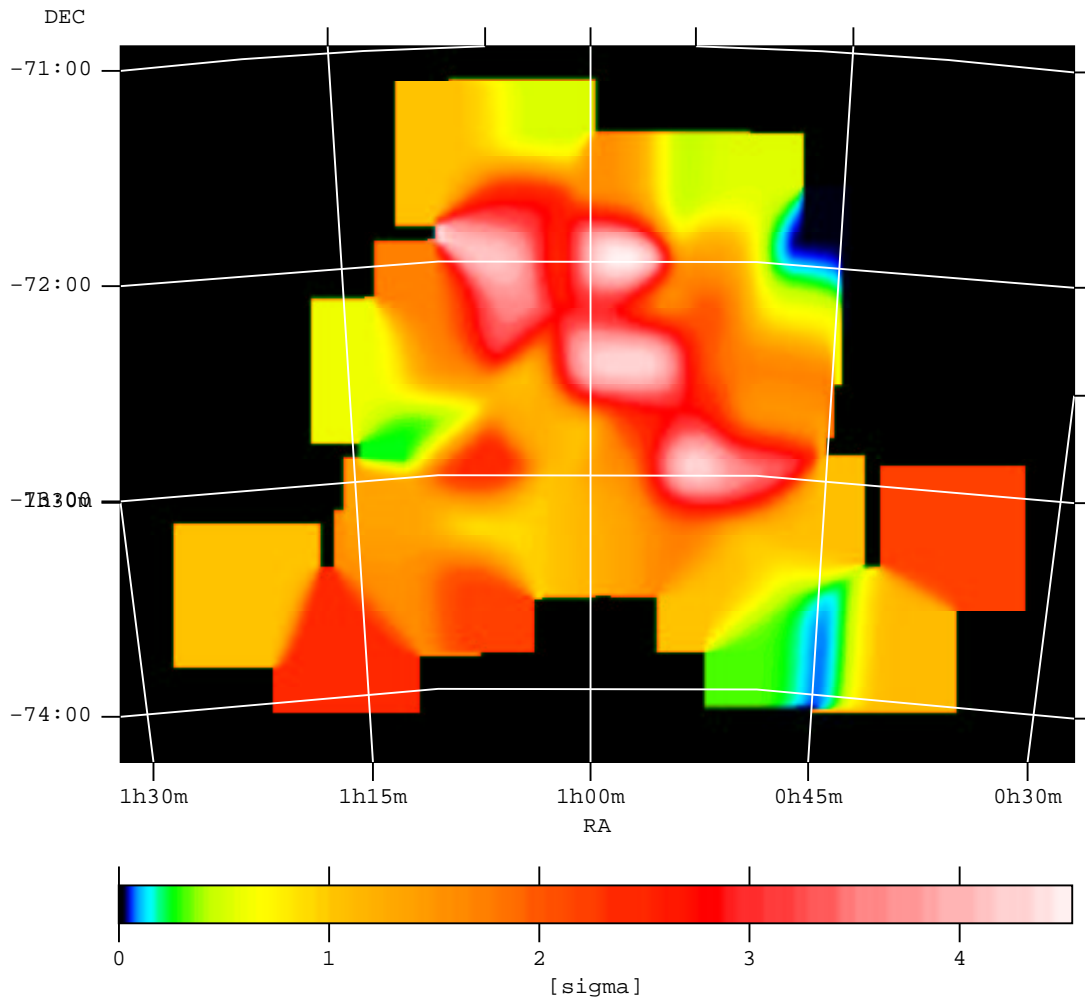
Figure 6.7: Significance image of the luminosity of the diffuse X-ray emission in the SMC.
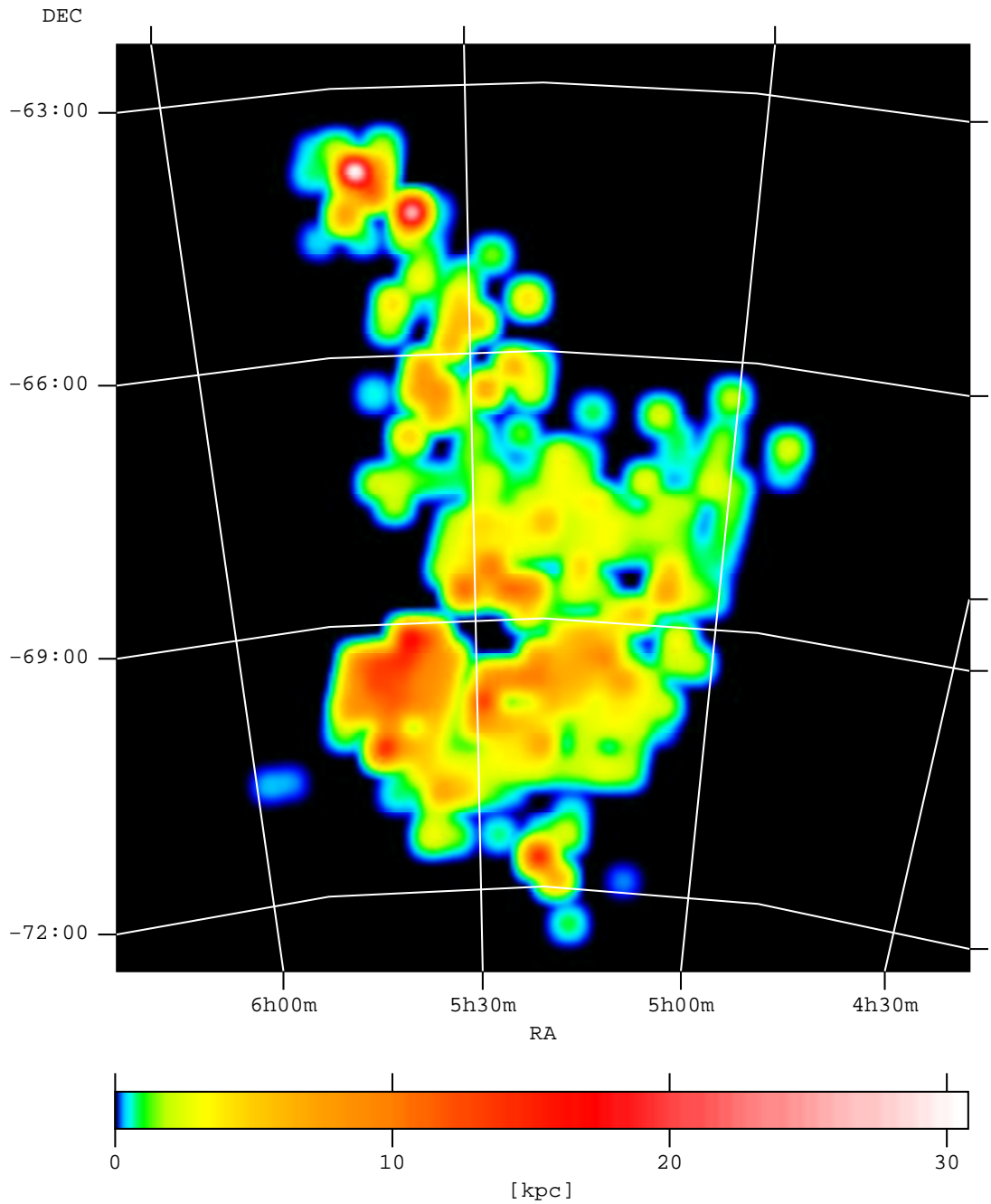
Figure 6.8: *The distribution of the depth of the X-ray emitting regions Δl in the LMC is shown as an image. Similar to the temperature distribution image, the regions used for spectrum extraction were filled with Δl and the image was smoothed.*

85
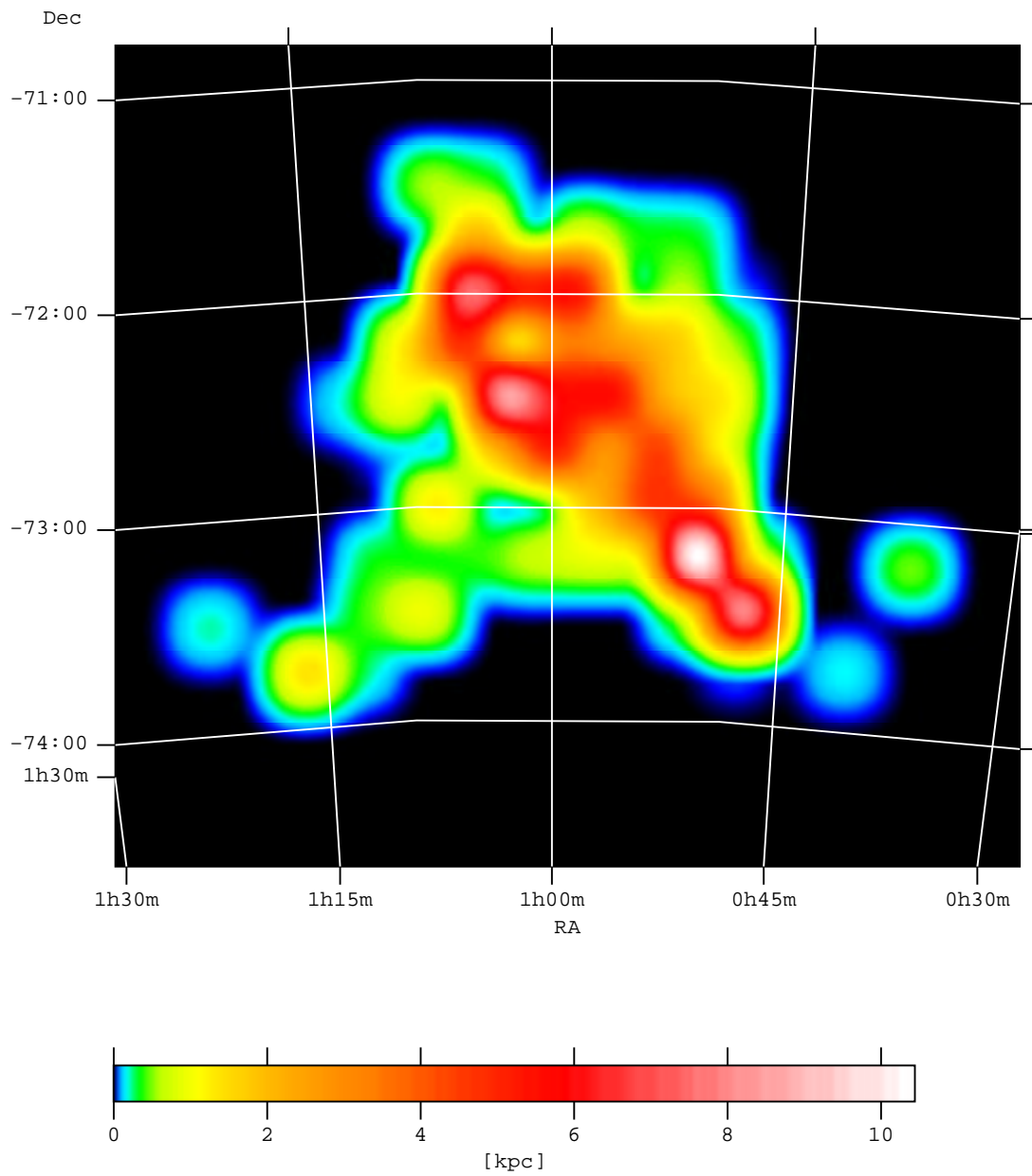
Figure 6.9: Δl distribution in the SMC.

Assuming $p = 3 \times 10^{-18}$ bar (Spitzer, 1990) and $T = 10^6$ K, the density is $n = 0.01$ cm^{-3}. Since the emission measure depends on the radiating volume (Eq. (6.3)), it can be used to derive the depth of the X-ray emitting region, while the pressure of the hot gas in the galaxy is assumed to be uniform. Spectra were extracted for regions of the size $0°\!\!.25 \times 0°\!\!.25$. Therefore, the emitting volume can be written as

$$V_\square = A_\square \Delta l = \left(\frac{0°\!\!.25}{360°} 2\pi D \right)^2 \Delta l. \tag{6.7}$$

Δl is the thickness of the radiating layer. Based on Equations (6.3) and (6.7) the depth Δl is

$$
\begin{aligned}
\Delta l &= \frac{EM_\square \times 10^{14} \times 4\pi D^2}{(1 + 0.23\zeta)\, n^2} \left(\frac{720}{\pi D} \right)^2 \\
&= \frac{4 \times (2 + 0.23\zeta)^2 \times 720^2 \times 10^{14} \times k^2}{(1 + 0.23\zeta)\, \pi\, p^2}\, EM_\square\, T^2 \\
&= 2.4 \times 10^4 \times EM_\square\, T_{\mathrm{keV}}^2 \quad [\mathrm{kpc}]
\end{aligned}
\tag{6.8}
$$

with $p = 3 \times 10^{-18}$ bar and $EM_\square$ in [cm^{-5}]. T_{keV} is the plasma temperature in [keV]. A typical value of $EM_\square = 0.001$ cm^{-5} and $T_{\mathrm{keV}} = 0.3$ keV yield $\Delta l = 2.2$ kpc. Distribution of Δl as derived from the fit values T_{keV} and $EM_\square$ for $p = 3 \times 10^{-18}$ bar are presented in Figures 6.8 and 6.9. The values for Δl are also listed in Tables D.1 and D.2.

In Figure 6.8 one can see that Δl is suspiciously high in the very north of the LMC, probably due to the source LMC X-3. The emission of this bright HMXB seems not to have been eliminated from the analyzed PSPC data in a satifying way, making both the temperature and the emission measure higher than what is typical for the hot interstellar gas (see also Fig. 6.2).

Shock Velocities

From the temperatures measured in X-rays, the expansion velocity of shock waves propagating through the hot gas can be derived with Equation (3.38). The shock velocity is

$$v = \sqrt{\frac{16}{3} \frac{RT}{\mu}} = 9.2 \times 10^2 \sqrt{T_{\mathrm{keV}}} \quad [\mathrm{km\ s}^{-1}] \tag{6.9}$$

with T_{keV} in [keV]. Both for the LMC and the SMC velocities of $v = 200 - 1100$ km s^{-1} were determined (see App. D). These values are in good agreement with the velocities reached by blast waves of stellar winds and supernova remnants as it was shown in Sections 3.2.1 and 3.2.2. Compared to expansion velocities of shells in the SMC measured in radio observations by Staveley-Smith et al. (1997), the shock velocities responsible for the heating of the shell interiors are about ten to hundred times higher.

6.2   XMM observation around SNR B 0540−69

SNR B 0540−69 in the LMC and the surrounding region were observed during the calibration phase of XMM-Newton. On the XMM EPIC-PN image of the observation on May 26, 2000, extended emission of the interstellar gas can be seen around the SNR (Fig. 6.10), especially at energies below ∼2 keV. In a comparison with the DSS image in Figure 6.11 one can see, that the regions in the south of the SNR coincide well with the H II region N 158 (Henize, 1956) which contains the OB association LH 104 (Lucke & Hodge, 1970). In order to study the spectral properties of the diffuse emission, two regions were selected: region 01 includes the brighter spot in the east of the SNR, region 02 covers the H II region N 158.

6.2.1   EPIC-PN Spectra

The spectra were fitted with thermal plasma models in XSPEC using the detector response matrices of July 2000. In both spectra emission peaks are found in the energy interval between 0.5 keV and 1.5 keV which can be interpreted as emission lines of highly ionized elements. The spectra are better reproduced by a non-equilibrium ionization model (Borkowski, 2000) than by the spectral model of Raymond & Smith (1977) assuming equilibrium ionization.

The applied non-equilibrium ionization model allows to vary the element abundances besides the effective temperature kT (keV), the ionization timescale $\tau = n_{\mathrm{e}}t$, and the time averaged temperature $\langle kT \rangle$. The ionization timescale τ is a measure for the plasma state once the gas was ionized: For small ionization timescales $\tau = n_{\mathrm{e}}t < 10^{12}\,\mathrm{s\,cm^{-3}}$, the electrons and ions are still not in thermal equilibrium. The X-ray emission is absorbed by the Galaxy in foreground ($N_{\mathrm{H\,fg}}$) and the matter in the LMC in the line of sight ($N_{\mathrm{H\,MC}}$) with abundances half of Solar. The Galactic foreground column density is $N_{\mathrm{H\,fg}} = 7.0 \times 10^{20}$ cm^{-2} in this region (Dickey & Lockman, 1990). In Figure 6.12 the spectra with the best fit model and the resulting parameters are shown. In the following, 90% errors are given for the derived values.

For region 01 the model fit suggests a plasma almost in thermal equilibrium. The characteristic parameters of the fit are: $N_{\mathrm{H\,LMC}} = (2.2 \pm 1.1) \times 10^{21}$ cm^{-2}, $\tau = (2 \pm 1) \times 10^{11}$ s cm^{-3}, $kT = (0.5 \pm 0.4)$ keV, and $\langle kT \rangle = (0.6 \pm 0.1)$ keV. The temperature has not changed significantly since the gas was ionized. The value determined for region 01 is higher than the result of the ROSAT PSPC analysis for this field ($0.3^{+0.1}_{-0.2}$ keV). This shows that with PSPC we only could see the overall characteristic of a larger region, whereas with EPIC-PN we can now resolve smaller (few arcminutes) structures of the hot ISM.

The interstellar plasma in the H II region N 158 seems to be further away from thermal equilibrium, indicated by the low ionization timescale $\tau = (8 \pm 1) \times 10^{9}$ s cm^{-3}. The temperatures are relatively high: $kT = (0.9 \pm 0.3)$ keV and $\langle kT \rangle = (2.8 \pm 1.2)$ keV. An overabundance of oxygen, neon, magnesium, silicon, iron, and nickel was measured. Additionally to the Galactic foreground column density, a relatively high absorption column density of $N_{\mathrm{H\,LMC+N158}} = (3.7 \pm 0.8) \times 10^{21}$ cm^{-2} was determined. The diffuse
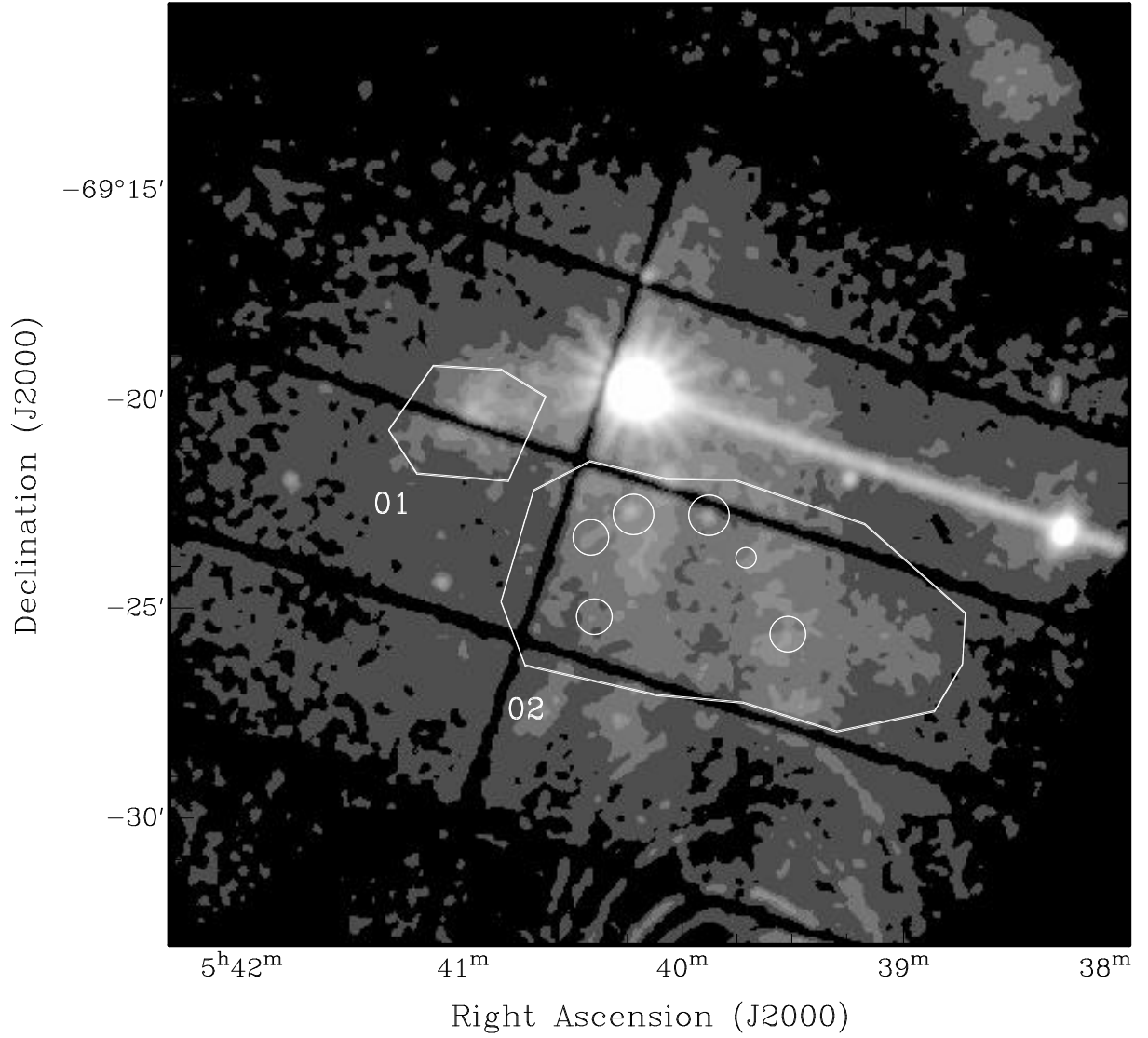
Figure 6.10: XMM EPIC-PN image (0.3 − 12 keV) of the SNR B 0540−69 and its surroundings. Regions used for spectral analysis are shown in white. The bright X-ray source at ∼RA = 05^h 40^m, Dec = –69° 20′ is SNR B 0540−69, the straight line feature to its west is caused by out-of-time events of this bright X-ray source. The gaps between the CCDs are seen as equally spaced dark lines and one line perpendicular to them, and the arc-shaped features south of region 02 stem from stray light from the bright X-ray source LMC X-1.

DSS2(R) + XMM EPIC–PN X–ray contours
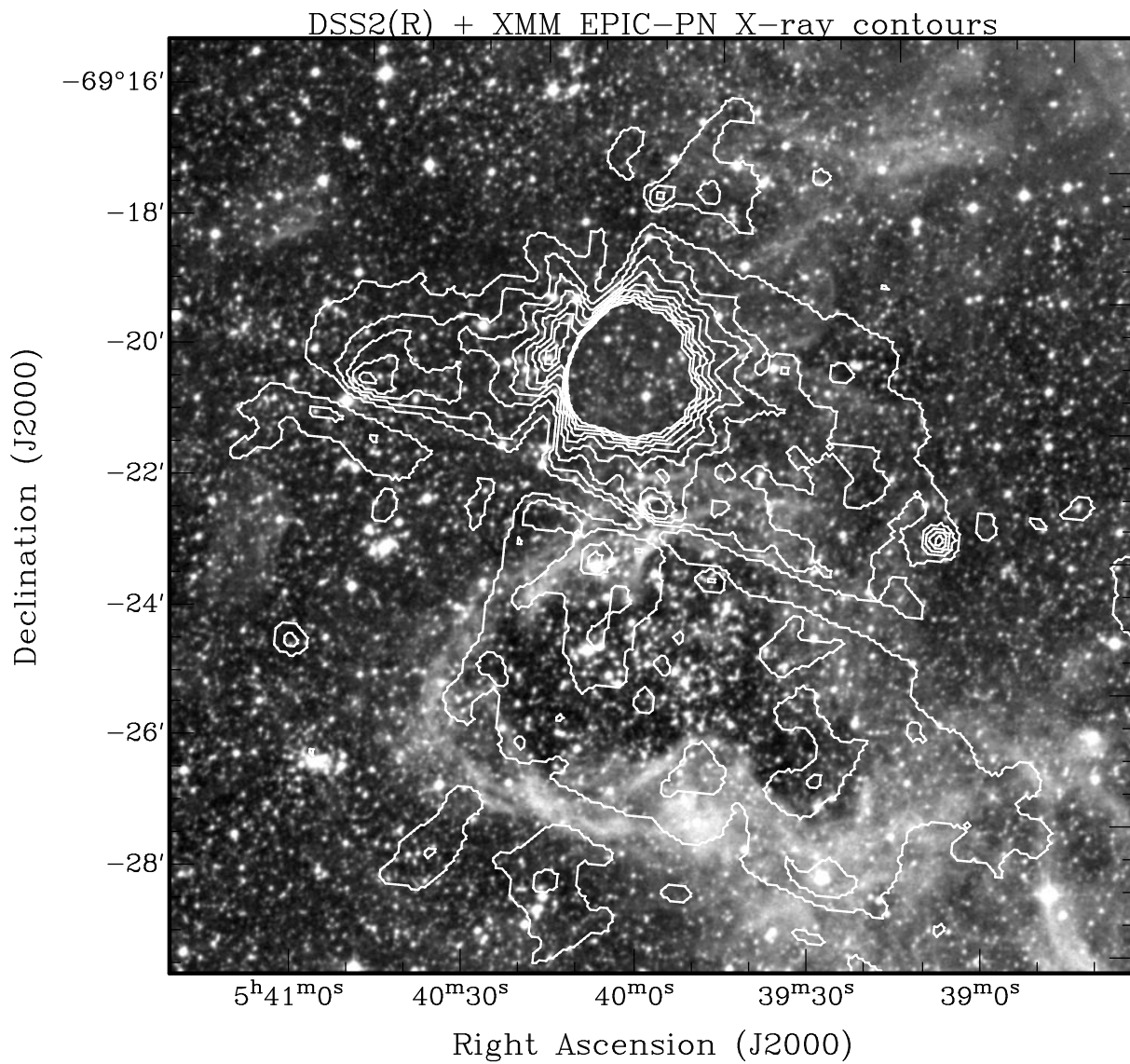
Figure 6.11: The X-ray contours of the same observation as in the image of Figure 6.10 (2 – 10 counts in steps of 1 counts) are overlaid on a DSS 2 (R) image. Again CCD gaps are visible, but the image has already been corrected for out-of-time events. In the south of SNR B 0540−69 diffuse emission is clearly seen which coincides well with the H II region N 158.
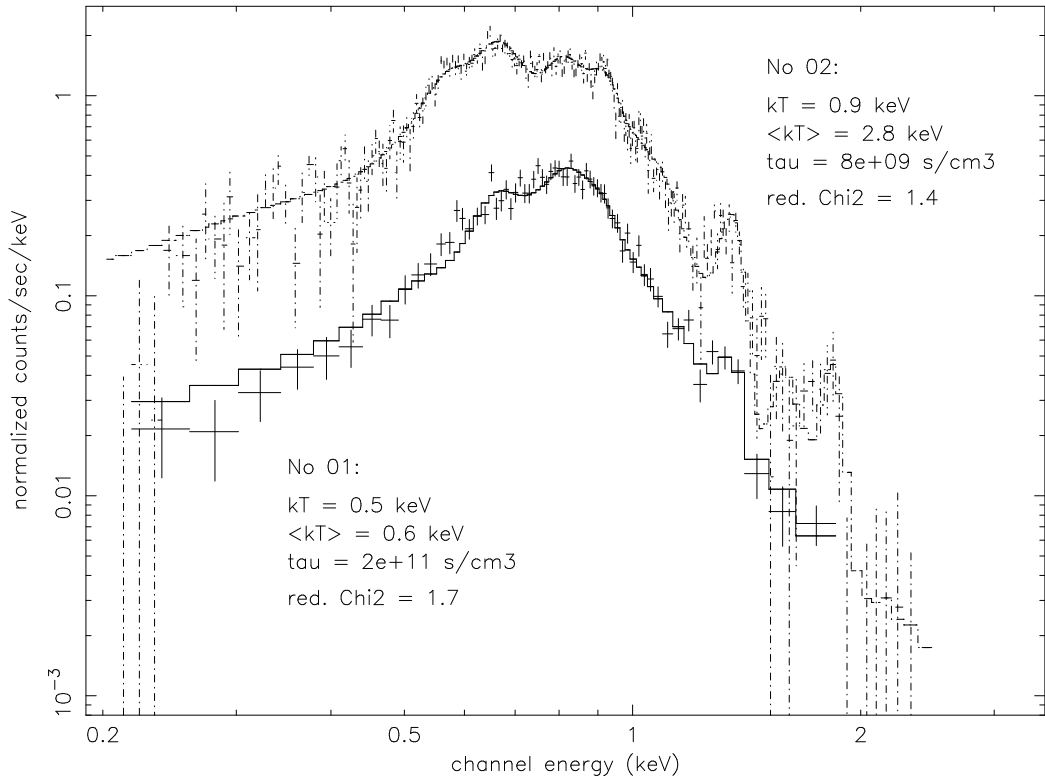
Figure 6.12: Spectra extracted from the XMM EPIC-PN observation of the diffuse emission around SNR B 0540−69. Region 01 (solid line) is located east of the SNR, region 02 (dash-dotted line) covers the H II region N 158.

X-ray emission arises most likely from the interior of the interstellar bubble shocked by stellar winds.

6.2.2   Interstellar Bubble in the H II Region N 158

Focusing on one of the hotter regions in the LMC, the XMM EPIC-PN pointing on the SNR B 0540−69 was analyzed with higher spectral resolution than it was possible with ROSAT. While in the east of the SNR the diffuse emission seems to arise from ionized gas close to thermal equilibrium with a temperature similar to the value determined from the ROSAT PSPC spectrum, in the south a smaller ionization timescale and higher temperatures are determined. Since the emission coincides spatially with the OB association LH 104 embedded in the H II region N 158, the conclusion is that the origin of the diffuse X-ray emission is the hot interstellar medium within the interstellar bubble. The gas in the bubble interior is shocked by stellar winds, and the cooler outer rim is visible as H II region. The total unabsorbed X-ray luminosity of the bubble is $L_X = 2.1 \times 10^{36}$ erg s^{-1}.

The emitting volume can be approximated by an ellipsoidal, although it is deformed in the south. From the EPIC-PN image the lengths of the two major axes were derived:

$a = 2\!'\!6 \pm 0\!'\!2 = (37 \pm 3)$ pc, $b = 4\!'\!1 \pm 0\!'\!3 = (60 \pm 5)$ pc $(D_{\mathrm{LMC}} = 50$ kpc). Assuming that the depth of the bubble is approximately equal to the visible extent of the H II region in projection, the third major axis is $c = (50 \pm 10)$ pc. The volume of the bubble is

$$V = \frac{4}{3}\pi abc = (1.3 \pm 0.3) \times 10^{61} \mathrm{\ cm}^{-3}. \tag{6.10}$$

Using the LMC metalicity $\zeta_{\mathrm{LMC}} = 0.5$ and the emission measure

$$
\begin{aligned}
EM &= \frac{1}{10^{14} \times 4\pi D_{\mathrm{LMC}}^2} \int n_{\mathrm{e}} n \mathrm{d}V \\
&\approx \frac{1}{10^{14} \times 4\pi D_{\mathrm{LMC}}^2} (1 + 0.23\zeta_{\mathrm{LMC}})\, n^2\, V \\
&= (2.9 \pm 2.3) \times 10^{-4} \mathrm{\ cm}^{-5},
\end{aligned}
\tag{6.11}
$$

resulting from the spectral fit, the gas density within the bubble can be estimated as:

$$
\begin{aligned}
n &= \sqrt{\frac{EM \times 10^{14} \times 4\pi D_{\mathrm{LMC}}^2}{(1 + 0.23\zeta_{\mathrm{LMC}})\, V}} \\
&= (2.4 \pm 2.0) \times 10^{-2} \mathrm{\ cm}^{-3}.
\end{aligned}
\tag{6.12}
$$

Although the size of the emitting region can be derived well from the image, the error of the gas density becomes relatively high (83%) because of the large error of the emission measure EM. Since the parameters of the spectral model EM, T, and N_{H} are coupled to each other, their relative errors are high ($\sim 30-80\%$), resulting in large errors for values computed in this section.

With temperature $T = (0.9 \pm 0.3)$ keV and density n given, the pressure of the gas is:

$$p = (n_{\mathrm{e}} + n)kT = (2 + 0.23\zeta_{\mathrm{LMC}})nkT = (7.3 \pm 6.4) \times 10^{-17} \mathrm{\ bar}. \tag{6.13}$$

Thus the pressure inside the bubble is about ten times higher than in the surrounding hot ISM of the galaxy ($p \approx 3 \times 10^{-18}$ bar). If we use the absorbing column density determined for the region 01 (besides the Galactic column density) as the mean LMC value $N_{\mathrm{H\,LMC}} = (2.2 \pm 1.1) \times 10^{21} \mathrm{\ cm}^{-2}$, the column density of the shell around LH 104 is

$$N_{\mathrm{H\,shell}} = N_{\mathrm{H\,LMC+N158}} - N_{\mathrm{H\,LMC}} = (1.5 \pm 1.4) \times 10^{21} \mathrm{\ cm}^{-2}. \tag{6.14}$$

In the model of Weaver et al. (1977) the expanding bubble sweeps up matter in the surrounding ISM, which finally collapses to a thin shell due to radiative cooling. Therefore the relation between the ambient gas density and the column density of the shell is easily found, if the radius of the bubble is known. They assume a spherically symmetric expansion of the bubble which is not the case for the bubble discussed here, easily verified on the DSS image. It seems to encounter a hindrance in the south. Nevertheless we can assume a mean radius R of the bubble for estimating the initial density of the swept-up gas. If a total of N particles originally filled the volume which

is occupied by the bubble, they are now gathered in the shell, and the column density of the gas (mainly hydrogen) is:

$$N_{\mathrm{H\,shell}} = \frac{N}{4\pi R^2} = \frac{4\pi}{3} R^3 n_0 \frac{1}{4\pi R^2} = \frac{n_0 R}{3}, \tag{6.15}$$

n_0 [cm^{-3}] being the ambient gas density. For $R = (50 \pm 10)$ pc we obtain

$$n_0 = \frac{3 N_{\mathrm{H\,shell}}}{R} = (29 \pm 28) \text{ cm}^{-3}. \tag{6.16}$$

The gas density in the surrounding ISM was two to three magnitudes higher than the hot gas in the bubble interior. Furthermore, we can calculate the age of the bubble from the ionization time scale of the emitting plasma. With $n_{\mathrm{e}} = (1 + 0.23\zeta_{\mathrm{LMC}})n = (0.027 \pm 0.022)$ cm^{-3} (Eq. (6.12)) and $\tau = (8 \pm 1) \times 10^9$ s cm^{-3} the resulting age is

$$t = \frac{\tau}{n_{\mathrm{e}}} = (9.4 \pm 7.7) \times 10^3 \text{ yrs.} \tag{6.17}$$

This result conforms well with the model predicting that interstellar bubbles reach the 'Snowplow'-phase after a few 1000 years of adiabatic expansion.

Chapter 7

Discussion

7.1 Observational Results

7.1.1 ROSAT HRI Catalogs of Distinct X-ray Sources of the MCs

The analysis of all ROSAT HRI pointed observations in the LMC and the SMC regions performed between 1990 and 1998 with exposure times higher than 50 seconds (543 observations of the LMC region and 71 observations of the SMC region) was presented. Source detection was carried out both on single pointings and on merged data applying a maximum likelihood algorithm. This resulted in a catalog of 397 sources for the LMC and a catalog of 121 sources for the SMC. Cross-correlation of HRI source catalogs with the TYCHO catalog or the SIMBAD data base enabled us to identify X-ray sources with optically observed objects with accurate coordinates. Further X-ray properties could be obtained for HRI sources contained in the PSPC catalog of HP99a and HFPK00.

100 HRI sources in the LMC region and 46 sources in the SMC region were identified with well known objects due to the positional coincidence as well as their X-ray characteristics like the extent and hardness ratios. The coordinates of most of the identified sources could be improved to more accurate positions and allowed the positional correction of other HRI sources. Thus the systematic boresight errors of these sources were reduced to values smaller than $7''$ which is the standard systematic error of ROSAT observations. For the LMC, coordinates of 254 HRI sources were corrected and the mean positional error of the whole HRI catalog was reduced to $6\rlap{.}''4$, and for the SMC, 99 positions were corrected and the errors were reduced to $5\rlap{.}''6$ on average.

For different source classes like SSSs, X-ray binaries, SNRs, Galactic stars, and background AGN classification criteria could be derived from the extent and hardness ratios of the identified sources. We looked for flux variability of the sources and for likely optical counterparts. In each MC region, 25 sources were classified additionally as MC members, foreground or background objects.

The combination of the ROSAT PSPC and the HRI source catalogs yields the first complete catalog of X-ray sources of the Magellanic Clouds in the soft X-ray band (0.1 – 2.4 keV). Their numbers and distribution give clues about the star formation history

of the galaxies, since SNRs, XBs, and SSSs are objects in the late stages of the stellar evolution. By interactions of these objects with their surroundings, the ambient ISM is heated up and becomes visible in the soft X-rays. Matter which once formed the stars and was processed in their interior is again set free into the interstellar space and is available for further galactic evolution. Moreover, the locally hot ISM influences the structure of the galaxies as a whole by the expansion of the high-temperature gas.

7.1.2 Temperature Distribution

In order to verify the regions with significant diffuse X-ray emission and to look for correlations between the hot ionized gas and other components within the galaxies, the temperature distribution images (Figs. 6.2 and 6.4) were overlaid on data from other observations of the MCs, i.e. merged image from PSPC data, DSS image, or H I maps. Figure 7.1 shows the H I map of the LMC with contours of X-ray temperatures, and in Figure 7.2, the contours are plotted on a DSS image of the SMC.

LMC

In general, regions with higher temperatures were found along and close to the optical bar of the LMC. Furthermore, the correlation between the hot gas and supergiant shells (SGSs) was verified. In the LMC, SGSs of hydrogen had been found in H I and Hα observations with diameters of the order of 1 kpc, i.e. each with a size of 5% – 10% of the total size of the galaxy. In X-rays there is an extended hot region in the southeastern quadrant of the LMC with a diameter of about 1 kpc as can be seen in Figure 6.2. This region covers the SGS LMC 2 (Meaburn, 1980) where many active objects like SNRs and OB associations were found (see Figs. 6.2 and 7.1). In a work on Einstein data, Wang & Helfand (1991b) derived a luminosity of $\sim 2 \times 10^{37}$ erg s^{-1} for the diffuse emission from SGS LMC 2 assuming a temperature of $\sim 5 \times 10^6$ K. Based on ROSAT PSPC data, Points et al. (2000) get a flux of 1.4×10^{-10} erg cm^{-2} s^{-1} in the energy band of 0.44 to 2.04 keV, which corresponds to $L_{\mathrm{X}} = 6 \times 10^{37}$ erg s^{-1} (0.1 – 2.4 keV). They used a model with $kT = 0.31$ keV. In the same region, the results of this work yield $L_{\mathrm{X}} = 6.4 \times 10^{37}$ erg s^{-1} with a mean $kT = 0.26$ keV, in good agreement with the values of Wang & Helfand (1991b) and Points et al. (2000).

High temperature was also determined at the boundary between SGS LMC 4 and SGS LMC 5. At such boundaries between the hot ISM and the cold dense supergiant shells, expanding gas encounters a strong discontinuity and the heating mechanism is highly effective. For SGS LMC 4, the integration of the X-ray luminosity gives $L_{\mathrm{X}} = 5.7 \times 10^{37}$ erg s^{-1} and the mean value for the temperature is $kT = 0.19$ keV. The temperature obtained by Bomans et al. (1994) for the northern part of SGS LMC 4 was 2.4×10^6 K, i.e. $kT = 0.21$ keV, and Points et al. (2000) derived a total luminosity of $\sim 2 \times 10^{37}$ erg s^{-1} from this result, assuming that the northern emission is representative for the whole SGS LMC 4.

As for the total diffuse emission of the LMC, Wang et al. (1991) determined a lower limit of $\sim 2 \times 10^{38}$ erg s^{-1} for the luminosity from Einstein data (0.16 – 3.5 keV). The
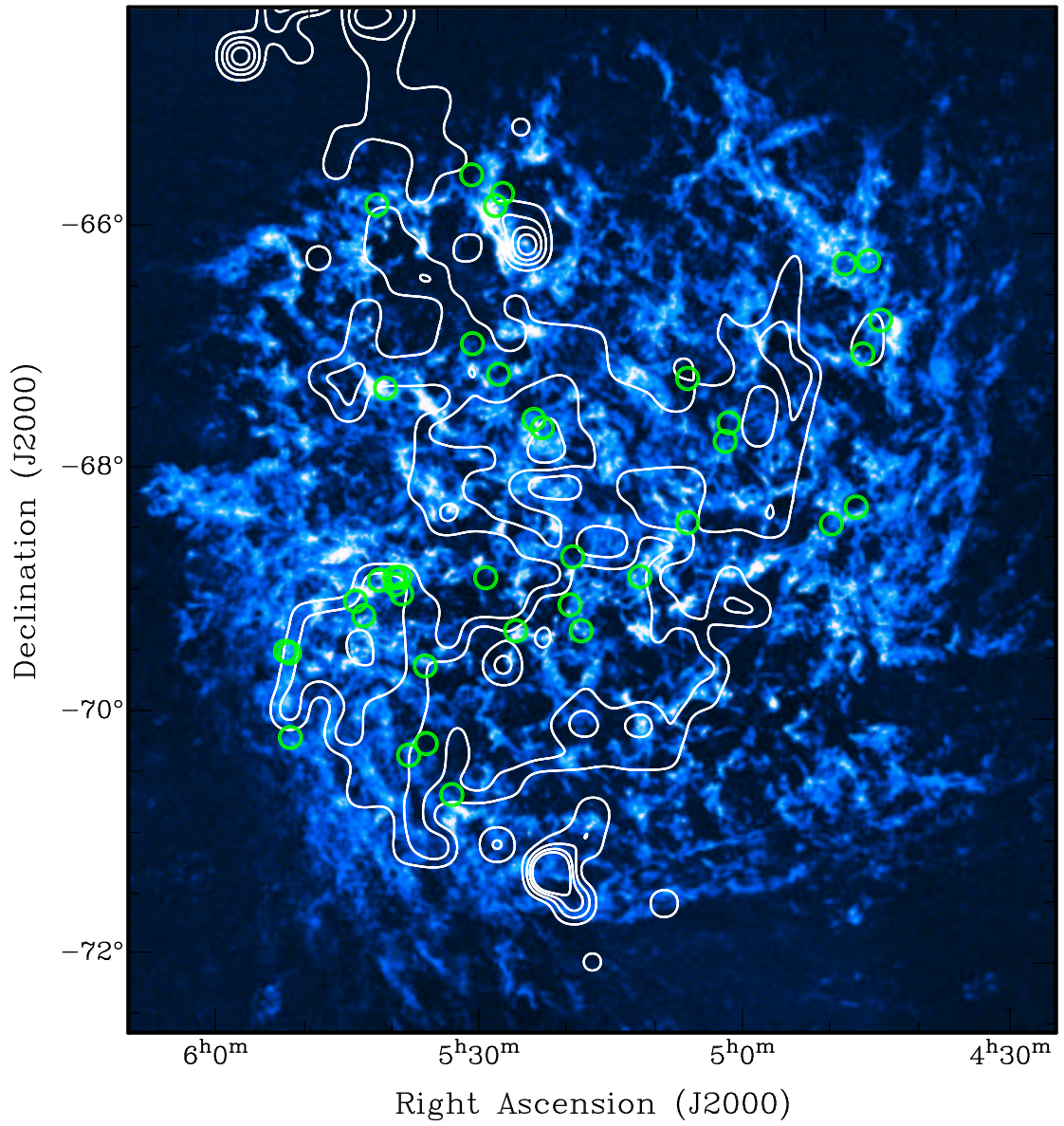
Figure 7.1: Temperature contours from 0.1 keV to 0.4 keV in steps of 0.1 keV are superimposed on a H I map (Kim et al., 1998) of the LMC with positions of SNRs observed by ROSAT marked as green circles.
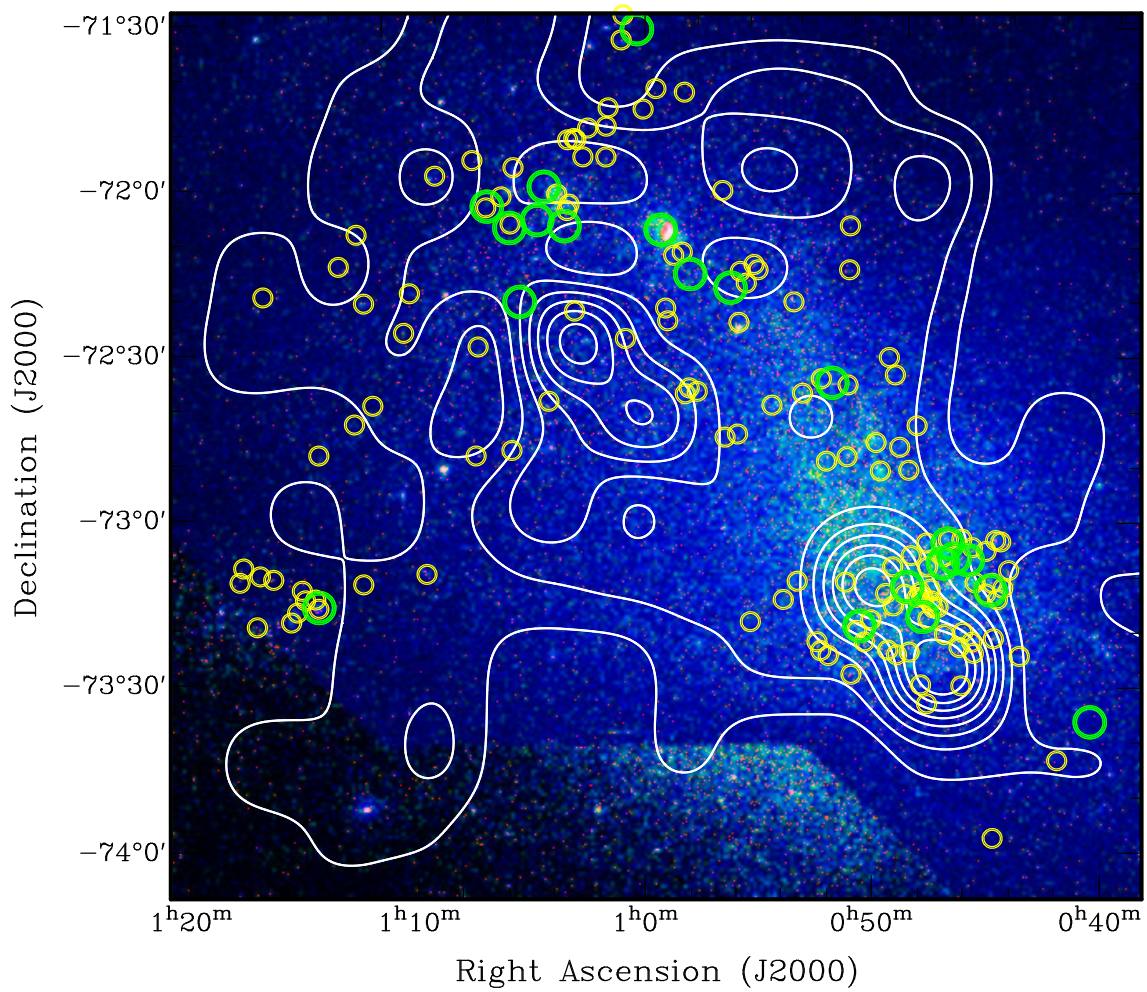
Figure 7.2: Overlay of the temperature distribution as contours from 0.1 to 0.8 keV in steps of 0.1 keV on a DSS image of the SMC. Green circles are SNRs observed by ROSAT and yellow circles are H II regions.

total luminosity derived from the ROSAT PSPC data in the energy band of 0.1 to 2.4 keV is 1.4×10^{39} erg s^{-1} (Sec. 6.1.5) with an error of $\sim -50\%, +200\%$, which is mainly due to uncertainties about the emission and absorption of the foreground gas.

SMC

The hot gas in the SMC is well correlated with the optical main body which can be seen on a DSS image with superimposed temperature contours (Fig. 7.2). Regions with the highest temperatures are found in the southern part of the galaxy with a large number of SNRs and H II regions. The total X-ray emission not only arises from the optically visible part of the galaxy, but also shows the emission from the galactic halo. This was already reported by Wang (1991) based on the analysis of Einstein data who obtained a total X-ray luminosity of the diffuse emission $L_{\mathrm{X}} = 5.0 \times 10^{38}$ erg s^{-1}. But this was not verified in later ROSAT observations (Snowden, 1999). As it was shown in Section 6.1.5, the ROSAT PSPC data yield $L_{\mathrm{X}} = 6.0 \times 10^{37}$ erg s^{-1}. A possible explanation for the discrepancy by a factor of about 10 between L_{X} derived from Einstein observation and that of ROSAT is the incompleteness of the list of the point sources which were removed from the Einstein data, since a large number of new point sources were found in subsequent X-ray observations.

Radio observations revealed shells and giant shells within the SMC and in the outer regions (Staveley-Smith et al., 1997), but supergiant shells with large cavities like in the LMC are not known. The X-ray emission measured by the PSPC in total is the superposition of the emission from the interior of the shells which was heated up by stellar winds and supernovae.

7.2   Recycling of Matter in Galaxies

Stars form out of high-density matter in the very cold part of the interstellar medium. They process matter in the interior which is partly set free in stellar winds, and finally perish in supernovae, returning matter back to interstellar space. In galaxies matter cycles in this way changing from gas to star and again back from star to gas.

The gaseous matter which was produced by a star, first fills an interstellar bubble as a thin high-temperature plasma. It is surrounded by colder gas like the H II gas ionized by the star. Repeated heating by stellar winds and supernovae in OB associations powers the growth and expansion of hot interstellar bubbles which sweeps up cold matter and form giant supershells in galaxies. Beside thermal energy and kinetic energy of expansion, the matter in the supershell has gravitational binding energy, which stabilizes the shell. If the sum of the kinetic energy and the thermal energy of the supershell becomes smaller than the gravitational binding energy due to radiative losses or breaking through the galactic disk, the supershell becomes gravitationally instable and fragmentates into interstellar clouds. These shell fragments grow rapidly and trigger star formation. Especially in irregular galaxies like the Magellanic Clouds, the supershell fragmentation is thought to be the dominating mechanism for propagating

star formation, whereas in spiral galaxies, gas is compressed by density waves in the spiral arms (McCray & Kafatos, 1987).

7.2.1 Star Formation in the Magellanic Clouds

In the LMC, stellar associations forming large scale systems were found (Shapley's constellations, McKibben Nail & Shapley, 1953) suggesting secondary star formation (Braunsfurth & Feitzinger, 1983; Isserstedt, 1984). The most prominent system is the Shapley's constellation III, located in the north of the LMC. It coincides spatially with the SGS LMC 4 and includes a large number of OB stars in about 20 young associations. The formation of these stars is thought to be caused by the gravitational instability of the SGS LMC 4. Another well known star formation region in the LMC is the 30 Doradus region located at the border between SGS LMC 2 and LMC 3. The comparison of the distribution of young stars in the LMC ($t_{age} \leq 2 \times 10^7$ yr, Isserstedt, 1984) and the diffuse X-ray emission shows that the hot gas is well correlated with the distribution of young stars. In regions with highest temperatures, i.e. around SGS LMC 4 or in the 30 Doradus region, there is a concentration of young supergiants ($t_{age} \leq 8 \times 10^6$ yr).

From optical observations it is known, that a young population of stars in the SMC is located along the bar (e.g. Brück, 1980), and in particular concentrated in the south. In this part of the SMC, the hot gas detected in X-rays coincides with the most active regions. This can be verified in Figure 7.2 showing the positions of H II regions, since associations of massive OB stars form H II regions by their ionizing radiation and winds. Star forming regions are located in the eastern wing of the SMC as well, extending from the northern end to the east (Gardiner & Hatzidimitriou, 1992). Hot gas is distributed between the wing and the optical main body of the SMC, in a region around RA = 01^h 00^m, Dec = $-72°$ $30'$ surrounded by SNRs and H II regions in the north. The wing region is thought to be caused by dynamical interactions between the SMC and the LMC and/or between the MCs and the Galaxy which triggered star formation (Murai & Fujimoto, 1980; Westerlund, 1990). A concentration of gas in the wing region was probably formed by forces acting between the halos of the MCs, rather than by an outflow of interstellar material from the main body of the SMC.

As was shown in Chapter 5, X-ray binaries discovered in the SMC are binary systems with a Be companion star, except for one system harboring a supergiant star. This suggest the occurrence of star formation in the SMC about 15 Myr ago (see also Sec. 5.5). The X-ray binary population of the SMC is different from that of the LMC, the former being rich in Be/X-ray binary systems. However, in contrast to our Galaxy, in both the LMC and the SMC the number of HMXBs is high, whereas only very few old LMXBs were found. Therefore one can assume, that both in the LMC and the SMC there was a period of enhanced star formation at about the same time, defining the stellar population of the following $\sim 10^7$ years.

7.2.2 Extragalactic H II Regions

The 30 Doradus region in the LMC is a very famous giant H II region, also known as the 'Tarantula Nebula'. It has a diameter of ~ 370 pc. H II regions, usually of smaller size, consist of interstellar gas ionized by young massive stars and are found in spiral and irregular galaxies. They are known in our Galaxy with the largest occurrence in the proximity of the Galactic center as well as in the spiral arms. Kennicutt (1984) studied giant H II regions in nearby galaxies, comparing their morphology and physical properties. The size of giant H II regions in the Galaxy ranges from 100 to 200 pc. In the SMC and the nearest spiral galaxy M 31, the Andromeda galaxy, giant H II regions of similar size were found. NGC 604 in its neighbor galaxy M 33 is a giant H II region on the scale of 30 Dor (~ 400 pc), and in M 101 much larger systems were found (NGC 5471 and NGC 5461 with diameters of up to 1000 pc). In addition, there are dwarf emission-line galaxies with spectra which resemble those of giant H II regions in nearby galaxies. The blue compact galaxies I Zw 18 and II Zw 40 (Zwicky, 1971) were the first dwarf galaxies classified as isolated giant extragalactic H II regions (Sargent & Searle, 1970).

All kinds of giant extragalactic H II regions are common objects for studying star formation in galaxies. The properties of the giant extragalactic H II regions themselves are best analyzed in the UV, but X-ray observations provide information about the physical processes responsible for their creation.

The EPIC-PN data of the XMM-Newton observation pointed at the rim of the SGS LMC 2 in the LMC enabled us to analyze the diffuse X-ray emission from the ISM in this field in detail. Beside the temperature of the emitting plasma, abundances were determined as well. Since the spectral resolution of the EPIC-PN is better in comparison to the PSPC, it showed for the first time, that the origin of the X-ray emission is a plasma in a state of non-equilibrium ionization. A region with enhanced emission coincides with the H II region N 158 with an diameter of ~ 100 pc surrounding an interstellar bubble. The X-ray emitting gas in the bubble is interpreted as to be heated up by the stars of the OB association LH 104 in the center. Pressure and gas densities of the interstellar bubble were derived from the spectral fit parameters, which are in good agreement with model predictions for stellar winds of massive stars, creating an interstellar bubble with an surrounding shell of H II and H I gas (Sec. 6.2.2).

7.3 Future Prospects

Complete ROSAT HRI source catalogs both for the LMC and for the SMC are available now. They summarize the detections of X-ray sources in the MCs and provide accurate positions with errors smaller than $16''$ for all sources, for the majority of sources about $7''$. Verification of the candidates for different source classes by a final optical identification is still needed.

As for the less luminous objects emitting X-rays like the Cataclysmic Variables (CVs), the sensitivity of past missions were not high enough to detect these sources. But in the future, we will be able to observe CVs not only in our Galaxy, but also

in the MCs. Additional observations in different energy ranges of the electromagnetic spectrum will achieve more precise characterization of the sources giving a better overall picture of the MCs.

It is commonly accepted that the ISM is enriched and heated up by the stellar evolution, forming high-density shells of cold matter by compression. Nevertheless, the physical properties of the thin interstellar plasma is still not well understood. Thin highly ionized gas with magnetic fields comparable to those in the interstellar space is difficult to create and to be maintained in the laboratories on Earth. Therefore, the heating and cooling mechanisms in such extreme conditions have not yet been studied in detail. In addition, the formation of supergiant shells like those discovered in the LMC is another still unsolved mystery of the galactic evolution. Up to now no observational evidences have been found which could explain the enormous energy input and the mechanism creating such large structures in the ISM in a satisfying way. As the first results of XMM-Newton observations of the LMC have shown, the X-ray telescopes with improved sensitivity and spectral resolution make it possible to study the thin plasma in interstellar space in full detail and determine its physical state. Knowing the nature of the hot interstellar gas, model predictions for interstellar bubbles and SNRs can be tested with observational results. Furthermore, future observations will achieve new discoveries of many more objects in the final stage of stellar evolution like X-ray emitting binary systems or SNRs which might prove that enough massive stars and supernovae existed in the past supplying energy for the formation of supergiant shells.

The existence of hot interstellar gas was observed not only in the Galaxy or the Magellanic Clouds, but also in other nearby galaxies. Coronal gas can be found in the galactic disk, often extending into the lower galactic halo. ROSAT observations of the nearly face-on spiral galaxy M 83 showed that its X-ray spectrum consists of two thermal components (Ehle et al., 1998; Immler et al., 1999). The soft component with a temperature of ~ 0.2 keV is thought to arise from the halo, the disk component is highly absorbed and yields a temperature of ~ 0.5 keV. In addition X-ray sources were found which coincide with H I holes in the galaxy as an evidence for the existence of hot gas in the expanding H I shells. Such a correlation of X-ray sources with H I shells was also observed in other nearby galaxies like M 51 (Ehle et al., 1995). Therefore, further observations of other nearby galaxies with new X-ray telescopes will allow more elaborate studies of single objects and the ISM of galaxies. The comparison of the results from the analysis of other nearby galaxies to those of the MCs will give additional observational proofs for the matter recycling within the galaxies and will improve the understanding of the evolution of galaxies.

Appendix A

ROSAT Pointings towards the Magellanic Clouds

Data analyzed in this work were taken from the ROSAT archive. For the source catalogs, HRI pointings in $10° \times 10°$ field around RA = 05^{h} 25^{m} 00^{s}, Dec = –67° 43′ 20″ (J2000.0) covering the Large Magellanic Cloud and $5° \times 5°$ field around RA = 01^{h} 00^{m} 00^{s}, Dec = $-73°$ 00′ 00″ (J2000.0) for the Small Magellanic Cloud were used. PSPC pointings in the same fields were selected for the spectral analysis of the diffuse X-ray emission from the Magellanic Clouds. All pointings with ID, pointing direction, and exposure time are listed in the following tables.

Table A.1: HRI pointings used for creating the source catalogue of the SMC region.

1	2	3	4
ROR key	Pointing direction		Exposure time
	RA	Dec	
	(J2000.0)		[s]
180240h	00 52 00.0	−72 28 12	7493.5
201687h	00 37 24.0	−72 14 24	807.0
201687h-1	00 37 24.0	−72 14 24	6839.6
300402h	01 03 14.4	−70 51 00	20060.2
300510h	00 37 19.2	−72 14 24	7312.6
300511h	00 37 19.2	−72 14 24	9482.2
300512h	00 37 19.2	−72 14 24	9491.6
300513h	00 48 16.8	−73 31 48	1582.4
400232h	00 37 19.2	−72 14 24	1512.8
400237h	00 53 26.4	−72 37 12	1096.0
400237h-1	00 53 26.4	−72 37 12	1167.6
400237h-2	00 53 26.4	−72 37 12	1301.5
400241h	00 58 36.0	−71 36 00	1847.5
400334h	01 05 50.3	−72 34 48	3649.1
400335h	00 52 48.0	−73 30 00	3814.0
400336h	01 17 09.6	−73 12 00	2590.0
400336h-1	01 17 09.6	−73 12 00	4476.0
400337h	00 59 00.0	−72 22 47	5001.0
400338h	00 53 04.8	−73 04 12	5838.5
400339h	00 55 04.8	−72 06 00	1310.0
400339h-1	00 55 04.8	−72 06 00	1427.5
400339h-2	00 55 04.8	−72 06 00	4325.0
400340h	00 46 28.8	−73 19 48	2601.5
400340h-1	00 46 28.8	−73 19 48	2564.5
400645h	00 58 36.0	−71 36 00	1954.5
400840h	00 32 55.1	−73 48 00	1897.6
400840h-1	00 32 55.1	−73 48 00	5961.9
400841h	00 49 04.8	−72 51 00	34899.8
500003h	01 04 02.4	−72 01 48	21882.8
500136h	00 47 16.8	−73 08 24	7523.8
500136h-1	00 47 16.8	−73 08 24	4461.1
500137h	01 03 16.8	−72 09 36	14071.7
500418h	00 59 26.4	−72 10 12	2005.0
500418h-1	00 59 26.4	−72 10 12	8264.0
500418h-2	00 59 26.4	−72 10 12	7531.4
500418h-3	00 59 26.4	−72 10 12	10973.8
500419h	00 51 04.8	−73 21 36	11280.4
500419h-1	00 51 04.8	−73 21 36	4343.0
500420h	01 17 04.8	−73 26 24	5943.6
500420h-1	01 17 04.8	−73 26 24	1943.5
500420h-2	01 17 04.8	−73 26 24	1084.0
500420h-3	01 17 04.8	−73 26 24	2127.0
500420h-4	01 17 04.8	−73 26 24	4889.0
500420h-5	01 17 04.8	−73 26 24	4240.8
500428h	01 05 04.8	−72 22 47	12997.3
500428h-1	01 05 04.8	−72 22 47	1111.4
500428h-2	01 05 04.8	−72 22 47	16919.3
600807h	01 00 24.0	−72 36 00	1920.9
600807h-1	01 00 24.0	−72 36 00	27919.4
600808h	00 57 12.0	−72 54 00	671.0
600808h-1	00 57 12.0	−72 54 00	2509.0
600808h-2	00 57 12.0	−72 54 00	24263.1
600809h	01 07 36.0	−72 24 00	29568.5
600810h	00 54 00.0	−72 24 00	6726.5
600810h-1	00 54 00.0	−72 24 00	4906.5
600810h-2	00 54 00.0	−72 24 00	15786.1
600811h	00 53 12.0	−73 12 00	27395.0
600812h	00 49 12.0	−73 30 00	11492.0
600812h-1	00 49 12.0	−73 30 00	17064.5
600926h	00 57 36.0	−73 21 00	15540.2
600926h-1	00 57 36.0	−73 21 00	10063.8
600927h	01 02 00.0	−73 00 00	23799.0
600928h	00 54 00.0	−71 56 59	26723.8
600928h-1	00 54 00.0	−71 56 59	1062.0
600929h	00 43 12.0	−73 42 00	24534.1
601044h	00 58 00.0	−71 45 00	8147.0
601045h	00 44 00.0	−73 25 12	9497.0
601048h	00 49 12.0	−72 30 00	2910.0
601051h	00 51 12.0	−72 11 59	1603.9
900445h	00 59 28.8	−72 09 36	14910.5
900445h-1	00 59 28.8	−72 09 36	34614.9

Table A.2: HRI pointings used for creating the source catalogue of the LMC region.

1	2	3	4
ROR key	Pointing direction		Exposure time
	RA	Dec	
	(J2000.0)		[s]
100193h	05 39 38.4	−69 44 24	39739.0
100219h	05 25 00.0	−69 38 24	295.0
100604h	05 38 55.2	−64 04 48	274.0
100613h	05 39 09.7	−63 55 20	144.0
100613h-1	05 39 33.0	−64 05 58	161.0
110220h	05 25 10.3	−69 34 20	494.0
110221h	05 24 12.0	−69 36 00	280.0
110222h	05 24 36.0	−69 43 12	344.0
110223h	05 25 55.2	−69 40 12	503.0
110224h	05 24 45.6	−69 33 35	580.0
110225h	05 24 04.8	−69 39 36	293.0
110226h	05 25 00.0	−69 38 24	128.0
110226h-1	05 26 06.0	−69 44 31	884.0
110227h	05 25 55.2	−69 36 36	765.0
110228h	05 25 50.4	−69 29 24	286.0
110229h	05 24 04.8	−69 30 00	800.0
110230h	05 23 09.6	−69 41 24	997.0
110230h-1	05 24 09.0	−69 35 03	433.0
110232h	05 24 12.0	−69 47 24	865.0
110233h	05 25 21.6	−69 48 35	225.0
110234h	05 26 50.4	−69 41 59	775.0
110235h	05 26 45.6	−69 34 12	498.0
110236h	05 26 26.4	−69 25 48	924.0
110237h	05 23 36.0	−69 25 48	747.0
110238h	05 22 40.8	−69 30 00	1426.0
110239h	05 22 14.4	−69 42 36	624.0
110240h	05 23 48.0	−69 52 12	1403.0
110241h	05 25 31.2	−69 53 24	474.0
110242h	05 27 31.2	−69 46 11	280.0
110243h	05 27 28.8	−69 31 11	618.0
110272h	05 39 43.2	−69 39 36	2800.0
110273h	05 38 40.8	−69 43 48	1708.0
110274h	05 39 28.8	−69 49 48	1205.0
110275h	05 40 33.6	−69 45 36	1794.0
110276h	05 39 09.6	−69 40 12	1782.0
110277h	05 38 50.4	−69 47 24	1806.0
110278h	05 40 07.2	−69 49 12	1148.0
110279h	05 40 28.8	−69 41 59	2557.0
110279h-1	05 40 57.7	−69 48 45	711.0
110281h	05 38 24.0	−69 37 12	2108.0
110282h	05 37 43.2	−69 43 48	1972.0
110283h	05 38 02.4	−69 50 23	1428.0
110284h	05 38 40.8	−69 53 24	1621.0
110285h	05 40 45.6	−69 52 47	1462.0
110286h	05 41 26.4	−69 48 00	1647.0
110287h	05 41 07.2	−69 38 24	1717.0
110288h	05 39 52.8	−69 29 24	1621.0
110289h	05 37 48.0	−69 33 00	1431.0
110290h	05 36 45.6	−69 43 12	1692.0
110291h	05 36 50.4	−69 48 35	1673.0
110292h	05 38 09.6	−69 57 36	2118.0
110293h	05 40 38.4	−69 58 48	1741.0
110294h	05 42 28.8	−69 47 24	3584.0
110295h	05 42 14.4	−69 38 24	2375.0
110605h	05 39 33.9	−64 20 00	189.0
110606h	05 39 00.0	−63 58 12	164.0
110608h	05 41 09.3	−64 04 32	433.0
110609h	05 36 45.1	−64 06 21	250.0
110610h	05 38 35.5	−64 10 17	579.0
110610h-1	05 38 22.2	−64 05 38	292.0
110611h	05 40 00.0	−64 03 35	242.0
110614h	05 39 02.4	−63 49 48	161.0
110615h	05 39 00.0	−63 58 12	328.0
110616h	05 38 52.8	−64 11 59	386.0
110617h	05 39 26.4	−64 19 48	237.0
110618h	05 36 38.4	−64 05 23	553.0
110619h	05 37 48.0	−64 03 45	242.0
110620h	05 40 06.1	−64 03 46	191.0
110621h	05 41 14.4	−64 04 12	359.0
120004h	05 28 45.6	−65 26 59	256.0
141003h	06 00 00.0	−66 33 35	620.0
141013h	05 28 45.6	−65 26 59	55.0
141531h	05 25 00.0	−69 38 24	3005.6

Table A.2: Continued (HRI LMC).

1	2	3	4	1	2	3	4
ROR key	Pointing direction RA	Dec	Exposure time	ROR key	Pointing direction RA	Dec	Exposure time
	(J2000.0)		[s]		(J2000.0)		[s]
141533h	05 25 00.0	−69 38 24	1410.0	201958h	05 28 45.6	−65 26 59	1006.5
141556h	05 25 00.0	−69 38 24	3694.9	201961h	05 28 45.6	−65 26 59	4497.9
141557h	05 25 00.0	−69 38 24	1672.0	201963h	05 28 45.6	−65 26 59	3078.0
141558h	05 25 00.0	−69 38 24	1353.0	201964h	05 28 45.6	−65 26 59	3192.5
141559h	05 25 00.0	−69 38 24	1355.0	201965h	05 28 45.6	−65 26 59	2636.1
141801h	05 25 00.0	−69 38 24	599.5	201966h	05 28 45.6	−65 26 59	2985.5
141802h	05 38 57.6	−64 04 48	1592.5	201967h	05 28 45.6	−65 26 59	713.5
141803h	05 37 09.6	−64 22 47	1966.5	201968h	05 28 45.6	−65 26 59	2413.5
141804h	05 41 19.2	−63 51 00	851.0	201969h	05 28 45.6	−65 26 59	1193.5
141846h	05 44 48.0	−65 43 48	5923.0	201970h	05 28 45.6	−65 26 59	29758.2
141875h	05 25 00.0	−69 38 24	2337.0	201996h	05 27 48.0	−69 54 00	8892.4
141882h	05 25 00.0	−69 38 24	1532.0	202002h	04 39 50.4	−68 09 00	2003.5
141906h	05 25 00.0	−69 38 24	1865.0	202003h	04 39 50.4	−68 09 00	2894.9
141936h	05 25 00.0	−69 38 24	3104.3	202004h	04 39 50.4	−68 09 00	3120.0
142000h	05 25 00.0	−69 38 24	1809.9	202005h	04 39 50.4	−68 09 00	2554.5
142001h	05 25 00.0	−69 38 24	2625.5	202007h	04 39 50.4	−68 09 00	4825.5
142001h-1	05 25 00.0	−69 38 24	3039.1	202008h	04 39 50.4	−68 09 00	320.0
142002h	05 25 00.0	−69 38 24	2542.0	202008h-1	04 39 50.0	−68 09 22	1080.5
142003h	05 25 00.0	−69 38 24	934.0	202012h	04 39 50.4	−68 09 00	2691.0
142003h-1	05 25 00.0	−69 38 24	1993.1	202013h	04 39 50.4	−68 09 00	4058.0
142004h	05 25 00.0	−69 38 24	2843.5	202014h	04 39 50.4	−68 09 00	3564.0
142004h-1	05 25 00.0	−69 38 24	2236.5	202015h	04 39 50.4	−68 09 00	2177.0
142005h	05 25 00.0	−69 38 24	3297.5	202016h	04 39 50.4	−68 09 00	4563.5
142005h-1	05 25 00.0	−69 38 24	2008.1	202018h	04 39 50.4	−68 09 00	4486.5
142020h	05 25 00.0	−69 38 24	2695.5	202019h	04 39 50.4	−68 09 00	1923.5
142520h	05 25 00.0	−69 38 24	1438.0	202020h	04 39 50.4	−68 09 00	2661.0
142521h	05 25 00.0	−69 38 24	2388.1	202021h	04 39 50.4	−68 09 00	1687.1
142522h	05 25 00.0	−69 38 24	4171.0	202022h	04 39 50.4	−68 09 00	772.5
142523h	05 25 00.0	−69 38 24	1706.1	202023h	04 39 50.4	−68 09 00	2702.1
142524h	05 25 00.0	−69 38 24	4028.4	202024h	04 39 50.4	−68 09 00	2821.0
142525h	05 25 00.0	−69 38 24	2377.4	202025h	04 39 50.4	−68 09 00	2952.5
142532h	05 25 00.0	−69 38 24	2239.0	202252h	05 28 45.6	−65 26 59	2144.9
142533h	05 25 00.0	−69 38 24	1057.4	202253h	05 28 45.6	−65 26 59	840.5
142534h	05 25 00.0	−69 38 24	2751.9	202254h	05 28 45.6	−65 26 59	2852.5
142536h	05 25 00.0	−69 38 24	2215.6	202256h	05 28 45.6	−65 26 59	3111.4
142537h	05 25 00.0	−69 38 24	1964.4	202257h	05 28 45.6	−65 26 59	2725.6
142551h	05 25 00.0	−69 38 24	3048.6	202258h	05 28 45.6	−65 26 59	1356.6
142552h	05 25 00.0	−69 38 24	966.4	202259h	05 28 45.6	−65 26 59	1497.4
142553h	05 25 00.0	−69 38 24	2101.0	202260h	05 28 45.6	−65 26 59	3190.9
142554h	05 25 00.0	−69 38 24	1938.0	202261h	05 28 45.6	−65 26 59	3017.4
142561h	05 25 00.0	−69 38 24	2289.8	202262h	05 28 45.6	−65 26 59	4430.0
142571h	05 25 00.0	−69 38 24	580.0	202263h	05 28 45.6	−65 26 59	2031.0
142572h	05 25 00.0	−69 38 24	2846.0	202277h	05 50 00.0	−71 52 12	4995.9
142573h	05 25 00.0	−69 38 24	2175.0	202278h	04 39 50.4	−68 09 00	1613.9
142574h	05 25 00.0	−69 38 24	2992.7	202278h-1	04 39 50.4	−68 09 00	2125.4
142579h	05 25 00.0	−69 38 24	2841.8	202279h	05 13 50.4	−69 51 36	2730.0
142580h	05 25 00.0	−69 38 24	2061.0	202279h-1	05 13 50.4	−69 51 36	1977.5
142581h	05 25 00.0	−69 38 24	2086.0	202280h	05 27 48.0	−69 54 00	4066.5
142582h	05 25 00.0	−69 38 24	3533.0	202281h	05 50 00.0	−71 52 12	5958.1
142583h	05 25 00.0	−69 38 24	2073.7	202282h	04 39 50.4	−68 09 00	3701.0
142584h	05 25 00.0	−69 38 24	2240.8	202283h	05 13 50.4	−69 51 36	3964.6
142591h	05 25 00.0	−69 38 24	3419.0	202381h	05 13 50.4	−69 51 36	1333.8
142592h	05 25 00.0	−69 38 24	2653.0	202382h	05 13 50.4	−69 51 36	1164.8
142593h	05 25 00.0	−69 38 24	2052.1	202383h	05 13 50.4	−69 51 36	1914.0
142594h	05 25 00.0	−69 38 24	1535.9	202385h	05 13 50.4	−69 51 36	1824.8
142595h	05 25 00.0	−69 38 24	2031.9	202386h	05 13 50.4	−69 51 36	2372.8
150008h	05 40 12.0	−69 19 48	18099.0	202387h	05 13 50.4	−69 51 36	782.0
150013h	05 39 38.4	−69 44 24	869.0	202388h	05 13 50.4	−69 51 36	1034.0
160077h	05 40 02.4	−63 52 12	585.5	202389h	05 13 50.4	−69 51 36	919.0
170254h	05 28 45.6	−65 26 59	1375.9	202390h	05 13 50.4	−69 51 36	1955.0
180109h	05 22 31.2	−69 37 12	1413.6	202391h	05 13 50.4	−69 51 36	968.2
180124h	05 43 33.6	−68 22 12	893.4	202392h	05 13 50.4	−69 51 36	1113.0
180124h-1	05 43 33.6	−68 22 12	908.0	202393h	05 13 50.4	−69 51 36	1757.8
180163h	05 43 33.6	−68 22 12	1527.0	202395h	05 13 50.4	−69 51 36	2114.8
180163h-1	05 43 33.6	−68 22 12	883.0	202398h	05 13 50.4	−69 51 36	2087.0
180165h	05 28 45.6	−65 26 59	6416.4	202399h	05 13 50.4	−69 51 36	3891.8
180208h	05 13 50.4	−69 51 36	4980.0	202400h	05 13 50.4	−69 51 36	2153.8
200575h	05 28 45.6	−65 26 59	6896.0	202401h	05 13 50.4	−69 51 36	2221.8
201677h	05 50 00.0	−71 52 12	4287.5	202403h	05 13 50.4	−69 51 36	1751.0
201689h	05 27 48.0	−69 54 00	8463.1	202404h	05 13 50.4	−69 51 36	2258.0
201692h	05 28 43.2	−65 26 59	1388.3	202407h	05 13 50.4	−69 51 36	807.0
201693h	05 28 43.2	−65 26 59	2262.9	202408h	05 13 50.4	−69 51 36	1335.8
201694h	05 28 43.2	−65 26 59	2350.4	202409h	05 13 50.4	−69 51 36	1743.7
201848h	05 24 09.6	−71 08 24	2200.5	202410h	05 13 50.4	−69 51 36	1094.8

Table A.2: Continued (HRI LMC).

ROR key	Pointing direction RA Dec (J2000.0)	Exposure time [s]	ROR key	Pointing direction RA Dec (J2000.0)	Exposure time [s]
202411h	05 13 50.4 −69 51 36	1087.8	202724h	05 28 45.6 −65 26 59	1811.9
202412h	05 13 50.4 −69 51 36	987.8	202726h	05 28 45.6 −65 26 59	1786.1
202413h	05 13 50.4 −69 51 36	1164.8	202730h	05 28 45.6 −65 26 59	2006.9
202414h	05 13 50.4 −69 51 36	1187.8	300516h	05 43 33.6 −68 22 12	4203.9
202415h	05 13 50.4 −69 51 36	1206.8	300516h-1	05 43 33.6 −68 22 12	2154.1
202417h	05 13 50.4 −69 51 36	1195.8	300517h	05 46 48.0 −71 09 00	13633.5
202418h	05 13 50.4 −69 51 36	1305.8	400056h	05 35 28.8 −69 16 11	23351.0
202419h	05 13 50.4 −69 51 36	1284.8	400066h	05 26 00.0 −66 04 48	20989.9
202420h	05 13 50.4 −69 51 36	1180.8	400121h	05 46 28.8 −68 34 12	1609.0
202421h	05 13 50.4 −69 51 36	1169.8	400122h	05 55 00.0 −67 48 35	932.0
202422h	05 13 50.4 −69 51 36	1902.8	400123h	05 46 57.6 −68 52 12	1399.0
202423h	05 13 50.4 −69 51 36	1162.2	400124h	05 18 40.8 −68 14 24	4541.0
202424h	05 13 50.4 −69 51 36	2220.7	400125h	05 32 07.2 −69 19 12	4923.0
202425h	05 13 50.4 −69 51 36	2025.8	400126h	05 31 33.6 −71 30 00	987.0
202426h	05 13 50.4 −69 51 36	2333.8	400127h	05 30 16.8 −70 46 11	1884.0
202427h	05 13 50.4 −69 51 36	2462.7	400153h	05 22 26.4 −67 58 12	5608.0
202428h	05 13 50.4 −69 51 36	2599.7	400153h-1	05 22 26.4 −67 58 12	3046.6
202429h	05 13 50.4 −69 51 36	1550.2	400230h	05 35 55.2 −69 21 00	4862.0
202430h	05 13 50.4 −69 51 36	1327.3	400231h-1	05 22 28.8 −69 26 24	3922.4
202431h	05 13 50.4 −69 51 36	1665.8	400233h	05 35 55.2 −69 56 24	4982.0
202432h	05 13 50.4 −69 51 36	2244.0	400234h	05 32 52.8 −67 43 12	5025.0
202433h	05 13 50.4 −69 51 36	2274.0	400234h-1	05 32 52.8 −67 43 12	1433.8
202434h	05 13 50.4 −69 51 36	2132.0	400236h	05 40 45.6 −70 11 59	1567.0
202435h	05 13 50.4 −69 51 36	2048.0	400238h	05 26 28.8 −69 46 48	4073.0
202436h	05 13 50.4 −69 51 36	2617.8	400239h	05 09 55.2 −68 44 24	880.0
202437h	05 13 50.4 −69 51 36	1501.8	400239h-1	05 09 55.2 −68 44 24	2275.0
202438h	05 13 50.4 −69 51 36	1782.0	400240h	05 17 19.2 −70 44 24	3704.8
202439h	05 13 50.4 −69 51 36	921.0	400240h-1	05 17 19.2 −70 44 24	3464.5
202440h	05 13 50.4 −69 51 36	1964.7	400242h	05 53 28.8 −70 24 36	5818.0
202441h	05 13 50.4 −69 51 36	930.8	400242h-1	05 53 28.8 −70 24 36	2789.0
202443h	05 13 50.4 −69 51 36	1060.8	400349h	05 41 26.4 −68 49 48	1130.5
202444h	05 13 50.4 −69 51 36	1151.8	400349h-1	05 41 26.4 −68 49 48	5425.0
202445h	05 13 50.4 −69 51 36	1126.8	400350h	05 52 55.2 −69 53 24	1855.5
202447h	05 13 50.4 −69 51 36	1341.8	400350h-1	05 52 55.2 −69 53 24	2905.0
202448h	05 13 50.4 −69 51 36	1463.0	400351h	05 45 52.8 −69 52 47	4073.3
202449h	05 13 50.4 −69 51 36	1617.8	400352h	05 35 04.8 −70 39 00	1345.5
202450h	05 13 50.4 −69 51 36	1331.0	400352h-1	05 35 04.8 −70 39 00	4117.5
202451h	05 13 50.4 −69 51 36	1408.8	400353h	05 26 07.2 −67 42 36	3517.5
202452h	05 13 50.4 −69 51 36	1488.0	400353h-1	05 26 07.2 −67 42 36	4461.1
202453h	05 13 50.4 −69 51 36	1414.8	400354h	04 58 16.8 −69 04 12	3867.0
202455h	05 13 50.4 −69 51 36	2205.8	400355h	05 28 43.2 −67 25 48	4584.0
202456h	05 13 50.4 −69 51 36	922.2	400356h	05 28 33.6 −68 36 36	3177.5
202457h	05 13 50.4 −69 51 36	891.0	400357h	05 53 00.0 −69 23 24	3864.0
202458h	05 13 50.4 −69 51 36	1022.2	400358h	05 15 09.6 −69 26 59	4010.9
202459h	05 13 50.4 −69 51 36	2346.0	400359h	05 16 55.2 −71 46 11	1954.4
202460h	05 13 50.4 −69 51 36	807.0	400359h-1	05 16 55.2 −71 46 11	3784.9
202461h	05 13 50.4 −69 51 36	1395.0	400360h	05 47 43.2 −67 45 36	3310.5
202462h	05 13 50.4 −69 51 36	2144.7	400456h-1	05 32 48.0 −66 22 12	14178.8
202463h	05 13 50.4 −69 51 36	3303.7	400457h	05 32 48.0 −66 22 12	1620.0
202465h	05 13 50.4 −69 51 36	1170.8	400457h-1	05 32 48.0 −66 22 12	13340.1
202466h	05 13 50.4 −69 51 36	2041.8	400458h	05 32 48.0 −66 22 12	3042.9
202467h	05 13 50.4 −69 51 36	2150.0	400459h	05 32 48.0 −66 22 12	8516.0
202468h	05 13 50.4 −69 51 36	1997.0	400642h	05 38 16.8 −69 24 00	2445.9
202469h	05 13 50.4 −69 51 36	1788.8	400643h	05 50 00.0 −71 51 00	2171.6
202470h	05 13 50.4 −69 51 36	1688.8	400644h	05 36 16.8 −67 18 00	4580.0
202471h	05 50 00.0 −71 52 12	5743.4	400648h	05 27 48.0 −69 54 00	4873.0
202472h	04 39 50.4 −68 09 00	7080.2	400649h	05 38 52.8 −69 01 48	2736.5
202473h	05 27 48.0 −69 54 00	22523.4	400650h	05 39 43.2 −69 45 00	1209.0
202474h	05 50 00.0 −71 52 12	8549.5	400651h	05 53 12.0 −67 54 00	7803.0
202475h	04 39 50.4 −68 09 00	9449.0	400653h	04 58 52.8 −66 28 12	2152.5
202482h	05 28 45.6 −65 26 59	3424.0	400654h	04 54 12.0 −66 43 12	2590.0
202483h	05 28 45.6 −65 26 59	1901.4	400655h	05 44 07.2 −71 01 11	6004.0
202484h	05 28 45.6 −65 26 59	1888.0	400656h	05 48 31.2 −71 13 12	9390.6
202485h	05 28 45.6 −65 26 59	2356.8	400657h	05 20 31.2 −69 31 48	3830.1
202486h	05 28 45.6 −65 26 59	1360.8	400658h	05 32 00.0 −69 19 48	1600.5
202487h	05 28 45.6 −65 26 59	1868.8	400658h-1	05 32 00.0 −69 19 48	4288.0
202488h	05 28 45.6 −65 26 59	2995.0	400659h	05 47 52.8 −68 22 47	5296.0
202489h	05 28 45.6 −65 26 59	2893.0	400660h	05 32 16.8 −71 40 12	5307.6
202490h	05 28 45.6 −65 26 59	3770.7	400720h	05 13 50.4 −69 52 12	1283.5
202491h	05 28 45.6 −65 26 59	603.2	400721h	05 13 50.4 −69 52 12	4564.5
202492h	05 28 45.6 −65 26 59	1877.0	400722h	05 13 50.4 −69 52 12	1839.5
202493h	05 28 45.6 −65 26 59	1803.7	400723h	05 13 50.4 −69 52 12	2212.0
202722h	05 28 45.6 −65 26 59	1795.0	400724h	05 13 50.4 −69 52 12	3406.9
202723h	05 28 45.6 −65 26 59	2157.7	400725h	05 13 50.4 −69 52 12	936.5

Table A.2: Continued (HRI LMC).

1	2	3	4	1	2	3	4
ROR key	Pointing direction RA	Dec	Exposure time	ROR key	Pointing direction RA	Dec	Exposure time
	(J2000.0)		[s]		(J2000.0)		[s]
400728h	05 13 50.4	−69 52 12	4026.9	500471h	05 35 28.8	−69 16 11	18705.9
400729h	05 13 50.4	−69 52 12	3192.0	500504h	05 35 28.8	−69 16 11	23181.2
400730h	05 13 50.4	−69 52 12	3769.1	500505h	05 35 28.8	−69 16 11	22518.3
400731h	05 13 50.4	−69 52 12	3711.0	500506h	05 35 28.8	−69 16 11	29088.7
400732h	05 13 50.4	−69 52 12	4501.0	500507h	05 35 28.8	−69 16 11	24209.5
400733h	05 13 50.4	−69 52 12	3550.0	500537h	05 06 04.8	−65 41 24	14528.7
400734h	05 13 50.4	−69 52 12	2032.5	500538h	04 49 40.8	−69 21 36	8985.6
400735h	05 13 50.4	−69 52 12	2107.1	500546h	05 35 28.8	−69 16 11	22036.1
400779h	05 38 00.0	−69 07 47	25888.5	500547h	05 35 28.8	−69 16 11	10822.2
400779h-1	05 38 00.0	−69 07 47	80103.4	600028h	05 00 40.8	−70 04 48	933.5
400782h	05 31 57.6	−66 15 00	2837.1	600029h	05 02 50.4	−66 26 24	869.0
400783h	05 31 57.6	−66 15 00	4420.1	600030h	05 19 40.8	−71 36 36	1468.0
400784h	05 31 57.6	−66 15 00	11391.0	600031h	05 25 55.2	−70 11 24	1272.0
400785h	05 31 57.6	−66 15 00	7192.0	600032h	05 25 43.2	−69 13 12	779.0
400786h	05 31 57.6	−66 15 00	1808.5	600033h	05 27 38.4	−69 10 48	1714.5
400828h	05 26 00.0	−66 04 48	9529.9	600034h	05 30 40.8	−66 54 36	972.0
400829h	05 26 00.0	−66 04 48	4280.2	600035h	05 36 02.4	−67 34 48	821.0
400830h	05 26 00.0	−66 04 48	12472.5	600036h	05 22 33.6	−69 18 35	1163.0
400831h	05 26 00.0	−66 04 48	7721.6	600037h	05 01 21.6	−70 33 35	1708.0
400832h	05 26 00.0	−66 04 48	12390.5	600228h	05 38 43.2	−69 06 00	30162.1
400833h	05 26 00.0	−66 04 48	9578.1	600631h	05 47 12.0	−69 30 36	25239.1
400834h	05 26 00.0	−66 04 48	10978.8	600632h	05 43 26.4	−69 10 48	26680.8
400835h	05 26 00.0	−66 04 48	10890.8	600633h	05 39 38.4	−68 51 00	21502.1
400836h	05 26 00.0	−66 04 48	15234.3	600634h	05 35 52.8	−68 51 00	23619.2
400837h	05 26 00.0	−66 04 48	11428.7	600635h	05 32 04.8	−69 10 48	21231.4
400838h	05 26 00.0	−66 04 48	15675.3	600636h	05 47 12.0	−69 10 48	20630.7
400839h	05 26 00.0	−66 04 48	10794.3	600637h	05 43 26.4	−68 51 00	22485.7
500002h	05 25 02.4	−69 38 24	26399.6	600638h	05 39 38.4	−68 30 36	25728.8
500036h	05 37 52.8	−69 10 12	8799.5	600639h	05 35 52.8	−68 30 36	25394.7
500171h	05 19 33.6	−69 02 24	1014.0	600639h-1	05 35 52.8	−68 30 36	19819.0
500171h-1	05 19 33.6	−69 02 24	5267.9	600640h	05 32 04.8	−68 51 00	24070.1
500171h-2	05 19 33.6	−69 02 24	11265.3	600641h	05 28 19.2	−69 10 48	26503.2
500172h	05 25 28.8	−65 59 24	284.0	600642h	05 47 12.0	−68 51 00	21102.8
500172h-1	05 25 28.8	−65 59 24	8170.0	600643h	05 43 26.4	−68 30 36	21450.7
500172h-2	05 25 28.8	−65 59 24	13270.1	600644h	05 47 12.0	−68 30 36	18765.7
500172h-3	05 25 28.8	−65 59 24	7534.8	600645h	05 32 04.8	−68 30 36	18980.5
500173h	05 35 43.2	−66 02 24	863.0	600646h	05 28 19.2	−68 51 00	23931.4
500173h-1	05 35 43.2	−66 02 24	2747.6	600647h	05 28 19.2	−68 30 36	23824.2
500174h	05 09 00.0	−68 43 48	7127.0	600648h	05 43 26.4	−69 51 00	1506.5
500174h-1	05 09 00.0	−68 43 48	4272.8	600650h	05 35 52.8	−69 51 00	2117.5
500175h	05 05 43.2	−67 52 47	3130.6	600655h	05 32 04.8	−70 10 48	11789.1
500177h	05 09 31.2	−67 31 11	2828.6	600754h-1	06 08 52.8	−65 43 48	2073.5
500178h	04 53 36.0	−68 29 24	6008.1	600773h	05 43 26.4	−69 30 36	15945.5
500228h	05 05 43.2	−67 52 47	872.5	600774h	05 39 38.4	−69 30 36	22437.1
500228h-1	05 05 43.2	−67 52 47	10142.2	600775h	05 35 52.8	−69 30 36	15550.0
500229h	05 05 55.2	−68 01 48	5724.8	600775h-1	05 35 52.8	−69 30 36	4156.5
500229h-1	05 05 55.2	−68 01 48	10264.9	600776h	05 32 04.8	−69 30 36	4536.0
500230h	05 09 31.2	−67 31 11	30791.3	600776h-1	05 32 04.8	−69 30 36	2877.4
500230h-1	05 09 31.2	−67 31 11	29625.7	600776h-2	05 32 04.8	−69 30 36	16270.2
500231h	04 53 36.0	−68 29 24	13073.0	600777h	05 28 19.2	−69 30 36	19478.6
500231h-1	04 53 36.0	−68 29 24	15524.6	600777h-1	05 28 19.2	−69 30 36	24082.7
500232h	05 47 09.6	−69 41 59	17716.2	600778h	05 43 26.4	−69 51 00	23770.9
500232h-1	05 47 09.6	−69 41 59	2899.9	600778h-1	05 43 26.4	−69 51 00	10217.1
500232h-2	05 47 09.6	−69 41 59	17434.1	600779h	05 39 38.4	−69 51 00	26195.4
500233h	05 47 50.4	−70 24 36	7719.0	600780h	05 35 52.8	−69 51 00	3187.4
500233h-1	05 47 50.4	−70 24 36	1391.5	600780h-1	05 35 52.8	−69 51 00	5760.0
500233h-2	05 47 50.4	−70 24 36	25080.8	600780h-2	05 35 52.8	−69 51 00	14315.3
500235h	05 43 07.2	−68 58 48	3876.4	600781h	05 30 45.6	−71 02 24	25238.5
500235h-1	05 43 07.2	−68 58 48	28014.8	600781h-1	05 30 45.6	−71 02 24	24041.9
500329h	05 35 28.8	−69 16 11	1615.6	600782h	05 28 19.2	−69 51 00	12793.7
500330h	05 35 28.8	−69 16 11	73.8	600782h-1	05 28 19.2	−69 51 00	7542.2
500330h-1	05 35 28.8	−69 16 11	5365.9	600792h	05 21 12.0	−69 09 00	664.6
500331h	05 35 28.8	−69 16 11	2536.5	600913h	05 22 02.4	−67 55 12	2155.0
500332h	05 35 28.8	−69 16 11	2371.9	600913h-1	05 22 02.4	−67 55 12	109869.0
500333h	05 35 28.8	−69 16 11	2125.0	600914h	05 43 26.4	−70 10 48	17669.7
500388h	05 41 48.0	−64 18 00	11571.5	600915h	05 39 38.4	−70 10 48	19996.4
500406h	05 35 28.8	−69 16 11	7924.4	600916h	05 32 04.8	−70 10 48	14141.4
500407h	05 35 28.8	−69 16 11	11067.3	600917h	05 28 19.2	−70 10 48	26823.1
500408h	05 35 28.8	−69 16 11	12041.0	600918h	05 24 48.0	−69 58 12	23501.6
500408h-1	05 35 28.8	−69 16 11	8887.4	600919h	05 21 12.0	−69 28 48	18099.3
500409h	05 35 28.8	−69 16 11	8220.2	600920h	05 35 52.8	−70 10 48	4512.7
500468h	05 35 28.8	−69 16 11	18118.4	600920h-1	05 35 52.8	−70 10 48	11171.4
500469h	05 35 28.8	−69 16 11	8205.6	600921h	05 24 48.0	−70 18 00	1502.2
500470h	05 35 28.8	−69 16 11	28749.4	600921h-1	05 24 48.0	−70 18 00	20718.1

Table A.2: Continued (HRI LMC).

1	2	3	4
ROR key	Pointing direction RA	Dec	Exposure time
	(J2000.0)		[s]
600922h	05 24 48.0	−69 18 35	1182.2
600922h-1	05 24 48.0	−69 18 35	25347.7
600923h	05 24 48.0	−68 39 00	26268.8
600924h	05 47 12.0	−70 01 11	9021.3
600924h-1	05 47 12.0	−70 01 11	2973.7
600924h-2	05 47 12.0	−70 01 11	5450.2
600925h	05 24 48.0	−68 58 48	3048.2
600925h-1	05 24 48.0	−68 58 48	15422.5
600938h	05 26 48.0	−63 45 36	5005.0
600938h-1	05 26 48.0	−63 45 36	12593.2
600974h	05 31 16.8	−65 56 59	66777.0
600989h	06 08 52.8	−65 43 48	19128.2
601023h	05 32 04.8	−69 51 00	2828.8
601033h	05 14 00.0	−69 09 00	16420.1
601034h	05 10 24.0	−69 18 35	2288.0
601034h-1	05 10 24.0	−69 18 35	2275.0
601035h	05 10 24.0	−68 58 48	3265.0
601036h	05 06 48.0	−69 09 00	14254.5
601037h	05 06 48.0	−68 49 12	7070.0
601040h	05 17 36.0	−69 58 12	20002.4
702853h	05 52 24.0	−64 02 24	2314.6
900321h	04 56 33.6	−66 28 12	12325.0
900321h-1	04 56 33.6	−66 28 12	14788.0
900321h-2	04 56 33.6	−66 28 12	5118.5
999992h	05 28 43.2	−65 26 59	1618.2
999992h-1	05 28 43.2	−65 26 59	824.5

Table A.3: PSPC pointings used for the spectral analysis of the SMC.

1	2	3	4
ROR key	Pointing direction RA	Dec	Exposure time
	(J2000.0)		[s]
201094p	00 50 48.0	−74 46 48	64636.0
300369p	01 22 55.2	−75 21 00	5640.0
300369p-1	01 22 55.2	−75 21 00	213.0
400022p	01 17 04.8	−73 26 24	16634.0
400022p-1	01 17 04.8	−73 26 24	8976.0
400022p-2	01 17 04.8	−73 26 24	11855.0
400149p	00 37 19.2	−72 14 24	6281.0
400299p	00 37 19.2	−72 14 24	5121.0
400299p-1	00 37 19.2	−72 14 24	1677.0
400299p-2	00 37 19.2	−72 14 24	2311.0
400300p	00 58 33.6	−71 36 00	5214.0
400300p-1	00 58 33.6	−71 36 00	7199.0
400300p-2	00 58 33.6	−71 36 00	4111.0
500142p	01 04 02.4	−72 01 48	4902.0
500249p	00 46 40.8	−73 12 36	19240.0
500250p	01 04 38.4	−72 05 23	20845.0
500251p	00 51 19.2	−73 24 00	2089.0
600195p-0	00 58 12.0	−72 16 48	16644.0
600195p-1	00 58 12.0	−72 16 48	9443.0
600196p-0	00 50 45.6	−73 13 48	1303.0
600196p-1	00 50 45.6	−73 13 48	22223.0
600197p	01 13 24.0	−72 49 12	21494.0
600452p	01 05 55.2	−72 33 35	14207.0
600452p-1	01 05 55.2	−72 33 35	16663.0
600453p	00 54 28.8	−72 45 36	17593.0
600454p	00 42 55.2	−73 38 24	9727.0
600454p-1	00 42 55.2	−73 38 24	8299.0
600455p	01 01 16.8	−71 49 12	3561.0
600455p-1	01 01 16.8	−71 49 12	1721.0
600455p-2	01 01 16.8	−71 49 12	4595.0
600455p-3	01 01 16.8	−71 49 12	4129.0

Table A.4: PSPC pointings used for the spectral analysis of the LMC.

1	2	3	4
ROR key	Pointing direction RA	Dec	Exposure time
	(J2000.0)		[s]
100067p	05 25 00.0	−69 38 24	40.0
100406p	06 00 00.0	−66 33 35	19614.0
110061p	05 22 38.1	−68 40 26	117.0
110062p	05 22 14.4	−68 51 00	302.0
110063p	05 22 45.6	−69 00 36	168.0
110064p	05 22 52.8	−69 10 48	296.0
110065p	05 24 20.1	−69 24 43	144.0
110066p	05 24 57.6	−69 31 48	222.0
110068p	05 25 26.4	−69 45 00	191.0
110069p	05 26 07.2	−69 52 12	149.0
110070p	05 27 48.0	−70 05 16	218.0
110071p	05 28 26.6	−70 15 14	221.0
110072p	05 28 50.4	−70 25 12	157.0
110073p	05 30 10.5	−70 33 57	88.0
110074p	05 35 21.3	−69 54 28	200.0
110076p	05 32 25.6	−69 50 06	217.0
110077p	05 30 19.4	−69 50 16	296.0
110078p	05 27 45.6	−69 43 12	366.0
110079p	05 26 31.2	−69 40 12	99.0
110080p	05 23 27.3	−69 35 34	41.0
110081p	05 22 21.6	−69 33 00	244.0
110082p	05 19 57.6	−69 24 36	218.0
110083p	05 19 02.4	−69 13 48	141.0
110084p	05 17 13.2	−69 10 58	478.0
110085p	05 16 46.5	−68 57 25	38.0
110086p	05 15 45.6	−69 52 47	295.0
110088p	05 17 50.4	−69 53 24	245.0
110089p	05 19 38.4	−69 49 48	484.0
110090p	05 23 40.8	−69 38 24	297.0
110092p	05 26 21.6	−69 38 24	279.0
110093p	05 27 52.8	−69 36 36	220.0
110094p	05 30 16.8	−69 26 59	143.0
110095p	05 32 14.4	−69 25 48	182.0
110096p	05 33 43.2	−69 18 35	245.0
110097p	05 36 07.2	−69 24 36	192.0
110098p	05 30 57.6	−68 47 24	483.0
110099p	05 31 25.2	−69 05 09	40.0
110100p	05 29 02.4	−69 05 06	203.0
110101p	05 27 36.0	−69 12 25	247.0
110102p	05 26 57.6	−69 27 36	362.0
110103p	05 25 38.4	−69 32 24	280.0
110104p	05 24 02.4	−69 43 44	92.0
110105p	05 23 54.4	−69 52 58	74.0
110106p	05 22 59.7	−70 05 02	46.0
110107p	05 22 38.4	−70 17 13	300.0
110108p	05 21 12.0	−70 24 36	184.0
110109p	05 21 28.5	−70 35 42	443.0
110128p	05 24 38.4	−69 24 00	24.0
110131p	05 25 26.4	−69 45 00	725.0
110136p	05 22 19.2	−69 33 18	19.0
110168p	05 37 07.2	−69 01 48	1835.0
110169p	05 44 26.4	−70 22 12	1902.0
110170p	05 41 00.0	−69 57 36	2150.0
110171p	05 42 19.2	−69 50 23	2138.0
110172p	05 46 38.4	−70 11 24	822.0
110173p	05 31 14.4	−69 34 12	2042.0
110174p	05 37 04.8	−69 37 47	2886.0
110175p	05 36 52.8	−69 49 12	2177.0
110176p	05 32 12.0	−70 08 24	2168.0
110177p	05 48 09.6	−69 37 47	2061.0
110178p	05 42 16.8	−69 39 00	2261.0
110179p	05 40 43.2	−69 30 36	2229.0
110180p	05 42 08.6	−69 01 55	1779.0
110181p	05 34 12.0	−70 19 48	1882.0
110182p	05 39 00.0	−69 59 24	2032.0
120003p	05 28 45.6	−65 26 59	1008.0
120006p	05 39 38.4	−69 44 24	1336.0
120101p	05 39 38.4	−69 44 24	1814.0
130001p	05 38 55.2	−64 04 48	1576.0
130002p	05 38 55.2	−64 04 48	1727.0
140002p	05 39 04.8	−63 50 24	472.0
140004p	05 39 24.0	−64 19 48	1426.0
140005p	05 37 24.0	−64 49 12	1512.0

Table A.4: Continued (PSPC LMC).

1	2	3	4	1	2	3	4
ROR key	Pointing direction RA Dec (J2000.0)		Exposure time [s]	ROR key	Pointing direction RA Dec (J2000.0)		Exposure time [s]
140006p	05 32 16.8	−63 54 36	1597.0	400246p	05 32 50.4	−66 22 12	14507.0
140007p	05 36 40.8	−64 05 23	1396.0	400263p	05 20 28.8	−71 57 36	11277.0
140008p	05 41 12.0	−64 04 12	1334.0	400263p-1	05 20 28.8	−71 57 36	12794.0
140009p	05 45 36.0	−63 54 36	1543.0	400298p	05 27 48.0	−69 54 00	1058.0
140631p	05 39 48.0	−63 20 24	1556.0	400298p-1	05 27 48.0	−69 54 00	7502.0
140632p	05 39 04.8	−63 50 24	1474.0	400298p-2	05 27 48.0	−69 54 00	7802.0
140634p	05 39 24.0	−64 19 48	1782.0	500004p	05 25 02.4	−69 38 24	1092.0
140635p	05 37 24.0	−64 49 12	1540.0	500037p	05 09 00.0	−68 43 48	6826.0
140636p	05 32 16.8	−63 54 36	1713.0	500052p-0	05 13 55.2	−67 20 23	4364.0
140637p	05 36 40.8	−64 05 23	2000.0	500052p-1	05 13 55.2	−67 20 23	8018.0
140638p	05 41 12.0	−64 04 12	1500.0	500053p	05 20 48.0	−65 28 12	8317.0
140639p	05 45 36.0	−63 54 36	1628.0	500054p-0	05 25 52.8	−67 30 00	3420.0
141506p	05 25 00.0	−69 38 24	706.0	500054p-1	05 25 52.8	−67 30 00	4452.0
141507p	05 25 00.0	−69 38 24	1332.0	500060p	05 05 43.2	−67 52 47	3909.0
141508p	05 25 00.0	−69 38 24	1153.0	500061p	05 19 33.6	−69 02 24	3804.0
141519p	05 25 00.0	−69 38 24	1101.0	500062p	05 25 28.8	−65 59 24	5870.0
141542p	05 25 00.0	−69 38 24	1672.0	500063p	05 09 31.2	−67 31 11	9944.0
141543p	05 25 00.0	−69 38 24	1517.0	500093p	05 22 02.4	−67 55 12	8720.0
141800p	05 25 00.0	−69 38 24	1040.0	500100p-0	05 35 28.8	−69 16 11	16957.0
141805p	05 38 57.6	−64 04 48	1026.0	500100p-1	05 35 28.8	−69 16 11	9657.0
141806p	05 37 09.6	−64 22 47	1234.0	500131p	05 38 33.6	−69 06 36	15959.0
141807p	05 41 19.2	−63 51 00	1158.0	500138p	05 26 36.0	−68 50 23	2478.0
141851p	05 44 48.0	−65 43 48	4566.0	500138p-1	05 26 36.0	−68 50 23	14531.0
141937p	05 25 00.0	−69 38 24	1978.0	500138p-2	05 26 36.0	−68 50 23	14581.0
142011p	05 25 00.0	−69 38 24	2643.0	500140p	05 35 28.8	−69 16 11	2642.0
150044p	05 40 12.0	−69 19 48	5315.0	500140p-1	05 35 28.8	−69 16 11	11627.0
160042p	05 41 02.4	−63 59 24	493.0	500140p-2	05 35 28.8	−69 16 11	10758.0
160068p	05 35 09.6	−64 42 36	1553.0	500141p	05 25 02.4	−69 38 24	5254.0
160071p	05 41 36.0	−63 23 24	1559.0	500141p-1	05 25 02.4	−69 38 24	6212.0
160084p	05 25 00.0	−69 38 24	1728.0	500258p	04 55 43.2	−68 39 00	12715.0
170253p	05 28 45.6	−65 26 59	259.0	500258p-1	04 55 43.2	−68 39 00	1069.0
180027p	05 28 43.2	−65 26 59	2586.0	500258p-2	04 55 43.2	−68 39 00	136.0
180033p	05 13 52.8	−69 51 00	2549.0	500259p	05 47 09.6	−69 41 59	4021.0
180033p-1	05 13 52.8	−69 51 00	1077.0	500263p	04 55 21.6	−67 09 00	12688.0
200136p	05 28 45.6	−65 26 59	905.0	500303p	05 35 28.8	−69 16 11	9416.0
200138p	05 28 45.6	−65 26 59	1606.0	600098p	05 00 04.8	−66 25 48	10510.0
200692p	05 30 45.6	−65 54 36	44759.0	600099p	05 26 24.0	−66 13 48	8804.0
200873p	05 28 45.6	−65 26 59	1204.0	600100p-0	05 35 38.4	−69 16 11	5803.0
200874p-0	05 28 45.6	−65 26 59	1404.0	600100p-1	05 35 38.4	−69 16 11	16865.0
200874p-1	05 28 45.6	−65 26 59	753.0	600577p	05 00 04.8	−66 25 48	9014.0
200875p-0	05 28 45.6	−65 26 59	1199.0	600578p	05 26 24.0	−66 13 48	10527.0
200877p	05 28 45.6	−65 26 59	1625.0	900174p	06 10 00.0	−71 30 00	6048.0
201248p	05 31 02.4	−65 54 00	1261.0	900175p	06 00 00.0	−70 40 12	6039.0
201249p	05 27 50.4	−65 56 24	1406.0	900320p	04 56 33.6	−66 28 48	17589.0
201250p	05 31 48.0	−65 50 23	3430.0	900320p-1	04 56 33.6	−66 28 48	13731.0
201251p	05 31 45.6	−65 51 00	1004.0	900398p	05 13 55.2	−69 52 12	1479.0
201252p	05 28 45.6	−65 26 59	619.0	900398p-1	05 13 55.2	−69 52 12	3718.0
201253p	05 32 52.8	−65 43 12	2122.0	900398p-2	05 13 55.2	−69 52 12	7201.0
201254p	05 31 24.0	−65 52 12	1390.0	900530p	05 39 36.0	−66 51 36	424.0
201255p	05 28 09.6	−65 56 59	1012.0	900531p	05 40 02.4	−66 59 24	535.0
201256p	05 33 00.0	−65 41 59	1362.0	900532p	05 38 45.6	−66 58 12	1244.0
201257p	05 29 48.0	−65 56 24	1381.0	900533p	05 39 09.6	−67 06 36	1578.0
201258p	05 27 57.6	−65 56 59	1891.0	900534p	05 37 04.8	−66 49 12	290.0
201588p	05 28 43.2	−65 26 59	2120.0	900535p-1	05 36 38.4	−67 04 12	855.0
201589p	05 30 55.2	−65 54 00	1235.0	900536p	05 34 33.6	−66 46 48	1006.0
201590p	05 32 09.6	−65 48 35	986.0	900537p	05 34 07.2	−67 01 48	359.0
201591p	05 29 33.6	−65 56 59	1465.0	900538p	05 32 02.4	−66 44 24	1377.0
201592p	05 27 57.6	−65 56 59	3636.0	900539p	05 31 36.0	−66 59 24	1377.0
201593p	05 28 43.2	−65 26 59	468.0	900540p	05 29 31.2	−66 41 59	1004.0
201610p	05 50 00.0	−71 52 12	7835.0	900541p	05 29 04.8	−66 56 24	1002.0
300126p	05 23 50.4	−70 00 36	7649.0	900542p	05 28 40.8	−66 48 35	1000.0
300129p	05 08 00.0	−68 37 47	4030.0	900543p	05 29 57.6	−66 49 48	1093.0
300172p	05 32 28.8	−70 21 36	6272.0	900544p	05 30 48.0	−66 43 12	2120.0
300172p-1	05 32 28.8	−70 21 36	2993.0	900545p	05 30 21.6	−66 58 12	357.0
300172p-2	05 32 28.8	−70 21 36	3880.0	900546p	05 33 16.8	−66 45 36	437.0
300335p	05 36 12.0	−70 45 00	11303.0	900546p-1	05 33 16.8	−66 45 36	596.0
400012p	05 46 45.6	−71 09 00	19651.0	900547p	05 32 52.8	−67 00 36	628.0
400013p	05 46 45.6	−71 09 00	16083.0	900547p-1	05 32 52.8	−67 00 36	774.0
400052p	05 40 12.0	−69 19 48	8823.0	900548p	05 35 50.4	−66 48 00	1071.0
400078p	05 38 57.6	−64 04 48	7490.0	900549p	05 35 24.0	−67 03 00	1326.0
400079p	05 39 38.4	−69 44 24	7429.0	900550p	05 38 21.6	−66 50 23	285.0
400133p	05 40 12.0	−69 19 48	1803.0	900550p-1	05 38 21.6	−66 50 23	970.0
400148p	05 27 48.0	−69 54 00	6064.0	900551p	05 37 52.8	−67 05 23	989.0
400154p	05 22 26.4	−67 58 12	6522.0	900552p	05 34 57.6	−66 55 12	1070.0
400161p	04 40 00.0	−68 10 12	2626.0	900553p	05 31 12.0	−66 51 36	1215.0

Appendix B

ROSAT HRI Source Catalogues

All sources in the fields of the Magellanic Clouds detected by the ROSAT HRI are listed in Tables B.1 and B.2 with coordinates and error (90% confidence), existence likelihood, HRI count rates, extent, extent likelihood, PSPC count rates, and PSPC catalogue number with hardness ratios.

For the HRI count rate, the value with the smallest positional error, determined by the maximum likelihood algorithm, was selected. Therefore HRI count rates in the tables are representative for one single observation (or for merged data if several observations in the same direction were available). For extended SNRs the given count rate may correspond to a knot within the source. PSPC count rates are taken from the PSPC catalogues (HP99a, HFPK00) if available. For HRI sources without PSPC detection we derived 2σ upper limit from the pointing with the highest exposure time. If the source was too close to the rim or the window support structure of the PSPC detector, no count rate is given in Tables B.1 and B.2. Neither was it possible to determine PSPC count rates or upper limits for sources located in regions with diffuse emission.

Notes to Tables B.1 and B.2

Column No 6:	HRI count rate ist the output value from maximum likelihood algorithm with the smallest positional error.
Column No 9:	For sources which are listed in HP99a (LMC, Table B.1) and HFPK00 (SMC, Table B.2) PSPC count rates are taken from the PSPC catalogues.
	Otherwise PSPC count rate is the 95.4% (2σ) upper limit from maximum likelihood algorithm of the pointing with maximum exposure.
Column No 10:	Catalogue number from HP99a and HFPK00.
Column No 13:	Candidates from literature are marked with ? behind the source class, new classification are put in $< >$.
	Abbreviations for references in square brackets are given in the list below.
	fg: foreground.
	Be/X: X-ray binary system with Be star as companion.

Abbreviations for References used in the Source Catalogues

C97	Chu (1997)
CCH84	Cowley, Crampton, Hutchings, Helfand, Hamilton, Thorstensen, & Charles (1984)
CGC97	Crampton, Gussie, Cowley, & Schmidtke (1997)
CKS97	Chu, Kennicutt, Snowden, Smith, Williams, & Bomans (1997)
CML98	Corbet, Marshall, Lochner, Ozaki, & Ueda (1998)
CSM97	Cowley, Schmidtke, McGrath, Ponder, Fertig, Hutchings, & Crampton (1997)
FHP00	Filipović, Haberl, & Pietsch (2000)
FHW95	Filipović, Haynes, White, Jones, Klein, & Wielebinski (1995)
FHW98	Filipović, Haynes, White, & Jones (1998)
GGO93	Gochermann, Grothues, Östreicher, Berghoefer, & Schmidt-Kaler (1993)
HFPK00	Haberl, Filipović, Pietsch, & Kahabka (2000)
HP99a	Haberl & Pietsch (1999a)
HP99b	Haberl & Pietsch (1999b)
HS94	Hughes & Smith (1994)
ISC98	Israel, Stella, Campana, Covino, Ricci, & Oosterbroek (1998)
ISC99	Israel, Stella, Covino, Campana, & Mereghetti (1999)
KP96	Kahabka & Pietsch (1996)
KPFH99	Kahabka, Pietsch, Filipović, & Haberl (1999)
LPM99	Lamb, Prince, Macomb, & Finger (1999)
M94	Morgan (1994)
OG99	Orio & Greiner (1999)

SCB99	Stevens, Coe, & Buckley (1999)
SCC99	Schmidtke, Cowley, Crane, Taylor, McGrath, Hutchings, & Crampton (1999)
SCF94	Schmidtke, Cowley, Frattare, McGrath, Hutchings, & Crampton (1994)
TDZ97	Tinney, Da Costa, & Zinnecker (1997)
YK98a	Yokogawa & Koyama (1998a)
YK99b	Yokogawa & Koyama (1998b)
WHHW91	Wang, Hamilton, Helfand, & Wu (1991)

Table B.1: *HRI sources in the LMC region.*

1	2	3	4	5	6	7	8	9	10	11	12	13
No	RA	Dec	r_{90}	ML_{exi}	Count rate	r_{ext}	ML_{ext}	Count rate PSPC	No PSPC	HR1	HR2	Remarks
	(J2000.0)		['']		[cts s^{-1}]	['']		[cts s^{-1}]				
1	04 38 23.9	−68 08 24	5.7	10.7	4.42e−03±1.82e−03	0.0± 0.0	0.0	<1.74e−03				
2	04 38 31.3	−68 12 01	3.0	32.7	2.81e−03±6.18e−04	0.0± 0.0	0.0	<1.71e−03				
3	04 39 44.7	−67 58 39	10.0	10.1	3.81e−03±1.21e−03	5.2± 5.7	0.4					
4	04 39 49.6	−68 09 01	0.4	6228.5	1.66e−01±4.89e−03	2.1± 0.6	138.9	1.15e+00	628	−1.00±0.01		SSS RX J0439.8-6809
5	04 40 07.7	−68 14 54	4.5	12.1	2.37e−03±8.84e−04	1.8± 2.4	0.2	<1.12e−03				
6	04 42 04.6	−68 08 30	12.0	11.1	1.11e−02±3.92e−03	0.0± 0.0	0.0					
7	04 53 36.5	−68 27 45	3.6	50.7	1.22e−03±2.12e−04	1.7± 1.5	0.9					<foreground star>
8	04 53 38.0	−68 29 20	3.2	392.8	1.66e−02±7.28e−04	6.3± 1.4	687.9	5.00e−01	670	0.86±0.01	−0.36±0.01	SNR 0453-68.5
9	04 53 43.5	−68 24 23	4.4	15.3	5.99e−04±1.63e−04	1.2± 1.9	0.1					foreground star G0 HD 268717 [GGO93]
10	04 54 10.7	−66 43 17	7.3	55.1	8.01e−03±1.82e−03	1.5± 1.5	0.6	2.69e−02	411	1.00±0.24	0.29±0.07	AGN RX J0454.2-6643, z=0.2279 [CGC97]
11	04 54 27.8	−68 33 53	4.5	13.2	5.60e−04±1.62e−04	0.0± 0.0	0.0	<1.31e−03				<foreground star>
12	04 54 30.2	−68 18 01	9.1	12.7	1.30e−03±3.20e−04	0.0± 0.0	0.0					foreground star HD 31961
13	04 54 47.3	−66 25 44	8.3	96.2	8.53e−03±7.03e−04	13.6± 4.5	46.7	2.74e−02	329	0.84±0.04	−0.24±0.05	SNR LHA 120-N 11L
14	04 55 39.6	−66 30 01	7.7	16.8	1.11e−03±3.35e−04	0.0± 0.0	0.0	<2.56e−03				
15	04 58 25.1	−69 08 22	4.1	39.8	5.77e−03±1.31e−03	2.3± 2.0	1.2	1.22e−02	816	1.00±0.51	0.29±0.13	foreground star F7V [CSM97]
16	04 58 43.9	−68 50 50	4.1	317.5	4.48e−02±3.74e−03	0.0± 0.0	0.0	1.23e−01	742	−0.04±0.05	0.09±0.07	foreground star dMe HD 268840 [CSM97]
17	05 01 23.9	−70 33 33	2.9	58.0	1.12e−02±2.64e−03	1.1± 1.5	0.1					HMXB RX J0501.6-7034 (CAL 9)
18	05 02 09.3	−66 20 36	5.3	16.2	7.81e−03±3.22e−03	0.4± 2.7	0.0	2.74e−02	304	0.68±0.06	0.08±0.08	foreground star K0III [SCF94]
19	05 02 51.6	−66 26 25	1.2	2361.6	4.35e−01±2.26e−02	1.8± 0.8	23.0	3.23e−03	331	1.00±0.67	0.43±0.18	HMXB RX J0502.9-6626 (CAL E)
20	05 03 04.0	−66 33 44	2.2	188.8	5.35e−02±8.03e−03	0.0± 0.0	0.0	1.17e−01	380	0.83±0.03	0.17±0.03	AGN RX J0503.1-6634, z=0.064 [SCF94]
21	05 04 31.5	−67 54 26	9.0	16.2	1.72e−03±4.38e−04	0.0± 0.0	0.0	<6.12e−03				
22	05 05 02.3	−65 42 50	8.2	10.3	8.15e−04±2.83e−04	1.0± 2.2	0.0					
23	05 05 21.8	−68 45 40	7.1	447.5	2.40e−02±1.93e−03	1.2± 1.4	0.3	2.10e−02	715	−0.03±0.13	−1.00±0.66	
24	05 05 27.1	−67 43 14	7.1	425.8	1.48e−02±1.10e−03	0.0± 0.0	0.0	4.44e−02	568	0.74±0.06	0.18±0.09	fg eclips. bin. star ASAS J050526-6743.2
25	05 05 42.0	−67 52 29	7.0	2223.3	5.83e−02±1.40e−03	6.8± 1.1	4214.3	1.61e+00	592	0.81±0.01	−0.21±0.01	SNR DEM L 71
26	05 05 50.5	−67 50 09	14.5	10.5	2.27e−03±6.06e−04	7.3± 7.6	0.7					
27	05 05 55.5	−68 01 51	7.0	7040.7	2.16e−01±3.25e−03	12.2± 1.7	5968.8	9.57e−01	614	0.89±0.01	−0.19±0.02	SNR LHA 120-N 23
28	05 05 58.4	−68 10 30	8.4	22.8	1.85e−03±4.21e−04	2.7± 3.4	0.2	<9.57e−03				<foreground star>
29	05 06 16.7	−68 15 09	9.7	30.5	3.82e−03±6.81e−04	0.0± 0.0	0.0	1.15e−02	635	1.00±0.76	−0.05±0.19	<foreground star>
30	05 06 25.5	−65 37 10	7.8	14.7	9.71e−04±3.01e−04	1.2± 2.0	0.1					
31	05 06 33.9	−69 10 47	7.1	249.1	6.66e−03±7.07e−04	1.3± 1.0	1.9	3.26e−02	830	1.00±0.08	0.22±0.09	hard [HP99a]
32	05 06 55.0	−69 00 32	9.0	11.1	1.09e−03±3.50e−04	0.0± 0.0	0.0					
33	05 07 09.0	−68 45 00	8.0	12.0	1.33e−03±4.89e−04	0.6± 2.1	0.0	<8.85e−03				
34	05 07 11.7	−67 43 14	11.8	15.0	9.46e−03±3.57e−03	0.0± 0.0	0.0					
35	05 07 37.1	−68 47 52	8.4	15.3	1.73e−03±4.81e−04	0.0± 0.0	0.0	7.74e−03	724	1.00±0.16	−0.02±0.16	hard [HP99a]
36	05 07 59.5	−67 28 34	9.1	12.1	7.95e−04±2.28e−04	0.0± 0.0	0.0	<2.36e−03				
37	05 08 06.2	−69 13 43	8.3	16.6	1.48e−03±3.97e−04	0.8± 2.7	0.0	7.91e−03	844	1.00±1.22		<foreground star>
38	05 08 15.0	−69 18 27	8.4	54.6	4.86e−03±7.26e−04	0.0± 0.0	0.0	1.84e−02	865			
39	05 08 22.0	−67 34 12	8.2	12.6	4.02e−04±1.11e−04	0.0± 0.0	0.0					
40	05 08 33.3	−68 54 28	9.0	23.9	2.89e−03±6.39e−04	0.0± 0.0	0.0	7.69e−03	756	1.00±0.37	0.35±0.16	
41	05 08 53.3	−67 24 03	8.3	11.3	6.21e−04±1.86e−04	0.0± 0.0	0.0	<2.16e−03				
42	05 08 54.5	−67 37 33	7.8	15.5	4.38e−04±1.11e−04	0.0± 0.0	0.0	<3.51e−03				
43	05 08 58.6	−68 43 35	7.0	13431.0	5.04e−01±7.44e−03	5.4± 0.8	8288.7	1.92e+00	707	0.97±0.00	0.13±0.01	SNR LHA 120-N 103B
44	05 09 01.7	−67 21 16	8.9	13.8	9.82e−04±2.57e−04	0.0± 0.0	0.0	<1.65e−03				
45	05 09 11.1	−67 33 55	7.7	18.2	4.66e−04±1.11e−04	2.4± 2.1	0.8	<3.24e−03				Planetary Nebula [M94] 18
46	05 09 14.2	−67 20 15	10.1	10.6	5.92e−04±1.59e−04	0.0± 0.0	0.0	<1.77e−03				
47	05 09 31.3	−67 31 17	7.0	5476.1	6.33e−02±1.11e−03	6.5± 0.9	7396.2	5.02e−01	542	0.78±0.01	−0.27±0.01	SNR 0509.0-67.5
48	05 10 24.6	−67 29 04	8.0	12.2	3.72e−04±1.03e−04	2.1± 2.2	0.5	<2.06e−03				
49	05 10 28.7	−67 37 41	7.1	484.0	5.01e−03±3.10e−04	0.0± 0.0	0.0	6.07e−03	559	1.00±0.71	0.26±0.16	<XB> or <AGN>
50	05 10 48.7	−68 45 27	7.6	21.3	4.16e−03±1.28e−03	0.0± 0.0	0.4	3.27e−02	712	1.00±0.10	0.34±0.07	SNR? [WHHW91]

Table B.1: Continued (LMC).

1	2	3	4	5	6	7	8	9	10	11	12	13
No	RA	Dec	r_{90}	ML_{exi}	Count rate	r_{ext}	ML_{ext}	Count rate PSPC	No PSPC	HR1	HR2	Remarks
	(J2000.0)		['']		[cts s^{-1}]	['']		[cts s^{-1}]				
51	05 10 50.4	−69 05 13	9.3	10.0	2.82e−03±1.08e−03	3.0± 3.2	0.3	<6.39e−03				
52	05 10 56.1	−69 22 14	7.9	16.5	3.49e−03±1.31e−03	0.0± 0.0	0.0	<8.88e−03				
53	05 11 51.1	−69 10 16	7.3	25.4	2.72e−03±5.46e−04	2.3± 3.8	0.1	<8.57e−03				
54	05 12 21.3	−69 08 29	7.5	10.7	1.11e−03±3.46e−04	0.0± 0.0	0.0	<3.21e−03				<foreground star>
55	05 12 29.0	−69 42 48	4.2	35.7	2.85e−03±4.05e−04	0.0± 0.0	0.0	4.12e−03	992	1.00±0.53	1.00±0.49	
56	05 12 30.2	−69 55 58	3.1	23.5	1.32e−03±2.44e−04	0.0± 0.0	0.0	<2.48e−03				
57	05 12 45.4	−69 39 01	14.0	11.0	5.03e−03±1.50e−03	0.0± 0.0	0.0	6.24e−03	976	1.00±0.27	0.15±0.18	
58	05 12 47.4	−69 49 23	6.0	11.7	4.67e−03±1.59e−03	3.8± 3.3	1.7					
59	05 12 48.9	−69 53 10	2.1	53.4	1.74e−03±2.36e−04	1.5± 1.5	0.7	<5.51e−03				
60	05 12 52.0	−70 05 18	14.4	15.1	1.00e−02±2.96e−03	6.5± 8.6	0.2	<2.40e−03				
61	05 12 57.3	−69 56 42	8.6	10.3	3.18e−03±1.27e−03	0.0± 0.0	0.0					
62	05 13 29.8	−69 59 30	10.8	12.6	5.57e−03±1.85e−03	5.1± 4.7	1.2	<2.22e−03				
63	05 13 39.4	−69 32 00	6.5	33.1	6.14e−03±1.40e−03	0.0± 0.0	0.0	2.42e−02	943			foreground star K1V [CSM97]
64	05 13 40.2	−69 44 23	8.4	12.2	4.92e−03±1.84e−03	0.0± 0.0	0.0	<8.99e−04				
65	05 13 50.7	−69 51 46	1.2	16279.1	3.09e−01±2.41e−03	2.8± 0.5	1161.2	1.94e+00	1030	−0.86±0.00	−0.98±0.01	SSS RX J0513.9-6951
66	05 13 59.1	−69 46 04	8.6	11.2	3.55e−03±1.82e−03	0.0± 0.0	0.0	<6.36e−04				
67	05 14 05.7	−69 53 35	4.5	15.2	3.25e−03±1.31e−03	0.0± 0.0	0.0	<2.26e−03				
68	05 14 11.9	−69 44 47	3.8	14.4	9.16e−04±2.11e−04	0.2± 2.9	0.0	<4.82e−03				
69	05 14 20.7	−69 55 53	2.9	19.7	8.93e−04±1.87e−04	1.6± 1.9	0.2	<2.31e−03				
70	05 14 25.9	−70 00 55	10.2	10.1	5.47e−03±2.13e−03	5.1± 5.2	0.5	<1.59e−03				
71	05 14 26.8	−69 57 05	1.7	160.7	3.52e−03±3.08e−04	1.7± 1.4	1.3	<4.65e−03				foreground star HD 269255
72	05 14 38.4	−69 48 56	1.4	385.7	5.79e−03±3.67e−04	1.6± 1.0	4.3	<6.21e−03				
73	05 14 43.0	−69 47 36	4.6	12.3	3.22e−03±1.26e−03	0.0± 0.0	0.0	<2.32e−03				
74	05 15 04.3	−71 43 44	11.2	41.0	4.53e−03±9.72e−04	0.0± 0.0	0.0					
75	05 15 09.7	−69 50 46	3.5	19.4	1.07e−03±2.19e−04	1.9± 2.5	0.1	<5.60e−04				
76	05 15 28.8	−69 49 51	9.0	10.0	5.09e−03±2.24e−03	0.0± 0.0	0.0	<1.30e−03				
77	05 15 42.1	−69 50 20	7.7	10.2	3.07e−03±1.08e−03	2.6± 4.0	0.1	<2.67e−03				
78	05 16 00.1	−69 16 09	7.3	30.3	7.25e−03±1.58e−03	0.0± 0.0	0.0	<5.86e−03				
79	05 16 07.2	−68 15 35	2.4	691.7	7.17e−02±4.31e−03	0.0± 0.0	0.0	1.10e−01	636	−0.03±0.06	−0.09±0.09	foreground star G1V [SCF94]
80	05 16 10.8	−69 54 38	11.2	10.6	7.64e−03±3.02e−03	0.0± 0.0	0.0	<2.70e−03				
81	05 16 11.8	−69 50 05	11.5	12.5	8.81e−03±2.73e−03	0.0± 0.0	0.0	<6.05e−03				
82	05 16 26.2	−69 48 19	2.7	238.1	1.23e−02±6.89e−04	0.0± 0.0	0.0	7.41e−03	1019	1.00±0.28	0.36±0.17	
83	05 16 37.0	−70 05 12	4.6	21.1	1.48e−03±3.44e−04	2.5± 3.0	0.2	<4.49e−02				
84	05 16 40.2	−71 45 58	11.5	21.4	3.28e−03±8.41e−04	4.2± 2.6	3.1	1.20e−02	1308	1.00±0.26	0.42±0.13	RX J0516.7-7146; B0517-7151 [FHW95]
85	05 17 14.8	−71 38 26	12.1	11.1	1.74e−03±6.51e−04	0.0± 0.0	0.0					
86	05 17 16.9	−70 44 01	2.2	186.4	1.03e−02±1.24e−03	2.5± 1.4	8.2					AGN RX J0517.3-7044, z=0.169 [CSM97]
87	05 17 25.8	−71 31 58	15.1	17.3	7.26e−03±1.82e−03	4.3± 6.2	0.1	1.90e−02	1284	1.00±0.79	−0.09±0.10	foreground star K2III& HD 35324
88	05 17 30.4	−71 51 42	11.6	11.0	1.49e−03±5.70e−04	0.0± 0.0	0.0	4.66e−03	1318	1.00±0.86	1.00±2.32	
89	05 17 46.9	−68 54 57	9.8	14.1	1.80e−03±4.61e−04	0.0± 0.0	0.0	8.40e−03	760	1.00±0.33	−0.12±0.23	
90	05 17 47.8	−71 44 05	11.4	15.9	1.96e−03±6.46e−04	1.9± 2.3	0.3	8.54e−03	1305	1.00±1.34	0.45±0.15	<foreground star>
91	05 18 32.3	−68 13 33	1.7	201.4	1.47e−02±1.85e−03	1.7± 1.2	2.8	3.67e−02	634	−1.00±1.37		fg star K3V HD 269320 [GGO93], [SCF94]
92	05 18 40.7	−69 32 06	10.5	10.0	2.80e−03±1.03e−03	0.0± 0.0	0.0	<1.03e−02				
93	05 18 52.2	−68 15 54	3.0	16.0	2.04e−03±7.09e−04	0.0± 0.0	0.0	<6.65e−02				RX J0518.9-6816
94	05 18 55.3	−69 56 01	2.4	69.3	2.56e−03±3.99e−04	0.0± 0.0	0.0	<8.78e−03				
95	05 19 19.9	−68 54 32	8.0	17.8	1.61e−03±4.44e−04	0.0± 0.0	0.0	<3.14e−02				Nova LMC 1992
96	05 19 33.4	−69 17 49	9.3	46.1	4.95e−03±7.26e−04	0.0± 0.0	0.0	1.38e−02	863	−0.16±0.18	−1.00±1.81	
97	05 19 34.3	−69 02 01	7.0	8929.9	2.58e−01±3.80e−03	6.2± 0.8	9883.6	1.46e+00	789	0.95±0.00	−0.02±0.01	SNR 0519-69.0
98	05 19 48.9	−69 26 09	7.9	45.9	8.54e−03±8.38e−04	10.4± 3.5	74.6	1.13e−01	915	0.36±0.08	−0.14±0.10	SNR 0520-69.4
99	05 19 56.2	−71 29 07	6.3	25.8	8.53e−03±2.61e−03	0.4± 2.7	0.0	1.34e−02	1280	0.30±0.13	0.35±0.10	foreground star K2III [SCF94]
100	05 20 19.5	−69 11 37	9.5	12.8	1.92e−03±5.48e−04	0.0± 0.0	0.0	<9.70e−03				

1	2	3	4	5	6	7	8	9	10	11	12	13
No	RA	Dec	r_{90}	ML_{exi}	Count rate	r_{ext}	ML_{ext}	Count rate PSPC	No PSPC	HR1	HR2	Remarks
	(J2000.0)		['']		[cts s^{-1}]	['']		[cts s^{-1}]				
101	05 20 54.9	–67 44 59	7.0	14.7	2.95e–03±6.37e–04	0.0± 0.0	0.0	<2.21e–03				
102	05 21 39.2	–68 53 43	13.8	10.9	2.86e–03±7.89e–04	2.9± 7.7	0.0	<3.85e–03				
103	05 22 08.2	–68 04 28	2.4	124.0	5.61e–03±5.50e–04	0.0± 0.0	0.0	<4.40e–03				foreground star HD 35862
104	05 22 19.6	–67 51 31	2.7	30.5	1.72e–03±3.14e–04	1.4± 1.5	0.4	<1.69e–03				foreground star HD 269422
105	05 22 23.5	–67 50 45	8.5	12.4	3.03e–03±1.13e–03	0.0± 0.0	0.0	<7.64e–04				
106	05 22 24.6	–69 30 33	9.8	12.0	1.32e–03±3.62e–04	5.0± 3.8	1.3	<1.80e–03				
107	05 22 29.2	–68 00 28	5.3	14.0	2.83e–03±5.44e–04	6.4± 2.8	5.9					knot in N44
108	05 22 32.8	–69 42 37	12.3	10.9	1.63e–02±6.56e–03	0.0± 0.0	0.0	<1.97e–03				
109	05 22 36.0	–67 56 05	7.9	10.6	1.04e–03±3.93e–04	0.8± 1.8	0.0					knot in N44
110	05 22 37.8	–67 47 44	4.2	13.9	1.55e–03±3.74e–04	0.0± 0.0	0.0	<4.89e–03				
111	05 22 42.7	–69 15 55	11.2	13.9	4.60e–03±1.36e–03	3.3± 5.2	0.1					
112	05 22 46.2	–69 28 35	7.3	78.6	3.33e–03±4.82e–04	0.0± 0.0	0.0	8.87e–03	931	1.00±0.19	0.32±0.16	hard [HP99a]
113	05 23 00.1	–70 18 32	3.6	37.2	2.00e–03±3.71e–04	0.0± 0.0	0.0	<2.17e–02				
114	05 23 02.4	–67 53 00	4.9	17.4	3.13e–03±5.53e–04	6.2± 2.8	6.5	1.66e–02	594	1.00±0.04	0.17±0.06	SNR 0523-67.9
115	05 23 04.5	–69 43 26	7.8	14.4	5.69e–03±1.81e–03	0.0± 0.0	0.0	<1.32e–03				
116	05 23 12.9	–70 15 32	4.1	19.3	1.27e–03±3.08e–04	0.0± 0.0	0.0	1.07e–02	1109	1.00±0.16	0.15±0.14	hard [HP99a]
117	05 23 13.3	–69 33 43	3.7	39.8	9.61e–04±1.36e–04	0.9± 3.2	0.0	7.13e–03	954	1.00±0.50		foreground star GSC 09166-00446
118	05 23 21.9	–67 53 35	5.0	25.1	3.77e–03±5.94e–04	6.4± 3.4	6.5					knot in N44
119	05 23 32.0	–69 35 28	6.9	11.4	7.74e–03±2.70e–04	3.2± 3.6	0.4	<4.46e–03				
120	05 23 38.1	–69 39 07	5.9	11.5	3.49e–03±1.35e–03	2.1± 3.2	0.1	<1.65e–03				
121	05 23 53.9	–67 57 35	6.2	12.9	2.00e–03±4.69e–04	0.0± 0.0	0.0	<1.55e–03				
122	05 23 55.1	–69 33 12	5.3	11.0	3.85e–03±1.68e–03	0.0± 0.0	0.0	<1.07e–02				
123	05 24 01.4	–71 09 33	7.1	455.0	5.64e–02±5.15e–03	3.0± 1.3	36.1	2.77e–01	1242	–0.17±0.12	0.24±0.19	foreground star M5e 1E 0524.7-7112
124	05 24 02.5	–70 11 09	1.6	800.1	1.57e–02±8.88e–04	1.6± 1.2	2.0	1.14e–01	1094	0.91±0.02	0.27±0.04	AGN RX J0524.0-7011, z=0.151 [SCF94]
125	05 24 11.1	–70 22 36	3.4	26.4	1.38e–03±2.94e–04	2.7± 2.3	1.8	<6.75e–03				
126	05 24 12.8	–66 00 33	13.1	10.9	2.69e–03±7.55e–04	4.4± 6.2	0.1	<3.79e–03				
127	05 24 19.4	–66 05 20	7.6	42.9	7.75e–04±1.09e–04	0.0± 0.0	0.0	<2.16e–03				
128	05 24 26.3	–69 36 13	1.6	76.9	9.41e–04±1.07e–04	2.4± 1.5	4.4					
129	05 24 29.9	–66 11 35	8.0	44.3	9.87e–04±1.31e–04	0.0± 0.0	0.0	3.52e–03	264	1.00±0.48	0.28±0.21	
130	05 24 47.2	–69 32 06	4.9	12.3	4.06e–03±1.45e–03	2.3± 2.6	0.5	<1.34e–03				
131	05 24 48.3	–66 03 47	8.2	17.3	1.43e–03±4.37e–04	0.0± 0.0	0.0	<2.88e–03				
132	05 25 01.9	–69 38 51	0.5	7939.5	2.66e–01±2.44e–03	6.4± 0.9	9439.5	7.37e+00	977	0.94±0.00	–0.04±0.01	SNR LHA 120-N 132D
133	05 25 02.3	–67 53 28	8.7	27.0	4.48e–03±9.35e–04	0.0± 0.0	0.0	1.81e–02	595	0.38±0.10	0.08±0.12	foreground star K2IV, RS CVn? [CSM97]
134	05 25 06.6	–70 16 42	2.1	81.9	2.74e–03±3.83e–04	2.6± 1.5	8.9	<9.08e–03				
135	05 25 22.5	–69 49 16	4.9	29.6	2.12e–03±3.86e–04	0.0± 0.0	0.0	3.99e–03	1025	1.00±0.64	1.00±2.40	<foreground star>
136	05 25 22.9	–65 59 17	7.0	2178.7	4.85e–02±5.97e–04	10.0± 1.4	5218.8	4.56e–01	219	0.94±0.01	–0.14±0.02	SNR LHA 120-N 49B
137	05 25 28.1	–69 14 24	7.2	73.0	1.94e–03±3.00e–04	0.0± 0.0	0.0	<1.09e–02				
138	05 25 28.7	–63 40 41	7.6	12.3	1.26e–03±3.61e–04	0.9± 4.0	0.0					
139	05 25 38.1	–69 37 20	3.5	11.0	2.34e–03±9.50e–04	0.0± 0.0	0.0					
140	05 25 38.4	–69 35 43	0.6	1847.2	7.64e–03±2.55e–04	2.5± 0.8	70.3	3.29e–02	964	0.30±0.08	–0.01±0.10	foreground star F7V HD 36436 [CSM97]
141	05 25 42.1	–63 41 54	3.3	75.3	2.92e–03±4.50e–04	0.0± 0.0	0.0					
142	05 25 48.9	–69 21 07	8.7	10.2	8.03e–03±3.59e–04	2.9± 4.6	0.1	<3.67e–02				
143	05 25 52.7	–69 44 56	2.1	56.0	8.42e–04±1.09e–04	0.8± 1.8	0.0	4.42e–03	1002	1.00±0.55	1.00±1.20	
144	05 25 55.4	–68 51 56	8.5	13.6	1.20e–03±3.32e–04	0.0± 0.0	0.0	<1.86e–03				
145	05 25 58.1	–70 11 07	2.1	259.6	7.57e–03±6.45e–04	0.0± 0.0	0.0	4.14e–02	1093	0.68±0.06	0.23±0.07	foreground star K2IV-V, RS CVn [SCF94]
146	05 26 00.1	–66 05 19	7.0	5983.6	7.83e–02±5.44e–04	6.8± 0.9	8459.6	2.06e+00	241	0.95±0.00	–0.02±0.01	SNR LHA 120-N 49
147	05 26 12.2	–69 33 59	5.0	13.1	4.59e–03±1.70e–03	0.0± 0.0	0.0	<3.59e–03				
148	05 26 15.2	–63 46 59	3.0	51.8	1.66e–03±3.31e–04	0.0± 0.0	0.0					
149	05 26 17.8	–66 02 32	7.8	11.8	7.99e–04±2.80e–04	0.0± 0.0	0.0	<6.15e–03				
150	05 26 20.1	–69 37 04	8.8	11.3	7.71e–03±3.08e–03	1.1± 2.6	0.0	<2.41e–03				

Table B.1: Continued (LMC).

1	2	3	4	5	6	7	8	9	10	11	12	13
No	RA	Dec	r_{90}	ML_{exi}	Count rate	r_{ext}	ML_{ext}	Count rate PSPC	No PSPC	HR1	HR2	Remarks
	(J2000.0)		['']		[cts s^{-1}]	['']		[cts s^{-1}]				
151	05 26 31.5	−66 01 04	8.1	11.1	5.62e−04±1.79e−04	0.0± 0.0	0.0	<2.46e−03				
152	05 26 32.1	−69 44 48	8.6	10.5	2.12e−03±7.00e−04	0.0± 0.0	0.0	<1.28e−03				
153	05 26 32.9	−69 54 12	4.7	18.1	6.00e−04±1.46e−04	0.0± 0.0	0.0	2.46e−03	1041	1.00±0.94	1.00±0.99	
154	05 26 34.9	−63 41 34	3.5	21.5	8.72e−04±2.44e−04	0.0± 0.0	0.0	<1.70e−02				foreground star HD 36355
155	05 26 50.5	−70 01 24	1.6	849.8	1.71e−02±9.32e−04	1.8± 1.5	1.0					Nova LMC 1995 [OG99]
156	05 26 59.8	−68 37 22	3.8	45.0	2.37e−03±3.87e−04	0.0± 0.0	0.0	1.13e−02	693	−0.46±0.09	−0.47±0.16	foreground star F0IV-V HD 36584
157	05 27 07.5	−70 04 57	5.7	14.3	1.26e−03±3.05e−04	3.7± 3.3	1.0	3.61e−03	1078	1.00±0.58	1.00±1.82	
158	05 27 14.8	−63 49 07	2.9	92.5	2.61e−03±4.09e−04	0.3± 1.3	0.0	<1.89e−02				
159	05 27 16.6	−69 39 31	4.3	26.0	1.27e−03±2.39e−04	0.0± 0.0	0.0	5.27e−03	980	1.00±0.89	1.00±3.10	
160	05 27 18.2	−65 19 10	5.0	22.6	2.40e−03±4.22e−04	0.0± 0.0	0.0	7.42e−03	108	1.00±2.67	−1.00±0.50	
161	05 27 19.0	−65 52 46	10.8	15.4	1.64e−03±3.76e−04	0.0± 0.0	0.0	9.57e−03	186	1.00±0.36	0.29±0.19	
162	05 27 21.0	−68 30 14	1.9	134.5	3.15e−03±3.92e−04	0.8± 1.3	0.1	5.19e−02	672		−1.00±0.58	
163	05 27 21.1	−63 52 29	3.5	53.2	2.26e−03±3.99e−04	0.0± 0.0	0.0					
164	05 27 25.4	−65 29 42	6.3	10.9	3.67e−03±1.46e−03	0.0± 0.0	0.0	<5.11e−03				
165	05 27 45.6	−70 18 08	2.4	68.7	2.31e−03±3.39e−04	1.0± 1.6	0.1	<2.43e−02				
166	05 27 45.6	−69 11 51	7.9	23.4	1.74e−03±3.23e−04	4.7± 2.5	8.7	4.37e−02	836	1.00±0.74	1.00±6.84	SNR 0528-69.2
167	05 27 49.4	−69 54 05	4.3	21.1	5.08e−04±1.24e−04	0.0± 0.0	0.0	1.11e−01	1039	−1.00±0.01		SSS RX J0527.8-6954
168	05 28 04.8	−65 20 11	2.3	47.3	2.07e−03±2.92e−04	0.0± 0.0	0.0	<2.00e−03				
169	05 28 06.3	−63 37 50	7.9	10.8	1.44e−03±4.55e−04	0.0± 0.0	0.0					
170	05 28 11.2	−65 20 16	2.2	43.9	1.90e−03±2.79e−04	0.0± 0.0	0.0	<3.11e−03				
171	05 28 11.7	−71 05 38	8.1	19.0	1.39e−03±2.79e−04	0.0± 0.0	0.0					foreground star F3/F5V HD 36877
172	05 28 12.7	−63 36 27	7.0	29.9	3.08e−03±5.75e−04	0.0± 0.0	0.0	3.21e−02	17			
173	05 28 17.8	−69 21 34	10.3	10.8	1.31e−03±3.50e−04	2.7± 4.1	0.1	<4.45e−02				
174	05 28 18.3	−65 33 40	2.1	36.7	1.55e−03±2.49e−04	0.0± 0.0	0.0	<1.73e−03				
175	05 28 25.4	−67 43 30	12.9	16.6	4.87e−03±1.12e−03	7.9± 6.6	0.9	<4.97e−03				
176	05 28 26.8	−70 54 02	8.3	24.1	2.81e−03±5.26e−04	0.0± 0.0	0.0	<4.58e−03				foreground star G0V HD 36890
177	05 28 29.6	−63 50 15	8.7	12.4	1.67e−03±4.79e−04	0.0± 0.0	0.0	<7.31e−03				
178	05 28 32.5	−68 36 13	1.5	734.8	1.18e−02±7.34e−04	2.2± 1.1	12.0	5.75e−02	687	1.00±0.19	0.01±0.05	foreground star G1V [CSM97]
179	05 28 39.0	−69 21 03	5.1	16.1	1.33e−03±3.23e−04	0.0± 0.0	0.0	<6.24e−02				
180	05 28 44.7	−65 26 56	0.2	31209.6	2.36e+00±2.90e−02	2.0± 0.4	421.5	8.07e+00	122	−0.00±0.01	0.07±0.01	fg star K1III& HD 36705 (AB Dor)
181	05 28 47.3	−65 39 57	2.7	150.0	7.81e−03±6.05e−04	0.0± 0.0	0.0	1.58e−02	147	1.00±0.15	0.27±0.18	hard [HP99a]
182	05 29 02.7	−69 40 09	6.6	11.1	7.64e−04±2.08e−04	0.0± 0.0	0.0	<2.16e−03				
183	05 29 04.8	−65 14 33	5.9	25.6	2.89e−03±4.75e−04	0.0± 0.0	0.0	<1.58e−03				
184	05 29 08.3	−68 37 36	4.0	10.3	1.73e−03±7.85e−04	0.0± 0.0	0.0	<1.84e−02				
185	05 29 09.6	−68 42 56	3.1	47.8	2.11e−03±3.54e−04	0.0± 0.0	0.0	8.58e−03	705	1.00±0.55	1.00±0.77	
186	05 29 16.0	−71 08 43	4.2	32.8	1.15e−03±2.05e−04	0.0± 0.0	0.0					
187	05 29 22.6	−65 20 33	2.7	29.9	1.52e−03±2.63e−04	0.0± 0.0	0.0	<1.72e−03				
188	05 29 23.8	−65 32 37	2.3	36.5	1.53e−03±2.49e−04	0.0± 0.0	0.0	<4.81e−03				
189	05 29 24.0	−68 49 12	2.3	54.3	1.89e−03±3.18e−04	2.1± 1.9	1.2	7.17e−03	728	0.23±0.14	0.02±0.17	foreground star? [HP99a]
190	05 29 24.8	−65 57 28	6.5	17.2	8.72e−04±1.86e−04	0.0± 0.0	0.0	4.37e−03	210	1.00±0.59	0.01±0.10	
191	05 29 26.0	−69 52 05	3.5	13.9	7.24e−04±2.24e−04	0.0± 0.0	0.0	3.53e−03	1032	1.00±0.40	1.00±0.57	
192	05 29 26.6	−69 46 58	3.3	34.3	2.85e−03±6.69e−04	0.0± 0.0	0.0	3.48e−03	1011	1.00±0.70	1.00±0.86	
193	05 29 27.0	−68 52 05	0.6	2800.3	3.33e−02±1.21e−03	1.9± 0.8	26.9	1.44e−01	749	0.06±0.02	0.04±0.03	foreground star G5 HD 269620 [CSM97]
194	05 29 28.2	−65 31 40	5.7	12.3	7.89e−03±3.84e−03	0.0± 0.0	0.0	<1.87e−03				
195	05 29 31.8	−69 12 18	8.4	11.1	7.33e−04±2.20e−04	1.9± 2.9	0.1	<1.32e−02				
196	05 29 32.0	−65 35 27	8.5	10.4	6.41e−03±2.10e−03	5.6± 4.5	2.1	<1.74e−03				
197	05 29 39.2	−66 08 06	20.1	12.7	1.96e−03±4.05e−04	17.1±10.8	2.2	<1.63e−03				<SNR>
198	05 29 41.0	−65 53 23	7.2	10.4	6.01e−04±1.60e−04	0.0± 0.0	0.0	2.11e−03	189	1.00±0.80	−0.22±0.15	
199	05 29 41.9	−65 27 41	0.9	244.0	4.60e−03±3.62e−04	0.2± 1.2	0.0	1.01e−02	124	−1.00±0.20		
200	05 29 44.0	−69 35 42	2.0	109.1	2.55e−03±2.87e−04	0.0± 0.0	0.0	<5.69e−03				

1	2	3	4	5	6	7	8	9	10	11	12	13
No	RA	Dec	r_{90}	ML_{exi}	Count rate	r_{ext}	ML_{ext}	Count rate PSPC	No PSPC	HR1	HR2	Remarks
	(J2000.0)		['']		[cts s^{-1}]	['']		[cts s^{-1}]				
201	05 29 45.0	−65 16 03	6.6	18.9	2.47e−03±4.65e−04	0.0± 0.0	0.0	<2.15e−03				
202	05 29 48.3	−65 56 46	2.0	119.2	1.94e−03±2.05e−04	0.0± 0.0	0.0	2.43e−01	204	0.84±0.04	0.49±0.06	HMXB RXJ0529.8-6556 [HP99b]
203	05 30 04.7	−65 20 08	5.4	17.3	1.81e−03±3.65e−04	0.0± 0.0	0.0	<3.64e−03				
204	05 30 09.3	−66 06 56	6.7	10.2	6.24e−04±1.68e−04	0.0± 0.0	0.0	2.19e−03	251	1.00±0.83	0.32±0.16	
205	05 30 11.9	−65 51 27	1.9	133.0	2.09e−03±2.10e−04	0.0± 0.0	0.0	6.00e−03	183	1.00±0.21	0.62±0.07	hard [HP99a]
206	05 30 15.3	−68 43 17	5.6	29.9	2.68e−03±4.72e−04	0.0± 0.0	0.0	<3.13e−03				2E 0530.5-6845
207	05 30 21.9	−66 15 38	4.0	32.2	1.58e−03±2.99e−04	0.0± 0.0	0.0	4.09e−03	281	1.00±0.59	0.31±0.18	
208	05 30 22.4	−65 29 32	9.1	11.0	3.36e−03±9.94e−04	3.1± 5.2	0.0	<1.61e−03				
209	05 30 25.9	−69 08 08	5.3	24.5	1.68e−03±3.61e−04	0.0± 0.0	0.0	<2.65e−02				
210	05 30 40.2	−66 05 37	7.7	12.3	1.39e−03±3.54e−04	0.0± 0.0	0.0	<3.65e−03				
211	05 30 40.3	−71 00 32	4.1	16.3	5.73e−04±1.38e−04	2.7± 2.3	1.8					
212	05 30 49.6	−67 05 55	10.0	20.9	1.18e−02±3.76e−03	0.0± 0.0	0.0	4.77e−02	478	−0.25±0.18	0.34±0.28	foreground star dMe [SCF94]
213	05 31 00.3	−66 12 37	2.7	28.4	9.63e−04±2.16e−04	0.0± 0.0	0.0	6.00e−03	267	1.00±0.44	0.30±0.13	
214	05 31 02.0	−66 04 30	3.1	17.9	4.58e−04±1.09e−04	0.0± 0.0	0.0	1.07e−03	237	1.00±2.58		
215	05 31 02.9	−66 06 55	2.5	76.0	1.57e−03±1.94e−04	0.0± 0.0	0.0					
216	05 31 03.1	−71 06 10	3.5	25.4	9.92e−04±2.34e−04	1.4± 1.8	0.2					foreground star GSC 09166-00859
217	05 31 13.1	−68 25 48	7.7	21.8	1.09e−03±2.78e−04	0.0± 0.0	0.0	5.32e−03	661		1.00±1.10	<foreground star>
218	05 31 13.5	−66 07 09	0.8	1133.4	9.42e−03±4.08e−04	0.0± 0.0	0.0	5.34e−01	252	0.64±0.03	0.27±0.04	HMXB EXO053109-6609 [HP99b]
219	05 31 15.7	−70 53 46	3.7	61.1	1.69e−03±2.32e−04	1.8± 2.3	0.2	2.42e−03	1210	1.00±0.43	1.00±1.22	
220	05 31 31.8	−71 29 46	3.5	46.4	1.19e−02±3.54e−03	0.0± 0.0	0.0					AGN RX J0531.5-7130, z=0.2214 [SCF94]
221	05 31 38.1	−68 47 48	3.4	22.4	1.48e−03±3.01e−04	3.8± 2.4	6.5	<1.02e−02				
222	05 31 54.4	−66 02 21	3.8	11.8	3.50e−04±9.86e−05	1.1± 2.3	0.0	2.90e−03	229	1.00±0.27	1.00±0.82	
223	05 31 56.7	−70 59 59	3.4	71.6	4.76e−03±3.79e−04	8.2± 2.5	110.9	8.73e−02	1222	1.00±0.09	−0.26±0.04	SNR LHA 120-N 206
224	05 31 59.9	−69 19 51	3.5	46.4	2.81e−03±5.53e−04	2.4± 1.9	2.3	1.33e−02	876	1.00±0.21	0.02±0.09	AGN RX J0532.0-6920, z=0.149 [SCF94]
225	05 32 11.9	−70 04 54	7.6	25.2	1.02e−03±2.34e−04	0.0± 2.0	0.0	<4.61e−03				
226	05 32 12.8	−69 31 37	3.1	51.2	2.02e−03±3.80e−04	1.5± 1.4	0.9	<4.88e−03				
227	05 32 13.4	−69 29 53	4.1	10.8	4.50e−04±1.62e−04	0.0± 0.0	0.0	<1.32e−02				
228	05 32 14.0	−71 10 10	3.7	110.3	2.95e−03±3.07e−04	1.2± 2.6	0.0					
229	05 32 15.6	−71 04 26	4.8	14.1	8.18e−04±2.30e−04	0.0± 0.0	0.0					<foreground star>
230	05 32 18.5	−71 07 43	3.9	302.5	4.69e−03±3.49e−04	0.0± 0.0	0.0	9.43e−03	1238	1.00±0.35	1.00±0.98	<XB> or <AGN>
231	05 32 27.3	−67 31 10	8.5	106.1	1.80e−02±1.99e−03	9.1± 4.8	9.8	6.67e−02	540	1.00±0.49	−0.45±0.09	SNR? 0532-67.5 [C97]
232	05 32 27.5	−69 00 15	4.1	78.4	4.02e−03±5.22e−04	0.0± 0.0	0.0	<2.80e−02				
233	05 32 33.1	−65 51 43	1.4	327.0	3.99e−03±2.80e−04	0.0± 0.0	0.0	1.11e−02	184	1.00±0.10	0.43±0.05	HMXB RX J0532.5-6551 (Sk -65 66)
234	05 32 34.4	−66 07 31	8.6	10.4	7.70e−04±1.98e−04	0.0± 0.0	0.0	<8.31e−04				
235	05 32 35.7	−65 54 47	5.6	10.7	5.00e−04±1.35e−04	2.7± 3.2	0.3	<4.27e−03				
236	05 32 37.1	−65 55 57	5.0	12.6	4.57e−04±1.21e−04	0.0± 0.0	0.0	<3.64e−03				
237	05 32 42.7	−71 48 51	5.9	13.0	2.55e−03±8.38e−04	0.0± 0.0	0.0					
238	05 32 42.8	−69 26 18	3.9	29.3	1.35e−03±2.82e−04	2.5± 2.1	1.1	1.84e−02	914	1.00±0.31	0.29±0.19	LMXB? RX J0532.7-6926 [HP99b]
239	05 32 49.5	−66 22 13	0.2	30957.4	2.82e+00±4.22e−02	1.6± 0.4	182.5	4.30e−01	316	0.51±0.01	0.12±0.02	HMXB LMC X-4, HD 269743 O8III
240	05 32 50.2	−69 40 21	7.3	12.6	3.56e−03±1.28e−03	0.0± 0.0	0.0	<6.19e−03				
241	05 32 51.4	−70 06 31	7.4	36.9	1.34e−03±2.64e−04	1.3± 1.8	0.1	7.64e−03	1082	1.00±1.38	1.00±2.45	
242	05 32 52.0	−66 28 39	2.8	17.6	5.91e−04±1.50e−04	0.0± 0.0	0.0	<3.49e−03				
243	05 33 02.2	−66 11 32	7.3	10.5	3.40e−03±1.25e−03	3.9± 4.0	0.6	<1.59e−03				
244	05 33 05.3	−66 12 41	3.5	18.9	8.75e−04±2.20e−04	0.0± 0.0	0.0	<1.41e−03				
245	05 33 34.8	−68 54 54	2.0	141.5	4.94e−03±5.22e−04	2.2± 2.0	0.7	4.80e−02	759	0.24±0.22	−1.00±1.21	
246	05 33 36.9	−67 32 43	11.6	15.2	4.15e−03±1.07e−03	6.3± 5.9	0.5	<2.45e−02				
247	05 33 39.5	−69 09 29	4.8	21.4	4.92e−04±8.61e−05	0.0± 0.0	0.0	<3.17e−03				
248	05 33 55.7	−69 54 47	8.1	102.9	4.42e−02±3.39e−03	15.7± 4.7	153.6	2.81e−01	1043	1.00±0.11	−0.20±0.05	SNR 0534-69.9
249	05 33 59.7	−71 45 26	3.5	139.0	1.53e−02±1.86e−03	2.0± 2.2	0.4					
250	05 34 08.2	−70 19 00	8.2	62.9	5.27e−03±7.29e−04	0.0± 0.0	0.0	1.31e−02	1124	1.00±0.19	0.46±0.11	hard [HP99a]

1	2	3	4	5	6	7	8	9	10	11	12	13
No	RA	Dec	r_{90}	ML_{exi}	Count rate	r_{ext}	ML_{ext}	Count rate PSPC	No PSPC	HR1	HR2	Remarks
	(J2000.0)		['']		[cts s^{-1}]	['']		[cts s^{-1}]				
251	05 34 15.8	−69 14 17	2.9	29.4	1.23e−03±2.52e−04	0.8± 2.1	0.0	<3.34e−03				
252	05 34 16.3	−70 33 43	10.6	10.5	3.99e−03±1.08e−03	7.4± 4.5	4.8	6.49e−02	1160	0.82±0.03	0.08±0.04	SNR DEM L 238
253	05 34 26.4	−69 28 56	6.1	10.4	2.25e−03±8.76e−04	0.0± 0.0	0.0	<1.46e−03				
254	05 34 27.7	−69 25 40	5.9	11.0	2.65e−03±9.41e−04	0.0± 0.0	0.0	<8.05e−04				
255	05 34 42.3	−69 21 14	3.1	12.3	1.75e−04±4.24e−05	0.0± 0.0	0.0	<2.40e−03				
256	05 34 44.0	−67 37 45	9.6	10.5	6.56e−03±3.08e−03	0.0± 0.0	0.0					
257	05 34 44.6	−67 38 56	8.5	41.1	6.03e−03±1.13e−03	0.0± 0.0	0.0	6.18e−02	561	1.00±0.15	−0.04±0.15	AGN RX J0534.8-6739, z=0.072 [CSM97]
258	05 35 03.3	−66 10 40	10.3	11.5	1.06e−02±3.97e−03	0.0± 0.0	0.0	<4.07e−02				
259	05 35 03.5	−69 21 03	2.9	12.9	1.57e−04±3.80e−05	0.0± 0.0	0.0	<3.33e−03				
260	05 35 07.9	−69 18 48	7.6	12.4	1.26e−03±4.43e−04	0.0± 0.0	0.0					
261	05 35 11.4	−69 57 05	7.9	13.6	1.07e−03±3.25e−04	0.0± 0.0	0.0	<1.47e−02				
262	05 35 22.8	−66 12 55	8.3	48.9	1.00e−02±1.88e−03	0.0± 0.0	0.0	3.35e−02	268	−0.24±0.13	−1.00±1.65	foreground star dM4e [CCH84]
263	05 35 26.9	−68 32 38	7.5	13.1	4.01e−04±1.18e−04	0.0± 0.0	0.0	1.36e−02	676			
264	05 35 28.7	−69 16 08	0.7	586.7	2.05e−03±9.58e−05	3.1± 1.0	86.8	4.38e−03	854	1.00±0.27	0.21±0.20	SN 1987A
265	05 35 33.7	−69 44 56	8.2	11.3	2.49e−03±9.84e−04	0.0± 0.0	0.0	<5.65e−02				
266	05 35 34.2	−69 08 25	4.7	11.6	7.04e−04±2.10e−04	0.0± 0.0	0.0					
267	05 35 41.2	−69 53 08	7.6	20.2	1.25e−03±3.34e−04	1.9± 1.9	0.8	<1.84e−02				
268	05 35 45.7	−69 18 00	1.5	63.8	1.36e−03±9.48e−05	5.8± 1.6	119.1	3.28e−02	866	1.00±0.09	−0.14±0.05	SNR Honeycomb Nebula
269	05 35 46.5	−66 02 23	7.0	3681.1	3.11e−01±6.77e−03	7.2± 1.1	5993.1	7.39e+00	226	0.94±0.00	−0.01±0.01	SNR LHA 120-N 63A
270	05 35 48.9	−69 09 31	2.8	47.9	9.83e−04±9.34e−05	6.8± 2.4	37.3					SNR 0536-69.2, 30 DOR C: knot
271	05 35 53.1	−69 34 58	3.0	16.0	7.53e−04±2.25e−04	0.7± 1.9	0.0	<4.17e−03				
272	05 36 00.7	−70 41 28	7.6	27.0	3.02e−03±8.02e−04	1.9± 2.0	0.7	1.03e−02	1181	1.00±0.14	0.39±0.10	hard [HP99a]
273	05 36 01.4	−70 17 36	8.2	10.9	8.29e−04±2.79e−04	0.0± 0.0	0.0	<1.44e−02				
274	05 36 06.6	−70 38 57	9.2	11.0	3.46e−03±1.06e−03	5.1± 3.5	4.0	6.02e−02	1173	1.00±0.02	−0.17±0.04	SNR DEM L 249
275	05 36 17.2	−69 03 43	9.1	10.2	2.32e−03±7.22e−04	0.0± 0.0	0.0	<3.05e−03				
276	05 36 17.3	−69 13 04	2.0	55.0	1.14e−03±9.25e−05	6.1± 1.9	72.0	2.47e−02	840	0.89± *	0.11± *	SNR 0536-69.2, 30 DOR C: knot
277	05 36 19.0	−69 09 30	3.2	64.0	1.37e−03±1.15e−04	8.5± 2.7	43.2					SNR 0536-69.2, 30 DOR C: knot
278	05 36 32.7	−65 56 40	8.3	12.2	2.74e−03±9.88e−04	0.0± 0.0	0.0	<1.17e−02				
279	05 36 57.1	−69 00 27	6.9	12.8	1.26e−03±3.20e−04	4.4± 3.9	1.0					
280	05 36 57.8	−69 13 26	2.2	59.4	5.51e−04±6.58e−05	0.6± 1.9	0.0					
281	05 37 00.1	−69 25 37	8.3	10.8	2.28e−03±6.65e−04	0.0± 0.0	0.0					
282	05 37 07.2	−69 03 09	6.4	11.9	7.18e−04±1.47e−04	7.5± 3.4	4.9					knot in 30 Dor
283	05 37 07.5	−69 18 54	10.4	13.0	9.60e−04±2.05e−04	8.4± 6.2	1.5					knot
284	05 37 28.6	−69 23 18	13.4	11.5	4.07e−03±1.05e−03	9.8± 7.6	1.5					<SNR>
285	05 37 31.8	−69 28 26	6.1	10.5	2.58e−03±9.41e−04	0.0± 0.0	0.0					
286	05 37 33.6	−69 18 43	6.8	18.2	4.89e−04±9.24e−05	3.5± 4.8	0.2					
287	05 37 35.9	−68 25 57	7.4	115.8	3.15e−03±3.26e−04	0.0± 0.0	0.0					<foreground star>
288	05 37 36.2	−69 16 42	9.7	16.3	8.36e−04±1.40e−04	11.5± 5.5	5.1					<SNR>
289	05 37 46.9	−69 10 18	0.4	8036.1	4.07e−02±6.36e−04	5.1± 0.7	3391.0	2.34e−01	826	1.00±0.02	0.47±0.02	SNR 0538-69.1, LHA 120-N 157B
290	05 37 50.3	−69 04 23	2.4	21.2	3.83e−04±8.80e−05	0.0± 0.0	0.0					<foreground star>
291	05 38 09.8	−68 56 56	2.5	109.7	1.85e−03±1.79e−04	1.5± 2.5	0.1					
292	05 38 14.6	−64 11 50	10.1	11.1	8.86e−03±4.22e−03	1.2± 3.5	0.0	<1.03e−03				
293	05 38 15.9	−69 23 30	0.9	2548.9	4.30e−02±1.46e−03	0.6± 1.1	0.0	1.72e−01	902	0.02±0.03	−0.00±0.04	foreground star dMe CAL 69 [CSM97]
294	05 38 21.3	−68 50 34	2.6	33.2	1.37e−03±2.89e−04	0.0± 0.0	0.0	<8.35e−03				foreground star G5V HD 269916
295	05 38 28.8	−69 08 33	15.8	18.1	5.14e−03±9.66e−04	16.1±10.1	2.4					knot in 30 Dor
296	05 38 34.4	−68 53 07	0.4	5091.4	5.56e−02±1.40e−03	0.0± 0.0	0.0	2.98e−01	752	−0.04±0.02	0.05±0.02	foreground star G2V, RS CVn? [CSM97]
297	05 38 38.4	−68 28 09	7.9	13.2	6.62e−04±2.00e−04	0.0± 0.0	0.0	<3.75e−03				
298	05 38 41.0	−69 55 54	11.7	11.7	9.82e−03±3.41e−03	2.8± 5.8	0.0	<3.56e−03				
299	05 38 41.4	−69 05 13	0.7	505.0	3.46e−03±2.23e−04	1.2± 1.0	1.5					knot in 30 Dor
300	05 38 42.4	−68 52 41	1.5	103.8	2.75e−03±3.86e−04	0.8± 1.3	0.1					<foreground star>

Table B.1: Continued (LMC).

1	2	3	4	5	6	7	8	9	10	11	12	13
No	RA	Dec	r_{90}	$\mathrm{ML_{exi}}$	Count rate	r_{ext}	$\mathrm{ML_{ext}}$	Count rate PSPC	No PSPC	HR1	HR2	Remarks
	(J2000.0)		['']		[cts s^{-1}]	['']		[cts s^{-1}]				
301	05 38 43.7	−69 06 05	0.7	1523.9	8.47e−03±3.04e−04	4.0± 1.1	165.4					cluster of stars HD 38268; RMC 136
302	05 38 43.8	−69 10 12	2.1	41.7	2.44e−03±1.98e−04	7.1± 2.0	107.4					knot in 30 Dor
303	05 38 46.7	−69 02 25	2.9	33.4	2.25e−03±2.06e−04	8.1± 2.6	71.9					knot in 30 Dor
304	05 38 49.8	−68 35 04	7.4	39.1	1.50e−03±2.80e−04	1.6± 2.0	0.2					
305	05 38 50.0	−69 44 27	4.1	36.0	1.46e−03±2.48e−04	0.0± 0.0	0.0	<5.74e−03				foreground star F2V HD 38329
306	05 38 56.3	−64 05 03	0.2	34020.7	7.37e+00±6.88e−02	1.9± 0.4	367.4	2.04e+01	41	0.84±0.00	0.28±0.01	HMXB LMC X-3
307	05 39 27.9	−69 33 12	12.0	15.7	2.49e−03±4.68e−04	12.8± 6.5	4.0					<SNR>
308	05 39 29.2	−69 57 09	4.4	20.3	8.84e−04±2.24e−04	0.0± 0.0	0.0	<1.47e−03				foreground star HD 269934
309	05 39 31.3	−69 05 12	4.7	31.4	2.05e−03±2.25e−04	10.3± 3.5	31.7					knot in 30 Dor
310	05 39 36.6	−70 01 58	9.3	27.1	4.28e−03±6.40e−04	10.1± 4.4	14.4	2.36e−02	1063	1.00±0.17	−0.17±0.10	SNR? [HP99a]
311	05 39 38.7	−69 44 32	3.0	32679.3	3.77e+00±4.68e−02	0.0± 0.0	0.0	1.27e+01	1001	0.99±0.00	0.74±0.00	HMXB LMC X-1, O8III
312	05 39 50.1	−69 08 03	7.4	18.9	1.44e−03±2.13e−04	10.6± 4.8	13.3					knot in 30 Dor
313	05 39 59.9	−68 28 42	7.1	315.3	6.31e−03±5.22e−04	2.7± 1.2	26.9	1.31e−02	668	1.00±0.62	1.00±1.88	<foreground star>
314	05 40 03.2	−68 20 36	8.4	25.3	1.65e−03±3.35e−04	0.0± 0.0	0.0					
315	05 40 04.5	−69 43 58	3.6	41.3	3.36e−03±3.52e−04	5.8± 2.0	61.8					SNR? [CKS97]
316	05 40 06.6	−70 14 21	7.4	24.1	1.04e−03±2.58e−04	1.1± 1.6	0.1	<2.12e−02				
317	05 40 07.8	−69 17 11	2.2	56.6	2.25e−03±3.87e−04	2.5± 1.7	3.1					
318	05 40 10.9	−69 19 52	0.7	17883.4	1.95e−01±3.32e−03	2.7± 0.5	781.3	8.40e−01	877	0.98±0.00	0.58±0.01	SNR LHA 120-N 158A, PSR B0540-69
319	05 40 23.7	−68 56 52	3.7	15.9	9.73e−04±2.65e−04	0.5± 2.2	0.0					
320	05 40 27.7	−69 37 17	4.9	11.6	5.29e−04±1.53e−04	0.0± 0.0	0.0					
321	05 40 30.1	−64 20 42	8.9	12.4	1.46e−03±4.49e−04	0.0± 0.0	0.0	<7.47e−03				
322	05 40 30.3	−69 46 58	5.1	11.3	3.85e−03±1.60e−03	0.0± 0.0	0.0					
323	05 40 31.5	−68 58 17	9.8	10.1	1.36e−03±3.67e−04	2.7± 5.4	0.0					
324	05 40 35.0	−68 32 28	9.0	11.7	8.02e−04±2.31e−04	3.3± 2.8	0.8	<8.69e−03				
325	05 40 37.2	−70 12 01	7.1	88.6	2.45e−03±3.75e−04	0.0± 0.0	0.0	<6.85e−03				
326	05 41 13.1	−64 11 51	7.4	48.1	2.81e−03±5.45e−04	0.0± 0.0	0.0	2.05e−02	50	1.00±0.70	1.00±0.43	
327	05 41 16.0	−69 41 36	3.8	20.8	5.97e−04±1.48e−04	0.0± 0.0	0.0					
328	05 41 22.2	−69 36 29	6.6	11.1	7.28e−04±2.03e−04	0.0± 0.0	0.0	<1.34e−02				<HMXB> LMC B2 supergiant SK -69 271
329	05 41 27.6	−69 44 53	4.2	12.5	4.44e−04±1.34e−04	0.0± 0.0	0.0					
330	05 41 29.9	−69 04 45	8.9	14.9	1.14e−03±2.76e−04	0.0± 0.0	0.0	<3.59e−02				CAL 80
331	05 41 35.4	−68 26 17	8.6	10.5	1.96e−03±5.94e−04	0.0± 0.0	0.0					
332	05 41 37.1	−68 32 32	4.5	33.6	2.34e−03±4.27e−04	0.0± 0.0	0.0	<2.23e−02				<HMXB> LMC O star BI 267
333	05 41 39.3	−69 02 36	8.1	11.1	8.19e−04±2.39e−04	0.0± 0.0	0.0	<1.40e−01				
334	05 41 44.5	−69 42 09	5.3	10.7	5.48e−04±1.63e−04	1.9± 2.7	0.1	<1.55e−02				
335	05 41 44.6	−69 21 53	4.4	15.1	1.06e−03±3.05e−04	0.0± 0.0	0.0	<7.96e−03				
336	05 41 52.5	−69 54 00	8.5	11.8	6.88e−04±1.95e−04	0.0± 0.0	0.0	<2.38e−03				
337	05 41 59.0	−68 15 42	7.5	14.4	2.47e−03±6.50e−04	2.1± 4.0	0.0					
338	05 42 01.2	−69 24 44	11.9	11.5	2.43e−03±5.91e−04	8.3± 5.6	2.8	<7.76e−03				<SNR>
339	05 42 04.2	−68 21 08	7.1	10.9	1.71e−03±5.17e−04	4.2± 4.2	0.7					
340	05 42 36.9	−68 32 03	3.2	23.5	1.17e−03±2.75e−04	2.0± 2.4	0.5					
341	05 42 39.2	−68 58 57	8.7	10.3	9.13e−04±2.78e−04	0.0± 0.0	0.0	<1.19e−03				
342	05 42 39.8	−68 50 49	6.7	32.9	1.04e−03±2.38e−04	0.0± 0.0	0.0	<3.90e−03				
343	05 42 45.4	−69 53 59	7.7	13.6	5.10e−04±1.49e−04	0.6± 2.2	0.0	<2.32e−03				
344	05 42 55.8	−68 41 42	13.3	10.5	6.72e−03±2.78e−03	0.0± 0.0	0.0	<2.40e−03				
345	05 43 04.3	−69 26 32	8.1	16.4	1.20e−03±3.31e−04	2.6± 2.8	0.4	<6.08e−03				
346	05 43 15.1	−69 49 52	8.0	10.6	1.78e−03±7.63e−04	0.0± 0.0	0.0	<1.51e−02				
347	05 43 22.2	−68 56 39	6.4	141.3	2.51e−03±3.01e−04	1.2± 1.1	0.8	<1.67e−02				<foreground star>
348	05 43 34.2	−68 22 21	1.1	17776.1	2.15e−01±3.26e−03	2.2± 0.7	46.1	8.66e−01	654	−0.87±0.02	−1.00±0.51	SSS CAL 83 [SCF94]
349	05 43 34.5	−64 22 55	7.2	624.1	3.06e−02±1.79e−03	0.0± 0.0	0.0	6.53e−02	61	−0.00±0.13	0.05±0.19	foreground star? [HP99a]
350	05 43 39.6	−69 17 18	8.7	11.0	8.77e−04±2.51e−04	4.1± 3.6	0.5	<2.29e−03				

1	2	3	4	5	6	7	8	9	10	11	12	13
No	RA	Dec	r_{90}	ML_{exi}	Count rate	r_{ext}	ML_{ext}	Count rate PSPC	No PSPC	HR1	HR2	Remarks
	(J2000.0)		['']		[cts s^{-1}]	['']		[cts s^{-1}]				
351	05 43 58.7	−65 39 55	4.4	16.4	1.88e−03±6.11e−04	0.0± 0.0	0.0	6.86e−03	148	1.00±0.87	1.00±0.66	
352	05 44 06.0	−71 00 51	7.8	12.3	1.34e−03±5.17e−04	0.0± 0.0	0.0	4.41e−02	1225	1.00±0.03	0.65±0.03	HMXB RX J0544.1-7100 [HP99a]
353	05 44 10.5	−69 46 49	7.9	11.3	6.22e−04±2.01e−04	0.0± 0.0	0.0	<2.21e−02				
354	05 44 29.3	−71 11 55	10.5	11.8	1.73e−03±5.03e−04	0.0± 0.0	0.0	<1.51e−03				
355	05 44 34.8	−69 46 25	8.8	10.8	7.12e−04±2.01e−04	3.0± 3.1	0.5	<1.08e−02				
356	05 44 46.4	−65 44 07	3.9	15.3	1.43e−03±5.16e−04	0.0± 0.0	0.0	6.57e−03	157	−0.20±0.22	−1.00±0.63	foreground star A7V HD 39014
357	05 45 00.4	−69 54 15	9.1	12.9	4.70e−03±1.90e−03	0.0± 0.0	0.0					
358	05 45 08.7	−68 19 37	7.2	10.7	6.64e−03±2.94e−03	0.0± 0.0	0.0					
359	05 45 43.4	−68 25 26	9.3	13.3	1.15e−03±3.21e−04	0.0± 0.0	0.0					
360	05 45 52.7	−69 54 45	16.3	10.5	2.01e−03±5.51e−04	0.0± 8.0	0.0	<3.10e−03				
361	05 45 56.2	−69 43 55	7.1	188.7	3.07e−03±3.11e−04	1.0± 1.4	0.1					
362	05 46 15.3	−68 35 23	7.3	90.4	2.94e−03±4.31e−04	0.0± 0.0	0.0	1.24e−02	686			RX J0546.3-6836 (CAL 86)
363	05 46 46.9	−71 08 52	7.0	3268.5	6.23e−02±2.17e−03	3.0± 0.8	242.1	1.24e−01	1240	0.80±0.01	−0.86±0.01	SSS CAL 87
364	05 46 55.7	−68 51 35	7.0	1146.0	2.02e−02±1.00e−03	3.6± 1.0	171.7	1.08e−02	747	1.00±0.21	1.00±0.60	<XB> or <AGN>
365	05 46 57.1	−69 42 40	10.7	32.2	7.62e−03±8.64e−04	16.8± 6.2	29.9	4.54e−02	993	0.95± *	0.21± *	SNR LHA 120-N 135 (DEM L 316), shell B
366	05 47 18.5	−69 41 28	7.4	29.7	3.41e−03±3.51e−04	6.7± 2.2	85.5	5.02e−02	987	1.00±0.10	0.22±0.07	SNR LHA 120-N 135 (DEM L 316), shell A
367	05 47 19.9	−68 31 33	7.5	21.7	8.99e−04±2.45e−04	1.4± 1.8	0.2					
368	05 47 21.7	−70 26 55	4.3	10.6	2.85e−03±1.46e−03	0.0± 0.0	0.0					
369	05 47 27.2	−70 06 27	7.7	26.1	1.42e−03±3.30e−04	2.1± 2.5	0.4	<1.82e−03				
370	05 47 34.7	−71 55 19	12.4	10.7	3.46e−03±1.04e−03	2.5± 6.0	0.0					
371	05 47 45.2	−67 45 05	2.6	89.0	9.63e−03±1.75e−03	2.1± 1.5	3.4					AGN RX J0547.8-6745, z=0.3905 [CSM97]
372	05 47 47.6	−70 24 46	3.0	37.3	8.31e−03±1.11e−03	6.4± 2.5	60.3	1.52e−01	1137	1.00±0.05	−0.10±0.06	SNR 0548-70.4
373	05 47 58.9	−68 35 41	8.4	11.8	7.84e−04±2.50e−04	1.6± 3.0	0.0					
374	05 48 01.3	−71 56 19	10.6	11.0	2.50e−03±7.26e−04	4.6± 4.7	0.6	<1.69e−03				
375	05 48 19.2	−70 20 44	1.7	216.6	3.57e−03±3.47e−04	2.3± 1.3	7.5	1.63e−02	1127			foreground star F3/F5IV/V HD 39756
376	05 48 28.8	−71 12 44	8.3	17.7	1.52e−03±4.14e−04	0.0± 0.0	0.0	8.27e−03	1247	1.00±0.09	0.27±0.08	hard [HP99a]
377	05 48 58.9	−68 54 08	8.5	23.0	1.40e−03±3.27e−04	0.0± 0.0	0.0					
378	05 49 12.5	−70 06 56	9.7	12.8	1.75e−03±4.63e−04	0.0± 0.0	0.0	<1.29e−02				
379	05 49 28.9	−69 47 14	9.9	24.2	1.81e−03±3.34e−04	0.0± 0.0	0.0	9.33e−03	1014	−1.00±0.89		foreground star F2V HD 39904
380	05 49 40.5	−69 44 12	13.7	14.3	1.52e−03±3.45e−04	5.0± 6.2	0.2	1.17e−02	999	1.00±0.73	0.48±0.21	
381	05 49 41.8	−70 23 14	8.4	10.2	4.75e−03±2.04e−03	0.0± 0.0	0.0					
382	05 49 46.0	−69 38 40	12.2	12.4	2.06e−03±5.30e−04	0.0± 0.0	0.0	6.39e−03	975	1.00±3.30	−1.00±1.76	
383	05 49 46.5	−71 49 36	7.1	570.5	9.56e−03±5.97e−04	3.3± 1.2	62.1	4.12e−02	1312	−0.02±0.06	−0.16±0.08	foreground star dMe [SCC99]
384	05 49 53.4	−68 19 46	10.9	11.7	3.12e−03±9.77e−04	0.0± 0.0	0.0					
385	05 50 31.5	−71 09 57	8.6	29.1	3.59e−03±7.58e−04	0.5± 3.7	0.0	2.86e−03	1243	1.00±0.75	1.00±1.61	AGN RX J0550.5-7110, z=0.4429 [CGC97]
386	05 51 00.5	−69 54 08	4.4	106.0	1.20e−02±1.73e−03	0.6± 3.0	0.0	5.99e−02	1036	−0.11±0.16	−1.00±3.23	foreground star F5V HD 40156
387	05 51 22.6	−70 27 37	9.0	24.8	3.98e−03±8.57e−04	0.0± 0.0	0.0	<1.19e−02				
388	05 51 38.8	−69 23 00	9.5	12.5	3.04e−03±1.03e−03	3.7± 3.7	0.3	1.42e−02	893	0.03±0.24	−1.00±2.55	
389	05 52 24.3	−64 02 12	7.1	464.0	4.82e−02±4.64e−03	2.3± 1.2	10.8	1.75e−01	37	0.57±0.11	0.17±0.12	AGN? PKS 0552-640 [HP99a]
390	05 52 32.0	−69 49 06	4.5	36.5	5.16e−03±1.12e−03	3.7± 2.3	6.8	7.30e−02	1024	1.00±0.14	0.46±0.15	2E 0553.0-6949
391	05 52 48.7	−69 26 35	7.5	39.8	4.85e−03±1.19e−03	1.9± 2.1	0.4	<1.15e−02				RX J0552.8-6927
392	05 53 02.2	−70 17 51	8.9	10.7	3.49e−03±1.29e−03	1.7± 3.0	0.1					
393	05 53 34.9	−70 30 24	7.9	21.8	2.38e−03±6.02e−04	2.4± 2.3	0.9	<5.16e−03				
394	05 54 13.5	−69 19 56	9.0	12.3	2.63e−03±9.49e−04	1.7± 3.0	0.0					
395	05 54 52.0	−67 51 10	9.1	10.3	5.05e−03±2.44e−03	2.9± 2.8	0.3					
396	06 08 50.6	−65 43 58	7.3	53.7	6.19e−03±6.36e−04	6.0± 2.1	85.2					S0 galaxy ESO 86- 62
397	06 08 55.0	−65 53 00	9.2	11.6	1.14e−03±3.18e−04	2.9± 3.4	0.4					<galaxy>

Table B.2: *HRI sources in the SMC region.*

1	2	3	4	5	6	7	8	9	10	11	12	13
No	RA	Dec	r_{90}	ML_{exi}	Count rate	r_{ext}	ML_{ext}	Count rate PSPC	No PSPC	HR1	HR2	Remarks
	(J2000.0)		['']		[cts s^{-1}]	['']		[cts s^{-1}]				
1	00 34 56.0	−72 16 48	7.8	10.9	1.02e−03±2.77e−04	0.0± 0.0	0.0	3.12e−03	187	1.00±1.34	1.00±0.89	
2	00 35 21.3	−72 12 43	4.8	23.0	1.40e−03±2.77e−04	3.5± 3.2	1.0	6.48e−03	167	1.00±0.46	0.30±0.12	
3	00 35 52.7	−72 09 19	6.0	12.3	8.57e−04±2.27e−04	2.9± 3.2	0.3	3.03e−03	144	1.00±2.57	0.33±0.23	AGN? [KPFH99]
4	00 36 01.8	−72 21 12	2.2	152.8	4.12e−03±3.99e−04	2.5± 2.1	1.2	7.34e−03	211	0.35±0.13	−0.04±0.13	AGN? [KPFH99]
5	00 36 04.7	−72 18 44	3.8	13.1	6.09e−04±1.72e−04	0.0± 0.0	0.0	1.83e−03	198	1.00±3.45	1.00±0.49	<XB> or <AGN>
6	00 36 11.4	−72 17 43	4.2	16.6	8.56e−04±2.06e−04	2.9± 2.7	0.8	3.68e−03	191	1.00±0.76	0.10±0.18	AGN? [KPFH99]
7	00 37 19.8	−72 14 13	1.1	10945.0	8.14e−02±1.54e−03	3.2± 0.6	1066.7	4.40e−01	176	−0.97±0.00	−1.00±0.06	SSS 1E0035.4-7230
8	00 37 20.5	−72 18 05	1.9	74.6	1.66e−03±2.41e−04	1.7± 1.4	1.7	7.49e−03	193	1.00±1.09	−0.06±0.12	AGN z=0.922 [TDZ97]
9	00 38 55.3	−72 05 37	4.1	54.4	2.73e−03±3.76e−04	1.2± 3.3	0.0	4.57e−03	127	1.00±0.56	0.32±0.15	
10	00 40 00.6	−73 45 42	8.8	33.7	3.18e−03±5.26e−04	0.0± 0.0	0.0	1.66e−02	562	−0.05±0.07	0.05±0.10	foreground star HD 3880
11	00 42 08.4	−73 45 02	7.2	14.8	7.94e−04±2.21e−04	2.3± 2.4	0.6	<1.18e−03				
12	00 42 41.8	−73 40 41	6.7	25.7	1.00e−03±2.30e−04	1.8± 1.7	1.0	2.87e−03	546	1.00±0.61	0.43±0.16	XB? or AGN? [KPFH99]
13	00 42 52.2	−73 25 38	7.9	11.4	9.70e−04±3.55e−04	0.0± 0.0	0.0	<6.17e−03				
14	00 43 56.8	−73 42 20	7.2	11.4	6.47e−04±1.98e−04	1.9± 1.9	0.8	1.41e−03	552	1.00±0.99	1.00±1.99	AGN? [KPFH99]
15	00 44 56.9	−73 22 38	5.7	10.2	2.31e−03±1.03e−03	0.0± 0.0	0.0					
16	00 45 10.9	−73 04 17	7.5	10.8	1.69e−03±5.81e−04	0.0± 0.0	0.0	6.36e−03	397	1.00±0.88	−0.18±0.12	<foreground star> GSC 9141.7926
17	00 45 24.7	−73 28 58	7.9	18.0	1.71e−03±4.89e−04	0.0± 0.0	0.0	3.62e−03	494	1.00±3.04	1.00±2.07	
18	00 46 41.8	−73 01 15	5.6	23.9	1.77e−03±4.42e−04	0.0± 0.0	0.0	7.18e−03	383	−0.26±0.10	−0.39±0.15	foreground star? [HFPK00]
19	00 46 48.1	−73 28 07	10.1	12.4	3.90e−03±1.09e−03	5.6± 4.2	2.3	<1.49e−03				
20	00 47 08.2	−72 43 04	9.6	11.3	1.55e−03±4.02e−04	0.0± 0.0	0.0	<4.83e−03				
21	00 47 29.2	−73 28 23	10.1	10.4	2.58e−03±8.74e−04	0.0± 0.0	0.0					
22	00 47 40.5	−73 09 28	6.3	11.7	1.74e−03±5.63e−04	3.6± 2.8	1.4	3.96e−02	419	1.00±0.09	0.27±0.04	SNR? [KPFH99]
23	00 48 19.6	−73 31 52	2.3	5165.4	6.56e−02±1.99e−03	1.2± 0.5	12.8	8.10e−03	512	−1.00±0.24		SSS RXJ0048.4-7332
24	00 48 42.1	−72 46 57	4.8	17.0	6.73e−04±1.88e−04	0.0± 0.0	0.0	<1.83e−03				
25	00 48 55.6	−73 33 37	3.3	28.7	1.18e−03±2.92e−04	0.0± 0.0	0.0	<2.28e−03				<foreground star> GSC 9141.7623
26	00 48 59.0	−72 58 13	5.3	18.9	1.03e−03±2.50e−04	0.0± 0.0	0.0	3.18e−03				<foreground star>
27	00 49 08.2	−73 21 39	6.4	10.8	1.23e−03±4.08e−04	0.0± 0.0	0.0	<1.35e−03				
28	00 49 30.8	−73 31 09	3.0	69.4	2.01e−03±2.94e−04	2.7± 1.7	7.0	2.39e−03	511	1.00±0.45	0.32±0.17	<Be/X>
29	00 49 43.9	−72 52 10	4.7	18.0	6.81e−04±1.89e−04	0.0± 0.0	0.0	<1.07e−02				
30	00 49 57.5	−73 12 52	9.1	13.5	1.72e−03±4.12e−04	0.0± 0.0	0.0	<5.34e−04				
31	00 50 00.0	−72 49 27	4.9	13.5	5.89e−04±1.79e−04	0.0± 0.0	0.0	<7.93e−03				
32	00 50 13.2	−72 09 16	5.7	10.6	4.08e−03±1.76e−03	1.3± 2.9	0.0					
33	00 50 19.7	−73 35 34	5.7	11.3	1.28e−03±4.08e−04	2.2± 2.9	0.2	<2.26e−03				
34	00 50 42.9	−73 16 08	1.8	126.2	4.23e−03±5.53e−04	1.6± 1.4	1.0	4.52e−03	444	1.00±0.24	0.58±0.10	HMXB Be star in SMC
35	00 50 49.3	−72 41 53	4.3	447.9	1.33e−02±8.11e−04	0.0± 0.0	0.0					<foreground star> SkKM 62
36	00 50 57.2	−73 10 06	3.3	53.4	2.24e−03±3.52e−04	0.8± 2.8	0.0	3.48e−03	421	1.00±0.33	0.52±0.12	<Be/X>
37	00 50 59.3	−72 13 26	2.6	115.1	2.11e−02±3.71e−03	0.4± 1.1	0.0	<7.20e−03				HMXB AXJ0051-722 [KP96]
38	00 51 02.4	−73 21 31	2.7	50.2	5.49e−03±6.58e−04	6.2± 2.3	56.6	1.41e−01	461	0.79±0.01	−0.26±0.02	SNR 0049-73.6
39	00 51 20.5	−72 16 41	4.6	10.1	3.53e−03±1.59e−03	0.0± 0.0	0.0	1.15e−02	188	1.00±0.80	1.00±0.56	XB? [KPFH99]
40	00 51 30.9	−72 25 04	7.3	11.0	1.11e−03±3.10e−04	0.0± 0.0	0.0					
41	00 51 52.0	−73 10 32	1.5	193.6	3.55e−03±3.83e−04	0.5± 1.1	0.0	1.46e−02	424	1.00±0.08	0.36±0.06	HMXB RXJ0051.9-7311 [CSM97]
42	00 51 59.6	−73 29 29	8.1	11.0	1.77e−03±5.25e−04	5.1± 4.5	0.9	9.39e−03	496	1.00±0.41	0.35±0.25	
43	00 52 07.7	−72 25 50	15.9	10.3	1.19e−02±3.69e−03	6.3± 9.8	0.1					HMXB SMC X-3
44	00 52 13.9	−73 19 18	1.1	23375.0	6.79e−01±5.10e−03	1.1± 0.6	4.5	2.15e−02	453	1.00±0.07	0.61±0.04	HMXB RXJ0052.1-7319 [LPM99],[ISC99]
45	00 52 54.8	−72 17 06	3.9	41.0	2.45e−03±4.59e−04	0.0± 0.0	0.0					
46	00 52 55.2	−71 58 06	3.0	83.6	2.37e−03±3.27e−04	2.9± 1.9	3.9	1.21e−02	94	1.00±0.43	0.44±0.13	HMXB RXJ0052.9-7158 [CSM97]
47	00 53 08.7	−72 39 56	7.7	15.2	2.22e−03±8.38e−04	0.0± 0.0	0.0	<4.03e−03				
48	00 53 24.1	−72 27 20	3.1	39.3	1.23e−03±2.40e−04	1.3± 1.6	0.2	3.82e−03	246	1.00±0.59	1.00±1.29	<Be/X>
49	00 53 38.7	−73 15 07	3.5	10.4	4.73e−04±1.61e−04	0.4± 1.8	0.0	<1.41e−03				
50	00 53 48.2	−72 02 01	3.5	18.5	7.16e−04±1.92e−04	0.0± 0.0	0.0	4.33e−03	104	1.00±0.57	1.00±1.06	

1	2	3	4	5	6	7	8	9	10	11	12	13
No	RA	Dec	r_{90}	ML_{exi}	Count rate	r_{ext}	ML_{ext}	Count rate PSPC	No PSPC	HR1	HR2	Remarks
	(J2000.0)		['']		[cts s^{-1}]	['']		[cts s^{-1}]				
51	00 53 56.0	–72 26 52	2.4	395.2	7.76e−03±5.59e−04	3.1± 1.2	56.3	9.20e−02	242	1.00±0.18	0.46±0.05	HMXB? XTEJ0053-724, pulsar [CML98]
52	00 54 12.5	–72 17 50	4.5	24.1	2.88e−03±7.40e−04	2.5± 2.7	0.4					
53	00 54 32.1	–72 18 13	3.7	27.4	1.23e−03±2.56e−04	2.4± 2.2	0.9	6.24e−03	196	1.00±1.37	1.00±0.59	<XB> or <AGN>
54	00 54 41.7	–72 17 29	5.0	15.3	1.02e−03±2.56e−04	3.0± 2.8	0.9	<3.82e−03				
55	00 54 46.2	–72 00 17	4.2	11.8	5.75e−04±1.80e−04	0.0± 0.0	0.0	<9.72e−03				
56	00 54 50.3	–71 51 18	4.9	15.3	8.20e−04±2.20e−04	1.5± 2.6	0.0	5.63e−03	76	1.00±1.21	1.00±0.98	
57	00 54 56.0	–72 45 06	9.7	34.7	3.02e−03±4.84e−04	0.0± 5.2	0.0	3.75e−03	324	1.00±0.71	0.58±0.14	<Be/X>
58	00 54 56.5	–72 26 52	2.6	127.8	2.82e−03±3.49e−04	1.5± 1.5	0.5	3.68e−02	241	1.00±0.04	0.56±0.03	HMXB XTEJ0055-724 [SCB99]
59	00 55 28.7	–72 10 55	3.8	25.9	2.58e−03±6.66e−04	1.6± 1.9	0.2	2.74e−02	157	1.00±0.04	0.36±0.04	AGN? Radio SMC B0053-7227 [FHW98]
60	00 55 35.1	–72 28 36	4.6	21.9	1.17e−03±2.68e−04	0.6± 2.8	0.0	4.47e−03	249	1.00±0.24	0.14±0.19	hard [HFPK00]
61	00 55 40.4	–72 20 29	5.0	11.4	9.54e−04±3.06e−04	0.0± 0.0	0.0	<1.17e−03				
62	00 55 43.2	–72 09 21	4.7	11.6	3.47e−03±1.61e−03	0.0± 0.0	0.0	<1.27e−02				
63	00 55 43.9	–73 23 43	9.0	11.1	1.52e−03±4.87e−04	0.0± 0.0	0.0					
64	00 55 49.3	–72 28 37	6.5	10.1	1.03e−03±3.35e−04	0.0± 0.0	0.0	<5.31e−03				<AGN>
65	00 55 51.2	–73 31 06	8.5	42.2	2.77e−03±4.38e−04	0.0± 0.0	0.0	1.83e−02	508	1.00±0.53	0.36±0.07	
66	00 55 59.5	–72 52 41	7.9	12.0	5.58e−04±1.74e−04	0.4± 2.1	0.0	<7.02e−03				
67	00 56 00.0	–71 52 37	9.7	10.6	1.40e−03±3.72e−04	6.2± 5.8	0.4					
68	00 56 50.3	–73 10 38	9.9	10.0	9.85e−04±2.90e−04	0.0± 0.0	0.0	2.96e−03	426	1.00±0.38	0.34±0.15	<foreground star> GSC 9141.7719
69	00 56 56.4	–73 30 21	9.8	11.8	1.23e−03±3.67e−04	2.2± 4.1	0.0					
70	00 57 26.7	–73 25 18	7.1	127.9	2.67e−03±3.45e−04	1.1± 1.3	0.3	8.40e−03	476	1.00±0.35	0.66±0.08	
71	00 57 31.7	–72 13 01	3.9	111.0	3.26e−03±3.40e−04	0.0± 0.0	0.0	5.48e−03	170	1.00±0.13	0.38±0.09	<XB> or <AGN>
72	00 57 35.5	–73 12 56	9.2	14.3	1.24e−03±3.04e−04	5.0± 3.8	1.6	6.38e−03	435	1.00±0.84	0.25±0.16	<XB> or <AGN>
73	00 57 48.5	–72 02 34	6.4	22.9	3.08e−03±6.79e−04	0.0± 0.0	0.0	3.03e−03	114	1.00±0.52	1.00±0.35	HMXB? AXJ0058-72.0, pulsar [YK98a]
74	00 57 49.3	–72 07 55	3.5	236.9	4.51e−03±3.66e−04	1.2± 1.5	0.2	8.82e−03	136	1.00±0.22	0.58±0.11	<Be/X>
75	00 57 58.0	–72 22 30	7.9	41.0	5.39e−03±8.32e−04	4.6± 5.7	0.2	<8.61e−03				
76	00 58 12.6	–72 30 50	4.5	103.7	4.28e−03±4.77e−04	0.0± 0.0	0.0	6.88e−04				HMXB [SCC99]
77	00 58 16.0	–72 18 04	4.5	69.4	3.00e−03±3.56e−04	3.7± 3.0	1.3	7.93e−03	194	1.00±0.14	0.15±0.07	SNR 0056-72.5
78	00 58 20.7	–72 16 18	6.3	10.9	6.78e−04±1.96e−04	2.3± 3.0	0.3	2.32e−03	185	1.00±0.81	0.58±0.09	<XB> or <AGN>
79	00 58 37.3	–71 35 49	1.5	700.3	5.17e−02±3.77e−03	2.3± 1.0	29.0	3.68e−01	47	−0.99±0.00	−1.00±0.26	SSS 1E0056.8-7146
80	00 59 13.6	–72 22 25	8.9	12.3	1.42e−03±3.37e−04	0.0± 0.0	0.0	9.64e−03				<foreground star>
81	00 59 21.5	–72 23 20	5.0	11.4	1.43e−03±5.84e−04	1.1± 2.0	0.0	9.64e−03	218	1.00±0.41	0.52±0.06	XB? [KPFH99]
82	00 59 26.2	–72 10 02	4.0	30.5	3.10e−03±3.37e−04	5.8± 2.0	56.5	5.73e−02	148	0.90±0.02	−0.12±0.03	SNR 0057-72.2
83	01 00 04.6	–71 57 24	8.9	12.6	1.50e−03±3.53e−04	0.0± 0.0	0.0	2.46e−03	91	1.00±1.30	1.00±1.93	XB? or AGN? [KPFH99]
84	01 00 08.9	–72 57 46	8.3	12.6	7.87e−04±2.34e−04	0.0± 0.0	0.0					
85	01 00 12.0	–72 20 17	5.3	10.3	1.35e−03±5.71e−04	0.0± 0.0	0.0	1.62e−03	204	1.00±0.99	1.00±0.58	<XB> or <AGN>
86	01 00 13.3	–73 07 24	7.2	234.9	6.94e−03±6.05e−04	0.0± 0.0	0.0	2.94e−02	408	−0.27±0.10	0.23±0.15	foreground star? [KPFH99]
87	01 00 13.2	–72 41 20	4.6	13.1	5.51e−04±1.70e−04	0.0± 0.0	0.0	1.56e−03	301	1.00±0.52	1.00±0.92	
88	01 00 15.0	–72 04 41	4.1	48.4	1.66e−03±2.47e−04	2.7± 2.0	1.9	1.43e−03	123	1.00±0.38	1.00±0.57	XB? [KPFH99]
89	01 00 36.5	–73 00 35	7.1	164.9	3.64e−03±4.18e−04	1.2± 1.2	0.5	2.29e−02				<foreground star>
90	01 00 42.2	–72 11 33	3.3	1610.5	1.59e−02±6.34e−04	2.1± 0.9	22.5	2.67e−02	162	1.00±0.07	0.33±0.04	AGN? [KPFH99]
91	01 00 49.2	–72 03 46	5.5	11.4	7.20e−04±1.97e−04	0.0± 0.0	0.0	<9.15e−03				
92	01 00 56.2	–72 33 54	4.7	14.7	7.57e−04±2.00e−04	2.4± 1.9	1.9	4.16e−03	273	1.00±1.61	1.00±0.47	foreground star HD 6171
93	01 01 02.1	–72 06 56	3.7	181.6	1.15e−02±1.31e−03	2.3± 1.8	1.7	5.37e−02	132	1.00±0.15	0.47±0.04	HMXB RXJ0101.0-7206 [KP96],[SCB99]
94	01 01 19.3	–72 58 21	8.1	10.8	5.54e−04±1.85e−04	1.7± 2.2	0.1					
95	01 01 19.5	–72 11 18	3.6	235.1	5.61e−03±4.24e−04	3.4± 1.9	5.9	1.51e−02	159	1.00±0.98	1.00±0.47	<Be/X>
96	01 01 36.4	–72 04 18	4.3	96.4	3.91e−03±4.05e−04	0.0± 0.0	0.0	8.93e−03	121	1.00±0.29	0.18±0.09	<Be/X>
97	01 01 53.3	–72 23 35	10.3	15.2	1.95e−03±4.45e−04	0.0± 0.0	0.0	9.98e−03	220	1.00±0.28	0.68±0.08	<Be/X>
98	01 02 41.8	–72 32 40	4.9	44.1	2.19e−03±3.48e−04	0.0± 0.0	0.0	6.73e−03	267	1.00±0.33	0.49±0.08	AGN? [KPFH99]
99	01 02 44.1	–72 15 22	4.4	24.6	1.44e−03±3.67e−04	0.0± 0.0	0.0	4.05e−03	182	1.00±0.55	0.08±0.15	
100	01 02 51.2	–72 44 36	14.3	11.0	7.88e−03±2.59e−03	0.0± 0.0	0.0	<1.19e−02				

1	2	3	4	5	6	7	8	9	10	11	12	13
No	RA	Dec	r_{90}	ML_{exi}	Count rate	r_{ext}	ML_{ext}	Count rate PSPC	No PSPC	HR1	HR2	Remarks
	(J2000.0)		["]		[cts s^{-1}]	["]		[cts s^{-1}]				
101	01 03 13.3	−72 09 17	3.8	48.4	2.30e−03±4.40e−04	1.8± 1.7	1.1	1.54e−02	143	1.00±0.10	0.24±0.06	HMXB SAXJ0103.2-7209 [HS94],[ISC98]
102	01 03 14.9	−70 50 57	7.4	43.5	2.84e−03±4.30e−04	4.2± 2.0	18.5					
103	01 03 26.1	−70 53 39	7.2	80.3	2.54e−03±3.84e−04	1.7± 1.4	1.8					
104	01 03 28.8	−72 47 27	9.7	40.2	3.88e−03±5.84e−04	0.0± 0.0	0.0	1.31e−02	334	1.00±0.33	−0.08±0.07	AGN? [KPFH99]
105	01 03 37.2	−72 01 35	3.6	53.9	1.72e−03±3.07e−04	0.6± 1.3	0.0	1.15e+00	106	1.00±7.13	0.41±0.07	<Be/X>
106	01 03 53.9	−72 54 41	7.3	197.6	6.00e−03±5.65e−04	0.0± 0.0	0.0	4.40e−02	361	−1.00±0.10		SSS RXJ0103.8-7254 [KP96],[KPFH99]
107	01 04 00.3	−72 02 03	3.3	9732.8	2.47e−01±2.75e−03	5.8± 0.8	8561.7	2.24e+00	107	0.92±0.00	−0.20±0.01	SNR 0102-72.3
108	01 04 35.9	−72 21 48	4.0	21.9	9.63e−04±2.63e−04	0.0± 0.0	0.0					<Be/X>
109	01 05 02.6	−72 22 57	3.6	92.7	6.71e−03±5.16e−04	6.3± 1.8	161.0	3.14e−01	217	0.66±0.01	−0.32±0.02	SNR 0103-72.6
110	01 05 09.3	−72 11 50	7.8	13.2	1.58e−03±3.99e−04	0.0± 0.0	0.0	6.35e−03	163	1.00±0.20	0.40±0.09	HMXB AXJ0105-722 [YK98b],[FHP00]
111	01 05 13.9	−72 33 46	7.5	11.1	1.02e−03±2.78e−04	0.0± 0.0	0.0	<1.69e−03				
112	01 05 33.7	−72 13 29	4.7	40.6	1.76e−03±2.99e−04	0.0± 0.0	0.0	7.34e−03	172	1.00±0.37	0.46±0.09	AGN? [FHP00]
113	01 06 14.9	−72 05 27	7.4	38.1	8.49e−03±9.16e−04	15.5± 5.3	35.5	3.42e−02	125	1.00±0.06	0.19±0.04	SNR 0104-72.3
114	01 06 19.9	−72 27 52	3.3	2101.1	2.35e−02±9.41e−04	0.0± 0.0	0.0					
115	01 06 28.0	−72 22 24	6.4	11.3	5.00e−03±2.28e−03	0.0± 0.0	0.0					
116	01 06 57.6	−72 24 48	3.5	136.4	3.08e−03±3.57e−04	2.3± 1.4	5.7	1.20e−02	230	1.00±0.13	0.43±0.06	hard [HFPK00]
117	01 08 37.5	−72 25 01	3.8	45.9	1.29e−03±2.38e−04	1.0± 1.5	0.1	4.93e−03	232	1.00±0.23	0.39±0.10	hard [HFPK00]
118	01 17 05.1	−73 26 37	0.7	26285.8	3.12e+00±5.42e−02	1.9± 0.4	289.2	5.82e+00	482	0.97±0.00	0.39±0.00	HMXB SMC X-1
119	01 17 28.9	−73 11 44	4.2	12.0	2.24e−03±7.85e−04	2.3± 2.4	0.9	5.51e−03	431	1.00±0.54	0.30±0.09	foreground star G [SCC99]
120	01 18 37.9	−73 25 27	0.9	1546.7	2.74e−02±1.21e−03	2.9± 1.1	40.5	1.11e−01	478	0.12±0.02	0.07±0.02	foreground star HD 8191 [CSM97]
121	01 19 39.2	−73 27 32	7.0	13.8	1.50e−03±3.90e−04	0.0± 0.0	0.0	2.84e−03	488	−0.19±0.15	−1.00±1.95	<foreground star>

Appendix C

Finding Charts for New Classified Sources

Positions of newly classified HRI sources are shown on DSS2-red images. The comments in brackets $<$ $>$ give the classifications, as discussed in Sec. 5.4. The X-ray source position is in the center of the image, circles mark the 90% confidence error. For Be/X-ray binary candidates with emission line stars as proposed optical candidate, the star is additionally marked with a cross.
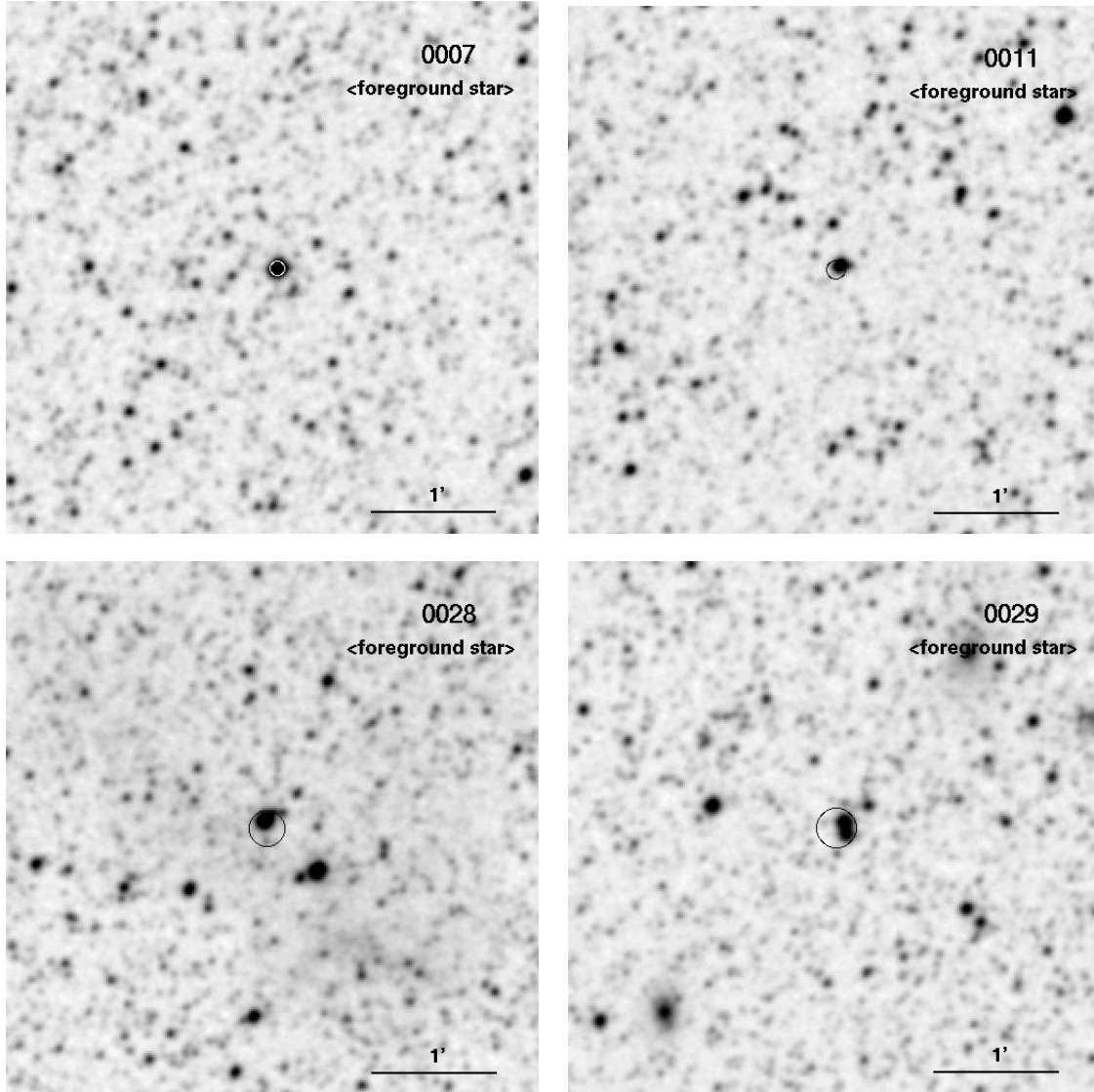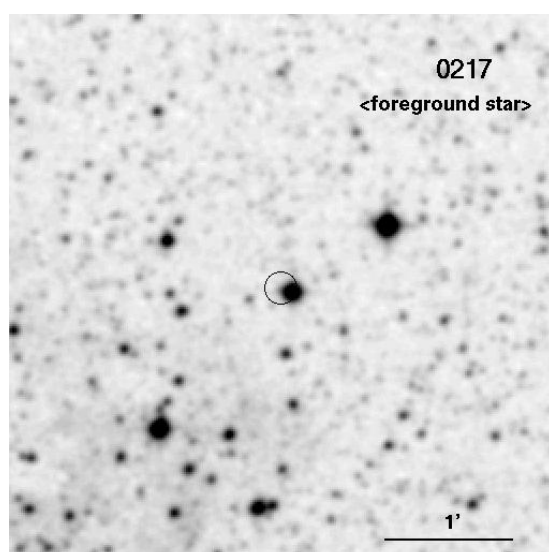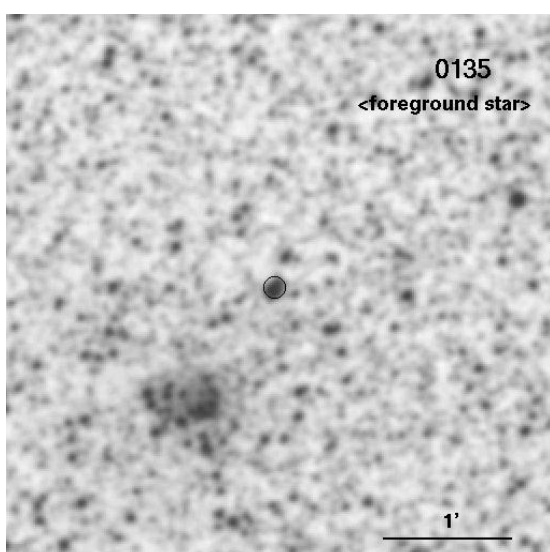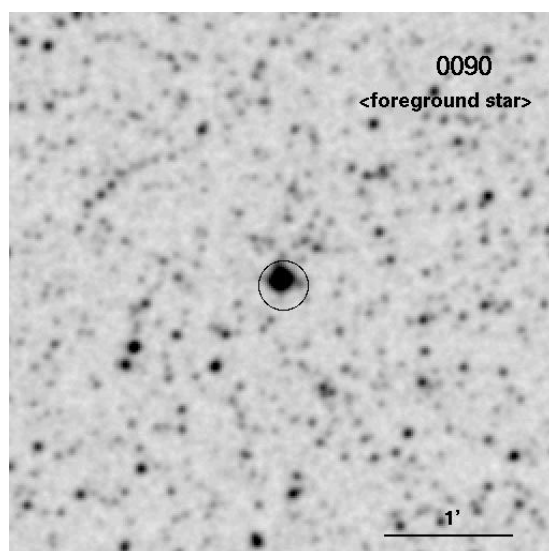
C.1 LMC Sources

Figure C.1: Finding charts for LMC sources.

0037
<foreground star>

1'

0049
<XB> or <AGN>

1'

0054
<foreground star>

1'

0090
<foreground star>

1'

0135
<foreground star>

1'

0217
<foreground star>

1'

0229
<foreground star>

1'

0230
<XB> or <AGN>

1'

0287
<foreground star>

1'

0290
<foreground star>

1'

0300
<foreground star>

1'

128

0313
<foreground star>
1'

0328
<HMXB>
1'

0332
<HMXB>
1'

0347
<foreground star>
1'

0364
<XB> or <AGN>
1'
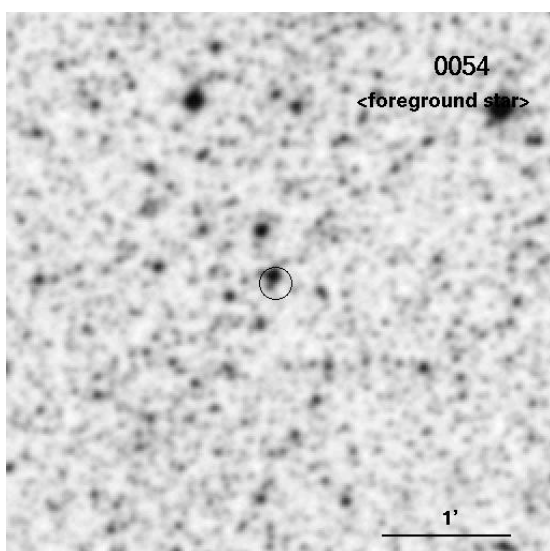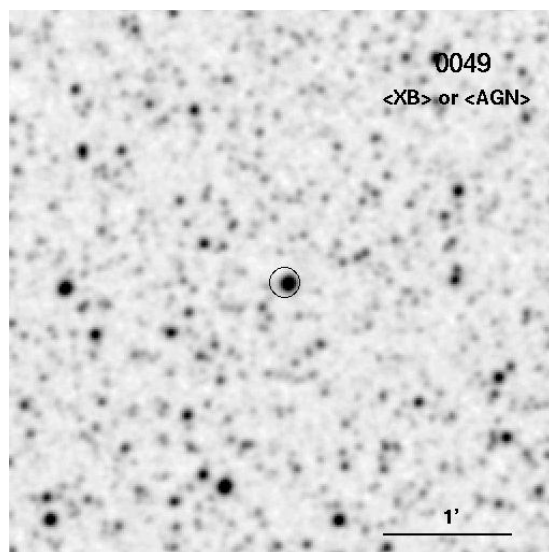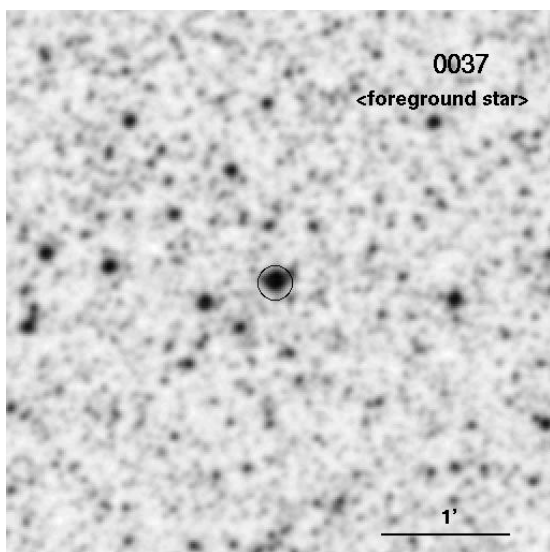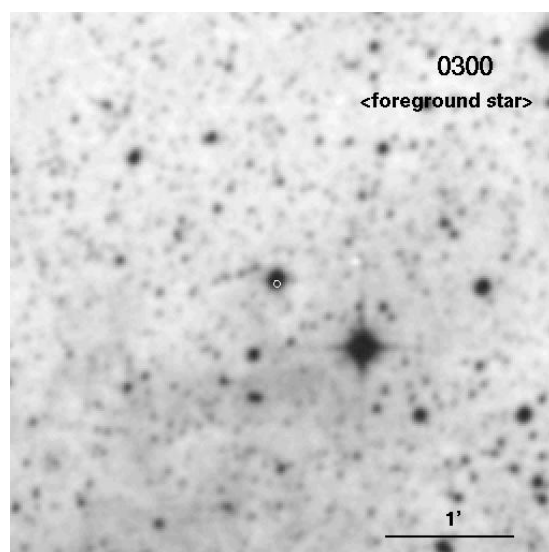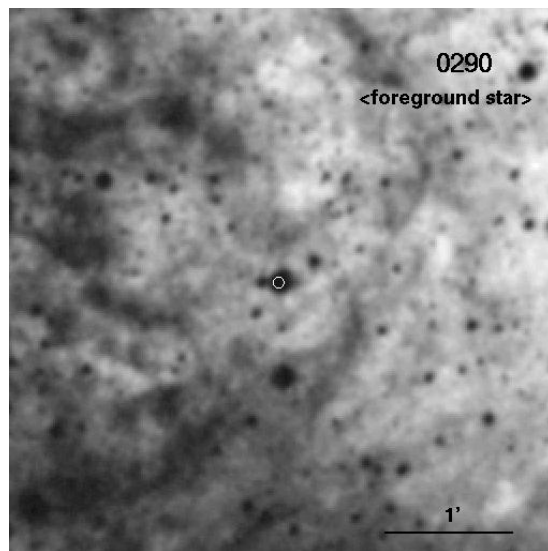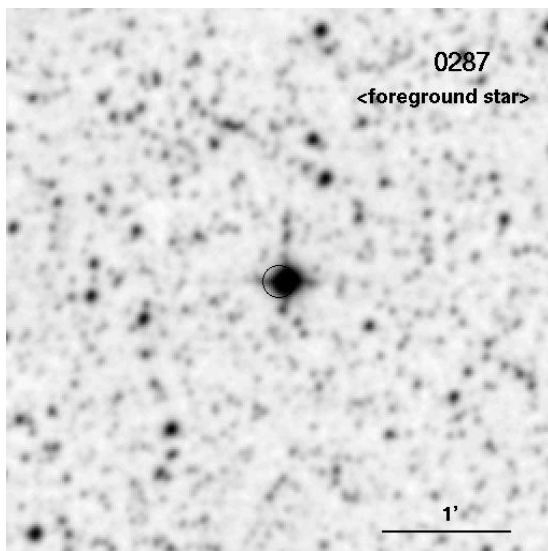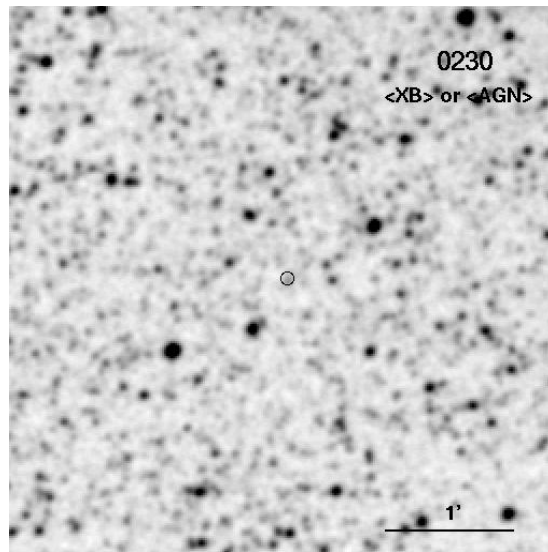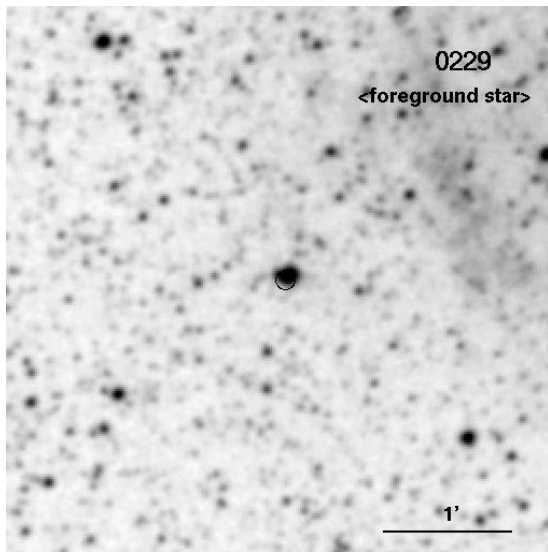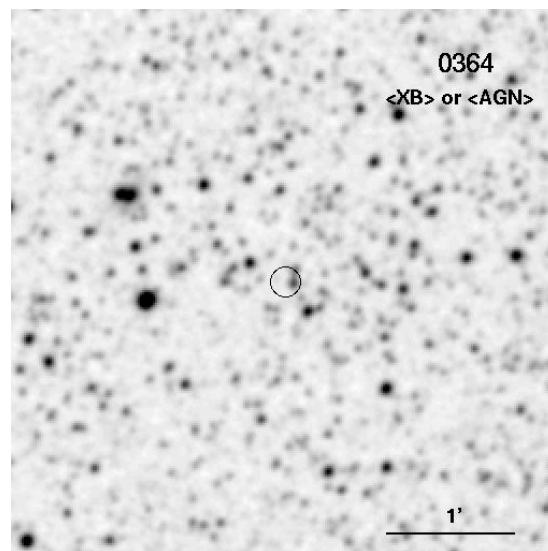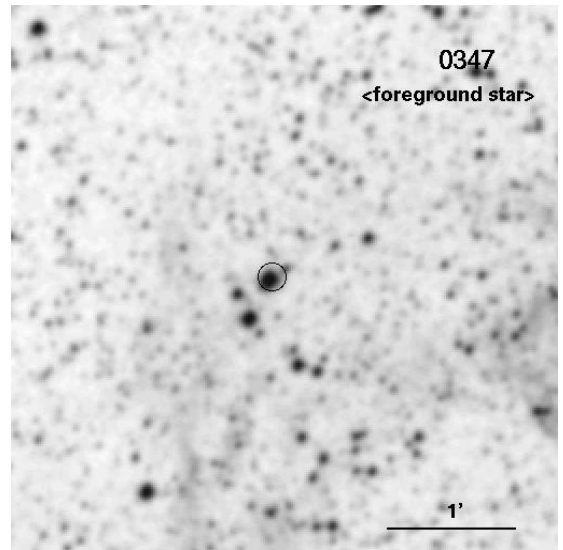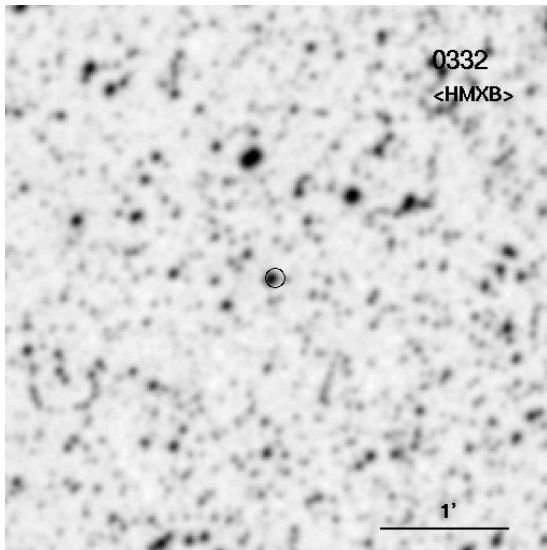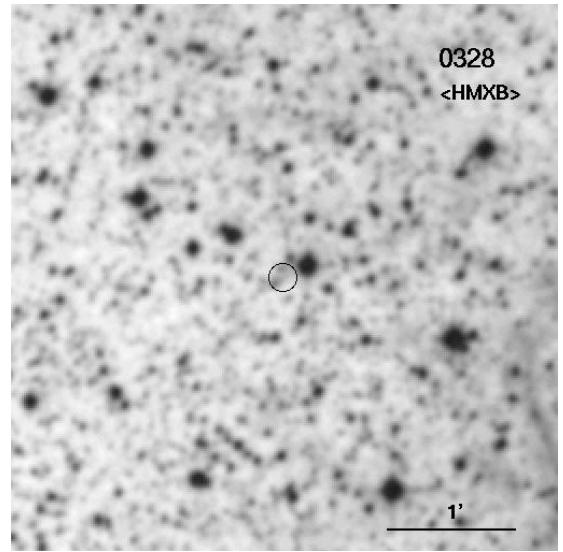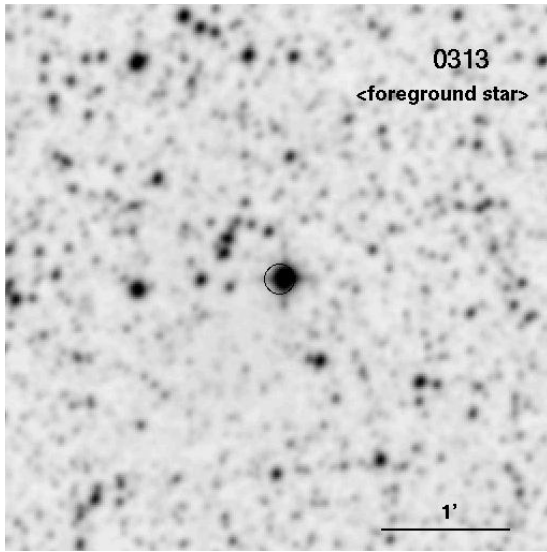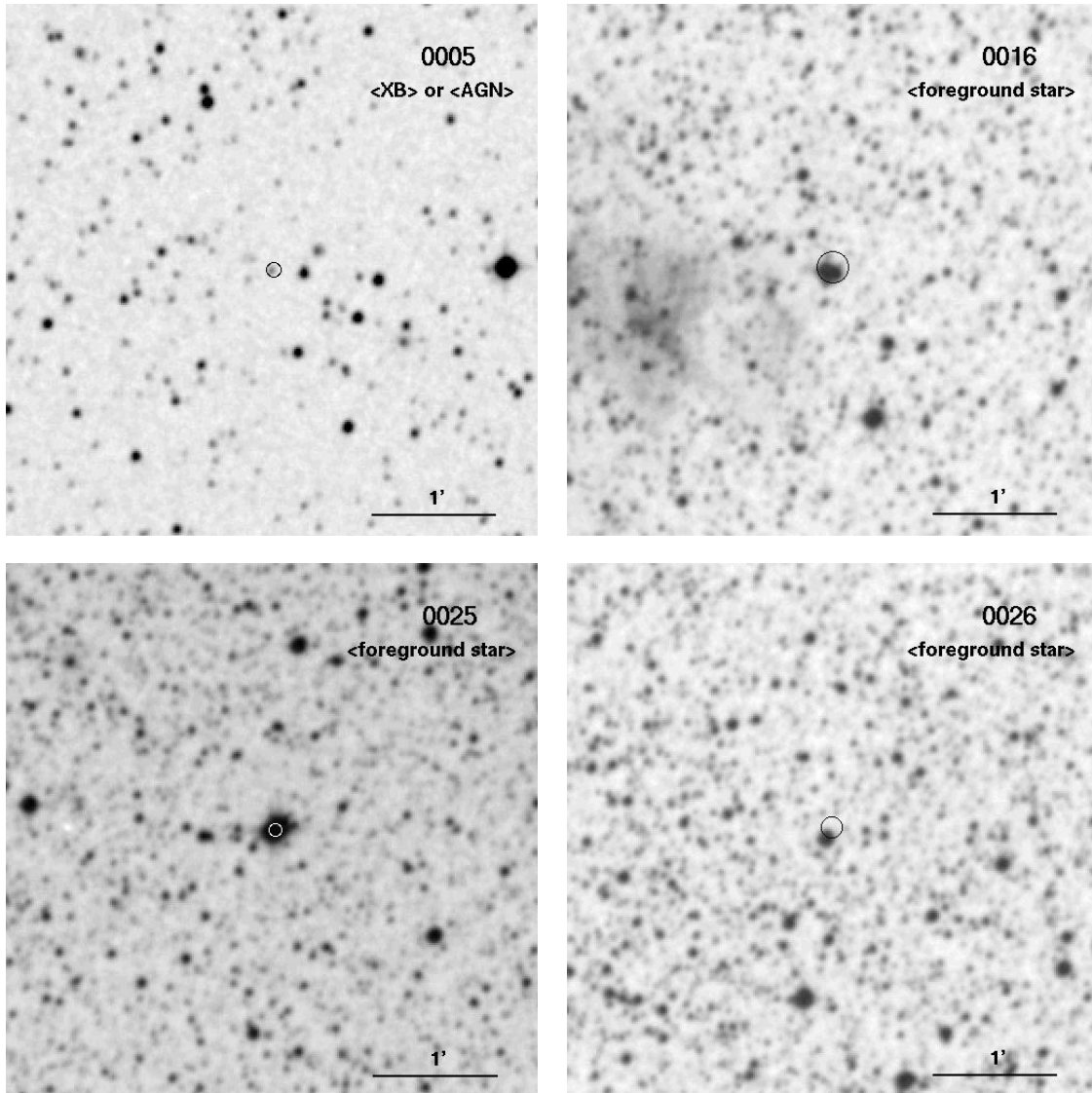
C.2 SMC Sources

Figure C.2: Finding charts for SMC sources.

0028
<Be/X>
1'

0035
<foreground star>
1'

0036
<Be/X>
1'

0048
<Be/X>
1'

0053
<XB> or <AGN>
1'

0057
<Be/X>
1'

0064
<AGN>
1'

0068
<foreground star>
1'

0071
<XB> or <AGN>
1'

0072
<XB> or <AGN>
1'

0074
<Be/X>
1'

0078
<XB> or <AGN>
1'

0080
<foreground star>
1'

0085
<XB> or <AGN>
1'

0089
<foreground star>
1'

0095
<Be/X>
1'

133

0096
<Be/X>
1'

0097
<Be/X>
1'

0105
<Be/X>
1'

0108
<Be/X>
1'

0121
<foreground star>
1'
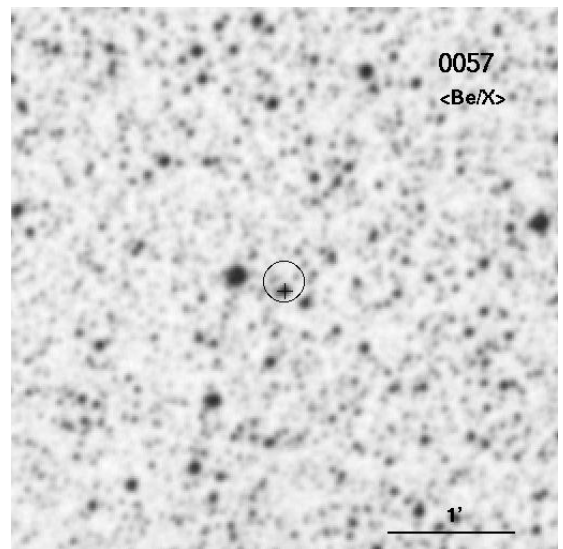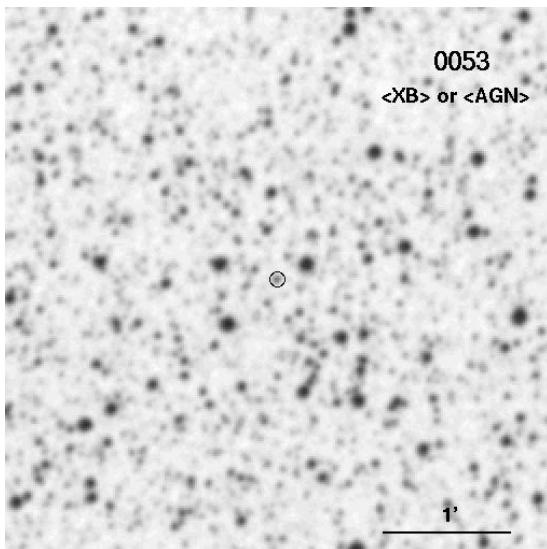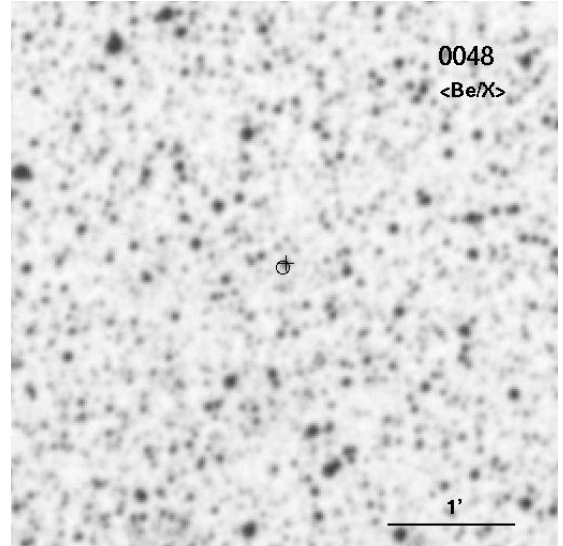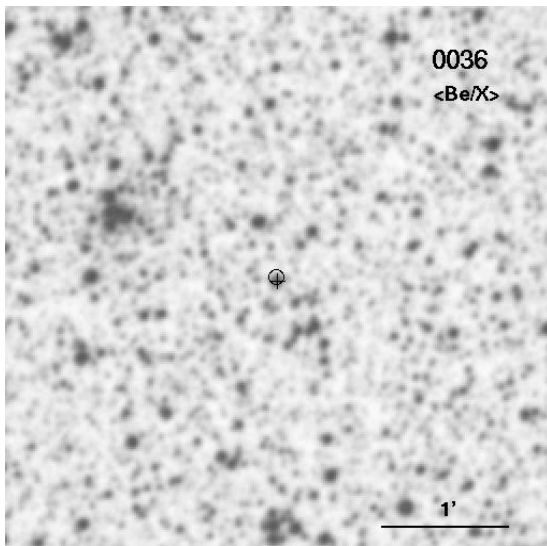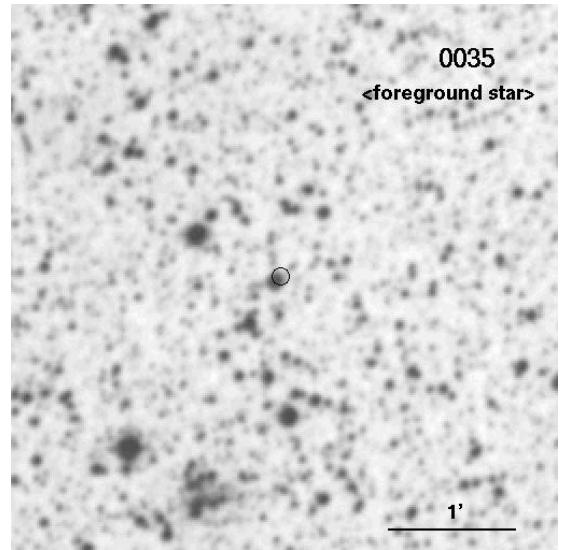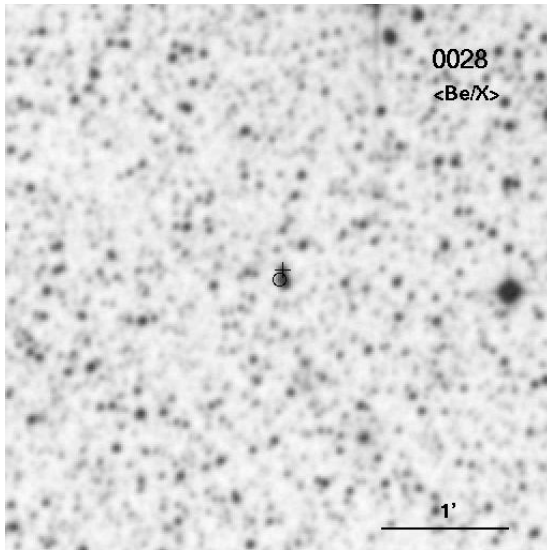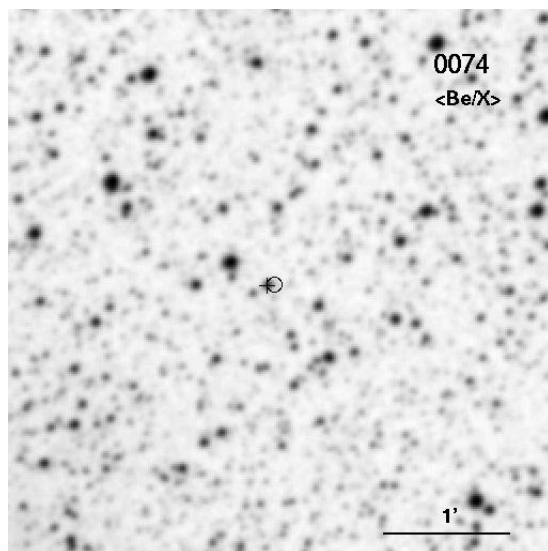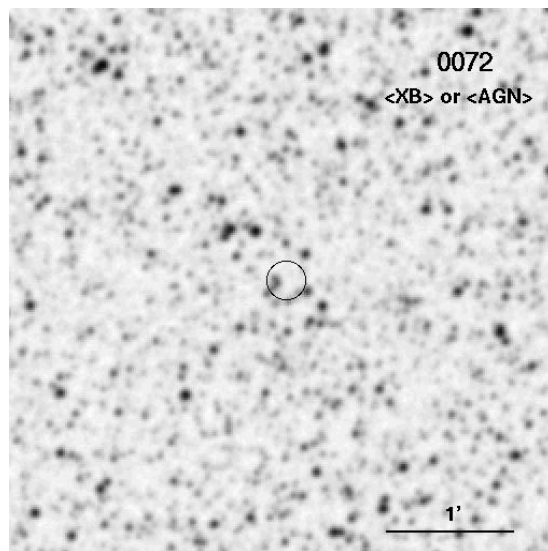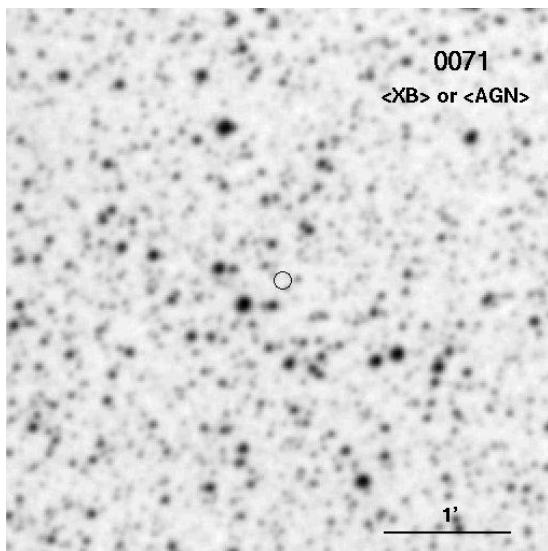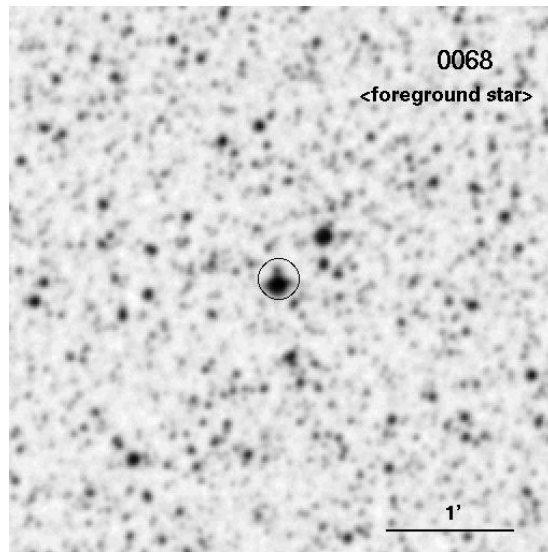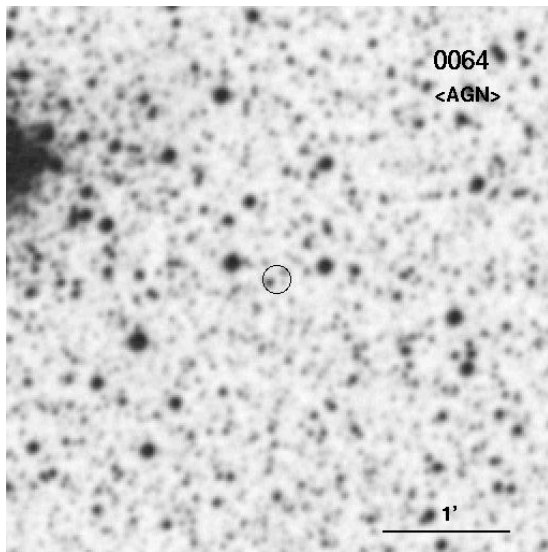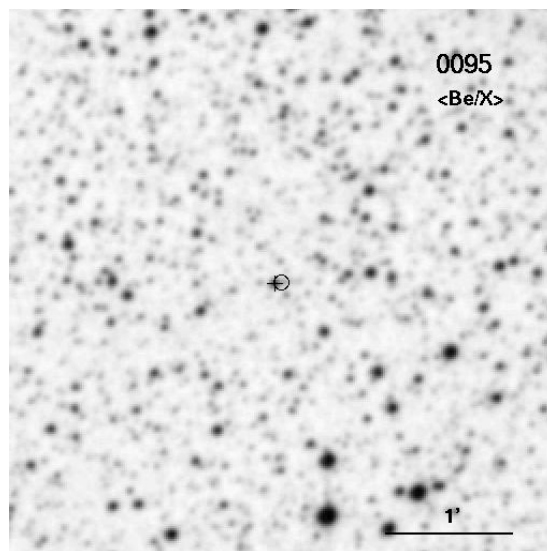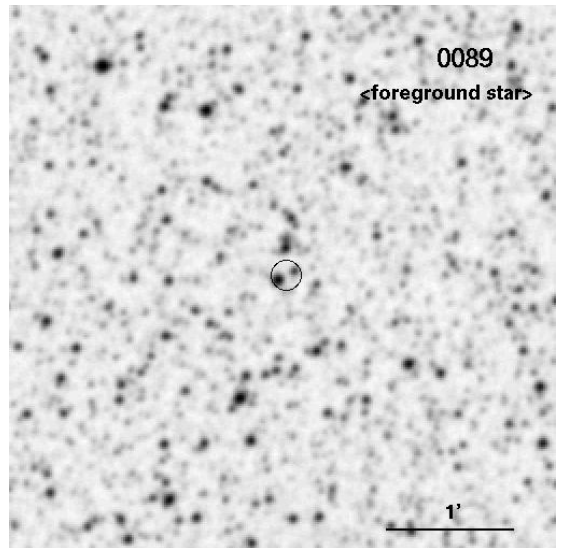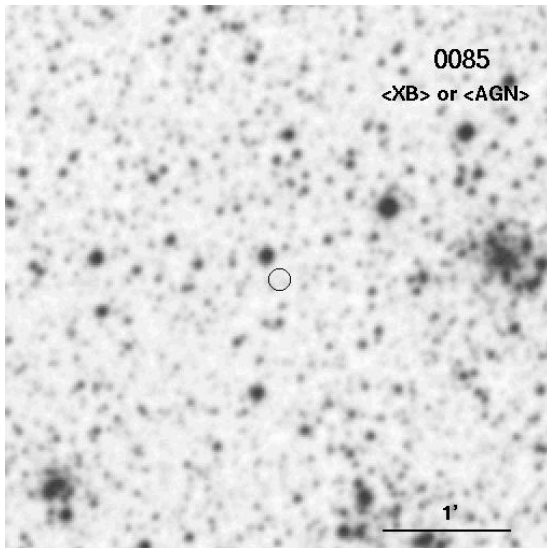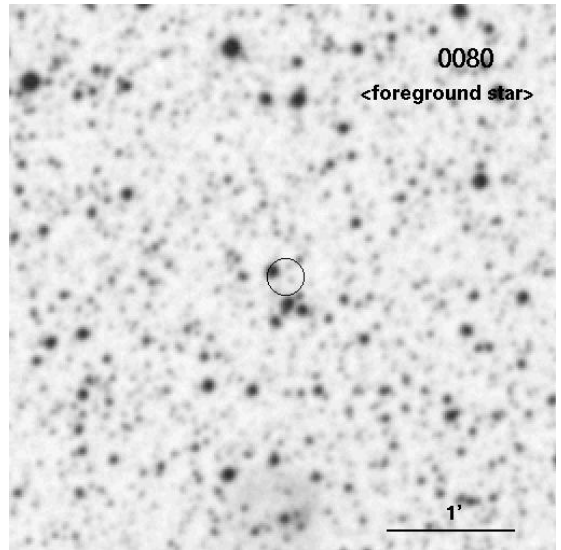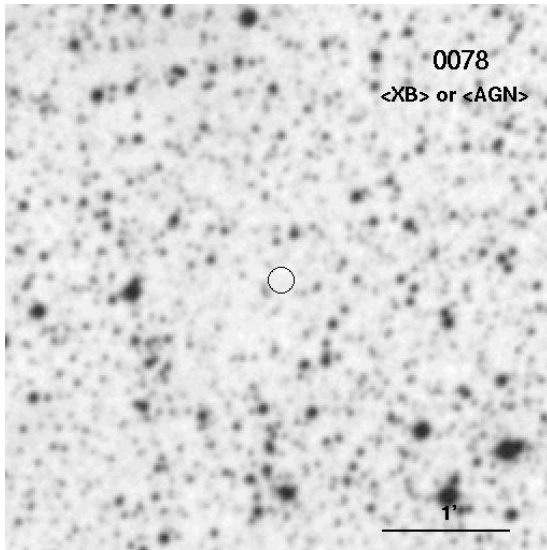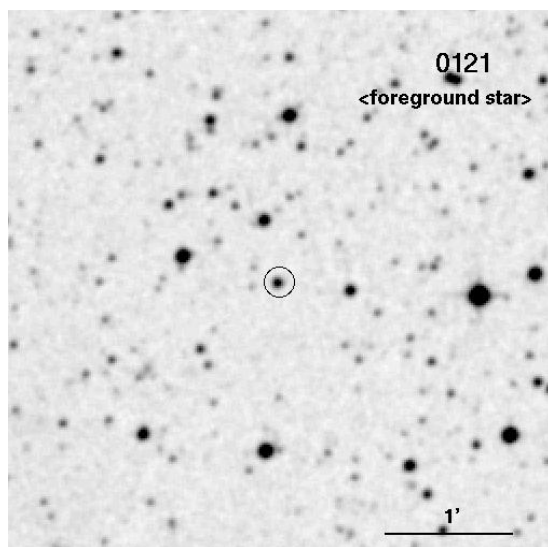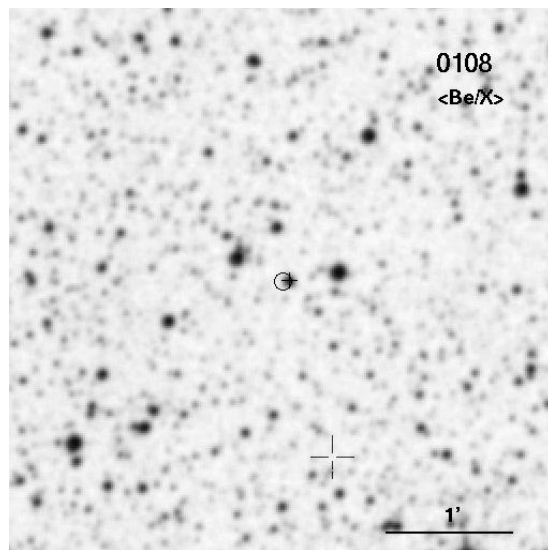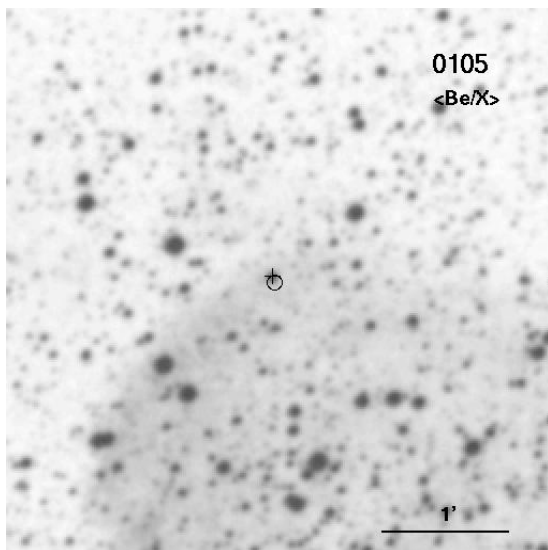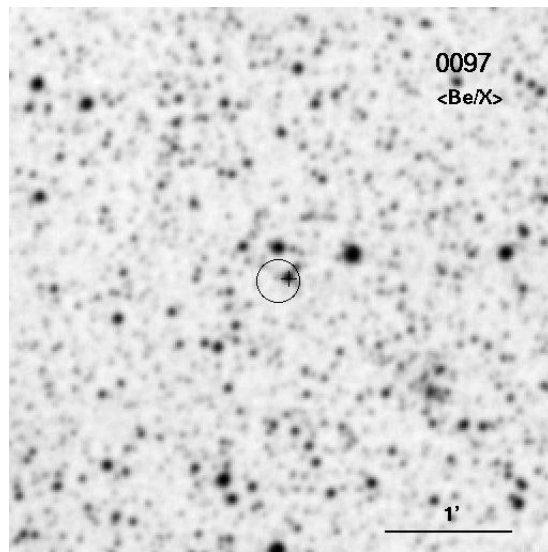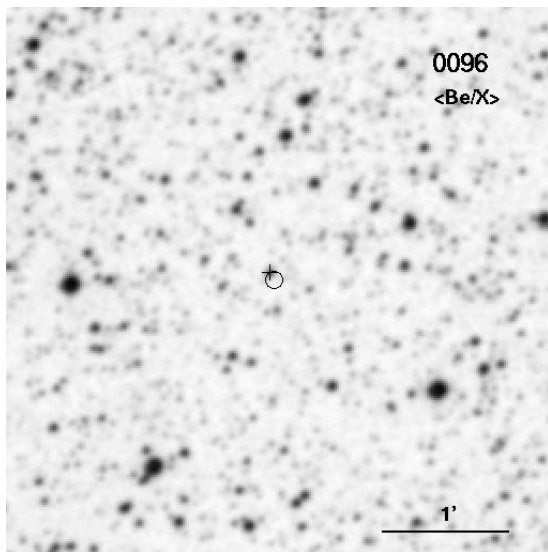
Appendix D

Spectral Parameters

Fit results of the spectral analysis of the ROSAT PSPC data are summarized in this part of the appendix. The diffuse X-ray emission from the Magellanic Clouds was modeled with a thermal spectrum (Raymond & Smith, 1977) for thin plasma with Galactic foreground absorption and absorbtion by the SMC or LMC. Tables D.1 and D.2 give the position of the regions within the galaxies selected for creating spectrum with number of events, plasma temperature T_{MC}, absorbing column density of the MCs $N_{\mathrm{H\,MC}}$, emission measure $EM_\square$ (see also Equation (6.3)), reduced χ^2, degrees of freedom (DOF), luminosity $L_\square$ of the selected square regions, thickness of the emitting gas Δl derived from the fit results, as well as the shock velocity corresponding to the measured temperature (see Sec. 6.1.5). For values resulting directly from the spectral fit the 90 % confidence range is given in bracketts. The systematic error is discussed in Section 6.1.4.

Table D.1: *Spectral fit parameters for the diffuse emission of the LMC.*

1	2		3	4	5	6	7	8	9	10	11
No	Center of Region RA	Dec (J2000.0)	No of events $[10^3]$	T_{MC} [keV]	$N_{H\,MC}$ $[10^{22}\ cm^{-2}]$	$EM_{\square}$ $[cm^{-5}]$	red. χ^2	DOF	$L_{\square}$ $[10^{36}$ erg/s]	Δl [kpc]	v [km/s]
1	04 53 58.8	-66 50 08	2.9	0.14 (+0.03,−0.01)	8.2e−01 (+8.7e−01,−4.1e−01)	6.9e−03 (+1.2e−02,−9.6e−04)	1.5	58	1.3e+01	3.0e+00	300
2	04 54 13.1	-67 05 08	1.2	0.22 (+0.03,−0.02)	3.3e−02 (+8.3e−02,−1.7e−02)	7.1e−04 (+1.0e−02,−9.9e−05)	2.5	25	9.7e−01	8.1e−01	400
3	04 59 39.2	-67 20 17	1.0	0.29 (+0.03,−0.03)	0.0e+00 (+5.0e−02,−0.0e+00)	8.0e−04 (+1.0e−02,−1.1e−04)	1.3	22	9.2e−01	1.6e+00	500
4	04 59 57.4	-67 35 17	1.5	0.24 (+0.03,−0.02)	0.0e+00 (+5.0e−02,−0.0e+00)	1.1e−03 (+1.0e−02,−1.6e−04)	1.9	36	1.5e+00	1.6e+00	500
5	05 00 16.2	-67 50 18	1.5	0.22 (+0.03,−0.02)	0.0e+00 (+5.0e−02,−0.0e+00)	1.2e−03 (+1.0e−02,−1.6e−04)	1.8	38	1.6e+00	1.3e+00	400
6	05 00 35.4	-68 05 18	1.3	0.20 (+0.03,−0.02)	0.0e+00 (+5.0e−02,−0.0e+00)	9.6e−04 (+1.0e−02,−1.3e−04)	1.7	29	1.4e+00	9.0e−01	400
7	05 00 55.2	-68 20 19	1.3	0.20 (+0.03,−0.02)	2.8e−02 (+7.8e−02,−1.4e−02)	5.6e−04 (+1.0e−02,−7.9e−05)	1.5	29	8.1e−01	5.6e−01	400
8	05 00 59.3	-66 20 19	4.1	0.11 (+0.03,−0.01)	7.5e−01 (+8.0e−01,−3.7e−01)	8.1e−03 (+1.2e−02,−1.1e−03)	1.4	63	1.7e+01	2.4e+00	300
9	05 01 15.2	-68 35 20	2.0	0.22 (+0.03,−0.02)	6.0e−02 (+1.1e−01,−3.0e−02)	1.1e−03 (+1.0e−02,−1.6e−04)	2.1	45	1.5e+00	1.3e+00	400
10	05 01 17.8	-66 35 20	4.5	0.15 (+0.03,−0.01)	3.8e−01 (+4.3e−01,−1.9e−01)	1.0e−03 (+1.0e−02,−1.4e−04)	1.6	79	1.7e+00	5.8e−01	400
11	05 01 36.5	-66 50 20	4.7	0.19 (+0.03,−0.02)	5.6e−02 (+1.1e−01,−2.8e−02)	2.2e−03 (+1.1e−02,−3.1e−04)	1.3	82	3.3e+00	1.8e+00	400
12	05 01 55.4	-67 05 21	3.0	0.31 (+0.03,−0.03)	0.0e+00 (+5.0e−02,−0.0e+00)	8.4e−04 (+1.0e−02,−1.2e−04)	1.8	59	9.2e−01	2.0e+00	500
13	05 02 15.0	-67 20 21	2.3	0.18 (+0.03,−0.02)	2.4e−01 (+2.9e−01,−1.2e−01)	4.4e−03 (+1.1e−02,−6.1e−04)	1.1	51	6.8e+00	3.2e+00	400
14	05 02 18.5	-69 20 21	1.3	0.23 (+0.03,−0.02)	0.0e+00 (+5.0e−02,−0.0e+00)	1.9e−03 (+1.1e−02,−2.7e−04)	1.3	29	2.6e+00	2.4e+00	400
15	05 03 16.2	-68 05 23	2.3	0.15 (+0.03,−0.01)	3.4e−01 (+3.9e−01,−1.7e−01)	1.2e−03 (+1.0e−02,−1.7e−04)	1.2	51	2.1e+00	6.5e−01	400
16	05 03 37.8	-68 20 24	1.6	0.18 (+0.03,−0.01)	0.0e+00 (+5.0e−02,−0.0e+00)	1.4e−03 (+1.0e−02,−2.0e−04)	1.2	40	2.2e+00	1.1e+00	400
17	05 03 59.6	-68 35 24	2.0	0.13 (+0.03,−0.01)	7.9e−01 (+8.4e−01,−4.0e−01)	6.8e−03 (+1.2e−02,−9.5e−04)	1.2	45	1.3e+01	2.9e+00	300
18	05 04 29.5	-67 05 25	4.2	0.15 (+0.03,−0.01)	3.4e−01 (+3.9e−01,−1.7e−01)	1.0e−03 (+1.0e−02,−1.4e−04)	1.4	75	1.8e+00	5.5e−01	400
19	05 04 45.0	-69 05 25	1.6	0.17 (+0.03,−0.02)	2.3e−01 (+2.8e−01,−1.2e−01)	5.1e−03 (+1.2e−02,−7.1e−04)	1.9	37	8.0e+00	3.6e+00	400
20	05 04 50.7	-67 20 25	1.6	0.12 (+0.03,−0.01)	1.0e−01 (+1.5e−01,−5.2e−02)	1.2e−03 (+1.0e−02,−1.7e−04)	2.3	38	2.3e+00	4.2e−01	300
21	05 05 08.6	-69 20 26	1.9	0.22 (+0.03,−0.02)	0.0e+00 (+5.0e−02,−0.0e+00)	2.0e−03 (+1.1e−02,−2.8e−04)	1.3	44	2.8e+00	2.4e+00	400
22	05 05 12.2	-67 35 26	1.6	0.15 (+0.03,−0.01)	1.5e−02 (+6.5e−02,−7.3e−03)	3.9e−03 (+1.1e−02,−5.5e−04)	2.1	35	6.8e+00	2.1e+00	400
23	05 05 34.3	-67 50 27	1.1	0.14 (+0.03,−0.01)	5.0e−01 (+5.5e−01,−2.5e−01)	3.1e−03 (+1.1e−02,−4.3e−04)	1.5	26	5.4e+00	1.5e+00	300
24	05 05 57.0	-68 05 27	1.1	0.19 (+0.03,−0.02)	8.1e−02 (+1.3e−01,−4.0e−02)	2.1e−03 (+1.1e−02,−2.9e−04)	1.2	26	3.1e+00	1.8e+00	400
25	05 05 57.7	-69 50 27	1.3	0.23 (+0.03,−0.02)	1.0e−01 (+1.5e−01,−5.1e−02)	2.1e−03 (+1.1e−02,−2.9e−04)	1.2	30	2.7e+00	2.7e+00	400
26	05 06 20.3	-68 20 28	1.6	0.16 (+0.03,−0.01)	3.3e−01 (+3.8e−01,−1.6e−01)	9.5e−03 (+1.3e−02,−1.3e−03)	1.0	37	1.6e+01	5.8e+00	400
27	05 06 23.0	-70 05 28	1.5	0.16 (+0.03,−0.01)	3.6e−01 (+4.1e−01,−1.8e−01)	1.1e−03 (+1.0e−02,−1.5e−04)	0.8	36	1.8e+00	6.5e−01	400
28	05 06 41.6	-66 50 29	3.0	0.11 (+0.03,−0.01)	3.5e−01 (+4.0e−01,−1.7e−01)	3.4e−03 (+1.1e−02,−4.7e−04)	1.4	55	7.0e+00	9.8e−01	300
29	05 06 44.0	-68 35 29	2.0	0.19 (+0.03,−0.02)	4.5e−01 (+5.0e−01,−2.2e−01)	1.0e−02 (+1.3e−02,−1.4e−03)	1.4	49	1.5e+01	8.3e+00	400
30	05 07 03.7	-67 05 29	1.4	0.11 (+0.03,−0.01)	1.6e−01 (+2.1e−01,−8.1e−02)	2.4e−03 (+1.1e−02,−3.4e−04)	0.9	31	5.0e+00	6.6e−01	300
31	05 07 49.6	-67 35 31	1.6	0.15 (+0.03,−0.01)	8.2e−03 (+5.8e−02,−4.1e−03)	4.2e−03 (+1.1e−02,−5.8e−04)	1.4	39	7.1e+00	2.3e+00	400
32	05 08 13.4	-67 50 31	3.0	0.17 (+0.03,−0.02)	0.0e+00 (+5.0e−02,−0.0e+00)	3.4e−03 (+1.1e−02,−4.7e−04)	1.5	62	5.3e+00	2.5e+00	400
33	05 08 24.8	-69 35 32	1.6	0.24 (+0.03,−0.02)	0.0e+00 (+5.0e−02,−0.0e+00)	2.3e−03 (+1.1e−02,−3.3e−04)	1.7	39	3.0e+00	3.3e+00	500
34	05 08 37.8	-68 05 32	2.0	0.14 (+0.03,−0.01)	5.1e−01 (+5.6e−01,−2.5e−01)	2.9e−03 (+1.1e−02,−4.1e−04)	1.5	45	5.3e+00	1.3e+00	300
35	05 08 50.8	-66 35 32	2.0	0.11 (+0.03,−0.01)	9.0e−02 (+1.4e−01,−4.5e−02)	9.3e−03 (+1.3e−02,−1.3e−03)	1.5	42	1.9e+01	2.9e+00	300
36	05 08 51.9	-69 50 32	1.6	0.25 (+0.03,−0.02)	0.0e+00 (+5.0e−02,−0.0e+00)	2.1e−03 (+1.1e−02,−2.9e−04)	1.1	38	2.7e+00	3.1e+00	500
37	05 09 19.2	-70 05 33	1.9	0.25 (+0.03,−0.02)	0.0e+00 (+5.0e−02,−0.0e+00)	1.9e−03 (+1.1e−02,−2.6e−04)	1.2	46	2.3e+00	2.7e+00	500
38	05 09 41.2	-71 50 34	1.3	0.19 (+0.03,−0.02)	1.8e−02 (+6.8e−02,−8.9e−03)	2.9e−04 (+1.0e−02,−4.1e−05)	1.3	30	4.3e−01	2.6e−01	400
39	05 09 47.5	-70 20 34	1.6	0.22 (+0.03,−0.02)	0.0e+00 (+5.0e−02,−0.0e+00)	1.5e−03 (+1.0e−02,−2.2e−04)	1.2	38	2.1e+00	1.8e+00	400
40	05 09 54.5	-68 50 34	1.8	0.22 (+0.03,−0.02)	3.2e−01 (+3.7e−01,−1.6e−01)	5.5e−03 (+1.2e−02,−7.7e−04)	2.0	44	7.5e+00	6.3e+00	400
41	05 10 02.2	-67 20 34	1.8	0.15 (+0.03,−0.01)	6.2e−02 (+1.1e−01,−3.1e−02)	6.6e−03 (+1.2e−02,−9.2e−04)	1.5	44	1.2e+01	3.4e+00	400
42	05 10 16.4	-70 35 35	1.3	0.19 (+0.03,−0.02)	1.2e−01 (+1.7e−01,−6.0e−02)	2.9e−03 (+1.1e−02,−4.1e−04)	1.3	33	4.4e+00	2.4e+00	400
43	05 10 48.7	-69 20 36	1.4	0.18 (+0.03,−0.02)	4.8e−01 (+5.3e−01,−2.4e−01)	1.6e−03 (+1.0e−02,−2.2e−04)	1.0	31	2.4e+00	1.2e+00	400
44	05 10 52.4	-67 50 36	3.1	0.17 (+0.03,−0.02)	6.1e−03 (+5.6e−02,−3.0e−03)	2.8e−03 (+1.1e−02,−4.0e−04)	1.2	63	4.5e+00	2.0e+00	400
45	05 11 16.8	-69 35 37	2.1	0.18 (+0.03,−0.02)	3.1e−01 (+3.6e−01,−1.6e−01)	1.0e−02 (+1.3e−02,−1.4e−03)	1.2	50	1.5e+01	8.1e+00	400
46	05 11 18.6	-68 05 36	1.4	0.15 (+0.03,−0.01)	0.0e+00 (+5.0e−02,−0.0e+00)	2.8e−03 (+1.1e−02,−3.9e−04)	1.8	32	4.9e+00	1.5e+00	400
47	05 11 46.0	-69 50 37	2.4	0.23 (+0.03,−0.02)	5.2e−03 (+5.5e−02,−2.6e−03)	3.3e−03 (+1.1e−02,−4.7e−04)	1.2	56	4.5e+00	4.1e+00	400
48	05 12 15.4	-70 05 38	2.0	0.23 (+0.03,−0.02)	0.0e+00 (+5.0e−02,−0.0e+00)	2.5e−03 (+1.1e−02,−3.5e−04)	1.3	48	3.3e+00	3.3e+00	400
49	05 12 40.7	-68 50 39	1.7	0.26 (+0.03,−0.02)	2.3e−02 (+7.3e−02,−1.2e−02)	2.1e−03 (+1.1e−02,−2.9e−04)	1.9	41	2.6e+00	3.5e+00	500
50	05 13 04.3	-67 35 40	2.8	0.11 (+0.03,−0.01)	2.3e−01 (+2.8e−01,−1.1e−01)	3.0e−03 (+1.1e−02,−4.2e−04)	1.0	58	6.1e+00	9.1e−01	300

Table D.1: Continued (LMC).

1	2		3	4	5	6	7	8	9	10	11
No	Center of Region RA Dec (J2000.0)		No of events [10^3]	T_{MC} [keV]	$N_{H\,MC}$ [10^{22} cm^{-2}]	$EM_\square$ [cm^{-5}]	red. χ^2	DOF	$L_\square$ [10^{36} erg/s]	Δl [kpc]	v [km/s]
51	05 13 09.4	-69 05 40	1.4	0.23 (+0.03,–0.02)	1.0e–01 (+1.5e–01,–5.1e–02)	3.8e–03 (+1.1e–02,–5.3e–04)	0.8	35	5.1e+00	4.8e+00	400
52	05 13 17.0	-70 35 40	1.2	0.20 (+0.03,–0.02)	2.7e–01 (+3.2e–01,–1.4e–01)	3.2e–03 (+1.1e–02,–4.5e–04)	1.8	25	4.7e+00	3.1e+00	400
53	05 13 31.5	-67 50 40	3.2	0.17 (+0.03,–0.01)	8.0e–04 (+5.1e–02,–4.0e–04)	5.0e–03 (+1.1e–02,–7.0e–04)	1.5	69	8.1e+00	3.3e+00	400
54	05 13 38.8	-69 20 41	3.2	0.24 (+0.03,–0.02)	2.3e–01 (+2.8e–01,–1.1e–01)	7.6e–03 (+1.2e–02,–1.1e–03)	1.4	72	9.9e+00	1.0e+01	400
55	05 13 59.4	-68 05 41	5.3	0.18 (+0.03,–0.02)	8.0e–02 (+1.3e–01,–4.0e–02)	4.2e–03 (+1.1e–02,–5.9e–04)	1.3	91	6.4e+00	3.3e+00	400
56	05 14 08.9	-69 35 42	2.6	0.25 (+0.03,–0.02)	0.0e+00 (+5.0e–02,–0.0e+00)	3.2e–03 (+1.1e–02,–4.5e–04)	1.9	62	4.0e+00	4.8e+00	500
57	05 14 40.1	-69 50 42	1.6	0.20 (+0.03,–0.02)	0.0e+00 (+5.0e–02,–0.0e+00)	2.7e–03 (+1.1e–02,–3.7e–04)	1.8	39	3.8e+00	2.6e+00	400
58	05 14 57.2	-68 35 43	1.2	0.17 (+0.03,–0.01)	0.0e+00 (+5.0e–02,–0.0e+00)	3.0e–03 (+1.1e–02,–4.1e–04)	2.2	28	4.8e+00	2.0e+00	400
59	05 15 11.7	-70 05 43	1.8	0.28 (+0.03,–0.03)	0.0e+00 (+5.0e–02,–0.0e+00)	1.5e–03 (+1.0e–02,–2.0e–04)	1.2	44	1.7e+00	2.7e+00	500
60	05 15 41.7	-67 35 44	3.1	0.16 (+0.03,–0.01)	9.4e–02 (+1.4e–01,–4.7e–02)	6.4e–03 (+1.2e–02,–9.0e–04)	1.7	64	1.1e+01	4.0e+00	400
61	05 15 44.3	-70 20 44	1.6	0.14 (+0.03,–0.01)	6.4e–01 (+6.9e–01,–3.2e–01)	4.6e–03 (+1.1e–02,–6.4e–04)	1.4	40	8.1e+00	2.3e+00	300
62	05 15 57.6	-69 05 45	3.6	0.23 (+0.03,–0.02)	1.1e–01 (+1.6e–01,–5.3e–02)	5.1e–03 (+1.2e–02,–7.2e–04)	1.5	79	6.7e+00	6.8e+00	400
63	05 16 10.6	-67 50 45	2.7	0.18 (+0.03,–0.02)	4.9e–02 (+9.9e–02,–2.4e–02)	3.7e–03 (+1.1e–02,–5.1e–04)	1.0	58	5.7e+00	2.8e+00	400
64	05 16 17.6	-70 35 45	1.0	0.16 (+0.03,–0.01)	8.3e–02 (+1.3e–01,–4.1e–02)	3.7e–03 (+1.1e–02,–5.2e–04)	1.3	23	6.3e+00	2.2e+00	400
65	05 16 23.9	-66 35 45	1.4	0.10 (+0.03,–0.01)	2.1e–01 (+2.6e–01,–1.1e–01)	4.1e–03 (+1.1e–02,–5.8e–04)	2.3	33	8.8e+00	1.1e+00	300
66	05 16 28.9	-69 20 46	2.4	0.26 (+0.03,–0.02)	0.0e+00 (+5.0e–02,–0.0e+00)	4.6e–03 (+1.1e–02,–6.5e–04)	1.1	58	5.8e+00	7.3e+00	500
67	05 16 40.2	-68 05 46	1.5	0.17 (+0.03,–0.02)	2.3e–01 (+2.8e–01,–1.1e–01)	3.8e–03 (+1.1e–02,–5.4e–04)	1.2	36	6.1e+00	2.7e+00	400
68	05 17 01.0	-69 35 47	2.1	0.24 (+0.03,–0.02)	0.0e+00 (+5.0e–02,–0.0e+00)	4.5e–03 (+1.1e–02,–6.3e–04)	0.9	50	5.8e+00	6.4e+00	500
69	05 17 10.7	-68 20 47	1.8	0.22 (+0.03,–0.02)	2.9e–01 (+3.4e–01,–1.5e–01)	4.7e–03 (+1.1e–02,–6.5e–04)	1.1	45	6.4e+00	5.3e+00	400
70	05 17 20.3	-67 05 47	2.0	0.11 (+0.03,–0.01)	2.6e–01 (+3.1e–01,–1.3e–01)	3.8e–03 (+1.1e–02,–5.4e–04)	1.2	45	7.8e+00	1.2e+00	300
71	05 17 20.9	-72 20 47	2.1	0.15 (+0.03,–0.01)	1.1e+00 (+1.2e+00,–5.6e–01)	2.2e–03 (+1.1e–02,–3.0e–04)	1.9	41	3.8e+00	1.1e+00	400
72	05 17 27.5	-71 05 47	1.2	0.23 (+0.03,–0.02)	6.6e–02 (+1.2e–01,–3.3e–02)	6.1e–04 (+1.0e–02,–8.5e–05)	1.4	27	8.1e–01	7.5e–01	400
73	05 17 34.3	-69 50 48	3.5	0.26 (+0.03,–0.02)	0.0e+00 (+5.0e–02,–0.0e+00)	3.0e–03 (+1.1e–02,–4.2e–04)	1.4	77	3.8e+00	4.7e+00	500
74	05 17 41.6	-68 35 48	2.4	0.14 (+0.03,–0.01)	6.8e–01 (+7.3e–01,–3.4e–01)	6.8e–03 (+1.2e–02,–9.5e–04)	1.2	57	1.2e+01	3.3e+00	300
75	05 17 49.5	-67 20 48	2.7	0.18 (+0.03,–0.02)	0.0e+00 (+5.0e–02,–0.0e+00)	3.5e–03 (+1.1e–02,–4.8e–04)	1.6	59	5.3e+00	2.7e+00	400
76	05 18 03.7	-71 20 49	2.2	0.22 (+0.03,–0.02)	6.1e–01 (+6.6e–01,–3.0e–01)	2.3e–03 (+1.1e–02,–3.2e–04)	1.0	43	3.2e+00	2.7e+00	400
77	05 18 07.9	-70 05 49	2.4	0.18 (+0.03,–0.02)	4.6e–01 (+5.1e–01,–2.3e–01)	1.3e–03 (+1.0e–02,–1.9e–04)	0.9	54	2.0e+00	1.1e+00	400
78	05 18 19.2	-67 35 49	3.4	0.19 (+0.03,–0.02)	6.9e–03 (+5.7e–02,–3.4e–03)	3.6e–03 (+1.1e–02,–5.0e–04)	1.3	71	5.3e+00	3.1e+00	400
79	05 18 45.7	-69 05 50	3.4	0.27 (+0.03,–0.02)	0.0e+00 (+5.0e–02,–0.0e+00)	2.9e–03 (+1.1e–02,–4.0e–04)	1.5	75	3.5e+00	4.9e+00	500
80	05 18 49.7	-67 50 50	3.1	0.19 (+0.03,–0.02)	0.0e+00 (+5.0e–02,–0.0e+00)	2.5e–03 (+1.1e–02,–3.4e–04)	2.0	62	3.7e+00	2.0e+00	400
81	05 19 18.2	-70 35 51	1.6	0.21 (+0.03,–0.02)	7.5e–02 (+1.3e–01,–3.8e–02)	1.8e–03 (+1.1e–02,–2.6e–04)	0.8	37	2.6e+00	1.9e+00	400
82	05 19 18.9	-71 50 51	1.6	0.43 (+0.03,–0.04)	2.4e+00 (+2.4e+00,–1.2e+00)	1.7e–03 (+1.1e–02,–2.4e–04)	1.3	40	1.5e+00	7.6e+00	600
83	05 19 19.0	-69 20 51	1.7	0.23 (+0.03,–0.02)	0.0e+00 (+5.0e–02,–0.0e+00)	4.6e–03 (+1.1e–02,–6.4e–04)	1.6	40	6.0e+00	5.8e+00	400
84	05 19 21.1	-68 05 51	1.4	0.28 (+0.03,–0.02)	1.0e–04 (+5.0e–02,–5.0e–05)	1.1e–03 (+1.0e–02,–1.5e–04)	1.8	30	1.3e+00	2.0e+00	500
85	05 19 53.1	-69 35 52	2.7	0.27 (+0.03,–0.02)	0.0e+00 (+5.0e–02,–0.0e+00)	4.1e–03 (+1.1e–02,–5.8e–04)	1.2	68	5.0e+00	7.3e+00	500
86	05 19 54.4	-67 05 52	2.2	0.14 (+0.03,–0.01)	6.9e–02 (+1.2e–01,–3.5e–02)	7.1e–03 (+1.2e–02,–9.9e–04)	1.9	47	1.2e+01	3.5e+00	300
87	05 20 25.3	-67 20 52	3.8	0.19 (+0.03,–0.02)	0.0e+00 (+5.0e–02,–0.0e+00)	3.7e–03 (+1.1e–02,–5.2e–04)	1.3	74	5.5e+00	3.2e+00	400
88	05 20 26.0	-68 35 53	5.0	0.20 (+0.03,–0.02)	4.8e–01 (+5.3e–01,–2.4e–01)	1.0e–03 (+1.0e–02,–1.4e–04)	1.2	92	1.5e+00	9.5e–01	400
89	05 20 28.5	-69 50 53	5.3	0.29 (+0.03,–0.03)	0.0e+00 (+5.0e–02,–0.0e+00)	3.1e–03 (+1.1e–02,–4.4e–04)	1.8	98	3.6e+00	6.3e+00	500
90	05 20 56.6	-67 35 53	2.8	0.23 (+0.03,–0.02)	0.0e+00 (+5.0e–02,–0.0e+00)	2.2e–03 (+1.1e–02,–3.1e–04)	1.4	59	2.9e+00	2.9e+00	400
91	05 20 59.5	-68 50 54	3.9	0.22 (+0.03,–0.02)	4.6e–01 (+5.1e–01,–2.3e–01)	1.0e–03 (+1.0e–02,–1.4e–04)	1.4	80	1.4e+00	1.2e+00	400
92	05 21 04.2	-70 05 54	3.6	0.26 (+0.03,–0.02)	0.0e+00 (+5.0e–02,–0.0e+00)	2.2e–03 (+1.1e–02,–3.1e–04)	1.2	70	2.7e+00	3.4e+00	500
93	05 21 11.4	-71 20 54	2.0	0.14 (+0.03,–0.01)	6.7e–01 (+7.2e–01,–3.3e–01)	2.4e–03 (+1.1e–02,–3.4e–04)	1.2	43	4.4e+00	1.1e+00	300
94	05 21 28.8	-67 50 54	3.1	0.33 (+0.03,–0.03)	0.0e+00 (+5.0e–02,–0.0e+00)	2.5e–03 (+1.1e–02,–3.5e–04)	1.6	70	2.6e+00	6.4e+00	500
95	05 21 41.1	-70 20 55	3.8	0.20 (+0.03,–0.02)	3.8e–01 (+4.3e–01,–1.9e–01)	8.0e–03 (+1.2e–02,–1.1e–03)	1.3	77	1.2e+01	7.9e+00	400
96	05 21 50.9	-71 35 55	2.3	1.15 (+0.02,–0.10)	0.0e+00 (+5.0e–02,–0.0e+00)	5.7e–04 (+1.0e–02,–8.0e–05)	1.1	47	2.9e–01	1.8e+01	1000
97	05 22 01.9	-68 05 55	1.9	0.39 (+0.03,–0.04)	0.0e+00 (+5.0e–02,–0.0e+00)	7.4e–04 (+1.0e–02,–1.0e–04)	0.9	46	7.1e–01	2.7e+00	600
98	05 22 09.2	-69 20 56	6.7	0.27 (+0.03,–0.02)	0.0e+00 (+5.0e–02,–0.0e+00)	4.6e–03 (+1.1e–02,–6.4e–04)	1.2	110	5.5e+00	8.1e+00	500
99	05 22 18.9	-70 35 56	3.4	0.23 (+0.03,–0.02)	9.5e–02 (+1.5e–01,–4.8e–02)	2.5e–03 (+1.1e–02,–3.5e–04)	2.3	67	3.3e+00	3.2e+00	400
100	05 22 28.6	-67 05 56	3.8	0.16 (+0.03,–0.01)	3.3e–01 (+3.8e–01,–1.6e–01)	1.0e–03 (+1.0e–02,–1.5e–04)	1.7	72	1.8e+00	6.2e–01	400

Table D.1: Continued (LMC).

1	2		3	4	5	6	7	8	9	10	11
No	Center of Region RA Dec (J2000.0)		No of events $[10^3]$	T_{MC} [keV]	$N_{\mathrm{H\,MC}}$ $[10^{22}\ \mathrm{cm}^{-2}]$	$EM_\square$ $[\mathrm{cm}^{-5}]$	red. χ^2	DOF	$L_\square$ $[10^{36}$ erg/s]	Δl [kpc]	v [km/s]
101	05 22 45.2	-69 35 57	5.6	0.32 (+0.03,−0.03)	0.0e+00 (+5.0e−02,−0.0e+00)	4.5e−03 (+1.1e−02,−6.3e−04)	1.7	107	4.9e+00	1.1e+01	500
102	05 22 53.9	-66 05 57	3.6	0.16 (+0.03,−0.01)	6.6e−01 (+7.1e−01,−3.3e−01)	3.2e−03 (+1.1e−02,−4.5e−04)	1.5	69	5.3e+00	2.0e+00	400
103	05 23 01.1	-67 20 57	3.8	0.17 (+0.03,−0.02)	2.9e−01 (+3.4e−01,−1.5e−01)	1.0e−03 (+1.0e−02,−1.4e−04)	1.5	75	1.6e+00	7.4e−01	400
104	05 23 10.4	-68 35 57	7.9	0.23 (+0.03,−0.02)	3.0e−01 (+3.5e−01,−1.5e−01)	8.3e−03 (+1.2e−02,−1.2e−03)	1.3	116	1.1e+01	1.1e+01	400
105	05 23 22.7	-69 50 58	8.2	0.28 (+0.03,−0.03)	3.5e−01 (+4.0e−01,−1.7e−01)	1.0e−03 (+1.0e−02,−1.4e−04)	2.4	122	1.2e+00	1.9e+00	500
106	05 23 25.0	-66 20 58	1.7	0.58 (+0.02,−0.05)	6.1e−02 (+1.1e−01,−3.1e−02)	4.5e−04 (+1.0e−02,−6.2e−05)	1.3	41	3.4e−01	3.6e+00	700
107	05 23 34.0	-67 35 58	2.8	0.21 (+0.03,−0.02)	0.0e+00 (+5.0e−02,−0.0e+00)	2.3e−03 (+1.1e−02,−3.2e−04)	1.4	58	3.2e+00	2.4e+00	400
108	05 23 45.8	-68 50 59	7.8	0.17 (+0.03,−0.02)	8.0e−01 (+8.5e−01,−4.0e−01)	7.7e−03 (+1.2e−02,−1.1e−03)	1.5	115	1.2e+01	5.1e+00	400
109	05 23 48.5	-65 20 59	5.1	0.15 (+0.03,−0.01)	4.2e−01 (+4.7e−01,−2.1e−01)	1.0e−02 (+1.3e−02,−1.4e−03)	1.8	76	1.7e+01	5.1e+00	400
110	05 24 00.4	-70 05 59	4.7	0.25 (+0.03,−0.02)	0.0e+00 (+5.0e−02,−0.0e+00)	3.5e−03 (+1.1e−02,−4.9e−04)	1.6	95	4.4e+00	5.5e+00	500
111	05 24 08.0	-67 50 59	2.6	0.24 (+0.03,−0.02)	0.0e+00 (+5.0e−02,−0.0e+00)	2.2e−03 (+1.1e−02,−3.1e−04)	1.7	60	2.9e+00	3.2e+00	500
112	05 24 29.7	-66 51 00	3.7	0.16 (+0.03,−0.01)	6.1e−01 (+6.6e−01,−3.0e−01)	2.4e−03 (+1.1e−02,−3.4e−04)	1.3	73	4.0e+00	1.5e+00	400
113	05 24 39.6	-70 21 00	2.6	0.25 (+0.03,−0.02)	0.0e+00 (+5.0e−02,−0.0e+00)	2.7e−03 (+1.1e−02,−3.8e−04)	1.7	60	3.4e+00	3.9e+00	500
114	05 24 42.8	-68 06 00	4.9	0.25 (+0.03,−0.02)	0.0e+00 (+5.0e−02,−0.0e+00)	2.2e−03 (+1.1e−02,−3.1e−04)	1.8	89	2.8e+00	3.3e+00	500
115	05 25 18.6	-68 21 01	5.2	0.20 (+0.03,−0.02)	4.9e−01 (+5.4e−01,−2.5e−01)	1.0e−03 (+1.0e−02,−1.4e−04)	1.5	89	1.5e+00	1.0e+00	400
116	05 25 19.5	-70 36 02	5.0	0.25 (+0.03,−0.02)	3.0e−04 (+5.0e−02,−1.5e−04)	2.2e−03 (+1.1e−02,−3.1e−04)	1.2	91	2.8e+00	3.3e+00	500
117	05 25 22.0	-66 06 01	4.9	0.23 (+0.03,−0.02)	1.4e+00 (+1.4e+00,−7.0e−01)	5.9e−03 (+1.2e−02,−8.2e−04)	1.9	95	7.8e+00	7.4e+00	400
118	05 25 36.9	-67 21 02	2.3	0.17 (+0.03,−0.02)	3.3e−01 (+3.8e−01,−1.7e−01)	1.0e−03 (+1.0e−02,−1.4e−04)	1.4	50	1.6e+00	7.0e−01	400
119	05 25 37.3	-69 36 02	9.1	0.22 (+0.03,−0.02)	7.7e−01 (+8.2e−01,−3.9e−01)	8.6e−03 (+1.3e−02,−1.2e−03)	2.7	131	1.2e+01	9.9e+00	400
120	05 25 54.9	-68 36 02	7.0	0.23 (+0.03,−0.02)	3.3e−01 (+3.8e−01,−1.6e−01)	1.0e−02 (+1.3e−02,−1.4e−03)	1.5	111	1.3e+01	1.3e+01	400
121	05 26 00.7	-70 51 03	1.4	0.16 (+0.03,−0.01)	3.2e−01 (+3.7e−01,−1.6e−01)	1.1e−03 (+1.0e−02,−1.5e−04)	1.7	29	1.7e+00	6.6e−01	400
122	05 26 11.4	-67 36 03	2.6	0.19 (+0.03,−0.02)	3.8e−01 (+4.3e−01,−1.9e−01)	1.0e−03 (+1.0e−02,−1.4e−04)	1.7	57	1.5e+00	8.4e−01	400
123	05 26 47.1	-67 51 04	3.2	0.25 (+0.03,−0.02)	0.0e+00 (+5.0e−02,−0.0e+00)	2.4e−03 (+1.1e−02,−3.3e−04)	1.5	69	3.0e+00	3.7e+00	500
124	05 26 56.7	-70 06 04	6.0	0.27 (+0.03,−0.02)	0.0e+00 (+5.0e−02,−0.0e+00)	3.9e−03 (+1.1e−02,−5.5e−04)	1.9	106	4.7e+00	6.8e+00	500
125	05 27 23.6	-68 06 05	6.6	0.17 (+0.03,−0.02)	7.0e−01 (+7.5e−01,−3.5e−01)	5.0e−03 (+1.2e−02,−7.0e−04)	1.5	108	7.9e+00	3.5e+00	400
126	05 27 26.7	-71 21 05	2.2	0.26 (+0.03,−0.02)	1.1e−01 (+1.6e−01,−5.6e−02)	5.6e−04 (+1.0e−02,−7.9e−05)	1.5	42	7.0e−01	9.1e−01	500
127	05 27 31.5	-64 51 05	1.6	0.12 (+0.03,−0.01)	1.3e−01 (+1.8e−01,−6.6e−02)	4.9e−03 (+1.1e−02,−6.8e−04)	1.3	35	9.4e+00	1.7e+00	300
128	05 27 37.0	-67 06 06	3.3	0.16 (+0.03,−0.01)	3.4e−01 (+3.9e−01,−1.7e−01)	1.1e−03 (+1.0e−02,−1.5e−04)	1.7	66	1.8e+00	6.8e−01	400
129	05 27 38.0	-70 21 06	3.5	0.26 (+0.03,−0.02)	0.0e+00 (+5.0e−02,−0.0e+00)	2.2e−03 (+1.1e−02,−3.1e−04)	1.5	75	2.7e+00	3.5e+00	500
130	05 28 01.2	-68 21 06	7.0	0.24 (+0.03,−0.02)	3.5e−01 (+4.0e−01,−1.8e−01)	8.7e−03 (+1.3e−02,−1.2e−03)	1.2	109	1.1e+01	1.2e+01	400
131	05 28 12.7	-67 21 07	1.7	0.21 (+0.03,−0.02)	0.0e+00 (+5.0e−02,−0.0e+00)	2.9e−03 (+1.1e−02,−4.1e−04)	1.1	44	4.2e+00	3.0e+00	400
132	05 28 20.1	-70 36 07	1.4	0.23 (+0.03,−0.02)	4.3e−02 (+9.3e−02,−2.2e−02)	2.4e−03 (+1.1e−02,−3.4e−04)	1.6	33	3.3e+00	3.0e+00	400
133	05 28 24.1	-66 21 07	7.5	0.19 (+0.03,−0.02)	4.7e−01 (+5.2e−01,−2.4e−01)	1.0e−02 (+1.3e−02,−1.4e−03)	2.2	110	1.5e+01	8.4e+00	400
134	05 28 29.5	-69 36 07	11.9	0.29 (+0.03,−0.03)	0.0e+00 (+5.0e−02,−0.0e+00)	4.5e−03 (+1.1e−02,−6.3e−04)	2.1	127	5.2e+00	9.1e+00	500
135	05 28 39.3	-68 36 08	4.3	0.17 (+0.03,−0.02)	8.6e−01 (+9.1e−01,−4.3e−01)	6.8e−03 (+1.2e−02,−9.5e−04)	1.2	86	1.1e+01	4.9e+00	400
136	05 28 48.9	-67 36 08	1.3	0.20 (+0.03,−0.02)	0.0e+00 (+5.0e−02,−0.0e+00)	2.9e−03 (+1.1e−02,−4.0e−04)	1.3	30	4.1e+00	2.8e+00	400
137	05 29 03.7	-70 51 08	1.1	0.24 (+0.03,−0.02)	0.0e+00 (+5.0e−02,−0.0e+00)	1.3e−03 (+1.0e−02,−1.8e−04)	0.8	25	1.7e+00	1.8e+00	400
138	05 29 09.4	-65 36 08	5.1	0.16 (+0.03,−0.01)	3.5e−01 (+4.0e−01,−1.8e−01)	1.0e−02 (+1.3e−02,−1.4e−03)	2.5	85	1.6e+01	6.5e+00	400
139	05 29 11.1	-69 51 09	6.8	0.25 (+0.03,−0.02)	2.2e−01 (+2.7e−01,−1.1e−01)	1.0e−02 (+1.3e−02,−1.4e−03)	1.3	113	1.3e+01	1.5e+01	500
140	05 29 26.2	-67 51 09	3.0	0.29 (+0.03,−0.03)	0.0e+00 (+5.0e−02,−0.0e+00)	2.3e−03 (+1.1e−02,−3.2e−04)	1.3	68	2.6e+00	4.7e+00	500
141	05 29 34.9	-66 51 09	4.0	0.16 (+0.03,−0.01)	7.0e−01 (+7.5e−01,−3.5e−01)	2.9e−03 (+1.1e−02,−4.1e−04)	1.1	74	4.8e+00	1.8e+00	400
142	05 29 53.0	-70 06 10	6.8	0.29 (+0.03,−0.03)	0.0e+00 (+5.0e−02,−0.0e+00)	4.0e−03 (+1.1e−02,−5.6e−04)	1.6	112	4.6e+00	8.1e+00	500
143	05 30 04.5	-68 06 10	5.5	0.16 (+0.03,−0.01)	7.8e−01 (+8.3e−01,−3.9e−01)	6.2e−03 (+1.2e−02,−8.7e−04)	1.1	98	1.0e+01	4.0e+00	400
144	05 30 11.2	-67 06 10	2.4	0.17 (+0.03,−0.01)	6.5e−01 (+7.0e−01,−3.2e−01)	2.5e−03 (+1.1e−02,−3.4e−04)	1.3	56	4.0e+00	1.6e+00	400
145	05 30 26.1	-65 06 11	3.6	0.18 (+0.03,−0.02)	3.2e−02 (+8.2e−02,−1.6e−02)	2.2e−03 (+1.1e−02,−3.1e−04)	1.6	65	3.4e+00	1.7e+00	400
146	05 30 36.4	-70 21 11	3.3	0.19 (+0.03,−0.02)	4.0e−01 (+4.5e−01,−2.0e−01)	1.0e−03 (+1.0e−02,−1.4e−04)	1.1	66	1.5e+00	9.1e−01	400
147	05 30 43.9	-68 21 11	3.0	0.17 (+0.03,−0.02)	9.6e−01 (+1.0e+00,−4.8e−01)	5.8e−03 (+1.2e−02,−8.2e−04)	1.2	65	9.2e+00	4.1e+00	400
148	05 30 48.5	-67 21 11	2.3	0.19 (+0.03,−0.02)	3.4e−01 (+3.9e−01,−1.7e−01)	1.0e−03 (+1.0e−02,−1.4e−04)	1.5	55	1.5e+00	8.4e−01	400
149	05 31 00.1	-65 21 12	4.5	0.14 (+0.03,−0.01)	2.6e−01 (+3.1e−01,−1.3e−01)	1.0e−02 (+1.3e−02,−1.4e−03)	2.0	75	1.8e+01	5.0e+00	400
150	05 31 20.8	-70 36 13	2.4	0.17 (+0.03,−0.02)	6.6e−01 (+7.1e−01,−3.3e−01)	4.0e−03 (+1.1e−02,−5.7e−04)	1.1	54	6.4e+00	2.9e+00	400

1	2		3	4	5	6	7	8	9	10	11
No	Center of Region RA Dec (J2000.0)		No of events [10^3]	T_{MC} [keV]	$N_{H\,MC}$ [10^{22} cm^{-2}]	$EM_{\square}$ [cm^{-5}]	red. χ^2	DOF	$L_{\square}$ [10^{36} erg/s]	Δl [kpc]	v [km/s]
151	05 31 23.8	-68 36 13	6.5	0.23 (+0.03,−0.02)	5.6e−01 (+6.1e−01,−2.8e−01)	1.0e−02 (+1.3e−02,−1.4e−03)	1.4	107	1.3e+01	1.3e+01	400
152	05 31 30.4	-66 36 13	5.2	0.23 (+0.03,−0.02)	2.9e−01 (+3.4e−01,−1.5e−01)	2.3e−03 (+1.1e−02,−3.2e−04)	1.9	89	3.0e+00	2.9e+00	400
153	05 31 34.7	-65 36 13	8.5	0.16 (+0.03,−0.01)	2.9e−01 (+3.4e−01,−1.4e−01)	1.0e−02 (+1.3e−02,−1.4e−03)	2.4	104	1.7e+01	5.9e+00	400
154	05 32 05.3	-69 51 14	11.4	0.23 (+0.03,−0.02)	3.0e−01 (+3.5e−01,−1.5e−01)	1.0e−03 (+1.0e−02,−1.4e−04)	2.3	128	1.3e+00	1.3e+00	400
155	05 32 05.4	-67 51 14	1.5	0.23 (+0.03,−0.02)	0.0e+00 (+5.0e−02,−0.0e+00)	1.7e−03 (+1.1e−02,−2.4e−04)	1.3	35	2.3e+00	2.2e+00	400
156	05 32 06.6	-70 51 14	1.1	0.19 (+0.03,−0.02)	4.1e−01 (+4.6e−01,−2.1e−01)	6.8e−03 (+1.2e−02,−9.5e−04)	1.0	26	1.0e+01	5.6e+00	400
157	05 32 09.9	-65 51 14	6.0	0.17 (+0.03,−0.02)	3.2e−01 (+3.7e−01,−1.6e−01)	1.0e−02 (+1.3e−02,−1.4e−03)	2.4	99	1.6e+01	7.2e+00	400
158	05 32 45.4	-68 06 15	2.1	0.15 (+0.03,−0.01)	6.6e−01 (+7.1e−01,−3.3e−01)	4.6e−03 (+1.1e−02,−6.4e−04)	1.6	51	7.9e+00	2.5e+00	400
159	05 32 48.6	-65 06 15	3.4	0.15 (+0.03,−0.01)	3.8e−01 (+4.3e−01,−1.9e−01)	1.0e−03 (+1.0e−02,−1.4e−04)	1.5	60	1.8e+00	5.5e−01	400
160	05 32 49.3	-70 06 15	4.3	0.22 (+0.03,−0.02)	3.9e−01 (+4.4e−01,−2.0e−01)	1.0e−03 (+1.0e−02,−1.4e−04)	1.4	91	1.4e+00	1.1e+00	400
161	05 33 23.3	-66 21 16	3.4	0.19 (+0.03,−0.02)	4.3e−01 (+4.8e−01,−2.1e−01)	1.0e−02 (+1.3e−02,−1.4e−03)	2.0	68	1.5e+01	9.1e+00	400
162	05 33 24.0	-65 21 16	5.4	0.15 (+0.03,−0.01)	3.2e−01 (+3.7e−01,−1.6e−01)	1.0e−03 (+1.0e−02,−1.4e−04)	2.0	81	1.7e+00	5.3e−01	400
163	05 33 24.3	-67 21 16	2.7	0.20 (+0.03,−0.02)	3.2e−01 (+3.7e−01,−1.6e−01)	1.0e−03 (+1.0e−02,−1.4e−04)	1.5	61	1.5e+00	9.3e−01	400
164	05 33 25.4	-64 21 16	1.1	0.31 (+0.03,−0.03)	2.5e−02 (+7.5e−02,−1.3e−02)	2.6e−04 (+1.0e−02,−3.6e−05)	1.4	24	2.9e−01	6.1e−01	500
165	05 33 26.6	-68 21 16	3.7	0.16 (+0.03,−0.01)	8.7e−01 (+9.2e−01,−4.4e−01)	4.7e−03 (+1.1e−02,−6.5e−04)	1.6	71	7.6e+00	2.9e+00	400
166	05 33 29.7	-69 21 17	17.3	0.18 (+0.03,−0.02)	6.8e−01 (+7.3e−01,−3.4e−01)	1.0e−02 (+1.3e−02,−1.4e−03)	2.5	139	1.5e+01	7.7e+00	400
167	05 33 34.9	-70 21 17	3.5	0.22 (+0.03,−0.02)	5.5e−01 (+6.0e−01,−2.7e−01)	1.0e−03 (+1.0e−02,−1.4e−04)	1.2	72	1.4e+00	1.2e+00	400
168	05 33 42.0	-71 21 17	1.1	0.32 (+0.03,−0.03)	0.0e+00 (+5.0e−02,−0.0e+00)	7.2e−04 (+1.0e−02,−1.0e−04)	1.9	24	7.7e−01	1.8e+00	500
169	05 33 59.6	-64 36 17	1.3	0.19 (+0.03,−0.02)	0.0e+00 (+5.0e−02,−0.0e+00)	5.1e−04 (+1.0e−02,−7.1e−05)	1.4	29	7.6e−01	4.3e−01	400
170	05 34 01.5	-66 36 18	5.4	0.18 (+0.03,−0.02)	4.9e−01 (+5.4e−01,−2.4e−01)	1.0e−02 (+1.3e−02,−1.4e−03)	2.1	89	1.5e+01	7.7e+00	400
171	05 34 13.8	-69 36 18	18.9	0.18 (+0.03,−0.02)	7.4e−01 (+7.9e−01,−3.7e−01)	1.0e−02 (+1.3e−02,−1.4e−03)	2.5	145	1.5e+01	7.9e+00	400
172	05 34 21.5	-70 36 18	2.2	0.28 (+0.03,−0.02)	3.3e−02 (+8.3e−02,−1.7e−02)	1.9e−03 (+1.1e−02,−2.7e−04)	1.3	49	2.3e+00	3.5e+00	500
173	05 34 35.0	-64 51 18	2.2	0.17 (+0.03,−0.02)	1.6e−01 (+2.1e−01,−8.1e−02)	2.2e−03 (+1.1e−02,−3.1e−04)	1.0	47	3.5e+00	1.6e+00	400
174	05 34 59.5	-69 51 20	8.3	0.18 (+0.03,−0.02)	7.0e−01 (+7.5e−01,−3.5e−01)	1.0e−02 (+1.3e−02,−1.4e−03)	2.5	120	1.6e+01	7.4e+00	400
175	05 35 09.6	-70 51 20	1.8	0.21 (+0.03,−0.02)	7.0e−01 (+7.5e−01,−3.5e−01)	7.4e−03 (+1.2e−02,−1.0e−03)	1.9	42	1.0e+01	8.1e+00	400
176	05 35 11.1	-65 06 20	3.7	0.14 (+0.03,−0.01)	2.2e−01 (+2.7e−01,−1.1e−01)	7.8e−03 (+1.2e−02,−1.1e−03)	1.2	63	1.4e+01	3.8e+00	300
177	05 35 14.4	-66 06 20	5.8	0.22 (+0.03,−0.02)	1.3e+00 (+1.4e+00,−6.6e−01)	7.6e−03 (+1.2e−02,−1.1e−03)	2.4	110	1.0e+01	8.9e+00	400
178	05 35 34.9	-69 06 21	16.2	0.23 (+0.03,−0.02)	1.2e+00 (+1.3e+00,−6.1e−01)	9.7e−03 (+1.3e−02,−1.4e−03)	2.5	154	1.3e+01	1.2e+01	400
179	05 35 44.1	-64 21 21	3.0	0.46 (+0.03,−0.04)	1.7e+00 (+1.8e+00,−8.7e−01)	6.7e−03 (+1.2e−02,−9.4e−04)	1.4	61	5.9e+00	3.4e+01	600
180	05 35 45.6	-70 06 21	10.5	0.15 (+0.03,−0.01)	9.8e−01 (+1.0e+00,−4.9e−01)	1.0e−02 (+1.3e−02,−1.4e−03)	2.5	129	1.7e+01	5.4e+00	400
181	05 35 47.8	-65 21 21	1.6	0.11 (+0.03,−0.01)	2.1e−01 (+2.6e−01,−1.0e−01)	1.3e−03 (+1.0e−02,−1.8e−04)	1.6	36	2.6e+00	3.8e−01	300
182	05 35 52.8	-66 21 21	7.1	0.18 (+0.03,−0.02)	3.9e−01 (+4.4e−01,−2.0e−01)	1.0e−02 (+1.3e−02,−1.4e−03)	2.4	106	1.5e+01	7.7e+00	400
183	05 35 59.1	-71 06 22	1.5	0.26 (+0.03,−0.02)	7.2e−02 (+1.2e−01,−3.6e−02)	1.3e−03 (+1.0e−02,−1.8e−04)	1.8	33	1.6e+00	2.2e+00	500
184	05 36 00.2	-67 21 21	2.5	0.17 (+0.03,−0.02)	4.8e−01 (+5.3e−01,−2.4e−01)	1.8e−03 (+1.1e−02,−2.5e−04)	2.2	55	2.8e+00	1.2e+00	400
185	05 36 19.5	-64 36 22	2.4	0.13 (+0.03,−0.01)	9.4e−01 (+9.9e−01,−4.7e−01)	8.7e−03 (+1.3e−02,−1.2e−03)	1.6	50	1.7e+01	3.3e+00	300
186	05 36 19.9	-69 21 22	21.6	0.20 (+0.03,−0.02)	7.8e−01 (+8.3e−01,−3.9e−01)	1.0e−02 (+1.3e−02,−1.4e−03)	2.5	156	1.4e+01	1.0e+01	400
187	05 36 33.4	-70 21 23	3.0	0.14 (+0.03,−0.01)	9.3e−01 (+9.8e−01,−4.6e−01)	9.9e−03 (+1.3e−02,−1.4e−03)	2.5	61	1.7e+01	4.9e+00	300
188	05 36 49.7	-71 21 23	3.0	0.19 (+0.03,−0.02)	1.2e−01 (+1.7e−01,−6.2e−02)	3.8e−03 (+1.1e−02,−5.4e−04)	1.6	57	5.7e+00	3.3e+00	400
189	05 37 06.0	-69 36 24	27.7	0.22 (+0.03,−0.02)	8.2e−01 (+8.7e−01,−4.1e−01)	7.8e−03 (+1.2e−02,−1.1e−03)	2.5	173	1.1e+01	9.1e+00	400
190	05 37 12.9	-66 51 24	2.7	0.19 (+0.03,−0.02)	5.5e−01 (+6.0e−01,−2.7e−01)	6.6e−03 (+1.2e−02,−9.2e−04)	1.3	55	9.6e+00	5.9e+00	400
191	05 37 22.2	-70 36 24	1.8	0.14 (+0.03,−0.01)	9.5e−01 (+1.0e+00,−4.8e−01)	9.9e−03 (+1.3e−02,−1.4e−03)	2.5	41	1.8e+01	4.8e+00	300
192	05 37 53.7	-69 51 25	11.0	0.30 (+0.03,−0.03)	1.4e+00 (+1.5e+00,−7.2e−01)	4.5e−03 (+1.1e−02,−6.3e−04)	2.5	155	5.0e+00	9.9e+00	500
193	05 37 53.8	-67 06 25	3.5	0.18 (+0.03,−0.02)	4.8e−01 (+5.3e−01,−2.4e−01)	1.0e−03 (+1.0e−02,−1.4e−04)	1.5	70	1.5e+00	8.2e−01	400
194	05 38 11.7	-65 21 25	2.7	0.15 (+0.03,−0.01)	3.1e−01 (+3.6e−01,−1.6e−01)	1.0e−02 (+1.3e−02,−1.4e−03)	1.6	53	1.7e+01	5.2e+00	400
195	05 38 12.5	-70 51 26	2.4	0.17 (+0.03,−0.02)	3.8e−01 (+4.3e−01,−1.9e−01)	1.0e−03 (+1.0e−02,−1.4e−04)	0.8	52	1.6e+00	7.0e−01	400
196	05 38 23.2	-69 06 26	22.7	0.29 (+0.03,−0.03)	1.0e+00 (+1.1e+00,−5.2e−01)	1.0e−02 (+1.3e−02,−1.4e−03)	2.5	166	1.2e+01	2.0e+01	500
197	05 38 30.3	-63 36 26	2.0	0.28 (+0.03,−0.03)	1.6e+00 (+1.6e+00,−7.8e−01)	1.2e−03 (+1.0e−02,−1.7e−04)	1.6	42	1.4e+00	2.3e+00	500
198	05 38 36.0	-67 21 26	1.6	0.23 (+0.03,−0.02)	2.0e−01 (+2.5e−01,−1.0e−01)	1.8e−03 (+1.1e−02,−2.6e−04)	1.3	36	2.4e+00	2.3e+00	400
199	05 38 42.0	-70 06 27	6.4	0.18 (+0.03,−0.02)	4.9e−01 (+5.4e−01,−2.5e−01)	1.0e−03 (+1.0e−02,−1.4e−04)	2.5	105	1.5e+00	8.3e−01	400
200	05 38 50.5	-65 36 27	5.3	0.17 (+0.03,−0.02)	5.9e−02 (+1.1e−01,−3.0e−02)	3.0e−03 (+1.1e−02,−4.2e−04)	1.9	82	4.7e+00	2.2e+00	400

Table D.1: Continued (LMC).

1	2		3	4	5	6	7	8	9	10	11
No	Center of Region RA Dec (J2000.0)		No of events [10^3]	T_{MC} [keV]	$N_{\mathrm{H\,MC}}$ [10^{22} cm^{-2}]	$EM_\square$ [cm^{-5}]	red. χ^2	DOF	$L_\square$ [10^{36} erg/s]	Δl [kpc]	v [km/s]
201	05 39 06.9	-63 51 27	3.9	0.47 (+0.03,−0.04)	1.9e+00 (+2.0e+00,−9.5e−01)	1.5e−03 (+1.0e−02,−2.1e−04)	2.5	79	1.3e+00	8.1e+00	600
202	05 39 10.1	-69 21 27	28.7	0.25 (+0.03,−0.02)	9.7e−01 (+1.0e+00,−4.9e−01)	1.0e−02 (+1.3e−02,−1.4e−03)	2.5	176	1.3e+01	1.5e+01	500
203	05 39 18.8	-67 36 28	1.1	0.23 (+0.03,−0.02)	8.6e−02 (+1.4e−01,−4.3e−02)	1.8e−03 (+1.1e−02,−2.5e−04)	2.7	25	2.4e+00	2.3e+00	400
204	05 39 31.9	-70 21 28	4.9	0.18 (+0.03,−0.02)	4.7e−01 (+5.2e−01,−2.4e−01)	1.0e−02 (+1.3e−02,−1.4e−03)	1.7	80	1.5e+01	7.7e+00	400
205	05 39 43.4	-64 06 28	1.2	0.73 (+0.02,−0.07)	2.0e+00 (+2.0e+00,−9.8e−01)	1.0e−03 (+1.0e−02,−1.5e−04)	1.8	24	7.0e−01	1.3e+01	800
206	05 39 58.2	-69 36 29	13.1	0.36 (+0.03,−0.03)	9.8e−01 (+1.0e+00,−4.9e−01)	3.9e−03 (+1.1e−02,−5.5e−04)	2.5	161	4.0e+00	1.2e+01	600
207	05 40 22.9	-70 36 30	4.3	0.18 (+0.03,−0.02)	4.2e−01 (+4.7e−01,−2.1e−01)	1.0e−03 (+1.0e−02,−1.4e−04)	1.6	76	1.6e+00	7.7e−01	400
208	05 40 48.0	-69 51 31	6.5	0.28 (+0.03,−0.03)	1.0e+00 (+1.1e+00,−5.1e−01)	6.3e−03 (+1.2e−02,−8.9e−04)	2.5	128	7.5e+00	1.2e+01	500
209	05 40 52.0	-66 21 31	1.5	0.17 (+0.03,−0.02)	4.3e−03 (+5.4e−02,−2.2e−03)	9.9e−04 (+1.0e−02,−1.4e−04)	1.4	34	1.6e+00	6.9e+00	400
210	05 40 59.2	-64 36 31	2.8	0.18 (+0.03,−0.02)	1.0e+00 (+1.1e+00,−5.2e−01)	1.0e−03 (+1.0e−02,−1.4e−04)	1.1	52	1.6e+00	8.1e−01	400
211	05 41 11.9	-67 21 31	1.2	0.23 (+0.03,−0.02)	1.3e−01 (+1.8e−01,−6.5e−02)	2.2e−03 (+1.1e−02,−3.1e−04)	2.2	27	3.0e+00	2.7e+00	400
212	05 41 15.5	-70 51 32	3.7	0.18 (+0.03,−0.02)	3.0e−01 (+3.5e−01,−1.5e−01)	1.0e−03 (+1.0e−02,−1.4e−04)	1.6	75	1.6e+00	8.0e−01	400
213	05 41 23.0	-63 51 31	3.8	0.41 (+0.03,−0.04)	1.8e+00 (+1.8e+00,−8.9e−01)	9.6e−03 (+1.3e−02,−1.3e−03)	1.9	71	9.1e+00	3.9e+01	600
214	05 41 38.3	-70 06 32	11.2	0.22 (+0.03,−0.02)	7.7e−01 (+8.2e−01,−3.9e−01)	8.2e−03 (+1.2e−02,−1.1e−03)	2.5	135	1.1e+01	9.5e+00	400
215	05 42 00.3	-69 21 33	19.2	0.24 (+0.03,−0.02)	9.9e−01 (+1.0e+00,−5.0e−01)	1.0e−02 (+1.3e−02,−1.4e−03)	2.5	161	1.3e+01	1.4e+01	400
216	05 42 00.7	-64 06 33	3.5	0.45 (+0.03,−0.04)	2.2e+00 (+2.3e+00,−1.1e+00)	1.0e−03 (+1.0e−02,−1.4e−04)	1.9	66	9.0e−01	4.9e+00	600
217	05 42 30.4	-70 21 34	7.2	0.26 (+0.03,−0.02)	3.6e−01 (+4.1e−01,−1.8e−01)	1.0e−02 (+1.3e−02,−1.4e−03)	2.1	118	1.2e+01	1.7e+01	500
218	05 42 40.0	-64 21 34	2.4	0.28 (+0.03,−0.03)	1.2e+00 (+1.2e+00,−5.8e−01)	4.6e−03 (+1.1e−02,−6.5e−04)	1.4	51	5.4e+00	8.8e+00	500
219	05 42 50.4	-69 36 35	24.6	0.24 (+0.03,−0.02)	8.3e−01 (+8.8e−01,−4.2e−01)	1.0e−02 (+1.3e−02,−1.4e−03)	2.5	166	1.3e+01	1.4e+01	400
220	05 43 00.2	-63 36 35	2.7	0.11 (+0.03,−0.01)	7.9e−01 (+8.4e−01,−3.9e−01)	8.4e−03 (+1.3e−02,−1.2e−03)	1.2	52	1.7e+01	2.4e+00	300
221	05 43 39.2	-63 51 36	3.5	0.19 (+0.03,−0.02)	9.6e−01 (+1.0e+00,−4.8e−01)	1.0e−03 (+1.0e−02,−1.4e−04)	1.8	62	1.5e+00	8.6e−01	400
222	05 43 42.3	-69 51 36	6.0	0.22 (+0.03,−0.02)	8.1e−01 (+8.6e−01,−4.1e−01)	8.3e−03 (+1.3e−02,−1.2e−03)	2.1	119	1.1e+01	9.6e+00	400
223	05 44 50.5	-69 21 39	13.0	0.23 (+0.03,−0.02)	1.3e+00 (+1.3e+00,−6.3e−01)	9.0e−03 (+1.3e−02,−1.3e−03)	2.5	147	1.2e+01	1.1e+01	400
224	05 45 15.2	-63 36 39	2.5	0.19 (+0.03,−0.02)	0.0e+00 (+5.0e−02,−0.0e+00)	8.1e−04 (+1.0e−02,−1.1e−04)	1.2	49	1.2e+00	6.9e−01	400
225	05 45 39.1	-64 36 40	1.5	0.59 (+0.02,−0.05)	0.0e+00 (+5.0e−02,−0.0e+00)	5.9e−05 (+1.0e−02,−8.3e−06)	0.9	36	4.5e−02	4.9e−01	700
226	05 45 42.6	-69 36 40	8.8	0.22 (+0.03,−0.02)	1.1e+00 (+1.2e+00,−5.6e−01)	7.1e−03 (+1.2e−02,−9.9e−04)	1.8	132	9.6e+00	8.6e+00	400
227	05 45 55.4	-63 51 40	2.9	0.18 (+0.03,−0.02)	6.9e−01 (+7.4e−01,−3.4e−01)	1.0e−03 (+1.0e−02,−1.4e−04)	1.3	57	1.6e+00	7.7e−01	400
228	05 46 36.6	-69 51 42	2.2	0.22 (+0.03,−0.02)	3.9e−01 (+4.4e−01,−1.9e−01)	7.2e−03 (+1.2e−02,−1.0e−03)	1.5	53	9.8e+00	8.4e+00	400
229	05 47 31.1	-70 06 44	1.0	0.29 (+0.03,−0.03)	0.0e+00 (+5.0e−02,−0.0e+00)	9.4e−04 (+1.0e−02,−1.3e−04)	1.4	22	1.1e+00	1.9e+00	500
230	05 55 26.7	-70 37 00	1.0	0.10 (+0.03,−0.01)	1.3e−01 (+1.8e−01,−6.7e−02)	1.1e−03 (+1.0e−02,−1.6e−04)	2.7	20	2.4e+00	2.9e−01	300
231	05 58 27.5	-70 37 06	1.0	0.11 (+0.03,−0.01)	2.7e−01 (+3.2e−01,−1.3e−01)	1.2e−03 (+1.0e−02,−1.7e−04)	2.6	19	2.6e+00	3.6e−01	300

Table D.2: Spectral fit parameters for the diffuse emission of the SMC.

1	2		3	4	5	6	7	8	9	10	11
No	Center of Region RA Dec (J2000.0)		No of events [10^3]	T_{MC} [keV]	$N_{\mathrm{H\,MC}}$ [10^{22} cm^{-2}]	$EM_\square$ [cm^{-5}]	red. χ^2	DOF	$L_\square$ [10^{36} erg/s]	Δl [kpc]	v [km/s]
1	00 36 39.8	-73 14 19	2.3	0.14 (+0.03,-0.01)	2.2e-02 (+7.2e-02,-1.1e-02)	1.4e-03 (+1.0e-02,-1.9e-04)	1.4	37	1.4e+00	6.1e-01	300
2	00 40 33.2	-73 44 26	2.3	0.12 (+0.03,-0.01)	5.6e-02 (+1.1e-01,-2.8e-02)	6.2e-04 (+1.0e-02,-8.7e-05)	1.3	37	6.8e-01	2.1e-01	300
3	00 41 59.8	-75 14 29	5.9	0.19 (+0.03,-0.02)	1.0e+00 (+1.0e+00,-5.0e-01)	2.4e-03 (+1.1e-02,-3.4e-04)	2.0	68	2.0e+00	2.2e+00	400
4	00 44 07.5	-73 44 32	2.4	0.11 (+0.03,-0.01)	1.0e+00 (+1.0e+00,-5.0e-01)	6.0e-06 (+1.0e-02,-8.4e-07)	1.6	36	6.7e-03	1.9e-03	300
5	00 45 38.9	-71 59 35	1.2	1.40 (+0.02,-0.13)	3.0e-02 (+8.0e-02,-1.5e-02)	1.0e-03 (+1.0e-02,-1.4e-04)	2.3	26	2.5e-01	4.7e+01	1100
6	00 47 04.1	-73 14 37	2.8	0.22 (+0.03,-0.02)	1.0e+00 (+1.0e+00,-5.0e-01)	6.0e-04 (+1.0e-02,-8.5e-05)	1.6	41	4.6e-01	6.8e-01	400
7	00 47 22.7	-73 29 38	3.3	1.15 (+0.02,-0.10)	2.4e-02 (+7.4e-02,-1.2e-02)	3.1e-04 (+1.0e-02,-4.4e-05)	1.4	48	8.9e-02	9.9e+00	1000
8	00 47 41.8	-73 44 39	4.1	0.14 (+0.03,-0.01)	5.6e-02 (+1.1e-01,-2.8e-02)	1.6e-04 (+1.0e-02,-2.2e-05)	2.0	48	1.6e-01	7.2e-02	300
9	00 48 53.0	-71 59 41	3.4	0.40 (+0.03,-0.04)	0.0e+00 (+5.0e-02,-0.0e+00)	1.3e-05 (+1.0e-02,-1.8e-06)	1.8	45	7.0e-03	4.9e-02	600
10	00 49 11.7	-72 14 41	2.4	0.26 (+0.03,-0.02)	0.0e+00 (+5.0e-02,-0.0e+00)	3.4e-04 (+1.0e-02,-4.8e-05)	2.0	41	2.3e-01	5.6e-01	500
11	00 49 31.0	-72 29 42	4.1	0.24 (+0.03,-0.02)	0.0e+00 (+5.0e-02,-0.0e+00)	1.0e-03 (+1.0e-02,-1.4e-04)	1.5	54	7.4e-01	1.4e+00	500
12	00 49 50.7	-72 44 42	1.8	0.24 (+0.03,-0.02)	8.5e-02 (+1.3e-01,-4.2e-02)	7.8e-04 (+1.0e-02,-1.1e-04)	1.6	35	5.7e-01	1.1e+00	500
13	00 50 11.1	-72 59 43	3.8	0.25 (+0.03,-0.02)	1.0e+00 (+1.0e+00,-5.0e-01)	2.8e-03 (+1.1e-02,-3.9e-04)	1.7	54	2.0e+00	4.0e+00	500
14	00 50 32.2	-73 14 44	2.3	1.04 (+0.02,-0.09)	3.7e-01 (+4.2e-01,-1.8e-01)	5.0e-04 (+1.0e-02,-7.0e-05)	1.3	40	1.5e-01	1.3e+01	900
15	00 50 53.9	-73 29 44	2.5	0.21 (+0.03,-0.02)	1.0e+00 (+1.0e+00,-5.0e-01)	5.8e-04 (+1.0e-02,-8.1e-05)	1.5	40	4.5e-01	5.9e-01	400
16	00 51 46.3	-71 44 46	3.1	0.23 (+0.03,-0.02)	0.0e+00 (+5.0e-02,-0.0e+00)	2.9e-04 (+1.0e-02,-4.0e-05)	1.3	44	2.2e-01	3.5e-01	400
17	00 52 07.1	-71 59 46	1.8	0.18 (+0.03,-0.02)	1.0e+00 (+1.0e+00,-5.0e-01)	8.3e-04 (+1.0e-02,-1.2e-04)	1.8	34	7.0e-01	6.8e-01	400
18	00 52 28.5	-72 14 47	1.9	0.24 (+0.03,-0.02)	2.0e-04 (+5.0e-02,-1.0e-04)	1.3e-03 (+1.0e-02,-1.9e-04)	1.4	38	9.6e-01	1.8e+00	500
19	00 52 50.4	-72 29 48	1.1	0.25 (+0.03,-0.02)	1.0e+00 (+1.0e+00,-5.0e-01)	1.1e-03 (+1.0e-02,-1.6e-04)	1.9	24	8.0e-01	1.7e+00	500
20	00 53 13.0	-72 44 49	2.2	0.33 (+0.03,-0.03)	1.0e+00 (+1.0e+00,-5.0e-01)	1.9e-03 (+1.1e-02,-2.7e-04)	1.3	39	1.1e+00	4.9e+00	500
21	00 53 36.3	-72 59 49	4.4	0.23 (+0.03,-0.02)	1.0e+00 (+1.0e+00,-5.0e-01)	4.0e-03 (+1.1e-02,-5.7e-04)	1.4	61	3.0e+00	5.1e+00	400
22	00 54 00.3	-73 14 50	3.6	0.19 (+0.03,-0.02)	1.0e+00 (+1.0e+00,-5.0e-01)	1.1e-03 (+1.0e-02,-1.5e-04)	1.6	48	8.8e-01	9.5e-01	400
23	00 54 35.3	-71 29 51	1.6	1.40 (+0.02,-0.13)	3.0e-02 (+8.0e-02,-1.5e-02)	1.0e-03 (+1.0e-02,-1.4e-04)	2.3	31	2.5e-01	4.7e+01	1100
24	00 54 57.9	-71 44 52	3.9	0.26 (+0.03,-0.02)	0.0e+00 (+5.0e-02,-0.0e+00)	2.1e-04 (+1.0e-02,-3.0e-05)	1.2	49	1.4e-01	3.6e-01	500
25	00 55 16.9	-73 59 52	8.5	0.19 (+0.03,-0.02)	1.0e+00 (+1.0e+00,-5.0e-01)	4.0e-04 (+1.0e-02,-5.6e-05)	2.3	74	3.3e-01	3.5e-01	400
26	00 55 45.2	-72 14 53	2.9	0.36 (+0.03,-0.03)	0.0e+00 (+5.0e-02,-0.0e+00)	7.4e-04 (+1.0e-02,-1.0e-04)	1.7	47	4.2e-01	2.4e+00	600
27	00 56 09.9	-72 29 54	2.7	0.26 (+0.03,-0.02)	1.0e+00 (+1.0e+00,-5.0e-01)	3.9e-03 (+1.1e-02,-5.5e-04)	1.5	45	2.7e+00	6.3e+00	500
28	00 56 35.3	-72 44 55	3.9	0.25 (+0.03,-0.02)	1.0e+00 (+1.0e+00,-5.0e-01)	1.6e-03 (+1.0e-02,-2.3e-04)	1.6	49	1.1e+00	2.3e+00	500
29	00 57 01.5	-72 59 56	5.5	0.31 (+0.03,-0.03)	1.0e+00 (+1.0e+00,-5.0e-01)	8.9e-04 (+1.0e-02,-1.2e-04)	1.9	61	5.5e-01	2.1e+00	500
30	00 57 28.5	-73 14 56	2.6	0.23 (+0.03,-0.02)	9.8e-01 (+1.0e+00,-4.9e-01)	7.8e-04 (+1.0e-02,-1.1e-04)	1.3	41	5.7e-01	1.0e+00	400
31	00 58 09.4	-71 44 58	3.1	0.20 (+0.03,-0.02)	0.0e+00 (+5.0e-02,-0.0e+00)	8.9e-04 (+1.0e-02,-1.3e-04)	1.6	44	7.3e-01	8.2e-01	400
32	00 58 35.4	-71 59 58	4.7	0.24 (+0.03,-0.02)	1.0e+00 (+1.0e+00,-5.0e-01)	4.4e-03 (+1.1e-02,-6.2e-04)	1.5	62	3.2e+00	6.2e+00	500
33	00 59 02.0	-72 14 59	2.9	0.28 (+0.03,-0.02)	0.0e+00 (+5.0e-02,-0.0e+00)	1.8e-03 (+1.1e-02,-2.5e-04)	1.1	50	1.2e+00	3.2e+00	500
34	00 59 29.5	-72 30 00	5.0	0.25 (+0.03,-0.02)	1.0e+00 (+1.0e+00,-5.0e-01)	3.7e-03 (+1.1e-02,-5.2e-04)	1.8	63	2.6e+00	5.8e+00	500
35	00 59 57.6	-72 45 01	6.2	0.71 (+0.02,-0.06)	3.7e-01 (+4.2e-01,-1.9e-01)	5.0e-04 (+1.0e-02,-6.9e-05)	1.3	70	1.9e-01	6.0e+00	800
36	01 00 56.7	-73 15 03	4.0	0.23 (+0.03,-0.02)	9.9e-01 (+1.0e+00,-4.9e-01)	6.2e-04 (+1.0e-02,-8.6e-05)	1.0	52	4.6e-01	7.9e-01	400
37	01 01 49.5	-72 00 05	4.8	0.43 (+0.03,-0.04)	0.0e+00 (+5.0e-02,-0.0e+00)	1.2e-03 (+1.0e-02,-1.7e-04)	1.4	68	6.2e-01	5.6e+00	600
38	01 02 18.8	-72 15 06	6.0	0.89 (+0.02,-0.08)	0.0e+00 (+5.0e-02,-0.0e+00)	9.3e-04 (+1.0e-02,-1.3e-04)	2.5	75	3.1e-01	1.8e+01	900
39	01 02 49.0	-72 30 07	5.1	0.92 (+0.02,-0.08)	0.0e+00 (+5.0e-02,-0.0e+00)	5.1e-04 (+1.0e-02,-7.1e-05)	1.5	62	1.6e-01	1.0e+01	900
40	01 03 19.9	-72 45 08	2.6	0.35 (+0.03,-0.03)	1.0e+00 (+1.0e+00,-5.0e-01)	6.7e-04 (+1.0e-02,-9.4e-05)	1.6	41	3.9e-01	1.9e+00	500
41	01 04 02.5	-71 30 09	3.0	0.24 (+0.03,-0.02)	9.7e-01 (+1.0e+00,-4.8e-01)	2.7e-04 (+1.0e-02,-3.8e-05)	1.4	40	2.0e-01	3.8e-01	500
42	01 04 24.9	-73 15 10	6.7	0.19 (+0.03,-0.02)	6.2e-01 (+6.7e-01,-3.1e-01)	4.9e-04 (+1.0e-02,-6.9e-05)	1.3	63	4.1e-01	4.2e-01	400
43	01 04 32.6	-71 45 10	7.3	0.21 (+0.03,-0.02)	9.9e-01 (+1.0e+00,-5.0e-01)	1.9e-03 (+1.1e-02,-2.7e-04)	1.7	68	1.5e+00	2.1e+00	400
44	01 05 03.7	-72 00 11	3.5	0.32 (+0.03,-0.03)	1.0e+00 (+1.0e+00,-5.0e-01)	3.5e-03 (+1.1e-02,-4.9e-04)	1.3	59	2.1e+00	8.7e+00	500
45	01 05 35.7	-72 15 12	4.2	0.29 (+0.03,-0.03)	1.0e+00 (+1.0e+00,-5.0e-01)	2.6e-03 (+1.1e-02,-3.6e-04)	1.2	60	1.7e+00	5.3e+00	500
46	01 06 08.5	-72 30 13	3.4	0.90 (+0.02,-0.08)	0.0e+00 (+5.0e-02,-0.0e+00)	5.1e-04 (+1.0e-02,-7.1e-05)	2.1	51	1.7e-01	9.8e+00	900
47	01 07 11.6	-71 30 15	4.3	0.23 (+0.03,-0.02)	1.0e+00 (+1.0e+00,-5.0e-01)	5.6e-04 (+1.0e-02,-7.9e-05)	1.8	51	4.2e-01	7.1e-01	400
48	01 07 17.1	-73 00 15	8.2	0.20 (+0.03,-0.02)	9.9e-01 (+1.0e+00,-5.0e-01)	1.7e-03 (+1.1e-02,-2.4e-04)	1.3	69	1.4e+00	1.6e+00	400
49	01 07 53.1	-73 15 16	9.1	0.16 (+0.03,-0.01)	0.0e+00 (+5.0e-02,-0.0e+00)	3.6e-04 (+1.0e-02,-5.1e-05)	1.9	73	3.4e-01	2.2e-01	400
50	01 08 30.2	-73 30 18	6.7	0.19 (+0.03,-0.02)	1.0e+00 (+1.0e+00,-5.0e-01)	1.4e-03 (+1.0e-02,-2.0e-04)	1.0	62	1.2e+00	1.2e+00	400

Table D.2: Continued (SMC).

1	2		3	4	5	6	7	8	9	10	11
No	Center of Region		No of events $[10^3]$	T_{MC} [keV]	$N_{\mathrm{H\,MC}}$ $[10^{22}\ \mathrm{cm}^{-2}]$	$EM_{\square}$ $[\mathrm{cm}^{-5}]$	red. χ^2	DOF	$L_{\square}$ $[10^{36}$ erg/s]	Δl [kpc]	v [km/s]
	RA Dec (J2000.0)										
51	01 08 52.5 -72 15 18		6.0	0.24 (+0.03,−0.02)	1.0e+00 (+1.0e+00,−5.0e−01)	1.0e−03 (+1.0e−02,−1.4e−04)	1.5	64	7.4e−01	1.4e+00	400
52	01 09 28.1 -72 30 19		4.9	0.22 (+0.03,−0.02)	1.0e+00 (+1.0e+00,−5.0e−01)	9.9e−04 (+1.0e−02,−1.4e−04)	0.9	55	7.4e−01	1.2e+00	400
53	01 10 04.7 -72 45 21		5.4	0.14 (+0.03,−0.01)	1.0e−04 (+5.0e−02,−5.0e−05)	1.3e−04 (+1.0e−02,−1.8e−05)	1.2	54	1.3e−01	5.7e−02	300
54	01 11 21.3 -73 15 23		5.0	0.14 (+0.03,−0.01)	0.0e+00 (+5.0e−02,−0.0e+00)	7.9e−04 (+1.0e−02,−1.1e−04)	1.8	50	7.8e−01	3.7e−01	300
55	01 12 01.5 -73 30 25		5.2	0.14 (+0.03,−0.01)	0.0e+00 (+5.0e−02,−0.0e+00)	8.9e−04 (+1.0e−02,−1.2e−04)	1.6	55	8.7e−01	4.5e−01	400
56	01 12 47.7 -72 30 26		3.2	0.16 (+0.03,−0.01)	2.0e−04 (+5.0e−02,−1.0e−04)	3.1e−04 (+1.0e−02,−4.3e−05)	1.3	44	2.8e−01	2.0e−01	400
57	01 13 27.1 -72 45 27		3.1	0.11 (+0.03,−0.01)	4.5e−01 (+5.0e−01,−2.3e−01)	1.8e−06 (+1.0e−02,−2.5e−07)	2.4	39	2.1e−03	4.9e−04	300
58	01 14 49.6 -73 15 30		5.1	0.14 (+0.03,−0.01)	0.0e+00 (+5.0e−02,−0.0e+00)	9.6e−04 (+1.0e−02,−1.3e−04)	2.2	54	9.6e−01	4.4e−01	300
59	01 16 17.2 -73 45 33		2.9	0.21 (+0.03,−0.02)	1.0e+00 (+1.0e+00,−5.0e−01)	1.6e−03 (+1.0e−02,−2.2e−04)	1.2	41	1.2e+00	1.8e+00	400
60	01 19 04.3 -73 30 39		1.8	0.11 (+0.03,−0.01)	4.0e−01 (+4.5e−01,−2.0e−01)	1.0e−02 (+1.3e−02,−1.4e−03)	2.3	36	1.1e+01	3.1e+00	300
61	01 20 58.3 -73 00 43		1.7	1.40 (+0.02,−0.13)	3.0e−02 (+8.0e−02,−1.5e−02)	1.0e−03 (+1.0e−02,−1.4e−04)	2.5	32	2.5e−01	4.7e+01	1100
62	01 22 35.7 -73 30 46		2.6	0.14 (+0.03,−0.01)	1.0e−04 (+5.0e−02,−5.0e−05)	5.7e−04 (+1.0e−02,−8.0e−05)	1.5	39	5.7e−01	2.6e−01	300

Bibliography

Abbott, D. C. 1982, ApJ, 263, 723

Antonucci, R. 1993, ARA&A, 31, 473

Ardavan, H. 1973, ApJ, 184, 435

Aschenbach, B. 1988, Appl.Optics, 27, 1404

Aschenbach, B., Briel, U. G., Haberl, F., Bräuninger, H., Burkert, W., Oppitz, A., Gondoin, P., & Lumb, D. 2000, Proc. SPIE, 4012, 731

Bildsten, L., Chakrabarty, D., Chiu, J., Finger, M. H., Koh, D. T., Nelson, R. W., Prince, T. A., Rubin, B. C., Scott, D. M., Stollberg, M., Vaughan, B. A., Wilson, C. A., & Wilson, R. B. 1997, ApJS, 113, 367

Bomans, D. J., Dennerl, K., & Kürster, M. 1994, A&A, 283, L21

Borkowski, K. J. 2000, in Revista Mexicana de Astronomia y Astrofisica Conference Series, Vol. 9, 288–289

Branch, D. & Tammann, G. A. 1992, ARA&A, 30, 359

Braunsfurth, E. & Feitzinger, J. V. 1983, A&A, 127, 113

Bregman, J. N. 1980, ApJ, 236, 577

Breitschwerdt, D., Freyberg, M. J., & Trümper, J. 1998, Berlin Springer Verlag Lecture Notes in Physics, v.506, 506

Brück, M. T. 1980, A&A, 87, 92

Bruhweiler, F. C., Klinglesmith, D. A., Gull, T. R., & Sofia, S. 1987, ApJ, 317, 152

Brunet, J. P., Imbert, N., Martin, N., Mianes, P., Prevot, L., Rebeirot, E., & Rousseau, J. 1975, A&AS, 21, 109

Burrows, A., Hayes, J., & Fryxell, B. A. 1995, ApJ, 450, 830

Burrows, D. N. & Mendenhall, J. A. 1991, Nature, 351, 629

Castor, J., Weaver, R., & McCray, R. 1975, ApJ, 200, L107

Chen, L., Fabian, A. C., & Gendreau, K. C. 1997, MNRAS, 285, 449

Chevalier, R. A. 1977, ARA&A, 15, 175

Chu, Y. 1997, AJ, 113, 1815

Chu, Y., Kennicutt, R. C., Snowden, S. L., Smith, R. C., Williams, R. M., & Bomans, D. J. 1997, PASP, 109, 554

Cioffi, D. F., McKee, C. F., & Bertschinger, E. 1988, ApJ, 334, 252

Cioni, M., Loup, C., Habing, H. J., Fouqué, P., Bertin, E., Deul, E., Egret, D., Alard, C., de Batz, B., Borsenberger, J., Dennefeld, M., Epchtein, N., Forveille, T., Garzón, F., Hron, J., Kimeswenger, S., Lacombe, F., Le Bertre, T., Mamon, G. A., Omont, A., Paturel, G., Persi, P., Robin, A., Rouan, D., Simon, G., Tiphène, D., Vauglin, I., & Wagner, S. 2000, A&AS, 144, 235

Cohn, H. & York, D. G. 1977, ApJ, 216, 408

Corbet, R., Marshall, F. E., Lochner, J. C., Ozaki, M., & Ueda, Y. 1998, IAU Circ., 6803, 1

Corbet, R. H. D. 1986, MNRAS, 220, 1047

Cowley, A. P., Crampton, D., Hutchings, J. B., Helfand, D. J., Hamilton, T. T., Thorstensen, J. R., & Charles, P. A. 1984, ApJ, 286, 196

Cowley, A. P., Schmidtke, P. C., McGrath, T. K., Ponder, A. L., Fertig, M. R., Hutchings, J. B., & Crampton, D. 1997, PASP, 109, 21

Cox, D. P. 1972, ApJ, 178, 143

Cox, D. P. & Smith, B. W. 1974, ApJ, 189, L105

Crampton, D., Gussie, G., Cowley, A. P., & Schmidtke, P. C. 1997, AJ, 114, 2353

David, L. P., Harnden, J. F. R., Kearns, K. E., & Zombeck, M. V. 1996, The ROSAT High Resolution Imager (HRI) (USRSDC/SAO Calibration Report, February 1996, revised)

Dickey, J. M. & Lockman, F. J. 1990, ARA&A, 28, 215

Dyson, J. E. & Williams, D. A. 1980, *Physics of the interstellar medium* (Manchester: Manchester University Press)

Egger, R. J. & Aschenbach, B. 1995, A&A, 294, L25

Ehle, M., Pietsch, W., & Beck, R. 1995, A&A, 295, 289

Ehle, M., Pietsch, W., Beck, R., & Klein, U. 1998, A&A, 329, 39

Feigelson, E. D. & Decampli, W. M. 1981, ApJ, 243, L89

Filipović, M. D., Haberl, F., & Pietsch, W. M. D. H. 2000, A&A, 353, 129

Filipović, M. D., Haynes, R. F., White, G. L., & Jones, P. A. 1998, A&AS, 130, 421

Filipović, M. D., Haynes, R. F., White, G. L., Jones, P. A., Klein, U., & Wielebinski, R. 1995, A&AS, 111, 311

Gahm, G. F. 1980, ApJ, 242, L163

Gardiner, L. T. & Hatzidimitriou, D. 1992, MNRAS, 257, 195

Gendreau, K. C., Mushotzky, R., Fabian, A. C., Holt, S. S., Kii, T., Serlemitsos, P. J., Ogasaka, Y., Tanaka, Y., Bautz, M. W., Fukazawa, Y., Ishisaki, Y., Kohmura, Y., Makishima, K., Tashiro, M., Tsusaka, Y., Kunieda, H., Ricker, G. R., & Vanderspek, R. K. 1995, PASJ, 47, L5

Giacconi, R., Murray, S., Gursky, H., Kellogg, E., Schreier, E., & Tananbaum, H. 1972, ApJ, 178, 281

Gochermann, J., Grothues, H., Östreicher, M. O., Berghoefer, T., & Schmidt-Kaler, T. 1993, A&AS, 99, 591

Goudis, C. & Meaburn, J. 1978, A&A, 68, 189

Grothues, H., Östreicher, M. O., Gochermann, J., Tappert, C., Zaum, A., Brugger, H. R., & Schmidt-Kaler, T. 1997, A&AS, 121, 247

Haberl, F., Filipović, M. D., Pietsch, W., & Kahabka, P. 2000, A&AS, 142, 41

Haberl, F. & Pietsch, W. 1999a, A&AS, 139, 277

—. 1999b, A&A, 344, 521

Hasinger, G. 1994, in Reviews of Modern Astronomy, Vol. 7, 129–150

Henize, K. G. 1956, ApJS, 2, 315

Hoeg, E., Bässgen, G., Bastian, U., Egret, D., Fabricius, C., Großmann, V., Halbwachs, J. L., Makarov, V. V., Perryman, M. A. C., Schwekendiek, P., Wagner, K., & Wicenec, A. 1997, A&A, 323, L57

Hughes, J. P. & Smith, R. C. 1994, AJ, 107, 1363

Hutchings, J. B. 1970, MNRAS, 147, 367

Immler, S., Vogler, A., Ehle, M., & Pietsch, W. 1999, A&A, 352, 415

Inoue, H., Koyama, K., Matsuoka, M., Ohashi, T., Tanaka, Y., & Tsunemi, H. 1979, ApJ, 227, L85

Israel, G. L., Stella, L., Campana, S., Covino, S., Ricci, D., & Oosterbroek, T. 1998, IAU Circ., 6999, 1

Israel, G. L., Stella, L., Covino, S., Campana, S., & Mereghetti, S. 1999, IAU Circ., 7101, 1

Isserstedt, J. 1984, A&A, 131, 347

Janka, H. & Müller, E. 1996, A&A, 306, 167

Jenkins, E. B. 1978a, ApJ, 219, 845

—. 1978b, ApJ, 220, 107

Jenkins, E. B. & Meloy, D. A. 1974, ApJ, 193, L121

Johnson, H. E. & Axford, W. I. 1971, ApJ, 165, 381

Jones, L. R., Pye, J. P., McHardy, I. M., & Fairall, A. P. 1985, Space Science Reviews, 40, 693

Kahabka, P. & Pietsch, W. 1996, A&A, 312, 919

Kahabka, P., Pietsch, W., Filipović , M. D., & Haberl, F. 1999, A&AS, 136, 81

Kahabka, P. & van den Heuvel, E. P. J. 1997, ARA&A, 35, 69

Kennicutt, R. C. 1984, ApJ, 287, 116

Kim, S., Staveley-Smith, L., Dopita, M. A., Freeman, K. C., Sault, R. J., Kesteven, M. J., & McConnell, D. 1998, ApJ, 503, 674

Kim, S., Staveley-Smith, L., & Sault, R. J. 2001, in Gas and Galaxy Evolution, eds. J.E. Hibbard, M.P. Rupen, & J.H. van Gorkom (ASP Conference Series)

Lamb, R. C., Prince, T. A., Macomb, D. J., & Finger, M. H. 1999, IAU Circ., 7081, 4

Landau, L. D. & Lifschitz, E. M. 1991, Lehrbuch der Theoretischen Physik, Band 6, *Hydrodynamik* (Berlin: Akademie Verlag)

Leong, C., Kellogg, E., Gursky, H., Tananbaum, H., & Giacconi, R. 1971, ApJ, 170, L67

Long, K. S., Helfand, D. J., & Grabelsky, D. A. 1981, ApJ, 248, 925

Lucke, P. B. & Hodge, P. W. 1970, AJ, 75, 171

Lucy, L. B. & Solomon, P. M. 1970, ApJ, 159, 879

Maccacaro, T., Gioia, I. M., Wolter, A., Zamorani, G., & Stocke, J. T. 1988, ApJ, 326, 680

Maiolino, R., Salvati, M., Antonelli, L. A., Comastri, A., Fiore, F., Ghinassi, F., Gilli, R., La Franca, F., Mannucci, F., Risaliti, G., Thompson, D., & Vignali, C. 2000, A&A, 355, L47

Mansfield, V. N. & Salpeter, E. E. 1974, ApJ, 190, 305

Mark, H., Price, R., Rodrigues, R., Seward, F. D., & Swift, C. D. 1969, ApJ, 155, L143

Mathews, W. G. & Baker, J. C. 1971, ApJ, 170, 241

McCray, R. & Kafatos, M. 1987, ApJ, 317, 190

McCray, R. & Snow, T. P. 1979, ARA&A, 17, 213

McKee, C. F. 1974, ApJ, 188, 335

McKee, C. F. & Ostriker, J. P. 1977, ApJ, 218, 148

McKibben Nail, V. & Shapley, H. 1953, Proceedings of the National Academy of Science, 39, 358

Meaburn, J. 1980, MNRAS, 192, 365

Meyssonnier, N. & Azzopardi, M. 1993, A&AS, 102, 451

Miller, D. L. & Branch, D. 1990, AJ, 100, 530

Minkowski, R. 1941, PASP, 53, 224

Miyaji, T., Ishisaki, Y., Ogasaka, Y., Ueda, Y., Freyberg, M. J., Hasinger, G., & Tanaka, Y. 1998, A&A, 334, L13

Monet, D. 1996, in American Astronomical Society Meeting, Vol. 188, 5404

Monet, D. G. 1998, in American Astronomical Society Meeting, Vol. 193, 12003

Morgan, D. H. 1994, A&AS, 103, 235

Murai, T. & Fujimoto, M. 1980, PASJ, 32, 581

Murphy, M. T. & Bessell, M. S. 2000, MNRAS, 311, 741

Nagase, F. 1989, PASJ, 41, 1

Nomoto, K. 1982a, ApJ, 257, 780

—. 1982b, ApJ, 253, 798

Orio, M. & Greiner, J. 1999, A&A, 344, L13

Pakull, M., Brunner, H., Staubert, A., Pietsch, W., & Beuermann, K. 1985, Space Science Reviews, 40, 379

Pfeffermann, E., Briel, U. G., Hippmann, H., Kettenring, G., Metzner, G., Predehl, P., Reger, G., Stephan, K., Zombeck, M., Chappell, J., & Murray, S. S. 1987, Proc. SPIE, 733, 519

Pietsch, W., Dennerl, K., Kahabka, P., Pakull, M., & Schaeidt, S. 1996, in Roentgenstrahlung from the Universe, 389–390

Plucinsky, P. P., Snowden, S. L., Briel, U. G., Hasinger, G., & Pfefferman, E. 1996, ApJ, 458, 861

Plucinsky, P. P., Snowden, S. L., Briel, U. G., Hasinger, G., & Pfeffermann, E. 1993, ApJ, 418, 519

Points, S. D., Chu, Y.-H., Snowden, S. L., & Staveley-Smith, L. 2000, ApJ, 545, 827

Price, R. E., Groves, D. J., Rodrigues, R. M., Seward, F. D., Swift, C. D., & Toor, A. 1971, ApJ, 168, L7

Raymond, J. C., Cox, D. P., & Smith, B. W. 1976, ApJ, 204, 290

Raymond, J. C. & Smith, B. W. 1977, ApJS, 35, 419

Rogerson, J. B., York, D. G., Drake, J. F., Jenkins, E. B., Morton, D. C., & Spitzer, L. 1973, ApJ, 181, L110

Russell, S. C. & Dopita, M. A. 1992, ApJ, 384, 508

Sanduleak, N. 1970, Contributions from the Cerro Tololo Inter-American Observatory, 89, 1

Sargent, W. L. W. & Searle, L. 1970, ApJ, 162, L155

Sasaki, M., Haberl, F., & Pietsch, W. 2000a, A&AS, 143, 391

—. 2000b, A&AS, 147, 75

Schmidtke, P. C., Cowley, A. P., Crane, J. D., Taylor, V. A., McGrath, T. K., Hutchings, J. B., & Crampton, D. 1999, AJ, 117, 927

Schmidtke, P. C., Cowley, A. P., Frattare, L. M., McGrath, T. K., Hutchings, J. B., & Crampton, D. 1994, PASP, 106, 843

Sedov, L. I. 1946a, Dokl. Akad. Nauk SSSR, 42, 17

—. 1946b, Prikl. Mat. Mekh., 10, 241, No. 2

Seward, F. D. & Mitchell, M. 1981, ApJ, 243, 736

Shapiro, P. R. & Field, G. B. 1976, ApJ, 205, 762

Shull, J. M. & York, D. G. 1977, ApJ, 211, 803

Snowden, S. L. 1999, in IAU Symp. 190: New Views of the Magellanic Clouds, Vol. 190, 32

Snowden, S. L. & Freyberg, M. J. 1993, ApJ, 404, 403

Snowden, S. L., McCammon, D., Burrows, D. N., & Mendenhall, J. A. 1994, ApJ, 424, 714

Snowden, S. L., Mebold, U., Hirth, W., Herbstmeier, U., & Schmitt, J. H. M. 1991, Science, 252, 1529

Snowden, S. L. & Petre, R. 1994, ApJ, 436, L123

Snowden, S. L., Plucinsky, P. P., Briel, U., Hasinger, G., & Pfeffermann, E. 1992, ApJ, 393, 819

Spitzer, L. J. 1956, ApJ, 124, 20

—. 1990, ARA&A, 28, 71

Stanimirovic, S., Staveley-Smith, L., Dickey, J. M., Sault, R. J., & Snowden, S. L. 1999, MNRAS, 302, 417

Staveley-Smith, L., Sault, R. J., Hatzidimitriou, D., Kesteven, M. J., & McConnell, D. 1997, MNRAS, 289, 225

Stevens, J. B., Coe, M. J., & Buckley, D. A. H. 1999, MNRAS, 309, 421

Strüder, L., Briel, U., Dennerl, K., Hartmann, R., Kendziorra, E., Meidinger, N., Pfeffermann, E., Reppin, C., Aschenbach, B., Bornemann, W., Bräuninger, H., Burkert, W., Elender, M., Freyberg, M., Haberl, F., Hartner, G., Heuschmann, F., Hippmann, H., Kastelic, E., Kemmer, S., Kettenring, G., Kink, W., Krause, N., Müller, S., Oppitz, A., Pietsch, W., Popp, M., Predehl, P., Read, A., Stephan, K. H., Stötter, D., Trümper, J., Holl, P., Kemmer, J., Soltau, H., Stötter, R., Weber, U., Weichert, U., von Zanthier, C., Carathanassis, D., Lutz, G., Richter, R. H., Solc, P., Böttcher, H., Kuster, M., Staubert, R., Abbey, A., Holland, A., Turner, M., Balasini, M., Bignami, G. F., La Palombara, N., Villa, G., Buttler, W., Gianini, F., Lainé, R., Lumb, D., & Dhez, P. 2001, A&A, 365, L18

Tanaka, Y. & Bleeker, J. A. M. 1977, Space Science Reviews, 20, 815

Taylor, G. I. 1950a, Proc. R. Soc. London A, 201, 159

—. 1950b, Proc. R. Soc. London A, 201, 175

Tinney, C. G., Da Costa, G. S., & Zinnecker, H. 1997, MNRAS, 285, 111

Truelove, J. K. & McKee, C. F. 1999, ApJS, 120, 299

Trümper, J. 1982, Advances in Space Research, 2, 241

Trümper, J., Hasinger, G., Aschenbach, B., Braeuninger, H., & Briel, U. G. 1991, Nature, 349, 579

van den Bergh, S. 1999, in IAU Symp. 190: New Views of the Magellanic Clouds, Vol. 190, 569

van den Heuvel, E. P. J., Bhattacharya, D., Nomoto, K., & Rappaport, S. A. 1992, A&A, 262, 97

van der Klis, M. 2000, ARA&A, 38, 717

Verbunt, F. 1993, ARA&A, 31, 93

Wang, Q. 1991, ApJ, 377, L85

Wang, Q., Hamilton, T., Helfand, D. J., & Wu, X. 1991, ApJ, 374, 475

Wang, Q. & Helfand, D. J. 1991a, ApJ, 373, 497

—. 1991b, ApJ, 379, 327

Wang, Q. & Wu, X. 1992, ApJS, 78, 391

Weaver, R., McCray, R., Castor, J., Shapiro, P., & Moore, R. 1977, ApJ, 218, 377

Weiler, K. W. & Sramek, R. A. 1988, ARA&A, 26, 295

Westerlund, B. E. 1990, A&A Rev., 2, 29

Wheeler, J. C. & Harkness, R. P. 1990, Reports of Progress in Physics, 53, 1467

Wheeler, J. C., Piran, T., & Weinberg, S., eds. 1990, Jerusalem Winter School for Theoretical Physics. Supernovae. Volume 6, Jerusalem, Dec. 28, 1988- Jan. 5, 1989.

Williamson, F. O., Sanders, W. T., Kraushaar, W. L., McCammon, D., Borken, R., & Bunner, A. N. 1974, ApJ, 193, L133

Wilms, J., Allen, A., & McCray, R. 2000, ApJ, 542, 914

Woosley, S. E., Langer, N., & Weaver, T. A. 1993, ApJ, 411, 823

Yokogawa, J. & Koyama, K. 1998a, IAU Circ., 6853, 2

—. 1998b, IAU Circ., 7028, 1

York, D. G. 1974, ApJ, 193, L127

—. 1977, ApJ, 213, 43

Zimmermann, H. U., Becker, W., Belloni, T., Döbereiner, S., Izzo, C., Kahabka, P., & Schwentker, O. 1994, EXSAS User's Guide (MPE report 257)

Zwicky, F. 1971, in Publ. F. Zwicky, Guemligen (BE), Switzerland-388 (1971), 1

Acknowledgments

I would like to express my gratitude to

- Prof. Dr. Joachim Trümper for giving me the opportunity to work in the field of X-ray astronomy in the ROSAT group of the Max-Planck-Institut für extraterrestrische Physik and supporting me in the intention to become a scientist,

- my supervisors Dr. Wolfgang Pietsch and Dr. Frank Haberl for their help and guidance, especially for providing me with all kinds of tools for analyzing X-ray data and how to write scientific papers,

- Dr. Dieter Breitschwerdt for the fruitful discussions about the Interstellar Medium and the modeling of X-ray spectrum of hot thin plasma,

- Dr. Miroslav Filipović for unveiling the understandings about supernova remnants in a radio observer's point of view and his advices about 'how to survive as a Ph. D. student',

- Dr. Sungeun Kim at the Harvard-Smithsonian Center for Astrophysics and Dr. Lister Staveley-Smith at the Australia Telescope National Facility for kindly providing with H I column density maps of the LMC and the SMC,

- Achim Bohnet, Lars Klose, and Joachim Paul not only for the support on computers and software, but also for arranging the after-work sport program, and in particular Achim for cycling together from Munich to Garching, offering tea, conversations about Perl, favorite colors, or buddhism, and being the second mandatory person to order a pizza in the evening,

- Harald Baumgartner for providing us always with quota and good hardware,

- Dr. Vadim Burwitz, Dr. Matilde Fernandez, Nuria Huélamo Bautista, Brigitte König, Dr. Thomas Reiprich, and Dr. Rodrigo Supper for scientific advices as well as nice coffee and merienda time conversations.

Curriculum Vitae

Name:	Manami Sasaki
Date of Birth:	September 27, 1972
Place of Birth:	Tokyo, Japan
Nationality:	Japanese

Education:

Apr. 1979 - Mar. 1981	Musashino-Daiichi-Shogakko (Primary School) in Tokyo, Japan
Apr. 1981 - Jul. 1985	Grundschule Steinbach im Taunus mit Förderstufe, Germany
Apr. 1981 - Mar. 1989	Japanische Schule Frankfurt am Main, Germany
May 1992	Graduation Highschool, 'Abitur', Adolf-Reichwein-Gymnasium, Heusenstamm, Germany
Sep. 1992 - Jul. 1994	Study of Physics, 'Vordiplom', Karl-Ruprechts-Universität Heidelberg, Germany
Aug. 1994 - Jul. 1997	Study of Physics, 'Diplom', Karl-Ruprechts-Universität Heidelberg, Germany

Diploma Thesis:

Jul. 1996 - Jul. 1997	Landessternwarte Heidelberg-Königstuhl, Karl-Ruprechts-Universität Heidelberg, Supervisor: Priv.-Doz. Dr. Stefan Wagner Title: *"Kurzzeitvariabilität von Blazaren im nahen Infraroten"*

Current Position:

Since Sep. 1998	Research Assistant at the Max-Planck-Institut für extraterrestrische Physik, Garching, Germany

Previous Positions:

Oct. 1996 - Feb. 1997	Teaching Assistant at the Karl-Ruprechts-Universität Heidelberg, Faculty of Physics and Astronomy
Oct. 1997 - Jan. 1998	Research Assistant at the Landessternwarte Heidelberg
Feb. 1998 - Aug. 1998	Research Assistant at the Technische Universität München, Physik-Department E19

List of Publications

Sasaki, M., Haberl, F., & Pietsch, W.
"ROSAT HRI catalog of X-ray sources in the LMC region"
Astronomy & Astrophysics Supplement, 2000, 143, 391

Haberl, F. & Sasaki, M.
"Doubling the number of Be/X-ray binaries in the SMC"
Astronomy & Astrophysics, 2000, 359, 573

Sasaki, M., Haberl, F., & Pietsch, W.
"ROSAT HRI catalog of X-ray sources in the SMC region"
Astronomy & Astrophysics Supplement, 2001, 147, 75

Sasaki, M., Stadlbauer, T.F.X., Haberl, F., Filipović, M.D., & Bennie, P.J.
"XMM-Newton EPIC-PN observation of SMC SNR 0102-72.3"
Astronomy & Astrophysics, 2001, 365, L237

Sasaki, M., Haberl, F., Keller, S., & Pietsch, W.
"Discovery of pulsations from the Be/X-ray binary RX J0101.3-7211 in the SMC
by XMM-Newton"
Astronomy & Astrophysics, 2001, 369, L29